

Extended and point defects assisted phenomena in ZnO nanorods

By

Avanendra Singh

PHYS11201204008

**National Institute of Science Education and Research
Bhubaneswar**

*A thesis submitted to the
Board of Studies in Physical Sciences*

*In partial fulfillment of requirements
For the Degree of*

**DOCTOR OF PHILOSOPHY
of**

HOMI BHABHA NATIONAL INSTITUTE

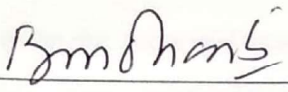
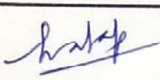
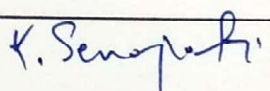
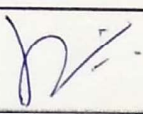
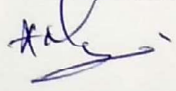
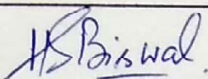


April, 2018

Homi Bhabha National Institute

Recommendations of the Viva Voce Committee

As members of the Viva Voce Committee, we certify that we have read the dissertation prepared by **Mr. Avanendra Singh** entitled "**Extended and point defects assisted phenomena in ZnO nanorods**" and recommend that it may be accepted as fulfilling the thesis requirement for the award of Degree of Doctor of Philosophy.

Chairman – Prof. Bedangadas Mohanty		Date: 20/4/2018
Guide / Convener – Dr. Pratap Kumar Sahoo		Date: 20/04/2018
Co-guide - Dr. Kartikeswar Senapati		Date: 20/04/2018
Examiner – Prof. Jitendra Pratap Singh		Date: 20/4/18
Member 1 - Dr. Prasanjit Samal		Date: 20-4-18
Member 2 - Dr. Ajaya Kumar Nayak		Date: 20/04/18
Member 3 - Dr. Himansu Sekhar Biswal		Date: 20/04/2018

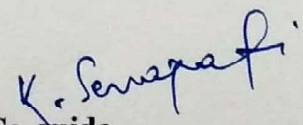
Final approval and acceptance of this thesis is contingent upon the candidate's submission of the final copies of the thesis to HBNI.

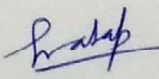
We hereby certify that I/we have read this thesis prepared under my/our direction and recommend that it may be accepted as fulfilling the thesis requirement.

Date: 20/04/2018

Place:

SPS, NISER

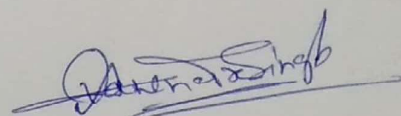

Co-guide
Dr. Kartikeswar Senapati


Guide
Dr. Pratap Kumar Sahoo

STATEMENT BY AUTHOR

This dissertation has been submitted in partial fulfillment of requirements for an advanced degree at Homi Bhabha National Institute (HBNI) and is deposited in the Library to be made available to borrowers under rules of the HBNI.

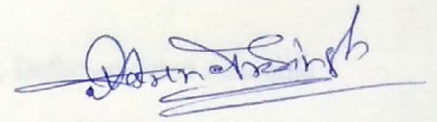
Brief quotations from this dissertation are allowable without special permission, provided that accurate acknowledgment of source is made. Requests for permission for extended quotation from or reproduction of this manuscript in whole or in part may be granted by the Competent Authority of HBNI when in his or her judgment the proposed use of the material is in the interests of scholarship. In all other instances, however, permission must be obtained from the author.



(Avanendra Singh)

DECLARATION

I, hereby declare that the investigation presented in the thesis has been carried out by me. The work is original and has not been submitted earlier as a whole or in part for a degree/diploma at this or any other Institution/University.



(Avanendra Singh)

List of Publications arising from the thesis

Journal:

1. **Avanendra Singh***, Kartik Senapati, Biswarup Satpati, Mohit Kumar, Pratap K. Sahoo, Nanoscale interface engineering in ZnO twin nanorods for proposed phonon tunnel devices, *Phys. Chem. Chem. Phys.*, 2015, 17, 4277-4282.
2. **Avanendra Singh***, Samir Kumar, Ritwick Das and Pratap K. Sahoo, Defect-assisted saturable absorption characteristics in Mn-doped ZnO nanorods, *RSC Adv.*, 2015, 5, 88767-88772.
3. **Avanendra Singh***, Kartik Senapati, K. K. Nanda, Pratap K. Sahoo, Strong Red luminescent twin ZnO nanorods for noncontact Nano-thermometry applications, *MRS Advances*, 2016, 1, 869-874.
4. **Avanendra Singh***, Kartik Senapati, Mohit Kumar, Tapobrata Som, Anil K. Sinha, and Pratap K. Sahoo, Role of work function in field emission enhancement of Au island decorated vertically aligned ZnO nanotapers, *Appl. Surf. Sci.*, 2017, 411, 117.
5. **Avanendra Singh***, K. Senapati, D. P. Datta, R. Singh, T. Som, S. Bhunia, D. Kanjilal, Pratap K. Sahoo, Synthesis of p-n junctions in ZnO nanorods by O⁺ ion implantation *Nucl. Instrum. Methods Phys. Res. B*, 2017, 409, 143-146.
6. **Avanendra Singh***, Kartik Senapati, Biswarup Satpati, Pratap K. Sahoo, Suppression of near band edge emission in specially engineered ZnO twin nanorods, *Phys. Chem. Chem. Phys.*, 2017, 19, 14012-14019.

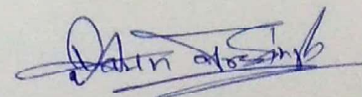
Conferences:

1. P. C. Pradhan, S. Bhartiya, **Avanendra Singh**, A. Majhi, A. Gome, R. Dhawan, M. Nayak, P. K. Sahoo, S. K. Rai, and V. R. Reddy Fabrication and characterization of W/B₄C lamellar multilayer grating and NbC/Si multilayer phase-shift reflector, *SPIE Conf. Proced.*, 2017, 10386, 1038605.

*Related to thesis.

Others:

1. Vantari Siva, Debi Prasad Datta, **Avanendra Singh**, T. Som, P. K. Sahoo, Nanocomposite Synthesis and photoluminescence properties of MeV Au-ion beam modified Ni thin films, *Appl. Surf. Sci.*, 2016, 360, 276.
2. Ranveer Singh, Mohit Kumar, Mahesh Saini, **Avanendra Singh**, Biswarup Satpati, Tapobrata Som Growth of TiO₂ thin films on chemically textured Si for solar cell applications as a hole-blocking and antireflection layer, *Appl. Surf. Sci.*, 2017, 418, 225.
3. Debi Prasad Datta, Vantari Siva, **Avanendra Singh**, Shalik Ram Joshi, D. Kanjilal, P. K. Sahoo, Ion-beam-induced nanodots formation from Au/Si thin films on quartz surface, *Nucl. Instrum. Methods Phys. Res. B*, 2016, 379, 48.
4. R. Panda, S. Bhattacharya, R. Samal, **Avanendra Singh**, P. K. Sahoo, P. K. Datta, S. K. Das, Second harmonic generation of femtosecond pulses using ZnO nanorods grown by chemical bath deposition with drop casted seed layer, *Journal of Nonlinear Optical Physics & Materials*, 2016, 25, 1650029.
5. D.P. Datta, V. Siva, **Avanendra Singh**, D. Kanjilal and Pratap K. Sahoo, Photoluminescent Au-Ge composite nanodots formation on the SiO₂ surface by ion-induced dewetting, *Nucl. Instrum. Methods Phys. Res. B*, 2017, 407, 141.
6. L. Khatua, R. Panda, **Avanendra Singh**, A. K. Nayak, P. Satapathy, D. Pradhan, Pratap Kumar Sahoo, S K S Parashar, S. K. Das, Growth of significantly low dimensional Zinc Orthotitanate (Zn₂TiO₄) nanoparticles by solid state reaction method, *Science of Sintering*, 2018, 50, 133.
7. Mohit Kumar, Biswarup Satpati, **Avanendra Singh**, Tapobrata Som, Colossal broadband antireflection form conformally grown Cu₂O on pyramidally-textured Si and its photovoltaic applications, *Solar RRL*, DOI: 10.1002/solr.201700216.



Avanendra Singh

To my Grandmother, & Mother

Acknowledgement

First and foremost, praises and thanks to the Almighty, for giving me the strength, knowledge, ability and opportunity to undertake, persevere and complete this research study satisfactorily. The best and worst moments of my doctoral journey have been shared with many people.

I would like to express my deep and sincere gratitude to my research supervisor, **Dr. Pratap Kumar Sahoo** and co-supervisor **Dr. Kartik Senapati** for transmitting great ideas of Physics in me from their unfathomable knowledge and experience. The faith and confidence they had in me matured into a deep-seated source of constant encouragement, which guided me to the very end of the project and is very much appreciated. Without their able guidance, this thesis would not have been possible and I shall eternally be grateful to both the supervisors for their assistance. I am extending my heartfelt thanks to their family members, especially, Mrs. Madhusmita Sahoo, and Mrs. Sarojini Senapati, for their acceptance and care like a mother.

No research is possible without infrastructure and requisite materials and resources. For this I extend thanks to former and present director of NISER Prof. V. Chandrasekhar and Prof. Sudhakar Panda, for providing me the requisite institutional facilities throughout my research tenure. I would also like to thank the members of my thesis monitoring committee, Prof. Be-dangadas Mohanty, Dr. Prasanjit Samal, Dr. Ajaya Kumar Nayak, and Dr. Himansu Sekhar Biswal for their relentless efforts in guiding me whenever I needed the most. I sincerely place on record my thanks to Dr. Ritwick Das for providing me his all the support to carry out the nonlinear optical measurements and his scientific and insightful discussions and suggestions. I thankfully acknowledge all the faculty members and technical staff of the School of Physical Sciences for all the support provided during my research.

I owe my deep gratitude to Prof. T. Som, Prof. Shikha Verma for providing me their lab facilities at IOP, Bhubaneswar. I wish to extend my hearty thank to Dr. Biswarup Satpati and Prof. S. Bhunia for providing me the TEM and PL facilities at SINP, Kolkata. I am thankful to Prof. K. K. Nanda for extending his help in microPL measurements in his lab at IISC, Bangalore. I wish to express my warm thanks to Dr. D. Kanjilal for providing me the low energy ion implantation facility at IUAC, New Delhi. I extend my acknowledgement to Dr. A. K. Sinha, Dr. S. N. Jha, Dr. Parasmani Rajput, Dr. Dinesh Kumar Shukla and Dr. M. Nayak for their help during measurements at synchrotron radiation lab of RRCAT, Indore.

I will forever be thankful to my former college advisor, Dr. Ram Manohar Yadav and Mr.

Anand Kumar. Both of them have been helpful in providing advice many times during my graduate school career. They were the reason why I decided to pursue a career in research. Their enthusiasm and love for teaching is contagious.

I would like to thank my present and former labmates, especially, Dr. Debi Prasad Datta, Mr. Vantari Siva, Mr. Siddharth Sahu, Ms. Ekta Bhatia and Ms. Pravasini Swain who have always offered their help whenever I needed. I would like to thank my all other PhD colleagues, with whom I have shared moments of deep anxiety but also of big excitement. I am much indebted to my friend Ms. Rita Maji for extending her help.

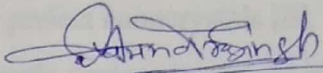
Its my fortune to gratefully acknowledge the support of some special individuals. Words are not enough to express my appreciation to Dr. Debashis Pattanaik for his untiring support, understanding and valuable contributions in shaping the entire thesis. This dissertation would not have been possible without his continual guidance, advice and kind efforts that he grants me. He was always beside me during the happy and hard moments of this journey to motivate me. I extend my warm thanks to my friend Mr. Samir Kumar for being with me always like brother and for his special concern and love. I treasure the friendship of Ms. Sony Singh for the years we were together and will always cherish her care. I extend my hearty thanks to Pradeep Bhai and Arvind Kumar, who have always shown belief in me and were always available whenever I needed. Some special words of gratitude go to my friends who have always been a major source of support when things would get a bit discouraging: Shrikant Kokate, Sachin Kumar, Mukesh Shukla, Arup Bhowmick, Nisha Singh, Charanpreet Singh, Subir Sen, and Jyoti Yadav. My heartfelt thanks to Mrs. Pallavi Singh for her affection, friendship and help. I extend my thanks to my friend Mr. Paresh Chandra Pradhan for taking care of my stay at RRCAT, Indore and his wife Mrs. Soma Maity for delicious food in RRCAT, Indore. I wholeheartedly thank my friend Dr. Vantari Siva and his wife Mrs. Geetha for hosting me several times at their home during my stay at NISER.

I owe my deepest sense of affection to my late mother **Mrs. Radha Devi** and my late grandmother **Mrs. Ganga Devi**. Today, even both of you are not with me, but your blessings will always be with me and show me the path to achieve my goals. Your love and positive approach have always inspired and strengthened me throughout this journey. I don't find enough words to express the gratitude and affection for the real hero of my life, my dad **Mr. Shailendra Singh Yadav**. You have always taught me that nothing can be bigger than your goals, and never hesitate to work hard to achieve them. You have been a role model of resilience, strength

and character. My great appreciation and enormous thanks to Dad and I am sure without his understanding this thesis would never have been completed. I am grateful for you and for the smart genes you passed onto me. Three special names, I must mention, are my sisters, **Ankita** and **Arpita** and brother **Shivendra Singh**, as they offered invaluable support and humor over the years. You have always kept things light and made me smiling. I am thankful to my wonderful bua Mrs. Sunita and Mrs. Bittarani for their continuous love and prayer for me, and promptness that brought investigation to completion.

Last but not the least; I would like to thank Department of Atomic Energy and NISER for providing financial support for my research work.

Date: 20/04/2018


Avanendra Singh

Contents

Table of Contents	xii
Acknowledgement	xiii
Synopsis	xvi
List of Abbreviations	xxv
List of Figures	xxvii
List of Tables	xxxiv
1 Introduction	1
1.1 ZnO: A promising direct and wide band gap semiconductor	2
1.1.1 Crystal structure	3
1.1.2 Optical properties	4
1.1.3 Electrical properties	7
1.2 Defects in ZnO and their influence on its optical and electrical properties	8
1.2.1 Influence on the optical properties of ZnO	10
1.2.2 Influence on the electrical properties of ZnO	11
1.3 Theme of the thesis	12
2 Experimental methods and analysis techniques	24
2.1 Sample preparation	24
2.1.1 Substrate cleaning	24
2.1.2 Seed layer coating	25
2.1.3 Room temperature growth of ZnO nanostructures	25
2.1.4 Nanorods grown on seeded Si	26
2.1.5 Nanorods grown on ITO coated glass	26
2.1.6 Growth process of ZnO nanostructures	27
2.2 DC magnetron sputtering	27

2.3	Ion implantation	28
2.4	Characterization techniques	29
2.4.1	Electron microscopes	30
2.4.2	X-ray diffraction	35
2.4.3	X-ray photoelectron spectroscopy	36
2.4.4	X-ray absorption fine structure spectroscopy	37
2.5	Optical properties measurement techniques	38
2.5.1	Ultraviolet-visible near-infrared spectroscopy	38
2.5.2	Photoluminescence spectroscopy	40
2.5.3	Raman spectroscopy	42
2.5.4	Z-scan technique	44
2.6	Electrical properties measurement techniques	47
2.6.1	Field emission study	47
2.6.2	Atomic force microscopy	48
2.6.3	Kelvin probe force microscopy	50
2.6.4	Tunneling atomic force microscopy	51
2.7	Summary	51
3	Growth dynamics and optical applications of ZnO twin nanorods	54
3.1	Methodology and growth mechanism of ZnO TNRs	55
3.2	Morphological and structural studies	57
3.2.1	XRD and SEM study	57
3.2.2	TEM analysis	61
3.2.3	Nanoscale interface engineering in ZnO twin nanorods for proposed phonon tunnel devices	64
3.3	Optical absorption properties of ZnO twin nanorods	66
3.4	Optical emission properties of ZnO twin nanorods	69
3.4.1	Room temperature photoluminescence study and phonon tunneling in CAC architecture	69
3.4.2	Suppression of near band edge emission in ZnO twin nanorods	72
3.4.3	Red luminescence from ZnO twin nanorods for nano-thermometry ap- plications	80

3.5	Summary	84
4	Au decoration on ZnO nanotapers for field emission applications	90
4.1	Methodology and growth of ZnO nanotapers	91
4.2	Morphological and structural studies	92
4.2.1	SEM and XRD study	92
4.2.2	TEM study	94
4.2.3	X-ray absorption fine structure study	95
4.3	Absorption characteristics	97
4.4	Field emission characteristics	98
4.5	Work function calculations using Kelvin probe force microscopy	101
4.6	Study of local conductance using tunneling atomic force microscopy	103
4.7	Summary	104
5	Point defects in vertically aligned ZnO nanorods by O⁺ ion implantation	109
5.1	Growth methodology and O ⁺ ion implantation in vertically aligned ZnO nanorods	112
5.2	Simulated projectile range	112
5.3	Morphological and structural studies	113
5.3.1	SEM and XRD study	113
5.3.2	XPS study	115
5.4	Optical studies	118
5.4.1	Room temperature UV-visible spectroscopy:	118
5.4.2	Photoluminescence spectroscopy	119
5.4.3	Raman spectroscopy	121
5.5	Local electrical transport studies	122
5.6	Summary	124
6	Nonlinear optical properties of Mn-doped ZnO nanorods	130
6.1	Experimental specification	131
6.2	Morphological and structural studies	132
6.2.1	SEM and XRD study	132
6.3	Optical properties	135
6.3.1	Study of near band edge emission and absorption edge	135

6.3.2	Nonlinear optical properties	137
6.4	Summary	140
7	Summary and future perspectives	143
7.1	Future perspectives	147

Synopsis

Since last few decades, direct and wide band gap semiconductor-based nanostructures and thin films have been studied extensively for various optoelectronic, photonic and electronic device applications including phonon tunnel devices, lasers, optical switches, field emitter etc [1–4]. At nanoscale regime, these semiconducting nanostructures often exhibit distinct properties from their bulk counterparts due to their size, shape, surface roughness, crystal defects and surface area to volume ratio [5, 6]. Therefore, by tuning preceding described parameters semiconducting materials can be potential candidates for various device applications like optoelectronic, photonic, sensors, solar cells, semiconductor memories. Often, crystal imperfections introduce unexpected phenomena in nanostructures unlike their perfect nanocrystals [6]. Thus, for technological aspects, the high-speed performance of nanoscale devices is desired and for that, better understanding of effects of crystal imperfections on their optical and electrical properties is indeed requisite. Except for the application based feasibility, crystal imperfections in semiconducting nanostructures also play a vital role in various fundamental theoretical concepts of Physics like electron-phonon coupling, electronic band structure, exciton emission, excitonic fine structure and recombination dynamics etc. This thesis is devoted to defects driven phenomena (applications) in ZnO nanorods. For this purpose different ZnO nanorods including twin nanorods, nanotapers, and nanorods have been grown by the wet chemical method on thin ZnO seed layer coated Si and Indium Tin Oxide (ITO) coated glass substrates. Extended and point defects in nanorods were incorporated intentionally. In the case of the extended defects, we introduced defects in ZnO nanorods by two methods. In the first method, a thin amorphous layer of ZnO was sandwiched between two identical crystalline segments of ZnO nanorods, which we called twin nanorods (TNRs) and in second method we coated Au nanoparticles on the surface of vertically aligned nanotapers. The point defects were created by adding impurities into host matrix using chemical doping route, and ion implantation technique. For the growth of TNRs, a simple hydrothermal reaction method was used, which allowed us to engineer the amorphous and the crystalline sections of nanorods via reaction temperature. A systematic study of the morphology and dimensions of the nanorods grown under various conditions was performed using a combination of scanning and transmission electron microscopes. Transmission electron microscopy (TEM) clearly showed an amorphous separation between the two crystalline segments of ZnO. The study of an optical band of TNRs

showed a redshift as a function of growth duration, which indicates slightly stressed growth of the crystalline segments. For longer growth duration, lateral growth of crystalline ZnO over amorphous gap fills the separation between two crystalline segments, and as a result the redshift in optical band gap saturates. The saturation in optical band gap confirms a true mechanical gap between the two crystalline segments of the nanorods. The room temperature photoluminescence (PL) spectra of TNRs exhibit a strong near band edge (NBE) emission with convoluted phonon side bands. Deconvolution analysis of these PL spectra showed that beyond a certain thickness, the amorphous interlayers becomes transparent for phonon modes. Results show that such oriented crystalline-amorphous-crystalline (CAC) structures may be a suitable test system for fundamental studies of phonon tunneling in nanorods. Obtained results showed the viability of engineering embedded interfaces via chemical routes. The temperature dependent PL spectra of these TNRs showed variation of free exciton (FX) emission energy, which fitted perfectly with a model including lattice dilation with the standard electron-phonon interaction. In low-temperature regime (below 180K) different visible emission peaks appear, due to the localization of defect centers and a loss in NBE emission intensity was observed as a consequence of a non-radiative carrier transfer from the conduction band to the defect centers. The enhanced exciton-acoustic phonon coupling strength obtained from temperature dependent linewidth of the FX peak supported our argument for non-radiative carrier transfer to defect centers. Confocal temperature dependent PL spectra of these TNRs recorded at an excitation energy 3.49 eV showed weak asymmetrical FX emission followed by a stable and strong red emission. Deconvolution analysis of FX emission peaks exhibits weakening of electron-phonon coupling at higher temperature range. The calculated integrated intensity ratio of red emission to FX emission showed a noticeable change in magnitude for the temperature range between liquid Nitrogen temperature to 175 K, which can be suitable for non-contact cryogenic thermometry applications. In continuation of the role of crystal defects on optical properties of ZnO nanorods, we doped ZnO nanorods with Mn dopants at four different doping concentration (0.5, 1.5, 2, and 2.5%) and compared their nonlinear optical behavior with as-grown ZnO nanorods. In this study, Mn-doped ZnO nanorods were grown on ITO coated glass substrates using low-temperature aqueous growth technique. UV-Vis absorption spectroscopy showed that after Mn doping the absorption edge of ZnO nanorods exhibit redshift, which remains almost constant for all doping concentrations. The measured absorption edges of Mn-doped nanorods closely matches with the Zn/O vacancies, and we expect a two-photon

absorption (TPA) in these nanorods, when to shine with frequency-doubled near-infrared lasers of wavelength 532 nm. Except for TPA, the defect states may also enhance the efficiency of the non-resonant nonlinear optical process. The nonlinear optical measurements were carried out using Z-scan technique in which a Q-switched diode-pumped solid-state laser ($\lambda = 532$ nm) emitting linearly-polarized, sub-nanosecond pulses in a TEM₀₀ mode intensity profile was used as an excitation source. The pulse energy varied from 1 μ J to 125 μ J for the measurements with pulse width $t_p \sim 0.7$ ns at 40 Hz repetition rate to minimize the impact of thermally induced optical nonlinearities. The beam was focused to a spot size of $\omega_0 \sim 45$ m using a converging lens ($f = 150$ mm) which resulted in a Rayleigh length ($z_0 = \pi\omega_0^2/\lambda$) of ~ 12 mm, which ensured negligibly small “sample + substrate” thicknesses compared to z_0 . The samples have translated a distance of 100 mm through the beam focal point and the transmitted power in an open-aperture (OA) as well as in a closed-aperture (CA) configuration was measured using a fast photodiode sensor. In nonlinear measurements, all samples showed a self-defocusing effect with the significantly higher nonlinear refractive index as compared to ZnO thin films. Un-doped and 0.5% Mn-doped nanorods showed TPA features although saturable absorption behavior was observed for other doping concentrations. Additionally, the difference in nonlinear absorption response for OA measurements, the magnitude of TPA absorption coefficient (β) for varies slightly against Mn concentration in ZnO nanorods. The investigations suggested that Mn-doped ZnO nanorods can be employed for designing ultrafast photonic devices like optical switches, optical limiters, and efficient optical phase shifters. Since coating of metallic nanoparticles on the surface of nanostructures modifies the surface states, which induces unusual changes in the electrical properties of nanostructures. In the same spirit, hydrothermally grown, ZnO nanotapers were coated with Au films of two different thicknesses of 3 and 5 nm. The uneven surface and rotation of substrate (20 rpm) caused the formation of Au islands on nanotapers, evaporated by electron beam technique. Since the metal coating may induce mid-gap states at the ZnO-Au interface, which essentially lowers the effective work function (Φ) of nanotapers. A direct measurement of Φ , using Kelvin probe force microscopy indeed showed a drop of 0.14 and 1.12 eV for 3 and 5 nm Au-coated samples respectively. Synchrotron radiation based, extended x-ray absorption fine structure spectroscopy measurements showed that Au decoration on ZnO nanotapers affected the bond length of both the Zn-O and Zn-Zn shells. Apart from that, a change in DebyeWaller factor (σ^2) indicates that Au decoration introduced disordered environment at Au-ZnO interface. The field emission studies on these Au-decorated

nanotapers showed significantly low turn-on fields compare to as grown nanotapers, and the tunneling atomic force microscopy measurements revealed a very uniform spatial emission profile for 5 nm Au-coated nanotapers which are essentially required for large scale efficient applications. From our experimental findings, we conclude that Au decoration on ZnO nanotapers, induced mid-gap states at Au-ZnO interface, and are responsible for lowering the Φ , which promoted enhanced field emission characteristics. In general, ZnO nanostructures show n-type conduction owing to the presence of intrinsic defects in the crystal including Zn interstitials (Zn_i), Oxygen vacancies (V_O), V_O complexes and residual impurities, the deep acceptor levels, low dopant solubility, which are also the bottlenecks for the p-type conduction. However, several experimental efforts have realized p-type conduction in ZnO nanostructures by various methods like doping of group V elements, N-implantation, Li doping and growth of ZnO nanostructures in Oxygen rich environment, wet chemical method etc. In order to conquer the low dopants solubility and achieve high-quality p-type conduction, ion implantation is suitable and widely used technique due to its ability of dopant selectivity and precise depth distribution features. The depth distribution feature may allow the formation of p-type ZnO over a selected depth, by which tandem p-n junctions can be formed in single ZnO nanostructure. With the same spirit, we successively implanted ZnO nanorods by O ions of two different energies (50 and 350keV respectively) with a fixed ion fluence 5×10^{16} ions/cm². The SRIM simulation showed that the maxima of distribution of O⁺ ions of energies 50 and 350keV are separated by 400 nm, which suggests that the successive implantation are leads to the formation of oxygen-rich/As grown/oxygen-rich/As grown tandem structures in ZnO nanorods. The room temperature PL spectra showed that after O⁺ implantation the NBE emission is completely suppressed as a consequence of the formation of competing non-radiative transitions which reappear followed by a dominant visible emission band, after annealing the samples in vacuum at 500⁰C for 3 hours. The deconvolution analysis of post-annealed PL spectra exhibited six peaks centered at around 377 nm (3.29 eV), 385 nm (3.22 eV), 557 nm (2.23 eV), 600 nm (2.07 eV), 660 nm (1.88 eV) and 732 nm (1.69 eV). Which are attributed as free exciton (FX) emission, longitudinal optical phonon mode (FX-1LO), transitions from conduction band (CB) to oxygen interstitial (O_i) and zinc interstitial (Zn_i) to O_i , transitions from CB to oxygen vacancies (V_O) and V_O to valance band respectively. The deconvolution analysis revealed that transitions initiated by O_i dominate over UV and red emissions which are attributed to acceptor levels in ZnO. In PL spectra, the relatively higher intensity of O_i compared to V_O is

an indication of p-type conductivity in the annealed samples. The conducting AFM mapped current images show that all the samples exhibit low-intensity current maps compare to pristine sample and we attribute it as trapping of free charge carriers in the defect states introduced by ion implantation. From mapped current images of implanted samples, the observed bright contrast on side facets of nanorods indicates that more free charge carriers are present on side facets. Comparison of I-V characteristics recorded from as grown and post annealed implanted samples showed that all the samples exhibit formation of Schottky junctions between C-AFM tip and nanorods, but as grown sample have low knee voltage than others. Thus on the basis of our experimental findings we conclude that p-n-p-n tandems are fabricated in ZnO nanorods by successive O^+ implantation. In summary, the experimental findings of this work indicate that defects created in ZnO nanorods lead to modifying their optical and electrical properties which can be used in various ZnO-based devices applications like phonon tunnel devices, optoelectronic, photonic, field emitting devices, electronic devices etc.

Bibliography

- [1] A. Singh, K. Senapati, B. Satpati, M. Kumar, P. K. Sahoo *Phys. Chem. Chem. Phys.*, **2015**, 17, 4277.
- [2] T. P. H. Sidripoulos, R. Roder, S. Geburt, O. Hess, S. A. Maier, C. Ronning, R. F. Oulton, *Nature Physics*, **2014**, 10, 870.
- [3] A. Singh, S. Kumar, R. Das and P. K. Sahoo, *RSC Adv.* **2015**, 5, 88767.
- [4] A. Singh, K. Senapati, M. Kumar, T. Som, A. K. Sinha, and P. K. Sahoo, *Appl. Surf. Sci.* **2017**, 411, 117.
- [5] F. Li, F. Gong, Y. Xiao, A. Zhang, J. Zhao, S. Fang, and D. Jia, *ACS, Nano*, **2013**, 7, 10482.
- [6] A. Singh, K. Senapati, B. Satpati, P. K. Sahoo, *Phys. Chem. Chem. Phys.*, **2017**, 19, 14012.

List of Publications

1. **Avanendra Singh***, Kartik Senapati, Biswarup Satpati, Mohit Kumar, Pratap K. Sahoo, Nanoscale interface engineering in ZnO twin nanorods for proposed phonon tunnel devices, *Phys. Chem. Chem. Phys.*, **2015**, 17, 4277.
2. **Avanendra Singh***, Samir Kumar⁺, Ritwick Das and Pratap K. Sahoo, Defect-assisted saturable absorption characteristics in Mn-doped ZnO nanorods, *RSC Adv.*, 2015, 5, 88767.
3. **Avanendra Singh***, Kartik Senapati, Mohit Kumar, Tapobrata Som, Anil K. Sinha, and Pratap K. Sahoo, Role of work function in field emission enhancement of Au island decorated vertically aligned ZnO nanotapers, *Appl. Surf. Sci.* 2017, 411, 117.
4. **Avanendra Singh***, K. Senapati, D. P. Datta, R. Singh, T. Som, S. Bhunia, D. Kanjilal, Pratap. K. Sahoo, Synthesis of p-n junctions in ZnO nanorods by O⁺ ion implantation, *Nucl. Instrum. Methods Phys. Res. B*, 2017, 409, 143.
5. **Avanendra Singh***, Kartik Senapati, Biswarup Satpati, Pratap K. Sahoo, Suppression of near band edge emission in specially engineered ZnO twin nanorods, *Phys. Chem. Chem. Phys.*, 2017, 19, 14012.
6. Vantari Siva, Debi Prasad Datta, **Avanendra Singh**, T. Som, P. K. Sahoo, Nanocomposite Synthesis and photoluminescence properties of MeV Au-ion beam modified Ni thin films, *Appl. Surf. Sci.*, 2016, 360, 276.
7. Ranveer Singh, Mohit Kumar, Mahesh Saini, **Avanendra Singh**, Biswarup Satpati, Tapobrata Som, Growth of TiO₂ thin films on chemically textured Si for solar cell applications as a hole-blocking and antireflection layer, *Appl. Surf. Sci.*, 2017, 418, 225.
8. D. P. Datta, V. Siva, **Avanendra Singh**, S. R. Joshi, D. Kanjilal, P. K. Sahoo, Ion-beam-induced nanodots formation from Au/Si thin films on quartz surface, *Nucl. Instrum. Methods Phys. Res. B*, 2016, 379, 48.
9. R. Panda, S. Bhattacharya, R. Samal, **Avanendra Singh**, P. K. Sahoo, P. K. Datta, S. K. Das, Second harmonic generation of femtosecond pulses using ZnO nanorods grown

by chemical bath deposition with drop casted seed layer, *Journal of Nonlinear Optical Physics and Materials* 2016, 25, 1650029.

10. D.P. Datta, V. Siva, **Avanendra Singh**, D. Kanjilal and Pratap K. Sahoo, Photoluminescent Au-Ge composite nanodots formation on the SiO₂ surface by ion induced dewetting, *Nucl. Instrum. Methods Phys. Res. B*, 2017, 407, 141.
11. L. Khatua, R. Panda, **Avanendra Singh**, A. K. Nayak, P. Satapathy, D. Pradhan, Pratap Kumar Sahoo, S K S Parashar, S. K. Das, Growth of significantly low dimensional Zinc Orthotitanate (Zn₂TiO₄) nanoparticles by solid state reaction method, *Science of Sintering* (Accepted).

Conference Proceedings

1. **Avanendra Singh***, Kartik Senapati, K. K. Nanda, Pratap K. Sahoo, Strong Red luminescent twin ZnO nanorods for noncontact Nano-thermometry applications, *MRS Advances* 2016, 1, 869.

Conference Presentations

1. **Avanendra Singh**, Mohit Kumar, K. Senapati, T. Som, and Pratap K. Sahoo, Enhanced field emission from gold-corrugated ZnO nanorods, *Indo-French Symposium on Functional Metal-Organics: Applications in Materials and Catalysis*, 2015, NISER, Bhubaneswar, India.
2. **Avanendra Singh**, and Pratap K. Sahoo, Room temperature ferromagnetism and optical properties of Mn doped ZnO Nanorods, *Indo-Japan workshop on Magnetism at Nanoscale (IJWMN)*, 2015, NISER, Bhubaneswar, India.
3. **Avanendra Singh**, Samir Kumar, Ritwick Das and Pratap Kumar Sahoo, Nonlinear optical switching in Mn-doped ZnO nanorods, *Current trends in condensed matter Physics (CTCMP)*, 2015, NISER, Bhubaneswar, India.
4. **Avanendra Singh**, Debi Prasad Datta, Kartik Senapati and Pratap K. Sahoo, Band Gap Tailoring and Optical properties of Aqueous Grown ZnO Nanowires by Oxygen Ion Implantation, *Radiation effects in Insulators*, 2015, MNIT, Jaipur, India.

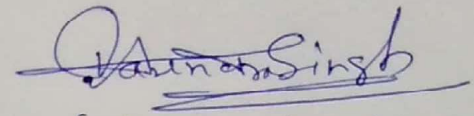
5. **Avanendra Singh**, Kartik Senapati, Karuna Kar Nanda and Pratap K. Sahoo, Red luminescent twin ZnO nanorods for proposed phonon tunnel device and nano-thermometry application, APS March meeting, 2016, Baltimore, USA.

Workshop/training

1. National Workshop on Fluorescence and Raman Techniques, 2014, IISER, Pune, India.

* indicates papers on which this thesis is based

+ indicates equal contribution.


(Avanendra Singh)

List of Abbreviations

1. Ultraviolet (UV).
2. Room temperature (RT).
3. Near band edge (NBE).
4. Valance band (V.B.).
5. Conduction band (C.B.).
6. Deep level emission (DLE).
7. Donor-acceptor pair (DAP).
8. Donor bound exciton (DBE).
9. Green luminescence (GL).
10. Two-electron satellite (TES).
11. Longitudinal optical (LO).
12. Photoluminescence (PL).
13. Free exciton (FX).
14. Twin nanorods (TNRs).
15. Temperature ramping rate (R_r).
16. Twin nanorod junctions (TNRJs).
17. Crystalline-amorphous-crystalline (CAC).
18. Metal-insulator-metal (M-I-M).
19. Field emission scanning electron microscope (FESEM).

20. Energy dispersive x-ray spectroscopy (EDX).
21. Transmission electron microscope (TEM).
22. High resolution transmission electron microscope (HRTEM).
23. Atomic force microscopy (AFM).
24. Conducting -atomic force microscopy (C-AFM).
25. Kelvin probe force microscopy (KPFM).
26. Tunneling atomic force microscopy (TUNA).
27. X-ray absorption fine structure (XAFS).
28. Extended X-ray absorption fine structure (EXAFS).
29. X-ray diffraction (XRD).
30. X-ray photoelectron emission spectroscopy (XPS).
31. Field emission (FE).
32. Nonlinear optical properties (NLO).
33. Close aperture (CA).
34. Open aperture (OA).
35. Two-photon absorption (TPA).
36. Electron-cyclotron resonance (ECR).
37. Zinc vacancies (V_{Zn}).
38. Oxygen vacancies (V_O).
39. Zinc interstitial (Zn_i).
40. Oxygen interstitial (O_i).

List of Figures

1.1	(a) Schematic diagram of a hexagonal wurtzite crystal structure. The blue solid lines show its unit cell of hexagonal structure. (b) shows ...ABABAB... stacking of atoms in hexagonal structure.	3
1.2	Schematic diagram of band splitting in E-K diagram of a direct band gap semiconductor.	5
1.3	The graphical theme of the thesis.	13
2.1	Schematic representation of types of ZnO nanorods used in this work.	26
2.2	Schematic representation of O ⁺ ion implantation in ZnO nanorods.	29
2.3	A schematic of typical field emission scanning electron microscope.	32
2.4	(a) and (b) show the schematic representation of the diffraction pattern operational mode and imaging mode of TEM, respectively. [21]	34
2.5	Typical ray-diagram of X-ray diffraction from a periodic chain of atoms.	35
2.6	Schematic diagram of conventional XPS unit.	37
2.7	Schematic diagram of UV-Visible spectrometer setup.	39
2.8	Tauc plot of AZO film deposited on Si substrate. The red line shows extraction of band gap by fitting a straight line.	40
2.9	(a) schematic of PL process in a direct band gap semiconductor. The dotted green lines show electronic transition. (b) schematic for density of states occupancy of electrons and holes in corresponding states.	41
2.10	Schematic block diagram of PL set-up used in this study.	42
2.11	The energy level diagram of Raman scattering process.	43
2.12	Schematic drawing of standard Z-scan technique [28].	44
2.13	Schematic diagram of field emission unit.	48
2.14	Schematic drawing of a conventional AFM setup.	49
2.15	Inter-atomic force versus distance curve.	49

2.16	Schematic presentation of electronic energy levels of the sample and AFM tip for three different cases: (a) tip and sample are separated by distance d with no electrical contact, (b) tip and sample are in electrical contact, and (c) external bias (V_{dc}) is applied between tip and sample.	50
3.1	(a) The schematics for sample preparation unit and the convection current in the reaction medium. (b) Schematic diagram of the effect of temperature ramp rate R_r on the twin nanorods.	57
3.2	(a - c) GIXRD patterns of twin ZnO nanorods grown at (a fixed molar concentration 0.01M) three different $T_R = 60, 80$ and 90°C respectively. (d) Molar concentration dependent GIXRD patterns of TNRs grown at a fixed $T_R = 80^\circ\text{C}$. The * mark represents GIXRD signal from Si substrate.	57
3.3	Scanning electron micrographs of ZnO TNRs prepared at a fixed reaction temperature 80°C and five different growth durations of 1, 3, 6, 9, and 12 hours. Panels (a - e) SEM images for duration 1, 3, 6, 9, and 12 hours respectively for molar concentration 0.01M, (g - l) 0.05M and (m - r) 0.1M respectively. Notice the bridging of the gap in panels (d), (f), (k), (l) (q) and (r).	58
3.4	Structure evolution of ZnO TNRs prepared with molar concentrations 0.01, 0.05 and 0.1M, at fixed time 6 hours, and different temperatures 60, 80, 90°C . (a - c) 0.01M, $T_R = 60^\circ\text{C}, 80^\circ\text{C}, 90^\circ\text{C}$ (d - f) 0.05M, $T_R = 60^\circ\text{C}, 80^\circ\text{C}, 90^\circ\text{C}$ and (g - i) 0.1M, $T_R = 60^\circ\text{C}, 80^\circ\text{C}, 90^\circ\text{C}$ respectively.	59
3.5	(a - c) Variation in length of TNRs grown at $T_R = 60, 80,$ and 90°C , respectively. (d - f) variation in diameter of TNRs grown at $T_R = 60, 80,$ and 90°C , respectively.	60
3.6	(a) The TEM image of single TNR grown at 80°C . (b) and (d) show the SAED patterns from the yellow circles of nanorod segments as indicated in figure. (c) the SAED pattern from the central groove of TNR.	61
3.7	(a) The transmission electron image of the central region of a twin nanorod. (f) The high-resolution image of the red marked area of panel (a). (b) - (d) the FFT patterns of the blue, red and yellow marked regions of the panel (f). (e) and (g) show the Fourier filtered images recorded from the blue and yellow marked regions of the nanorod segments of the TNR.	62

3.8	(a) the STEM image of a typical twin ZnO nanorod. (b) the HAADF-STEM image for compositional sensitivity. (c), (d) and (e) the elemental mapping for Zn, O and the composite image, respectively. (f) the line scan across the junction. (g) the STEM-EDX spectrum of the selected region in panel (a).	62
3.9	(a) The HAADF image of twin ZnO nanorods, (b) EELS spectra acquired from points O ₁ , O ₂ and O ₃ of panel (a).	63
3.10	(a), (b), and (c) The scanning electron images of TNRs prepared at R _r = 1 ⁰ C/min, 1.7 ⁰ C/min and 2 ⁰ C/min, respectively.	65
3.11	(a) - (c) the high resolution TEM images of the amorphous region at mid-length of the twin nanorods. (d) plots the average thickness of the amorphous layer as a function of the temperature ramp rate. The solid line is a fit showing linear scaling of the amorphous barrier thickness with the temperature ramp rate. The variation in the thickness of the amorphous layers at various spots is shown as the error bars.	66
3.12	(a) The RT UV-Visible absorption spectra of TNRs grown at fixed T _R = 80 ⁰ C, and molar concentration 0.05M. (b) The Tauc plots converted from the absorption spectra, (c) Tauc plot for 1 hour growth duration fitted with a straight line. (d) Variation in band gap against growth time. The error bars were obtained from the fitting of straight line in Tauc plots.	67
3.13	Variation in the band gap of TNRs with the change in growth parameters: growth duration, molar concentration and reaction temperature. (a), (b) and (c) The plots for the change in the band gap of TNRs as a function of growth duration for three molar concentration 0.01M, 0.05M and 0.1M, respectively. For each molar concentration, the variation in band gap is plotted for all three T _R = 60, 80 and 90 ⁰ C. The error bars were obtained from the fitting of the straight line in the Tauc plots.	68
3.14	(a), (b) and (c) the room temperature PL spectra of the TNRs for all growth durations at T _r 60 ⁰ C, 80 ⁰ C and 90 ⁰ C, respectively. (d) The position of the FX peaks extracted from deconvolution of PL spectra. The solid lines in the panel (d) are only guides to the eye. The error bars were obtained from the deconvolution analysis of the respective PL spectra.	70

3.15	FESEM images of TNRs grown for 3, 6, 9, and 12 hours duration ($T_r = 60^{\circ}\text{C}$). Notice the bridging of the amorphous gap at 9 hours and 12 hours.	71
3.16	(a) sample deconvolution of the PL spectrum of TNRJs grown at 60°C for 9 hours. (b), (c) and (d) plots the difference between the peak position of FX and FX-1LO peaks as a function of growth duration for nanorods with amorphous layer thickness ~ 10 nm, 4 nm and 1.5 nm, respectively. The error bars were obtained from the deconvolution analysis of the respective PL spectra.	72
3.17	(a) Temperature dependent PL spectra of TNRs. (b), (c) and (d) Deconvoluted PL spectra of TNRs recorded at temperatures 78K, 180K and 300K, respectively.	73
3.18	The redshift of FX, FX1LO, FX-1LO and FX-2LO features of TNRs. (a), (b) fitting of redshift of FX emission using Vina model and Manoogian model, respectively. (c), (d) and (e) plot the redshift of different phonon sidebands, where solid lines show the theoretical fitting of their redshift.	75
3.19	Plots the temperature dependent integrated intensity of the FX and deep level emissions. The solid lines are fit to thermally activated intensity quenching model. The shaded region shows the loss of intensity region compared to the theoretically expected value.	77
3.20	Schematic ray diagram of electron-hole pair recombination dynamics in presence of additional defect states in conventional E-k diagram.	78
3.21	The line broadening plots of FX peaks. The inset shows line broadening of defect peaks centred at 411 nm, 434 nm, and 463 nm. The solid lines in each plot are theoretical fits to experimental observed line broadening.	79
3.22	(a) FESEM micrograph of Twin ZnO Nanorods, (b) enlarged image of marked region of panel (a).	80
3.23	(a) Optical image of TNRs, (b) Room temperature PL emission mapping image of selected area of panel (a), (c) PL spectrum of an individual TNR, recorded from the marked circular area of panel (b).	81
3.24	(a) Temperature dependent micro-PL spectra of TNRs. (b) Deconvoluted PL spectrum recorded at 83K. (c) - (d) magnified deconvoluted spectra of UV band recorded at 83K and 373K respectively.	82
3.25	Plot of difference in peak position between FX and FX-1LO versus temperature.	83

3.26	(a) Red and black dotted curves show the variation in integrated intensity as a function of temperature. The inset shows temperature dependent ratio of integrated intensity of Red emission to UV emission. (b) A plot for temperature dependent absolute sensitivity of TNRs. The error bars were obtained from the deconvolution of PL spectra.	84
4.1	A schematic for the sample preparation unit.	92
4.2	Cross-sectional FESEM images of nanopapers decorated with Au of thickness (a) 3 nm and (b) 5 nm. The inset of (a) shows top view FESEM micrograph of as-grown ZnO nanopapers.	93
4.3	EDX spectrum acquired from 3 nm Au coated ZnO nanopapers (a) and X-ray diffraction patterns of as-grown and Au coated nanopapers.	94
4.4	(a) ADF STEM image of 5nm Au decorated ZnO nanopapers. The Au particles on the surface can be easily seen. (b) O-K edge EELS spectra extracted across the Au-ZnO interface and away along the green line as shown in panel (a). . . .	94
4.5	Normalized X-ray absorption spectra of as-grown and Au coated samples (a) and (b - d) around Zn K-edge, Fourier transform of k^2 -weighted EXAFS spectra of as-grown, 3 and 5 nm Au decorated ZnO nanopapers respectively.	96
4.6	(a) - (f) RT absorption spectra of as-grown and 1-5 nm Au decorated samples, respectively. Their corresponding Tauc plots are shown in (g) - (h) respectively.	97
4.7	Extracted bandgap of nanopapers vs thickness of Au. The error bars were obtained from the straight line fitting of Tauc plots.	98
4.8	(a) Emission current density vs applied electric field, (b) F-N plots of samples a, b and c. (c - d) emission stability plots of as-grown nanopapers, 3 and 5nm Au-decorated ZnO nanopapers, respectively.	99
4.9	(a), (c) and (e) The AFM images of samples a, b, and c, respectively from where the V_{CPD} values were mapped. (b), (d) and (f) 2D maps of V_{CPD} of samples a, b, and c, respectively.	101
4.10	(a) The continuum of Au Bloch state leaking into the ZnO forbidden gap and representation of reduced work function, (b) Au induced gap states (interface states) caused by leaking of Bloch states.	102

4.11	(a) C-AFM image of as-grown ZnO nanotapers. (b - d) 2D tunneling current maps of as-grown, 3 nm and 5 nm Au-decorated ZnO nanotapers respectively. The inset of (c) and (d) show C-AFM images of 3nm and 5 nm Au-decorated nanotapers respectively.	104
5.1	Simulated electronic and nuclear energy losses of O ⁺ ions in ZnO with respect to different energies.	111
5.2	The simulated projectile range profile of O ⁺ ions in ZnO for different energies 50, 100, 150, 250, and 350 keV respectively. The inset shows the schematic diagram for the distribution of oxygen ions of two different energies of 50 and 350keV in a single ZnO nanorod.	113
5.3	(a) Cross sectional FESEM image of as-grown ZnO nanorods (sample A). (b - c) Top-view FESEM images of ZnO nanorods implanted with 50 (sample B) and gradual 50 & 350 keV (sample C), respectively. (d - f) Post-annealed FESEM images of samples A, B and C (called as samples D, E and F) respectively.	114
5.4	(a) - (c) Grazing angle X-ray diffraction patterns recorded from the samples implanted with Φ 5×10^{14} ions/cm ² , 5×10^{15} ions/cm ² , and 5×10^{16} ions/cm ² , respectively. (d), (e) & (f) XRD patterns of samples A, B and C, respectively. .	115
5.5	Zn 2p core level XPS spectra recorded from the as-grown and 100keV O ⁺ ions implanted samples. The spectra from implanted samples were recorded from the samples implanted with Φ 5×10^{14} ions/cm ² , 5×10^{15} ions/cm ² , and 5×10^{16} ions/cm ² , respectively.	116
5.6	(a) O 1s XPS spectrum of as-grown sample. (b) - (d) O 1s core level XPS spectra of nanorods implanted with O ⁺ ions with Φ 5×10^{14} ions/cm ² , 5×10^{15} ions/cm ² , and 5×10^{16} ions/cm ² , respectively.	117
5.7	(a - b) Absorption and Tauc plots of samples A, B and C, respectively. (c) Demonstration of band gap extraction from the Tauc plot of sample A by fitting a straight line. (d) A plot for extracted band gap of samples A, B, and C, where the solid line is a guide for the eyes. The error bars were obtained from the fitting of a straight line in the Tauc plots.	118

5.8	(a - b) Pre-annealed and post-annealed room temperature PL spectra of samples A, B and C, respectively. (c - d) Deconvoluted PL spectra of samples E and F respectively [27].	120
5.9	(a) Deconvoluted PL spectrum of sample D, (b) Plots the integrated intensity ratio of $I_{Defectstates}/I_{FX}$ peaks for the samples D, E and F.	121
5.10	(a) and (b) RT Raman spectra of samples implanted with 100 keV energy, and samples A, B, and C, respectively.	122
5.11	(a - c) First derivative 2D current map of sample A, B and C respectively. The inset of (a) shows topography of corresponding sample. (d - f) Post-annealing First derivative 2D current map of sample A, B, and C, respectively. The spatial scale in topography image and all current maps is kept fixed at 600nm.	123
5.12	(a) and (b) Magnified view of first derivative 2D current map of samples A and B, respectively.	124
6.1	(a) FESEM micrograph of undoped ZnO nanorods,(b) enlarge view of red marked area of panel (a). (c - f) FESEM images of Mn-doped ZnO nanorods at molar concentration 0.5%, 1.5%, 2.0% and 2.5% respectively [5].	132
6.2	(a) EDX image of the nanorods doped with 2.0% of Mn. The red-marked zone represents the area from where the elemental mapping was performed. (b), (c) and (d) EDX mapped elemental maps of Zn, O, and Mn signals, respectively. (e) EDX spectrum acquired from the 0.5% Mn-doped ZnO nanorods.	133
6.3	(a) Glancing angle XRD patterns of undoped and 2.5% Mn-doped ZnO nanorods. (b) The magnified view of (100), (002) and (101) Bragg diffracted peaks. The Green vertical lines are guide for eyes and show the difference between two Bragg peaks [5].	134

6.4	(a) Room temperature (RT) PL spectra of Mn-doped ZnO nanorods. The inset shows RT PL spectrum of undoped ZnO nanorods. (b) Absorption spectra of undoped and Mn-doped ZnO nanorods. (c) Tauc plots of Mn-doped nanorods, the dotted lines are eye guide for extracting band gap from these plots. The inset depicts extraction of the band gap from the Tauc plot of undoped nanorods by fitting a straight line (Black solid line). (d) A symbolic plot for extracted band gap of undoped and Mn-doped nanorods. The black solid lines are eye guides for variation in band gap [5]. The error bars were obtained from the fitting of straight line in the respective Tauc plots.	136
6.5	(a), (b) Sample deconvoluted spectra of un-doped and 0.5% Mn-doped ZnO nanorods, respectively. (c) Plots for the $I_{Defect-state}/I_{FX}$ versus Mn-doping percentage.	137
6.6	(a, c) Close aperture (CA) transmittance plots of undoped and 0.5% Mn-doped nanorods respectively. (b, d) open aperture (OA) transmittance plots undoped and 0.5% Mn-doped nanorods, respectively. In each plot, solid lines are the theoretical fits to the experimental data.	139

List of Tables

1.1	Comparison between basic physical properties of ZnO and other widely used semiconductors.	4
3.1	Extracted fitting parameters for redshift of FX feature	76
4.1	Extracted EXAFS fitting parameters	96
4.2	Summary of recent updates on field emission characteristics of ZnO nanostructures	103
5.1	Concentration variation of O^{2-} , O_V , and O_C states.	117

Chapter 1

Introduction

Materials at nanoscale length exhibit distinct physical, chemical and mechanical properties from their bulk counterparts, owing to their size, shape, and surface area to volume ratio. In nanostructures, crystal imperfections often add/modify many important crystal properties, unlike their perfect nanocrystals [1]. The magnitude of these properties far exceeds that from their perfect nanocrystals. Thus, their in-depth understanding is essential for both the technological aspects and fundamental theoretical concepts of physics. Despite several reports on defects induced phenomena in nanostructures, a systematic study of influence of crystal imperfections on crystal properties is still remains an open topic for research [2–4]. A systematic approach on proving crystal imperfections over available large surface area of nanostructures can bring an upsurge for both the fundamental physics and nanotechnology applications. The fundamental importance of one-dimensional (1D) inorganic semiconductor nanostructures of diverse morphologies including nanorods, nanotapers, nanotubes, nanobelts etc. in nanoscience, and their wide range of technological applications in nanotechnology have received much attention [5–11]. Among the wide range of inorganic semiconductor nanostructures, ZnO based 1D nanostructures are of immense interest owing to their applicability in versatile applications like optoelectronic, photonic, electronic devices, sensors [8–25], and are in trend for different research interests. In order to utilize the extended and point imperfections in the optical and electrical device applications this work is focused on the engineering of these defects in the matrix of ZnO nanorods by using different methods.

In material point of view, ZnO is a direct and wide band gap semiconductor having peerless material properties suitable for versatile applications [26, 27]. At room temperature (RT), its direct and wide bandgap of around 3.4eV along with large exciton binding energy of 60 meV enables it a suitable candidate for RT optoelectronic and photonic devices [13–18]. Its high

cohesive energy enables it as highly mechanical stable and the non-toxic nature makes it as an environment-friendly material. The absence of inversion symmetry incorporates inbuilt polarity in the ZnO matrix, which causes the excitation of phonon modes, suitable for phonon based optical studies. Except for the inbuilt polarity, the absence of inversion symmetry makes it a suitable material for both the piezoelectric and nonlinear optical studies also. The ZnO exhibit inherent n-type conductivity nature and can be easily doped with n-type dopants like Al, In, Ga, Si etc. [28–32]. The ZnO doped with n-type dopants can be used as a cost-effective alternative to ITO for transparent conducting electrodes due to its highly conducting nature and transparent behavior in the visible region. In literature, ZnO nanostructures and thin films have been grown by various methods including wet chemical, molecular beam epitaxy (MBE), sputtering, pulsed laser deposition (PLD), atomic layer deposition (ALD) etc [33–38]. Depending on the degree of defects, the optical and electrical properties of ZnO nanostructures and thin films can be tailored, irrespective of intrinsic or extrinsic in nature. The degree of intrinsic defects/disorders in ZnO nanostructures and thin films depends on many factors including growth temperature, the vacuum of the deposition chamber, method of preparation, mismatch between the lattice parameters of ZnO and substrate used for the growth etc., whereas the extrinsic defects/disorders are artificial and their characteristics depend on the nature of dopant/impurity. Band gap narrowing/broadening and emission of different deep level emissions are few examples of the influence of defects on the optical properties of ZnO nanostructures and thin films [39,40]. The presence of defects may provide additional free charge carriers and their excess presence may bring a transition from semiconductor to the metallic phase [41,42]. In case of higher defect density, the charge carriers can be strongly localized resulting the transition from semiconductor to insulator phase [45].

1.1 ZnO: A promising direct and wide band gap semiconductor

ZnO is known for its potential in efficient optoelectronic and photonic applications with high carrier mobility, high electrical breakdown voltage, high melting point, and strong RT luminescent properties [15, 26, 43, 44]. This section is devoted to the general properties of ZnO.

1.1.1 Crystal structure

ZnO is a II-VI binary compound semiconductor sharing three different crystal structures named as wurtzite, zinc blende, and rocksalt (or Rochelle salt). In all these structures each anion is surrounded by four cations at the corners of a tetrahedron, and vice versa [26]. The tetrahedral coordination of ZnO shares sp^3 covalent bonding. A report by Ozgur et al. [28] state that it's between covalent and ionic bonding. Under different ambient conditions, the wurtzite structure of ZnO is a thermodynamically most stable phase, whereas the zinc blende and rocksalt phases are stable only for the growth on cubic substrates and relatively high pressure, respectively. The unit cell of wurtzite structure of ZnO is hexagonal in nature and belongs to the space group C_{4v}^6 or $P6_3mc$. In wurtzite structure, there are three parameters which describe the lattice: a , the length of sides of the basal plane, c ($c/a = \sqrt{8/3}$), the height of the hexagonal cell, and the internal parameter u . The internal parameter (u) is defined as the length of the bond parallel to the c -axis divided by the lattice parameter c .

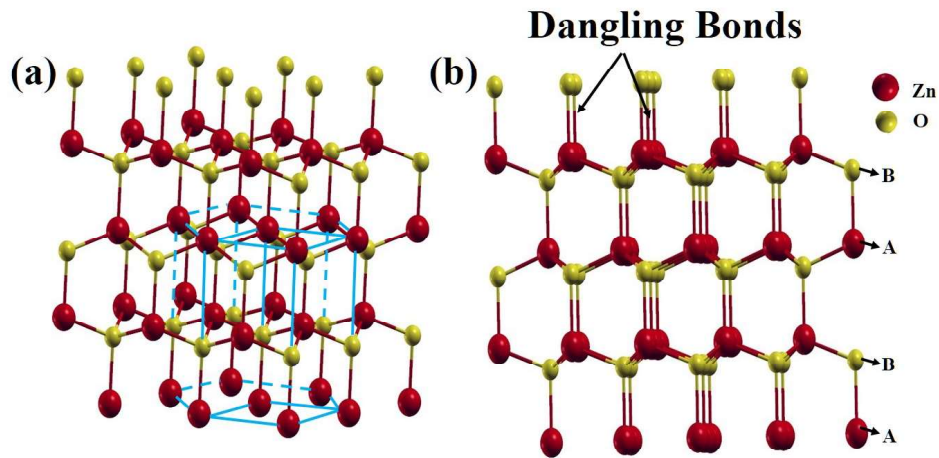


Figure 1.1: (a) Schematic diagram of a hexagonal wurtzite crystal structure. The blue solid lines show its unit cell of hexagonal structure. (b) shows ...ABABAB... stacking of atoms in hexagonal structure.

The schematic picture of the conventional wurtzite structure of ZnO is shown in figure 1.1(a), where the wurtzite structure is made of two interpenetrating hexagonal close-packed sub-lattices and each atom shares tetrahedral coordination. In each sub-lattice there are four atoms per unit cell and each atom of group II is surrounded by the four atoms of the group VI, or vice versa [26, 28]. Figure 1.1(b) represents the ABABAB type stacking of Zn and O atoms (through dangling bonds) along the c -axis. In wurtzite structure, the crystallographic vectors

\vec{a} , \vec{b} and \vec{c} are described as $\vec{a} = a(1/2, \sqrt{3}/2, 0)$, $\vec{b} = a(1/2, -\sqrt{3}/2, 0)$, $\vec{c} = a(0, 0, c/a)$ and the cartesian coordinates of basis atomic sites are $(0, 0, 0)$, $(0, 0, uc)$, $a(1/2, \sqrt{3}/6, c/2a)$ and $a(1/2, \sqrt{3}/6, [u+1/2]c/a)$. A brief comparison of the major properties of ZnO with other generally used semiconductors is summarized in table 1.1, where ZnO turns out to be a multifunctional material suitable for various applications [44, 46–50].

Table 1.1: Comparison between basic physical properties of ZnO and other widely used semiconductors.

Physical Property	Si	AlN	GaAs	GaN	ZnO	TiO ₂
Electronic band structure	Indirect	direct	direct	direct	direct	quasi-direct
Band gap (eV)	1.1	6.2	1.4	3.4	3.37	3.03, 3.20
Exciton binding energy (meV)	–	57	4.8	22	60	130
Bohr radius (nm)	5	1.9	14	2.9	1.4	1.5
Breakdown field (MV/cm)	0.3	1.8	0.4	3.0	-	-
Thermal conductivity(W/cm.K)	1.5	2.9	0.5	2.1	0.6 - 1	0.58
Dielectric constant (ϵ_r)	11.8	8.5	12.8	8.9	10.4	17.0

1.1.2 Optical properties

The direct band gap characteristics of ZnO aligns the minima of the conduction band (CB) and maxima of valance band (VB) at the Γ point of the Brillouin zone, which allows the deep UV absorption from VB to CB and NBE emission from CB to VB. The VB and CB of ZnO comprise of filled 2p states of O²⁻ and empty 4s states of Zn²⁺ respectively, where the VB further splits into three sub-bands because of the spin-orbit (S.O., as shown in figure) and crystal field splitting. The excitonic transitions taking place from these sub-bands are marked as A, B, and C, and the schematic of these excitonic levels in the valence band is shown in figure 1.2. The splittings of A-B and B-C exciton levels are associated with spin-orbit splitting and crystal field splitting respectively, which are of magnitude ~ 6 meV and 38meV respectively. [28]. The electrons in CB experience the Coulombian force caused by the presence of holes in the VB, which may lead to the splitting of CB (0.22eV) as shown by dotted line in the figure 1.2. The absorption of a photon of energy equal or greater than the band gap generates electron hole pairs in CB and VB, respectively, forming the hydrogenic bound states (exciton) as a consequence of Coulomb interaction between them.

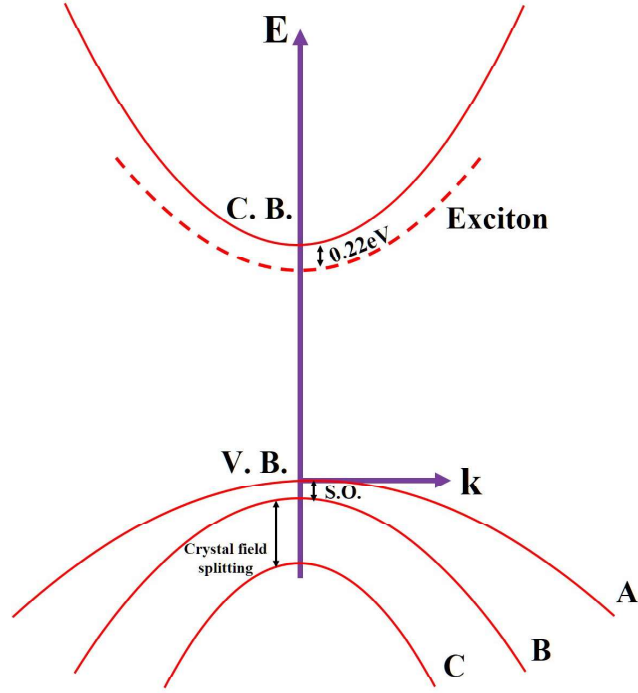


Figure 1.2: Schematic diagram of band splitting in E-K diagram of a direct band gap semiconductor.

The binding energy of an exciton can be described in a similar fashion like a hydrogen atom and is described as follows:

$$E_{exciton} = -\frac{\mu^* e^4}{2\hbar^2 \epsilon^2 n^2} = -\frac{E_B}{n^2} \quad (1.1)$$

Where, e , \hbar , ϵ and n are electronic charge, the Planck constant, dielectric permittivity of ZnO, and principal quantum number, respectively. The effective reduced mass of the exciton is represented by μ^* and is expressed as following:

$$\frac{1}{\mu^*} = \frac{1}{m_e^*} + \frac{1}{m_h^*} \quad (1.2)$$

Here, m_e^* and m_h^* represent the effective mass of electrons and holes, respectively. The high exciton binding energy (60 meV) of ZnO preserves its excitonic transitions even at above room temperature, which are desired for operating optoelectronic and photonic devices at room temperature [27]. The line width of excitonic transitions (at Γ ($k=0$) point) exhibits temperature dependent behavior, which normally broadens with increasing temperature [45, 51]. The excitonic transitions associated with the levels $n > 1$ can be seen in low temperature optical absorption/emission spectrum of pure ZnO crystals. However the population of excitonic transitions associated with higher n values is quite low compare to $n = 1$ [52]. The ionic bonding

between cations and anions of ZnO leads them to vibrate in opposite directions to each other, resulting in a long range polarization field and is considered as a superposition of longitudinal optical (LO) phonons. The scattering of free excitons from these LO phonon modes results in LO phonon assisted excitonic transitions. The energy of these transitions in optical emission spectrum is described as following [39]:

$$h\nu = E_g - E_{exciton} - n\hbar\omega_{LO} \quad (1.3)$$

where, $h\nu$, E_g , $n\hbar\omega_{LO}$ are energy of LO mode mediated excitonic feature, band gap and energy of LO phonon mode of corresponding n value, respectively. The excitons screen strong influence of defects/impurities present in ZnO matrix and are normally trapped inside them. The trapped excitons give rise to bound excitons and are called donor or acceptor bound excitons, depending on the nature of defect state. Sometimes, bound excitons form two electron satellites (TES), in which the excitons associated with neutral donor bound states recombine by leaving donor in an excited state. The transition energy of TES is less than the transition energy of donor bound excitons (DBE) [28]. Although the bound excitons are localized in trapping centers, but at the higher temperature they decay to free exciton states. The spread of kinetic energy of bound excitons is quite small resulting in narrower transitions compare to free excitons. Normally, the LO phonon replicas of bound excitons of ZnO can be observed in low-temperature (liquid helium temperature) photoluminescence spectrum. Except for the DBE donor-acceptor pair (DAP) transitions are also observed in ZnO, in which the excitonic transitions take place between shallow donor and acceptor species. Apart from such transitions, other defects/impurities mediated emissions in the visible range including green emission, red emission, white emission, orange emission are also seen. Such emissions are associated with various vacancies or interstitial like Zn vacancy (V_{Zn}), O vacancy (V_O), Zn interstitial (Zn_i), O interstitial (O_i) and other extrinsic impurities [53–58].

ZnO also shows nonlinear optical properties including second harmonic generation (SHG), third harmonic generation (THG) owing to the non-centrosymmetric nature of wurtzite crystal structure of ZnO. A perturbation in linear susceptibility caused by high external electric field introduces nonlinear polarizability in the bonds of ZnO. The polarizability of higher order can be expressed by Taylor series expansion of polarizability and is expanded as following:

$$P = \epsilon_0\chi^{(1)}E + \epsilon_0\chi^{(2)}E^{(2)} + \epsilon_0\chi^{(3)}E^{(3)} + \dots \quad (1.4)$$

Where, P is polarizability, χ is nonlinear optical susceptibility, ϵ_0 is the permittivity of ZnO.

Crystal defects / imperfections contribute to the nonlinear optical transitions in ZnO by providing some additional states/levels suitable for nonlinear transitions to take place. Despite few reports on nonlinear optical studies on ZnO nanostructures including SHG, saturable absorption, two photon absorption, a detailed and systematic study of nonlinear optical transitions based on crystal defects / imperfections is still an open problem [5, 59–61]. In general, the optical properties of ZnO are studied using absorption spectroscopy, photoluminescence and Raman spectroscopy. From the analysis of the data of these techniques the information about the optical transitions in ZnO like absorption edge, NBE emission, different exciton complexes, phonon modes etc. can be extracted.

1.1.3 Electrical properties

ZnO exhibit n-type conductivity and in literature the native defects (shallow donor levels) like Zn_i , V_O , zinc anti-sites, and deep acceptor levels are believed to be responsible for this characteristics [27, 63–65]. However, there exist controversies on the contribution from the few of these defects to the n-type conductivity. The first-principles based studies counter with the logic that Zn_i have high formation energy albeit it is a shallow donor, and even though V_O has low formation energy, but a deep donor, which can hardly contribute to the high concentration of carrier electrons [2, 66–71]. The calculations proposed other possible candidates like unintentionally incorporated H impurities into an interstitial site or into the O site [72, 73], metastable shallow donor state of the V_O [68], complex of Zn_i [74], and Zn_i stabilizes in the presence of high concentration of the V_O [26]. In literature, some experimental efforts have been carried out to obtain p-type conductivity in ZnO by using different methods like doping of Li, group V elements, and Nitrogen implantation [76–81]. In these reports authors observed that post-doping of above dopants, the concentration of hole charge carriers measured using Hall measurements significantly increases. Except for these methods, creating O-rich environment in ZnO matrix is an another possible method, where O_i also contribute to the p-type conductivity by acting as acceptor levels [18, 19, 21]. However, the stability and reproducibility of p-type conductivity in ZnO is still an open issue to be resolved. The deep acceptor levels, intrinsic defects and low dopant solubility are the bottlenecks for the stable p-type conductivity in ZnO [15]. In general, the electrical properties of ZnO thin films and nanostructures are studied using different techniques like Hall measurements, C-AFM, and typical I-V measurements tools.

1.2 Defects in ZnO and their influence on its optical and electrical properties

Defects/crystal imperfection (intrinsic and/or extrinsic) exhibit profound influence on optical and electrical properties of ZnO nanostructures. For the successful utilization of these defects in device applications, the in-depth understanding on their genesis, behavior and control over them is essentially required. The native defects are often believed to be source of unconventional properties of ZnO like inherent n-type conductivity, RT ferromagnetism etc. However, most of the proposal are based on circumstantial evidences. In ZnO, typically Zn_i , V_O , O_i , V_{Zn} , Zn and O anti-sites are considered as native point defects. Before going into the details of native defects in ZnO, theoretical understandings on their concentration and formation energy can provide better insights. The concentration of native defects depends on the formation energy of the respective defect centers and at thermodynamic equilibrium is described as following [2]:

$$C = N_{sites} \exp\left(\frac{-E^f}{k_B T}\right) \quad (1.5)$$

In above equation, the E^f and N_{sites} describe the defect formation energy and the number of sites where defects are incorporated, respectively. Essentially the formation energy of defects is a controlling parameter for the different possible defects. As an example, forming a V_{Zn} requires removal of one Zn atom and the energy required for this which we called formation energy is described as following [2]:

$$E^f(V_{Zn}^q) = E_{total}(V_{Zn}^q) - E_{total}(ZnO) + \mu_{zn} + q(E_F + E_v) \quad (1.6)$$

Here, $E_{total}(V_{Zn}^q)$ is the net energy of supercell which have V_{zn} in charge state q, $E_{total}(ZnO)$ is the total energy of ideal ZnO crystal in the same supercell, μ_{zn} , E_F and E_v are zinc chemical potential, Fermi level and maxima of valance band, respectively. Similarly the formation energy of other defect states can be calculated by using the initial parameters of the respective defect states. Among the native defects described in above the donor defects Zn_i , Zn anti-sites and V_O are associated with Zn excess and oxygen deficiency respectively, and the acceptor defects O_i , O anti-sites and V_{Zn} are associated with oxygen excess and zinc deficiency respectively. Normally, the Zn_i and O_i are located at the octahedral and tetrahedral sites, respectively. However, the phonon calculations predict that the Zn_i associated with the tetrahedral site are dynamically unstable [17]. The first principle calculations predicted that oxygen vacancy has deep donor level, and for any value of E_F each + charge state belonging to it is unstable [2, 66–69, 71].

Later on this was experimentally verified by Vanheusden et. al. [87]. The first principle calculations have proposed Zn_i as shallow donor. In the context of experimental verification, Look et. al [88] reported its donor energy of 30 meV, which is roughly similar to the theoretical predictions. At thermal equilibrium, the concentration of Zn_i in n-type ZnO is quite low owing to its high value of formation energy of amount 4eV. A report by Kim and Park et. al [26] proposed that Zn_i can be stabilized in the presence of high concentration of V_O . In the O-rich environment, the formation energy of V_O and Zn_i is about to zero and ~ 0.5 eV respectively, whereas in the O-poor environment it is negative for both the V_O and Zn_i . Hence, in p-type ZnO both the V_O and Zn_i can strongly compensate for the holes. The theoretical calculations suggest that in ZnO, V_{Zn} is a dominating acceptor type defects [2, 66–70] with the lowest formation energy in the O-rich environment, whereas in the O-poor environment the high E^f (~ 4 eV) is unfavorable for the formation of V_{Zn} . The native defect Zn anti-site is defined as an additional Zn ion situated at the O site. Theoretically it shows a transition level near the minima of the conduction band, except for that it also has two deep levels which are located below the middle of the band gap. The first principle calculations predict that in the n-type environment the preferential formation of highly positive charge states leads to very low formation energy of the Zn anti-site and negative formation energy in the O-poor environment [67]. With such characteristics of E^f in the O-rich and O-poor environment, the Zn anti-site is also predicted to compensate for the holes in p-type ZnO. In case of O_i , theoretically, they are expected to occur in various configurations like dumbbell [89] or split [2] interstitials, where an O ion is located at the octahedral interstitial site and in O_2 molecule-like configurations. In addition, the octahedral interstitial configuration has higher E^f value than the V_{Zn} , and propels two deep acceptor levels [2]. The first principle calculations show that the split configuration exists in the neutral charge state over the entire range of the Fermi level. The oxygen anti-sites are rarely formed owing to their higher formation energy compared to oxygen interstitial [2].

In a real crystal of ZnO, except for native defects, extended defects often occur and are related to stacking faults, clusters of defects, interface disorder, random grain boundaries and much more. Such defects are called as grown-in or process-induced defects and can be formed by growth parameters, external mechanical forces, extrinsic doping etc. The extended defects have significant impact on the optical and electrical properties of ZnO nanostructures and thin films. From fundamental physics and device applications point of view, the extended and point defects in ZnO nanorods are expected to play an important role on the optical and electrical

properties of ZnO nanorods. In this context, this thesis is focused on the engineering of both the extended and point defects using different methods and studied their influence on the optical and electrical properties of ZnO nanorods.

1.2.1 Influence on the optical properties of ZnO

At RT, the optical emission spectrum of a perfect crystal of ZnO exhibit only band to band optical transitions, which are associated with exciton recombination. The band to band transitions are also called as near band edge emissions (NBE), which appear in the UV range of electromagnetic spectrum. The presence of crystal imperfections incorporates localization of charge carriers, which give rise to various additional optical transitions together between different defect centers and the valence band or conduction band. However, the strength of such emissions depend on their localization energy. In a recent report by Singh et. al. [58] (a part of the thesis) showed temperature dependent quenching behavior of deep level emissions in twin ZnO nanorods originating from extended crystal imperfections and attributed it to the de-localization of imperfections at above certain temperature (180K). In literature, the optical transitions associated with crystal imperfections are mainly classified into three color emission bands named as: green, yellow, and red luminescence band [87,92,93].

In PL spectrum of ZnO, the green luminescence (GL) band genesis around between 2.4eV and 2.5eV in the visible range of radiation spectrum, and there can be multiple sources for the origin of this band including V_{Zn} , V_O [53, 54, 80, 87, 90–93]. The first principle calculations by Janotti et. al. [67] predicted the GL emissions from V_{Zn} , where V_{Zn} level occurs at 2.5eV. Since the hydrogen atoms passivate the V_{Zn} in ZnO by establishing strong O-H chemical bonds [95]. The experimental efforts by Sekiguchi et al. [94] and Lavrov et al. [95] showed robust passivation of GL using this concept, which reveals that V_{Zn} are responsible GL band. The yellow luminescence (YL) in ZnO appears at around 2.2eV, with a large life time compare to GL band [96]. The experimental results are in agreement with theoretical studies and confirm that the YL originates from the transitions between shallow donor levels to deep acceptor levels associated with additional oxygen (O_i) in ZnO [4, 96, 97]. However, a report by Radoi et al. [99] proposes that dislocations related luminescence centres can also contribute to the emission of yellow band. In PL spectrum of undoped ZnO, the red luminescence (RL) emerges at ~ 1.75 eV. The origin of RL is still under debate. Few reports attribute it to the transitions from hybridized Zn_i to V_O^{++} , whereas few from C.B. to O_i [100–102]. Except for

the native point defects, extended defects/imperfections also modify the optical properties of ZnO. These extended defects may include edge dislocation, slips, line imperfection etc. In this thesis, we introduced extended defects in twin ZnO nanorods by sandwiching an amorphous layer between two crystalline segments of nanorods, where the amorphous layer acts like a phonon barrier and becomes transparent for phonons beyond a certain thickness of 10nm [24]. Subsequently we also showed that extended defects have a strong influence on NBE emission of twin ZnO nanorods, where nonradiative optical transitions take place between minima of the conduction band to defect states followed by radiative transitions from these defect states to the maxima of valence band [58]. In a study by Azarov et. al [103] it has been shown that extended defects can be utilized as trappers for highly mobile vacancies. In their study Azarov et. al created extended defects in ZnO by the implantation of B and Ag, and trapped the Zn_i by using Li atoms as tracers.

Apart from optical emissions, defects/crystal imperfections also have significant impact on the absorption of ZnO. Generally, a perfect crystal of ZnO, exhibit absorption in UV range of electromagnetic spectrum. Imperfections/defects in ZnO, introduce modifications in the absorption spectrum, depending on their nature and concentration. Band tailing and band gap narrowing/broadening are some of the exemplary phenomena caused by defects/crystals imperfections. The Burstein-Moss (BM) effect broadens the optical gap in ZnO, where with an increase in donor concentration shifts Fermi level upward into the conduction band [104, 105]. In this process the Pauli exclusion blocking prevents transitions from valence band maximum to conduction band minimum and transitions take place between the maximum of the valence band and unoccupied higher states of the conduction band, resulting in an increase in the band gap [104, 105]. The localized shallow donor and acceptor levels (V_O , V_{Zn}) create band tailing (Urbach tailing) in ZnO. In literature, experimental studies predict the band tailing in ZnO due to cumulative effect of impurities, crystal imperfections, and exciton lattice interaction [104, 106]. In addition the lattice strain also causes the band gap narrowing/broadening of the ZnO depending on its nature, tensile/compressible [107, 108].

1.2.2 Influence on the electrical properties of ZnO

As it is already discussed that defects in ZnO can alter the conductivity (n-type to p-type and vice versa) of ZnO depending on their nature, formation energy, and concentration. In semiconductors, when concentration of donor/acceptor exceeds certain value depending on mate-

rial, semiconductor to metal transitions may take place by following Mott-transition phenomena [41, 109, 110]. However, for attaining Mott transition, the density of free electrons and Bohr radius (a_B) of donor/acceptor must satisfy the relation $N^{1/3} a_B \simeq 0.25$. In case of ZnO, theoretical Mott critical concentration value is $\approx 5 \times 10^{19} \text{ cm}^{-3}$. However, the experimental values may differ depending on the experimental conditions. In literature, several reports claim semiconducting-to metallic behavior of ZnO by using different dopants [30, 111–113]. Report by Brochen et al. [111] observed Mott-transition in Al and Ga doped ZnO thin films at critical concentration of carriers = $4.2 \times 10^{18} \text{ cm}^{-3}$. Similarly, in other recent reports by F. Singh et al. [112], Bhosle et al. [30] and Lu et al. [113] reported Mott-transitions in ZnO by doping of Ni, Ga, Ti respectively.

The extended defects residing at the surface of semiconductors modify the surface electronic states, causing modifications in the electrical properties. As an example the thin metallic layers deposited on the surface of a semiconductor effectively tailors the interface properties of metal-semiconductor interface [114–117]. The utmost accepted mechanism is metal induced mid gap states caused by pinning of the Fermi level, where the pinning of Fermi level is introduced by the persisting surface states. Such metal induced mid gap states leads to band bending at the interface. A report by Heine [114] has shown that such band bending can reduce the effective work function of the semiconductor leading to enhanced electronic activity of the semiconductors in response to external stimulus. Subsequent calculations and experiments by Nakato et al. [116, 117] have shown that nano-scale metallic islands on a semiconductor surface, can also result in very effectively band bending in the metal free part of the surface. Reports by Park et al. and Sheng et al. have shown that coating of Au on ZnO nanorods and Ag on ZnO thin films, respectively exhibit much improved electrical characteristics owing to the existence of interfacial layer and surface states [118, 119]. A report by Brillson et al. reported the influence of near-interface defects in Au-ZnO and Pt-ZnO diodes, on their Schottky barrier heights. The results show that resident native defects in ZnO single crystals and native defects created by the metallization process dominate metal-ZnO Schottky barrier heights and ideality factors [120].

1.3 Theme of the thesis

This thesis explores the engineering of extended and point defects in ZnO nanorods and their applications in optical and electrical devices. In this context, the extended defects in ZnO

nanorods were created in two ways: (i) Twin nanorods, and (ii) Au coating on the nanorods.

i. In twin nanorod architecture, intentionally we introduced extended defects in terms of the amorphous layer between two crystalline segments of ZnO nanorods and studied the influence of extended defects on the optical properties of nanorods and application to phonon tunnel device.

ii. The influence of extended defects formed at the Au-ZnO interface on the electron emission properties of ZnO nanorods were studied.

On the other hand, the point defects in ZnO nanorods were created by two methods : (i) Oxygen ion implantation, and (ii) Chemical doping of Mn in ZnO nanorods.

i. The oxygen ion implantation was carried out to create an oxygen-rich environment in ZnO nanorods, which can create the p-n junction in a single nanorod depending on the energy of incident oxygen ions. In this part, we studied the optical and electrical properties of implanted nanorods.

ii. The Mn doping in ZnO nanorods of different molar concentration was carried out using chemical doping method. In this section, we studied the influence of Mn-induced point defects on nonlinear optical properties (two-photon absorption and saturable absorption) of ZnO nanorods. Figure 1.3 represents the graphical theme of this thesis.

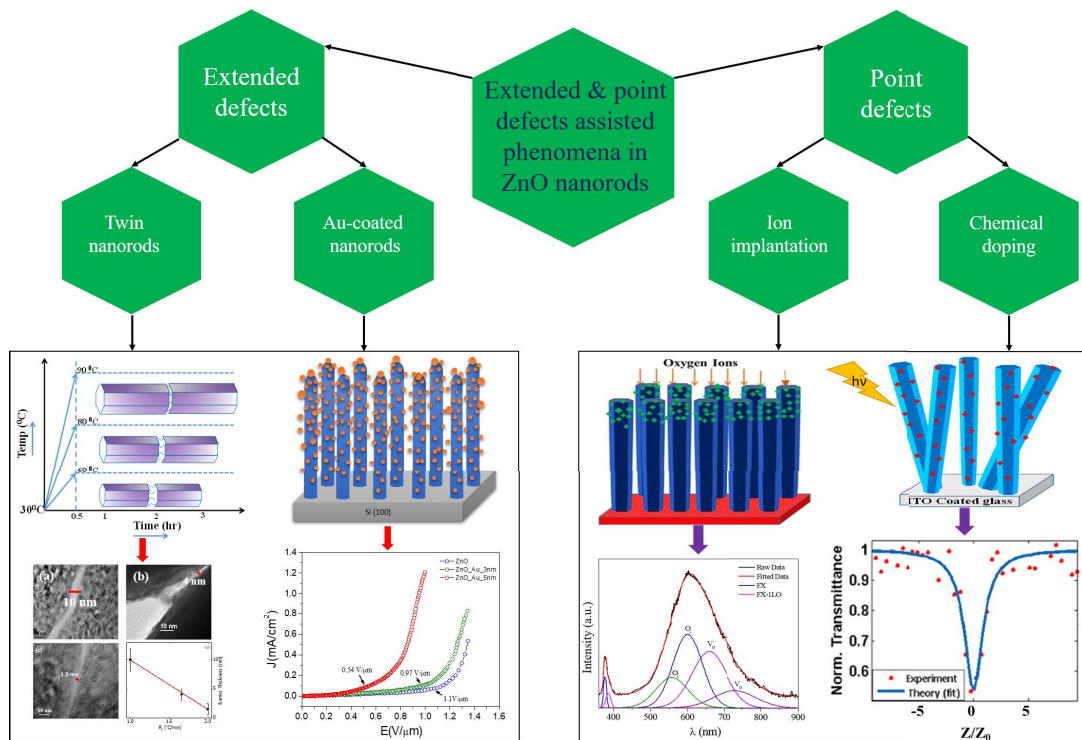


Figure 1.3: The graphical theme of the thesis.

Chapter 1 provides the motivation for the study of extended and point defects in one-dimensional nanostructures of ZnO including pervasive review of latest advancement and discussion on possible prospects. It also includes basic physical properties of ZnO, and influence of extended and point defects on the optical and electrical properties of ZnO.

Chapter 2 sheds light on the experimental methods and characterization techniques used for this thesis. In this context, the DC magnetron sputtering used for the deposition of the seed layer on Si substrates and aqueous growth of ZnO nanorods on different substrates are detailed. In addition to this, the working principle of various characterization techniques including FESEM, HRTEM, XRD, XPS, PL, Raman, UV-Visible spectroscopy, Z-scan technique, EXAFS AFM, KPFM, and TUNA is also briefly discussed. For the doping of O^+ ions, the working principle of ECR ion source for low energy ion implantation is also discussed.

Chapter 3 covers the aqueous growth and optical properties of unique twin ZnO nanorods (TNRs), in which an amorphous layer (extended defects) is sandwiched between two crystalline segments of nanorods. Initially, to synthesize the twin nanorods, the growth parameters were optimized by interplaying with the temperature ramping rate of the aqueous reaction medium, growth time and molar concentrations of precursors. A simple model is used for the growth of TNRs and is discussed in details. The FESEM, HRTEM, EDX, XRD techniques were utilized to explore the underlying growth mechanism of TNRs and investigate their crystal structure as well. The UV-Visible and PL studies were performed to study their optical properties. The deconvolution analysis of phonon replicas of FX emissions showed that the amorphous layer (extended defects) of a certain thickness (10nm) in TNRJs blocks the phonon modes and acts as effective phonon barrier. The results showed that the engineering of the thickness of the amorphous layer makes it transparent (4nm and 1.5nm) for the phonon modes and the TNRJs can be used as phonon tunnel device. This is a major finding of this work and has never been reported earlier. The results of temperature dependent PL spectra showed strong electron-phonon interaction in TNRs, which along with the lattice dilation contribute to the redshift of FX emissions. The results of temperature sensitivity of TNRs showed their applicability as temperature sensors in cryogenic temperature regime.

The hydrothermal growth and FE characteristics of Au decorated ZnO nanotapers are presented in chapter 4. The corrugated Au decoration on nanotapers was carried out using simple evaporation technique. The FESEM and XRD techniques were employed for investigating the topography and crystal structure of nanotapers, respectively. The study of influence of extended

defects present at Au-ZnO interface on the local crystal structure of Au-decorated nanotapers around the Zn-K edge was performed using EXAFS technique. The nanotapers display efficient FE characteristics with low turn on field by a corrugated decoration of Au and are consistent with the KPFM results where the work function of nanotapers decreases with Au coating. We believe that metal induced mid-gap states formed at the Au-ZnO interface are responsible for the observed low turn-on field, as a consequence of the drop in the effective work function of Au decorated ZnO nanotapers. The study of local conductance of nanotapers was carried out using TUNA measurements, and the results showed a very uniform and efficient tunneling current profile for Au-decorated nanotapers compared to as-grown nanotapers.

Chapter 5 includes the aqueous growth of vertically aligned ZnO nanorods and influence of O^+ ions on their optical and electrical properties. The O^+ ions were implanted in nanorods with three different energies 50, 100 and 350 keV. The O^+ ions of 100keV were implanted in nanorods at three different fluence (Φ): $\Phi = 5 \times 10^{14}$ ions/cm², $\Phi = 5 \times 10^{15}$ ions/cm², $\Phi = 5 \times 10^{16}$ ions/cm². The FESEM and XRD techniques were employed for the morphological and structural characterization, respectively. The concentration of point defects at all the three Φ values was calculated using XPS technique. In order to create point defects at different depths in a single nanorod itself the O^+ ions of energies 50 and 350keV were implanted successively in nanorods. The influence of point defects induced by O^+ ion implantation on RT optical properties of nanorods were studied by UV-visible, PL and Raman spectroscopy. After implantation, the optical absorption edge of samples showed a red shift compared to as-grown nanorods. The PL studies exhibit formation of nonradiative transition centres leading to complete suppression of NBE emission of ZnO nanorods. The post-annealing treatment in a vacuum, exhibit recovery of NBE emission followed by deep level emissions. C-AFM technique was employed to investigate the local electrical transport characteristics of implanted samples.

Chapter 6 covers the aqueous growth of Mn doped ZnO nanorods on the ITO coated glass substrates and study the influence of point defects created by Mn doping on their nonlinear optical properties. In this context the Mn-doping in nanorods was confirmed using EDX technique. The shift towards lower 2θ value of (002) peak in XRD pattern further confirmed the doping of Mn at Zn sites resulting in expansion of ZnO unit cell. The deconvolution analysis of PL spectra showed that Mn-doping in ZnO nanorods introduces various defect centers including Zn_i , O_i , V_{Zn} , and V_O , where the Zn_i dominate over other centers. The presence of dominating Zn_i supports the shift in XRD pattern and confirms the Mn doping at Zn sites. Plots for the

$I_{Defect-state}/I_{FX}$ versus Mn-doping percentage showed that with increasing doping percentage of Mn the defect densities in nanorods increases and was found maximum for 2.5% Mn-doping concentration. The investigations on NLO characteristics suggest that point defects in ZnO nanorods created by Mn-doping facilitate improved NLO interactions. The NLO results suggest that Mn-doped ZnO nanorods can be utilized for fabricating ultra-fast photonic switches, efficient optical phase-shifters, and optical limiters etc.

A brief summary of this thesis along with the future prospective is given in Chapter 7, where we conclude that how extended and point defects in ZnO nanorods were engineered to enable them to be utilized in different optical and electrical device applications.

Bibliography

- [1] C. Kittel, Wiley, **1976**, ISBN: 0-85226-469-0.
- [2] A. Janotti and C. G. Van de Walle, Phys. Rev. B, **2007**, 76, 165202.
- [3] F. Oba, M. Choi, A. Togo and I. Tanaka, Sci. Technol. Adv. Mater., **2011**, 12, 034302.
- [4] A. Janotti and C. G. Van de Walle, J. Cryst. Growth, **2006**, 287, 58.
- [5] P. Moriarty, Rep. Prog. Phys., **2001**, 64, 297.
- [6] A. P. Alivisatos, Science, **1996**, 271, 933.
- [7] C. Burda, X. Chen, R. Narayanan and M. A. El-Sayed, Chem. Rev., **2005**, 105, 1025.
- [8] S. Zhuiykov, Elsevier, **2013**, ISBN: 978- 1-78242-220-4.
- [9] P. D. Yang et al., Adv. Funct. Mater., **2002**, 12, 323.
- [10] Y. Xia et al., Adv. Mater., **2003**, 15, 353.
- [11] R.K. Joshi and J. J. Schneider, Chem. Soc. Rev, **2012**, 41, 5285.
- [12] S. Xu, Y. Qin, C. Xu, Y. Wei, R. Yang and Z. L. Wang, Nature Nanotech., **2010**, 5, 366.
- [13] R. R. Prabhakar, N. Mathews, K. B. Jinesh, K. R. G. Karthik, S. S. Pramana, B. Varghese, C. H. Sow, and S. Mhaisalkar, J. Mater. Chem., **2012**, 22, 9678.
- [14] Y. Li, A. Paulsen, I. Yamada, Y. Koide and J. J. Delaunay, Nanotechnology, **2010**, 21, 295502.
- [15] M. H. Huang, S. Mao, H. Feick, H. Yan, Y. Wu, H. Kind, E. Weber, R. Russo, P. Yang, Science, **2001**, 292, 1897.

- [16] X. Zhang, X. Han, J. Su Q. Zhang, Y. Gao, Appl. Phys. A, **2012**, 107, 255.
- [17] S. Wang, C. Song, K. Cheng, S. Dai, Y. Zhang and Z. Du, Nanoscale Res. Lett., **2012**, 7, 246.
- [18] D. Vanmaekelbergh and L. K. van Vugt, Nanoscale, **2011**, 3, 2783.
- [19] X. Wang, J. Song, J. Liu, Z. L. Wang, Science, **2007**, 316, 102.
- [20] S. Chu, G. Wang, W. Zhou, Y. Lin, L. Chernyak, J. Zhao, J. Kong, L. Li, J. Ren, and J. Liu, Nat. Nanotechnol., **2011**, 6, 506.
- [21] S. H. Jo, D. Banerjee, and Z. F. Ren, Appl. Phys. Lett., **2004**, 85, 1407.
- [22] Z. Zhao, C. Jiang, X. Pu, C. Du, L. Li, B. Ma, and W. Hu, Appl. Phys. Lett., **2016**, 108, 153104.
- [23] A. Orsini and C. Falconi, Nat. Scient. Rep., **2014**, 4, 6285.
- [24] A. Singh, K. Senapati, B. Satpati, M. Kumar and P. K. Sahoo, Phys. Chem. Chem. Phys., **2015**, 17, 4277.
- [25] A. Singh, K. Senapati, M. Kumar, A. K. Sinha, T. Som, P. K. Sahoo, Appl. Surf. Sci., **2017**, 411, 117.
- [26] H. Morkoc and U. Ozgur, Wiley-Vech, **2009**, ISBN: 978-3-527-40813-9.
- [27] C. Jagadish and S. Pearton(Editors), Elsevier, **2006**, ISBN: 9780080447223.
- [28] U. Ozgur et al., J. Appl. Phys., **2005**, 98, 04130.
- [29] S. Y. Myong, S. J. Baik, C. H. Lee, W. Y. Cho, and K. S. Lim, Jpn. J. Appl. Phys., **1997**, 36, L1078.
- [30] V. Bhosle, A. Tiwari, and J. Narayan, Appl. Phys. Lett., **2006**, 88, 032106.
- [31] H. Agura, A. Suzuki, T. Matsushita, T. Aoki, and M. Okuda, Thin Solid Films, **2003**, 445, 263.
- [32] T. Minami, H. Sato, H. Nanto, and S. Takata, Jpn. J. Appl. Phys., **1986**, 25, L776.

- [33] O. Lupan, G. Chai, and L. Chow, *Microelectronic Engineering*, **2008**, 85, 2220.
- [34] L. Znaidi, *Materials Science and Engineering B*, **2010**, 174, 18.
- [35] A. El-Shaer, A. C. Mofor, A. Bakin, M. Kreye, and A. Waag, *Superlattices and Microstructures*, **2005**, 38, 265.
- [36] D. C. Agarwal et al. *J. Appl. Phys.*, **2006**, 99, 123105.
- [37] S. L. King, J. G. E. Gardeniers, and I. W. Boyd, *Appl. Surf. Sci.*, **1996**, 96, 811.
- [38] E. Guziewicz et al., *J. Appl. Phys.*, **2009**, 105, 122413.
- [39] J. I. Pankove, Dover Publishing Inc. New York, **1975**, ISBN: 1 3-638023-9.
- [40] S. C. Jain and D. J. Roulston *Solid-State Electronics*, **1991**, 34, 453.
- [41] N. F. Mott, *Philos. Mag.*, **1961**, 6, 287.
- [42] V. F. Gantmakher, Oxford, **2005**, ISBN: 978-0-19-856756-1.
- [43] L. Liao, H. B. Lu, M. Shuai, J. C. Li, Y. L. Liu, C. Liu, Z. X. Shen and T. Yu, *Nanotechnology*, **2008**, 19, 175501.
- [44] K. Takahashi, A. Yoshikawa, A. Sandhu, **2007**, ISBN 978-3-540-47235-3.
- [45] C. Klingshirn, Springer, **2005**, ISBN: 13 978-3-540-38345-1.
- [46] Z. C. Feng, Imperial college London press, **2006**, ISBN-1-86094-636-4.
- [47] A. Di Carlo, *Physica status solidi (a)*, **2001**, 183, 81.
- [48] T. Yao, S. K. Hong, Springer, **2009**, ISBN: 978-3-540-88846-8.
- [49] W. Kang and M. S. Hybertsen, *Phys. Rev. B*, **2010**, 82, 085203.
- [50] D. O. Scanlon et al. *Nat. Mater.*, **2013**, 12, 798.
- [51] R. Hauschild, H. Priller, M. Decker, J. Bruckner, H. Kalt, and C. Klingshirn, *Phys. stat. sol. C*, **2006**, 3, 976.
- [52] B. K. Meyer et al., *Phys. stat. sol. b*, **2004**, 241, 231.

- [53] D. C. Reynolds, D. C. Look, B. Jogai, J. E. V. Nostrand, R. Jones, and J. Jenny, *Solid State Commun.*, **1998**, 106, 701.
- [54] A. F. Kohan, G. Ceder, D. Morgan, and C. G. Van de Walle, *Phys. Rev. B*, **2000**, 61, 15019.
- [55] A. Singh, K. Senapati, B. Satpati, K. K. Nanda and P. K. Sahoo, *MRS Advances*, **2016**, 1, 869.
- [56] Q. X. Zhao, P. Klason, M. Willander, H. M. Zhong, W. Lu, and J. H. Yang, *Appl. Phys. Lett.*, **2005**, 87, 211912.
- [57] Z. Gu, F. Liu, X. Li, J. Howe, J. Xu, Y. Zhao, and Z. Pan, *J. Phys. Chem. Lett.*, **2010**, 1, 354.
- [58] A. Singh, K. Senapati, B. Satpati, M. Kumar and P. K. Sahoo, *Phys. Chem. Chem. Phys.*, **2017**, 19, 14012.
- [59] M. C. Larciprete and M. Centini *Appl. Phys. Rev.*, **2015**, 2, 031302.
- [60] C. Y. Liu, B. P. Zhang, N. T. Binh, Y. Segawa, *Optics Communications.*, **2004**, 237, 65.
- [61] S. W. Chan, R. Barille, J. M. Nunzi, K. H. Ta, Y. H. Leung, W. K. Chan, A. B. Djurusic, *Appl. Phys. B - Lasers and Optics*, **2006**, 84, 351.
- [62] A. Singh, S. Kumar, R. Das, P. K. Sahoo, *RSD Adv.*, **2015**, 5, 88767.
- [63] F. A. Kroger, **1974**, vol 2, ISBN 10: 0720402824 / ISBN 13: 9780720402827
- [64] K. I. Hagemark *J. Solid State Chem.*, **1976**, 16, 293.
- [65] G. Neumann, *Phys. Status Solidi b*, **1981**, 105, 605.
- [66] S. Lany, and A. Zunger, *Phys. Rev. Lett.*, **2007**, 98, 045501.
- [67] A. Janotti, and C. G. Van de Walle, *Appl. Phys. Lett.*, **2005**, 87, 122102.
- [68] S. Lany, and A. Zunger, *Phys. Rev. B*, **2005**, 72, 035215.
- [69] F. Oba, A. Togo, I. Tanaka, J. Paier and G. Kresse, *Phys. Rev. B*, **2008**, 77, 245202.

- [70] P. Erhart, K. Albe and A. Klein, Phys. Rev. B, **2006**, 73, 205203.
- [71] T. R. Paudel and W. R. L. Lambrecht, Phys. Rev. B, **2008**, 77, 205202.
- [72] A. Janotti and C. G. Van de Walle, Nat. Mater., **2007**, 6, 44.
- [73] C. G. Van de Walle, Phys. Rev. Lett., **2000**, 85, 1012.
- [74] D. C. Look, G. C. Farlow, P. Reunchan, S. Limpijumnong, S. B. Zhang and K. Nordlund, Phys. Rev. Lett., **2005**, 95, 225502.
- [75] Y. S. Kim and C. H. Park, Phys. Rev. Lett., **2009**, 102, 086403.
- [76] D. C. Look, D. C. Reynolds, C. W. Litton, R. L. Jones, D. B. Eason, G. Cantwell, Appl. Phys. Lett., **2002**, 81, 1830.
- [77] D. K. Hwang, H. S. Kim, J. H. Lim, J. Y. Oh, J. H. Yang, S. J. Park, K. K. Kim, D. C. Look, Y. S. Park, Appl. Phys. Lett., **2005**, 86, 151917.
- [78] V. Vaithianathan, B. T. Lee, S. S. Kim, Appl. Phys. Lett., **2005**, 86, 062101.
- [79] Y. J. Zeng, Z. Z., Ye, W. Z. Xu, D. Y. Li, J. G. Lu, L. P. Zhu, B. H. Zhao, Appl. Phys. Lett., **2004**, 88, 062107.
- [80] S. B. Zhang, S. H. Wei, A. Zunger, Phys. Rev. B, **2001**, 63, 075205.
- [81] Q. L. Gu et al., Appl. Phys. Lett., **2008**, 92, 222109.
- [82] Z. Z. Ye, J. G. Lu, H. H. Chen, Y. Z. Zhang, L. Wang, B. H. Zhao, J. Y. Huang, J. Cryst. Growth, **2003**, 253, 258.
- [83] M. S. Oh, S. H. Kim, T. Y. Seong, Appl. Phys. Lett., **2005**, 87, 122103.
- [84] Y. Ma, G. T. Du, S. R. Yang, Z. T. Li, B. J. Zhao, X. T. Yang, T. P. Yang, Y. T. Zhang, D. L. Liu, J. Appl. Phys., **2004**, 95, 6268.
- [85] U. Ilyas, R.S. Rawat, T.L. Tan, P. Lee, R. Chen, H.D. Sun, L. Fengji, S. Zhang, J. Appl. Phys., **2011**, 110, 093522.
- [86] F. Oba, M. Choi, A. Togo, A. Seko and I. Tanaka J. Phys.: Condens. Matter, **2010**, 22, 384211.

- [87] K. Vanheusden, W. L. Warren, C. H. Seager, D. R. Tallant, J. A. Voigt and B. E. Gnade, *J. Appl. Phys.*, **1996**, 79, 7983.
- [88] D. C. Look, J. W. Hemsky and J. R. Sizelove, *Phys. Rev. Lett.*, **1999**, 82, 2552.
- [89] P. Erhart, A. Klein and K. Albe, *Phys. Rev. B*, **2005**, 72, 085213.
- [90] D. C. Reynolds, D. C. Look, B. Jogai, and H. Morkoc, *Solid State Commun.*, **1997**, 101, 643.
- [91] F. H. Leiter, H. R. Alves, A. Hofstaetter, D. M. Hofmann, and B. K. Meyer, *Phys. Status Solidi B*, **2001**, 226, R4.
- [92] R. Dingle, *Phys. Rev. Lett.*, **1969**, 23, 579.
- [93] K. C. Mishra, P. C. Schmidt, K. H. Johnson, B. G. DeBoer, J. K. Berkowitz, and E. A. Dale, *Phys. Rev. B*, **1990**, 42, 1423.
- [94] T. Sekiguchi, N. Ohashi, and Y. Terada, *Jpn. J. Appl. Phys.*, **1997**, Part 2 36, L289.
- [95] E. V. Lavrov, J. Weber, F. Brnert, C. G. Van de Walle, and R. Helbig, *Phys. Rev. B*, **2002**, 66, 165205.
- [96] O. F. Schirmer, and D. Zwingel, *Solid State Communications*, **1970**, 8, 1559.
- [97] Y. W. Heo, D. P. Norton, and S. J. Pearton, *J. Appl. Phys.*, **2005**, 98, 073502.
- [98] A. B. Djurisic, Y. H. Leung, K. H. Tam, L. Ding W. K. Ge, H. Y. Chen and S. Gwo, *Appl. Phys. Lett.*, **2006**, 88, 103107.
- [99] R. Radoi, P. Fernandez, J. Piqueras, M. S. Wiggins, and J. Solis, *Nanotechnology*, **2003**, 14, 794.
- [100] K. Bandopadhyay and J. Mitra, *RSC Adv.*, **2015**, 5, 23540.
- [101] T. Chen, G. Z. Xing, Z. Zhang, H. Y. Chen and T. Wu, *Nanotechnology* **2008**, 19, 435711.
- [102] N. H. Alvi, K. ul Hasan, O. Nur, M. Willander, *Nanoscale Research Letters*, **2011**, 6, 130.

- [103] A. Azarov, P. Rauwel, A. Hallen, E. Monakhov, and B. G. Svensson Appl. Phys. Lett., **2017**, 110, 022103.
- [104] B. E. Sernelius, K. F. Berggren, Z. C. Jin, I. Hamberg, and C. G. Granqvist Phys. Rev. B, **1988**, 37, 10244.
- [105] A. P. Roth, J. B. Webb, and D. F. Williams, Phys. Rev. B, **1982**, 25, 7836.
- [106] R. C. Rai, J. Appl. Phys., **2013**, 113, 153508.
- [107] Y. F. Li et. al, Appl. Phys. Lett., **2007**, 91, 021915.
- [108] V. Srikant and D. R. Clarke, J. Appl. Phys., **1997**, 81, 6357.
- [109] N. F. Mott, Proc. Phys. Soc. (London), **1949**, A62, 416.
- [110] N. F. Mott, Rev. Mod. Phys., **1968**, 40, 677.
- [111] S. Brochen et al., J. Appl. Phys., **2017**, 121, 095704.
- [112] F. Singh, B. Chaudhary, V. Kumar, R. G. Singh, S. Kumar, and A. Kapoor, J. Appl. Phys., **2012**, 112, 073101.
- [113] J. J. Lu, Y. M. Lu, S. I. Tasi, T. L. Hsiung, H. P. Wang and L. Y. Jang, Optical Materials, **2007**, 29, 1548.
- [114] V. Heine, Phys. Rev. A, **1965**, 138, 1689.
- [115] M. W. Allena, and S. M. Durbin, Appl. Phys. Lett., **2008**, 92, 122110.
- [116] Y. Nakato, H. Tsubomura, J. Photochem., **1985**, 29, 257.
- [117] Y. Nakato, H. Tsubomura, Electrochim. Acta, **1992**, 37, 897.
- [118] W. I. Park, G. C. Yi, J.W. Kim, and S. M. Park, Appl. Phys. Lett., **2003**, 82, 4358.
- [119] H. Sheng, S. Muthukumar, N. W. Emanetoglu, and Y. Lu, Appl. Phys. Lett., **2002**, 80, 2132.
- [120] L. J. Brillson et al., Appl. Phys. Lett., **2007**, 90, 102116.

Chapter 2

Experimental methods and analysis techniques

This chapter includes a brief description of experimental methods and analysis techniques used in this thesis. The ZnO nanostructures studied in this work were grown by relatively low-temperature aqueous growth method. Morphological and structural studies of nanostructures were carried out using FESEM, TEM, XRD, EXAFS techniques. UV-visible, PL, and Raman spectroscopy were employed to investigate their optical properties, and Z-scan technique was utilized to study the nonlinear optical properties. Extrinsic doping in nanorods was carried out using two different methods: **(i)** chemical doping and **(ii)** low energy ion implantation. The electrical and emission properties of ZnO nanostructures were investigated using AFM and field emission techniques. The work function of ZnO nanotapers was mapped using Kelvin probe force microscopy.

2.1 Sample preparation

2.1.1 Substrate cleaning

In this thesis, the ZnO nanorods were grown on two different substrates: **(a)** Si p-type (100), and **(b)** Indium Tin Oxide (ITO) coated glass. Depending on the substrates, two different standard cleaning processes were used which are described below.

Prior to the growth of nanorods, Si substrates were cleaned for 5 minutes in a solution of de-ionized water (DI-H₂O) and hydrofluoric acid (HF) prepared in a ratio of 9:1. Post-cleaning in this solution, substrates were ultrasonically cleaned in three different media of acetone, isopropyl alcohol (IPA) and DI-H₂O, for 10 minutes in each media. After completion of the cleaning process, the substrates were dried by the purging of Nitrogen gas.

ITO coated glass substrates were cleaned in freshly prepared aqua regia ($3\text{HCl} + \text{HNO}_3$) solution for 5 minutes in an ultrasonic bath followed by thorough ultrasonic cleaning in acetone, ethanol and DI- H_2O for 10 minutes each. After cleaning, substrates were desiccated by Nitrogen purging.

2.1.2 Seed layer coating

The cleaned Si substrates were placed on a rotatable sample holder with a rotation speed of 20 rpm, in a vacuum chamber at a base pressure of 2×10^{-7} mbar. Using pulsed DC magnetron sputtering technique, a thin layer of 1% Aluminum-doped ZnO (AZO) of thickness ~ 30 nm was deposited at a normal incident angle between target and substrates. The sole purpose of using seed layer was to ensure a fixed surface chemistry through out the substrate and avoid the lattice mismatch.

2.1.3 Room temperature growth of ZnO nanostructures

In recent years, miniaturization of devices has gained immense interest, and achieving an easier and adaptable method for the growth of nanostructures for the fabrication of such devices is essentially required. In commonly used growth techniques the engrossed complex growth parameters, sophisticated equipment, high growth temperature and uncontrollable orientation of nanowire/nanostructures prevent their growth over the large scale for commercial utilization. To overcome these issues, in this work we used room-temperature based wet chemical aqueous growth process, which requires a simple experimental setup and easily scalable parameters unlike the other growth techniques and also maintains the standard properties of ZnO. To study the influence of extended and point defects on optical and electrical properties of ZnO nanorods, we have grown three different types of ZnO nanorods, which are subdivided into two categories and a pictorial view of their subdivision is shown in figure 2.1.

- Nanorods grown on ZnO seeded Si.
- Nanorods grown on ITO coated glass.

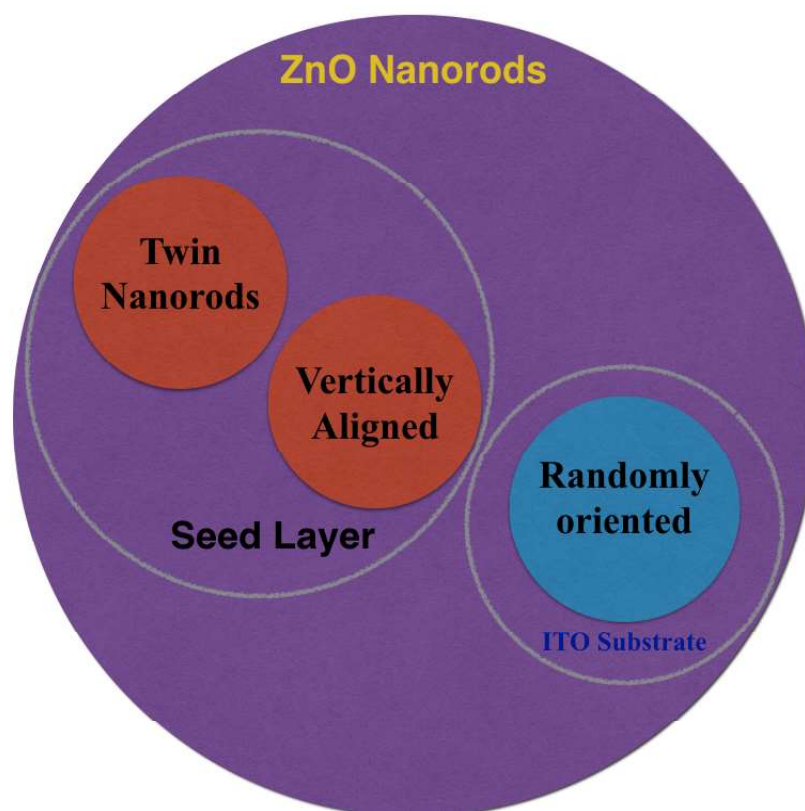


Figure 2.1: Schematic representation of types of ZnO nanorods used in this work.

2.1.4 Nanorods grown on seeded Si

In this part of work, prior to growth, the p-type Si (100) substrates were coated by a thin seed layer of ZnO. The Coating of seed layer on substrates ensures a fixed surface chemistry for all samples and efficiently lowers the interfacial energy between ZnO, and substrate [21]. On varying the growth parameters, ZnO seeded substrates allowed the growth of two different types of ZnO nanorods.

- Twin nanorods. (TNRs)
- Vertically aligned nanorods/nanotapers.

2.1.5 Nanorods grown on ITO coated glass

In this part of work, we measured the transmission spectra of ZnO nanorods, to study their optical switching behaviour. For this purpose, we have grown ZnO nanorods on commercially purchased Indium Tin Oxide (ITO) coated glass substrates. The nanorods were found randomly

oriented, owing to the lattice mismatch between ZnO and ITO, unlike the vertically aligned nanorods.

2.1.6 Growth process of ZnO nanostructures

ZnO nanostructures used in this work, were synthesized by a wet chemical aqueous growth method [2], for which the substrates were immersed into the aqueous solution of precursors Zinc nitrate hexahydrate ($\text{Zn}(\text{NO}_3)_2 \cdot 6\text{H}_2\text{O}$, 99%) and hexamethylenetetramine (HMT, $(\text{CH}_2)_6\text{N}_4$, 99.99%) of GR grade. The aqueous solution of precursors were prepared at 1:1 ratio. After immersion of substrates, the aqueous solution was allowed to react at a fixed temperature in a laboratory oven for a desired growth duration. The substrates were immediately taken out from the solution after reaching desired growth duration, followed by rinsing in deionized water for removing residuals from the surface.

2.2 DC magnetron sputtering

Sputtering is a physical vapor deposition (PVD) process in which the atoms are ejected from a solid target material by the bombardment of highly energetic particles. In the laboratory, usually Ar ions are used for bombardment. In this process, positively charged ions from the plasma of gas species are accelerated towards the target, a negatively charged electrode, whereupon collision with the target the incident ions transfer their momentum to the target atoms, resulting in the ejection of atoms from the target material. In a typical magnetron sputtering technique a magnetic field is applied near the target for trapping the ions, causing the enhanced efficiency of the initial ionization process. During this process, the ejected atoms condense on the surfaces of the substrates placed in the proximity of the magnetron sputtering cathode.

For this thesis, AZO films were deposited at a normal incident angle using a pulsed DC magnetron sputtering technique with an additional load-lock feature. The substrates were mounted on a rotating substrate holder kept at a distance of 10 cm from the target. For deposition, the base pressure was maintained at 2×10^{-7} mbar. Prior to deposition, ultra-pure (99.999%) Ar gas was injected into the chamber at a flow rate of 30 sccm (standard cubic centimeters per minute), until the pressure reaches a working pressure of 5×10^{-3} mbar. In order to generate the plasma of Ar gas, a DC voltage (Pinnacle Plus, Advanced Energy, USA) was applied between the target and the substrate. In addition, prior to deposition, pre-sputtering for 5 minutes

was carried out to remove the trapped impurities from the surface of the target, and during this process, a movable shutter was used to protect the substrate from getting contaminated. The entire deposition process was carried out at room temperature.

2.3 Ion implantation

Ion implantation is a powerful and unique technique for extrinsic doping in materials. The depth selectivity and spatial implantation features make it more suitable compared to other doping methods like chemical doping. In ion implantation process, the energetic ions interact with the target atoms, and come to rest by losing their energy. As a consequence of this, several processes including modification in lattice composition, displacement of atomic position, and sputtering take place. The ion implantation also builds-up of the concentration profile of impurity atoms within the host matrix, and alters the composition and lattice structure in the implanted zone. However, the spatial distribution of implanted impurities depends on the nuclear and electronic stopping processes and energy of incident ions.

Generally, low energy (keV) ion implantation causes sputtering of the target, whereas high energy (MeV) implantation results in the structural modifications of the material. During the interaction of energetic ions with surface of solids, the energy transfer mechanism takes place by following two energy loss processes: Nuclear energy loss ($S_n = (\frac{dE}{dx})_n$) and electronic energy loss ($S_e = (\frac{dE}{dx})_e$). Here $\frac{dE}{dx}$ is stopping power and defined as energy transfer per path length. Normally, in case of elastic collisions, energy loss mainly occurs through S_n , whereas for inelastic collisions it occurs through S_e . However, the dominant collision process depends on the energy regime.

For this thesis work, ZnO nanorods were implanted with low energy oxygen ions at the normal incident as shown in figure 2.2, using low energy ion beam facility (LEIBF) at Inter University Accelerator Centre (IUAC), New Delhi, India. The LEIBF uses Nanogan type Electron Cyclotron Resonance (ECR) based ion source, equipped with a permanent magnet (NdFeB), which is designed for radial and axial confinement of the plasma. All peripheral electronics (10 GHz (200 W) ultrahigh frequency transmitter, power supplies and vacuum components together with ECR ion source are installed on a 400 kV HV platform. The high current of multiply charged positive ions, with energy varying, from few tens of keV to few MeV, can be extracted from this ion source.

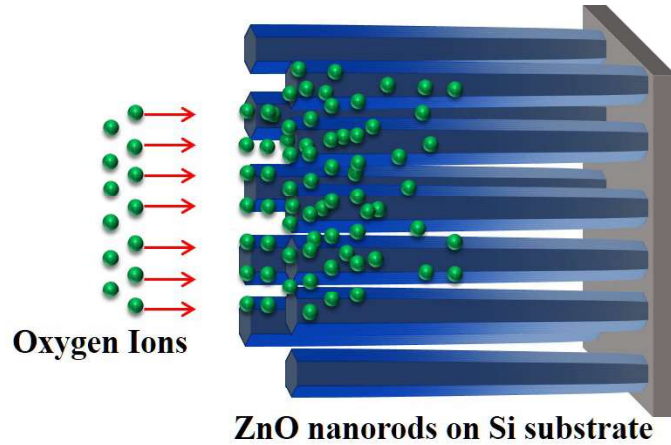


Figure 2.2: Schematic representation of O^+ ion implantation in ZnO nanorods.

In a conventional ECR implanter, a beam of positively charged ions is produced from the plasma of injected gas molecules, under a high vacuum of the order of $\sim 10^{-6}$ mbar. The ions are extracted by applying an external electrostatic field and are accelerated inside the accelerating tube by creating a potential gradient between the high potential deck and the ground. The beam of accelerated ions is bent at 90° using a bending electromagnet, and is focused by using quadrupole-triplet, placed in the path of beam-line. A magnetic steerer placed in the path of the beam aligns the beam on the surface of the samples. The beam can be seen on the display in two perpendiculars (x and y) directions using a beam profile monitor and the size of the beam spot is controlled by a double slit. A Faraday cup is placed in the path of the beam to stop it, when needed. During the beam tuning, a mass selection magnet is used for detecting the ions by analyzing their mass as well as for focusing them into fine circular spots. An electromagnetic beam scanner is used for homogeneous irradiation. For implantation, the beamline is always kept at a high vacuum of the order of $\sim 10^{-6}$ mbar.

2.4 Characterization techniques

In this work, for characterizing ZnO nanostructures, the emerging nano-characterization techniques of high spatial and analytical resolution including field emission electron microscope (FESEM), transmission electron microscopy (TEM), X-ray diffraction (XRD), X-ray photoelectron spectroscopy (XPS), and X-ray absorption fine structure (XAFS) were employed. The optical and electrical properties of ZnO nanorods were studied using UV-Visible spectroscopy, Photoluminescence (PL) spectroscopy, Micro-Raman scattering, Z-Scan technique, Field emis-

sion, and Atomic force microscopy (AFM) respectively.

2.4.1 Electron microscopes

The electron microscopes are meant for high resolution imaging. The resolution of a microscope is defined as the minimum separation between two objects by which they can be separated and distinguished as two distinct objects. The Rayleigh criterion [19] describes the spatial resolution (δ) of a microscope and is as follows.

$$\delta = \frac{0.61\lambda}{\mu \sin\alpha} \quad (2.1)$$

where δ , λ , μ and α are the spatial resolution, the wavelength of light source, the refractive index of medium and semi-angle of the magnifying lens, respectively.

However, at the dimension of sub-wavelength regime of photons, the resolution of optical microscopes is limited by the Fraunhofer diffraction limit and can be further exalted by replacing the photons with the sources of relativistic wavelength like electrons, having wavelength up to 10^5 times shorter than photons. The relativistic corrected wavelength of an electron is as follows -

$$\lambda = \frac{h}{\sqrt{2m_0eV \left(1 + \frac{eV}{2m_0C^2}\right)}} \quad (2.2)$$

where h is Plank's constant, m_0 is the mass of the electron, e is the electronic charge, V is the applied electric potential and $[1+(eV/2m_0C^2)]^{1/2}$ is the relativistic correction term applied when the incident electron energy is ≥ 100 keV.

Implementation of relativistic wavelength concept has replaced the optical microscopes by high spatial resolution electron microscopes like scanning electron microscopes, transmission electron microscopes.

Scanning electron microscope

Scanning electron microscope (SEM) is an extensively used equipment for the studies of the surface topography of microstructures and chemical compositional characterization of species [20]. In a typical SEM, an energetic beam of electrons interacts with the substance and transfer its kinetic energy to the electrons present in the sample, causing the emission of secondary electrons as a consequence of inelastic scattering, back-scattered electrons by elastic scattering along with electromagnetic radiation. The electrons, ejected through these phenomena are

collected at some special detectors attached with the system, followed by their conversion into intensity for each pixel on a computer which gives rise the morphology of the sample. The narrow electron beam used in SEM insists a large depth of field, yielding a 3-D appearance of the SEM micrographs.

In a conventional SEM, the electron gun of small energy dispersion(source) is utilized for achieving a stable electron beam with high current, and small spot size, which is mainly two types:

- Thermionic electron gun
- Field emission electron gun

In a typical thermionic electron gun, electrical heating of the filament induces the emission of electrons from the filament. However, the relatively low brightness, low thermal drifting while in operation, and a high-temperature requirement for electron emission hinder the use of thermionic electron guns in conventional SEM systems. The utilization of field emission electron gun in SEM yields high spatial resolution ($\sim 2\text{nm}$) with bright contrast and low electrostatic distortion, owing to less crossover diameter, small spot diameter, and coherent emission, unlike thermionic guns. In a conventional field emission electron gun, the electron emission is induced by an applied electrostatic field. A better spatial resolution with bright contrast and low electrostatic distortion enable field emission electron guns, superior to thermionic electron guns and are widely used in present day scanning electron microscopes. In the present thesis, the field emission scanning electron microscope (FESEM) of Zeiss (model-Sigma) was used to investigate the morphology and interface structure of ZnO nanorods. The schematic ray diagram of a standard FESEM system is shown in figure 2.3, where a field emission electron gun is used as a source of electrons. An extracting voltage is applied to the anode to accelerate the electrons. This model of FESEM allows the maximum extracting voltage up to 30 kV, however, all the images presented in this thesis were captured at an extracting voltage 5kV. For imaging, the column chamber was maintained at a vacuum range between 2×10^{-5} to $\sim 10^{-6}$ mbar, whereas a base pressure of around $\sim 3 \times 10^{-9}$ mbar was always maintained for the gun chamber. In the figure, the electromagnetic lens marked as the condenser lens is used to render the divergent beam into a converging/parallel beam, whereas the focusing lens is used for aligning the beam on the specimen.

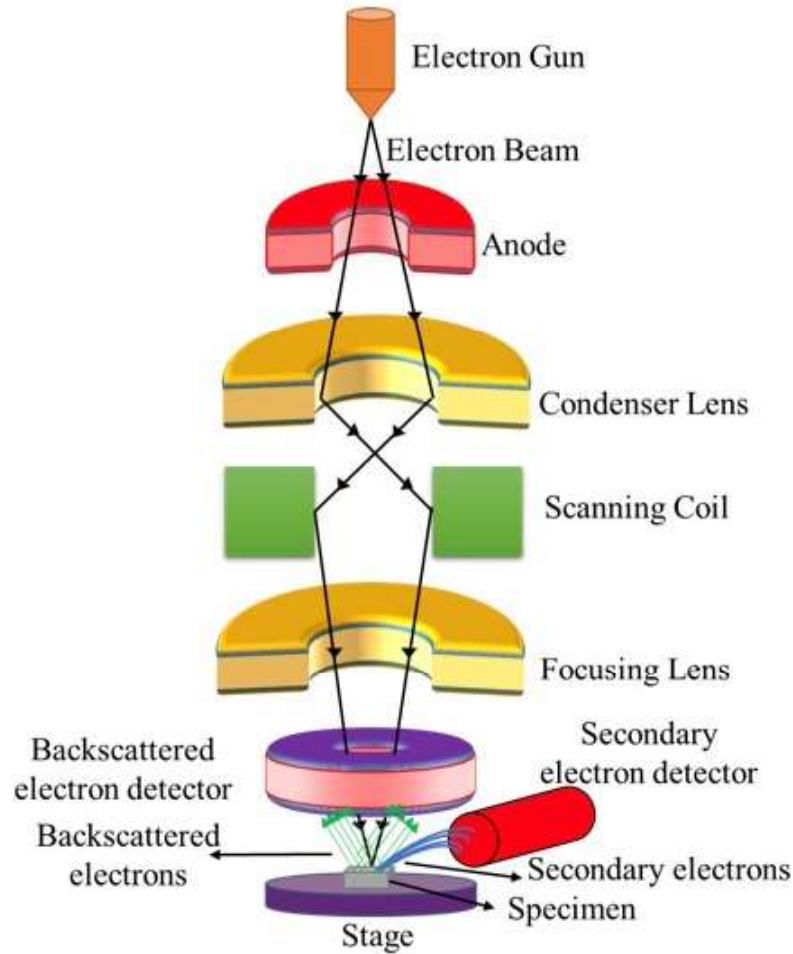


Figure 2.3: A schematic of typical field emission scanning electron microscope.

Transmission electron microscope

As described above, the resolution δ of an optical microscope is defined in terms of classical Rayleigh criterion, where the maximum spatial resolution can be $\delta = \lambda/2$, if $\mu \sin \alpha = 1$. For an example, the δ for the green light ($\lambda \sim 550$ nm), is ~ 300 nm. The spatial resolution 300 nm corresponds to the diameters of about 1000 atoms, but several materials, exhibit unusual properties on a scale below the resolution of the optical microscopes. Therefore, the details of the materials down to the atomic level are inevitable.

TEM is a powerful technique, for disclosing the material details down to the atomic level using the highly energetic beam of electrons. By ignoring the relativistic effects, we can correlate the resolution of a TEM with the energy of incident electrons with the Louis de-Broglie relation:

$$\lambda = \frac{1.22}{\sqrt{E}} \quad (2.3)$$

Where λ and E are wavelength (nm) and energy (eV) of incident electrons, respectively. As an example, for the electrons of energy 100 keV, the corresponding wavelength is ~ 4 pm (0.004nm) and is much below than the atomic diameter. Such features of TEM, provide precious information about crystallography and chemistry of the specimen.

The technical advancements have introduced a wide range of TEM, named as High voltage electron microscope (HVEM), analytical electron microscope (AEM), high-resolution transmission electron microscope (HRTEM), scanning transmission electron microscope (STEM), and are capable of providing more accurate insights about the specimen at atomic resolution limit.

- **Working principle**

In a typical TEM, a beam of energetic electrons is transmitted through an ultra-thin specimen, where the interaction between transmitted electrons and atoms within the specimen leads to the formation of the image/diffraction pattern depending on the focusing of the electro-magnetic lenses and apertures. In order to obtain selected area diffraction (SAD) pattern of the specimen, an aperture (SAD) is placed around the selected area of the specimen above the intermediate lens, whereas for conventional imaging, the SAD aperture is replaced by an objective aperture as shown in figure 2.4. For both modes, the diffracted beam of electrons follow Bragg diffraction condition ($2d \sin\theta = n\lambda$), where the constructive and destructive interference of diffracted electrons results in a phase contrast in the image. The phase contrast of an image can be described by the following relation:

$$T(U) = 2A(U) \times \sin(X(U)) \quad (2.4)$$

Where U , $A(U)$ and $X(U)$ are reciprocal lattice vector, aperture function and phase distortion function respectively. The appearance of phase contrast depends on the $T(U)$, if $T(U)$ is positive, a negative phase contrast appears (atoms appear bright against a dark background) and vice-versa. The SAD or SAED pattern offers the information of the crystallographic structure of the specimen, in reciprocal space. In SAED patterns, the central bright spot is corresponding to the direct beam of electrons with few scattered electrons and its distribution depends on the nature of the specimen. The spherical aberrations of the objective lens constraint the areal selectivity. For imaging of a very small area, usually a different method is preferred than SAED, known as fast Fourier transform (FFT) of HRTEM image, in which, the FFT is collected

from the area of interest. The FFT processing of the interference pattern of an HRTEM image provides the similar pattern like SAED. In figure 2.4, two basic working modes, diffraction pattern mode and imaging mode of a TEM are demonstrated.

- **Limitations**

1. Poor depth sensitivity
2. Limited projection
3. Ultra-thin specimen requirement
4. Limited sampling capability
5. Complex sample preparation process

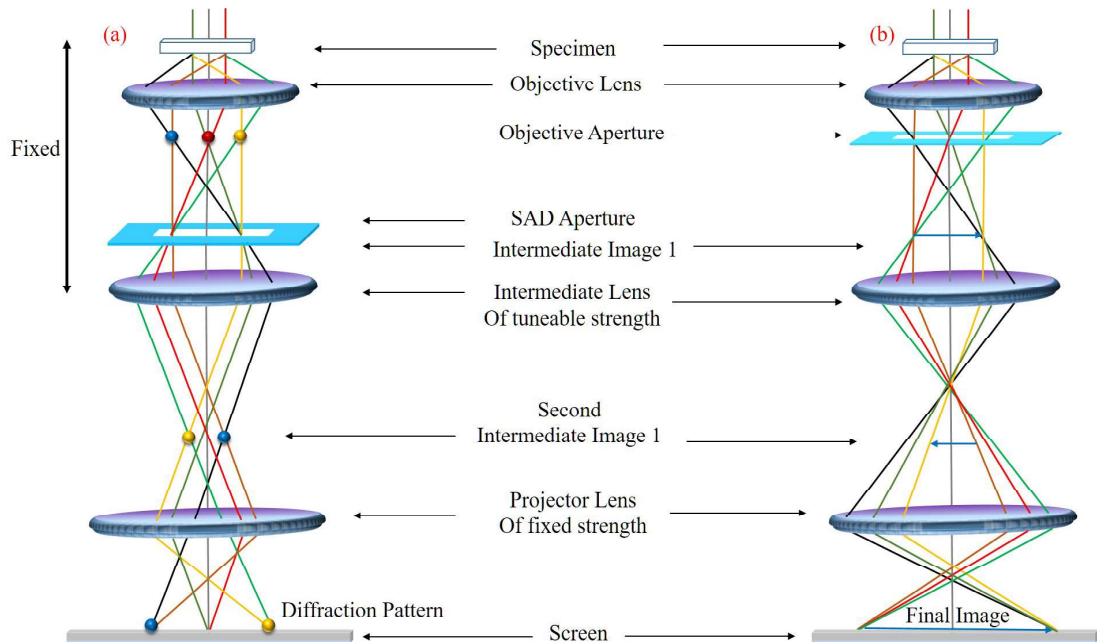


Figure 2.4: (a) and (b) show the schematic representation of the diffraction pattern operational mode and imaging mode of TEM, respectively. [21]

However, in recent years, the technical advancements have reduced some of the the above mentioned limitations. In this thesis work, a high resolution transmission electron microscopy from TITAN (Model: FEI Tecnai G² S-Twin) having 200keV electron energy was employed. The electron energy loss spectroscopy (EELS) was performed using an EELS detector (electron spectrometer) attached with HRTEM. In conventional EELS a beam of electrons of narrow range kinetic energy is exposed on specimen, where the incident electrons lose their energy through inelastic scattering with the atoms of specimen. The lose in energy of electrons is

measured by the electron spectrometer. The electron specimen interaction include phonon excitations, inter- and intra-band transitions, plasmon excitations, inner shell ionizations, and Cherenkov radiation. A typical EELS spectrum plots electron energy loss (eV) vs number of electrons detected by the detector.

2.4.2 X-ray diffraction

X-Ray diffraction (XRD) is a widely used technique for determining the crystal structure of a material. When a monochromatic X-ray beam encounters on a target material, is scattered by the specimen atoms and undergoes by the constructive and destructive interference. The interference of X-rays of the comparable wavelength to the atomic periodicity provides diffraction pattern of the specimen. The Bragg's law describes the criteria on the incident angle θ for the maximum constructive interference. [22]

$$n\lambda = 2d\sin\theta \quad (2.5)$$

Where n is an integer, λ is wavelength of incident X-rays, θ is incident angle, and d is the spacing between adjacent planes. Figure 2.5 represents the schematic diagram of X-ray diffraction from a periodic chain of atoms. The structural information of materials is extracted from diffraction patterns, which can be recorded in various geometrical configurations like θ to 2θ , grazing angle etc. In this work, Bruker D8 Advance diffractometer was used to record the XRD patterns of ZnO nanorods.

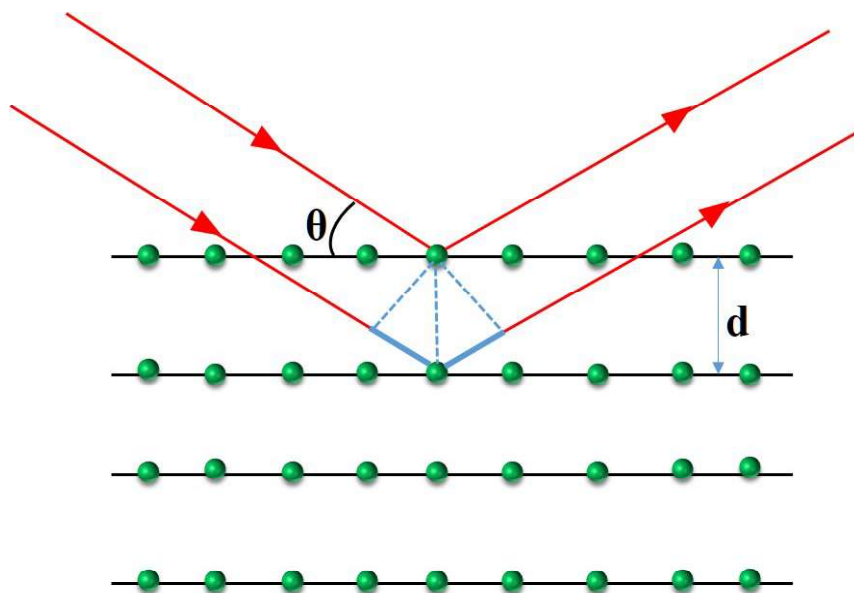


Figure 2.5: Typical ray-diagram of X-ray diffraction from a periodic chain of atoms.

2.4.3 X-ray photoelectron spectroscopy

The X-ray photoelectron spectroscopy (XPS) is a surface sensitive technique, which is employed for measuring elemental composition, electronic states and chemical states existing in the material. In a typical XPS measurement, the sample is illuminated with a beam of X-rays with simultaneously measuring the kinetic energy and electrons escaping from the surface (~ 1 to 10nm) of the material. Usually the measurements require ultra-high vacuum ($\sim 10^{-9}$ mbar). The illumination of x-ray photons of energy greater or equal to the binding energy of the electrons on a solid leads to ionization of atoms by ejecting the core/inner shell electrons from the atoms in the solid. The binding energy of the ejected electrons and energy of incident photons are related by the following relation:

$$E_{binding} = E_{photon} - (E_{kinetic} + \Phi) \quad (2.6)$$

Where, E_{photon} is the energy of the x-ray photon, $E_{kinetic}$ is the kinetic energy of the electron, and Φ is the work function of the material. The ejected electrons from different shells are effectively separated out in a desired narrow band of energies using electron analyzers, which are ideally electrostatic/magnetic lens units. The atomic species dependent characteristics of binding energy of electrons result in the identification of the existing element in/on the surface of the analyzed material. The characteristic spectral peaks in XPS spectrum correspond to the electron configuration of the electrons within the atoms. The area under the curve of spectral peaks describes the amount of the element within the sampling volume.

In this thesis, the XPS measurements were carried out using an experimental setup obtained from VG Instruments. During experiments, the base pressure of main chamber was maintained at 1×10^{-10} Torr. The system is equipped with a load-lock feature, and an Ar-ion gun is attached with the load-lock chamber as shown in figure 2.6. Dual Mg/Al anodes, a hemispherical analyzer and a channel electron detector are attached with the XPS unit, where the dual anodes generate non-monochromatic X-ray emissions of energies 1253.6 eV for Mg- K_{α} and 1486.6 eV for the Al- K_{α} lines. The analyzer is operated with the pass energy of 200 eV for the large survey scans in the range of 11000 eV, and 20 eV for the high-resolution scans.

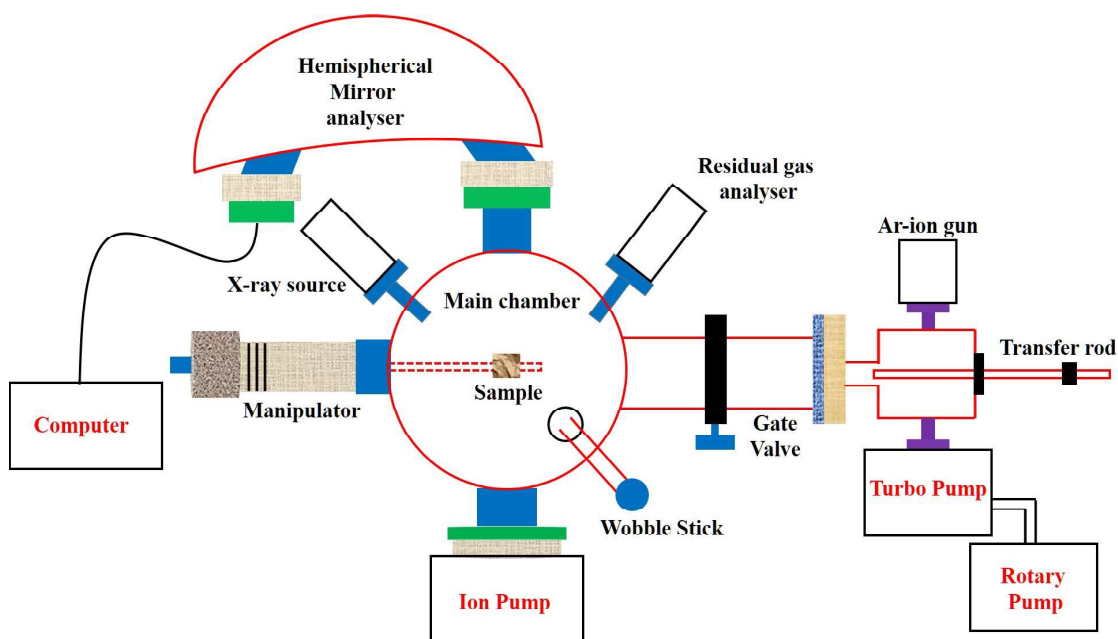


Figure 2.6: Schematic diagram of conventional XPS unit.

2.4.4 X-ray absorption fine structure spectroscopy

The X-ray absorption fine structure (XAFS) spectroscopy is a unique technique for the study of local crystal structure around a selected element within the material at atomic/molecular scale. The XAFS is a purely intrinsic quantum mechanical process, based on the X-ray photoelectric effect. In this process, the X-ray photons incident on an atom within a sample is absorbed, which results in the ejection of electrons from the inner atomic orbitals. However, for this process to take place, the energy of incident photons must be greater or equal to the binding energy of the respective orbitals. The interference between the photon waves scattered from the absorbing atoms and photoelectrons lead to an energy dependent variation in the X-ray absorption probability. The absorption probability is proportional to the X-ray absorption coefficient (μ), a measurable quantity. In experiments, the μ can be measured in two ways, either on transmission mode or fluorescent mode, depending on the sample. For this thesis, the measurements were performed in fluorescent mode, where the absorption coefficient is defined by the following equation:

$$\mu(E) \propto \frac{I_f}{I_0} \quad (2.7)$$

where, $\mu(E)$ is energy dependent absorption coefficient, I_f and I_0 are intensity of fluorescent and incident photons, respectively. The absorbing atoms get excited and the transition probability from ground state to excited state is governed by Fermi's golden rule. The absorption

coefficient depends on the transition probability between ground state and excited state. The mathematical expression for absorption coefficient from an isolated atom is described as:

$$\mu(E) = \frac{4\pi^2\omega e^2}{C} N_a \sum_f |\langle f|z|i \rangle|^2 \delta(E_f - E_i - \hbar\omega) \quad (2.8)$$

Where, ω , C and N_a are frequency of incident photons, speed of light and Avogadro's number respectively. The first term after summation represents transition probability between initial and final states, E_f , E_i , $\hbar\omega$ are energy of final unoccupied states, energy of initial (ground state) state and energy of incident photons respectively. In XAFS spectrum the interference patterns at high energy side give rise to extended X-ray absorption fine structure (EXAFS).

For this thesis, the EXAFS measurements were performed around Zn K-edge, at BL-9, Scanning EXAFS Beam-line of Indus-2, RRCAT, Indore, India. The beam-line mainly consists of Rh/Pt coated meridional cylindrical mirror for collimation and Si (111) based double crystal monochromator to select excitation energy. The X-ray absorption near edge structure (XANES) and EXAFS measurements were carried out in fluorescence mode using Vortex energy dispersive detector (VORTEX-EX). The energy range of EXAFS was calibrated by simultaneous measurements on a commercial Zn foil.

2.5 Optical properties measurement techniques

Reflectance, Transmittance, Photoluminescence (PL) and Raman spectroscopy are widely used techniques for studying the optical properties of materials. In this work, PL, Raman spectroscopy, and Z-scan technique were employed to study the influence of extended and point defects on optical transitions in ZnO nanorods.

2.5.1 Ultraviolet-visible near-infrared spectroscopy

When we shine electromagnetic radiation on the surface of a material, three different processes Absorption, Reflection, and Transmission of radiation take place depending on the nature of the material. These processes hold the law of conservation of energy in an optical medium by following the relation: $A+R+T = 1$. These processes are powerful analytical tools to characterize the optical properties of a material and are utilized for this thesis, and their details are described in following paragraphs.

The absorptance (A) of a medium is a measure of the effectiveness of absorbing power of the

medium and can be described as the ratio of the absorbed light to incident light.

Reflectance is the quantum of the incident light reflected from a surface [23]. The optical reflectance measurements were performed using Shimadzu (Model: UV 3101PC) UV-Vis-NIR spectrometer setup equipped with a specular reflectance measurement accessory, having the spectral range from 200 to 3200nm. The schematic of UV-Visible spectrometer is shown in figure 2.7. However, in this thesis, all the spectra were recorded over a wavelength regime between 300 to 800 nm. For calculating reflectance, initially, setup measures the absorbance spectrum which is converted into reflectance spectrum using Kubelka Munk function [24] followed by their conversion into Tauc plots using Tauc relation [25].

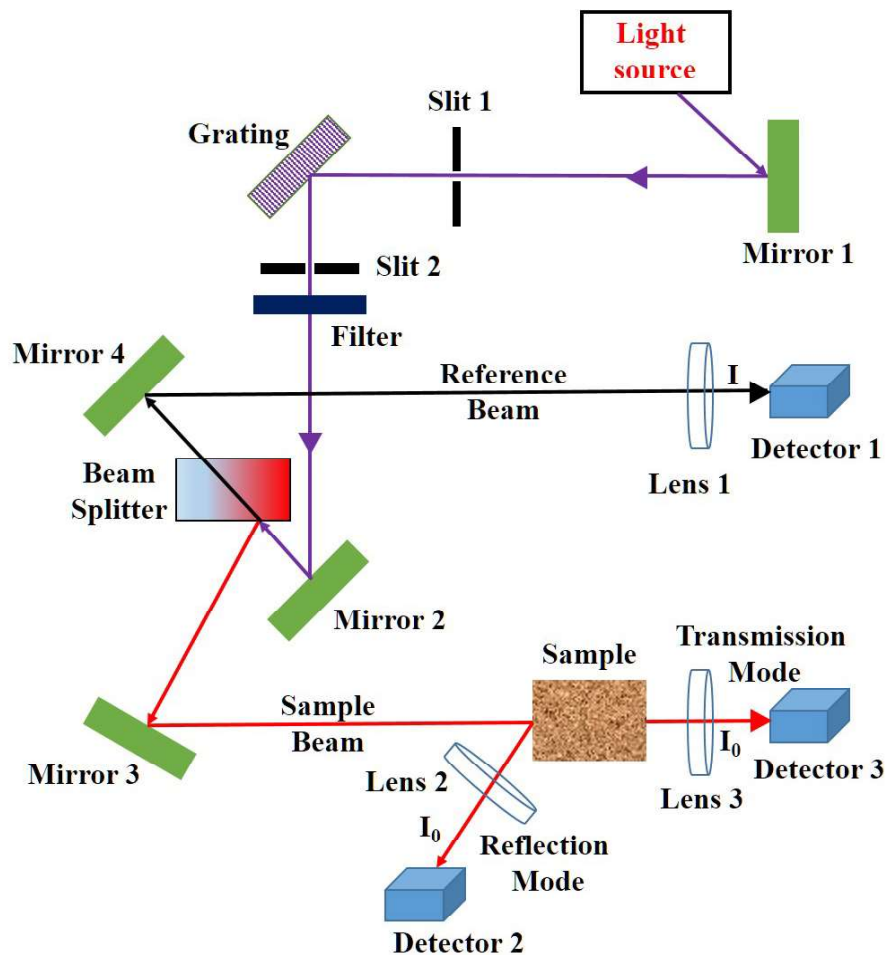


Figure 2.7: Schematic diagram of UV-Visible spectrometer setup.

For example the Tauc plot of AZO seed layer on Si substrate is shown in figure 2.8. The transmittance (T) of a medium is defined as its efficiency for transmitting the incident light. Mathematically, this can be described as the ratio of the intensity of the transmitted to incident

light. The transmission process occurs by following the diffusion and scattering phenomenon, where both the processes can take place simultaneously. In absence of diffusion, the incident beam follows the laws of geometrical optics resulting unidirectional transmitted beam called specular transmission. The net T of a medium is a superposition of specular transmittance T_s and diffuse transmittance T_d .

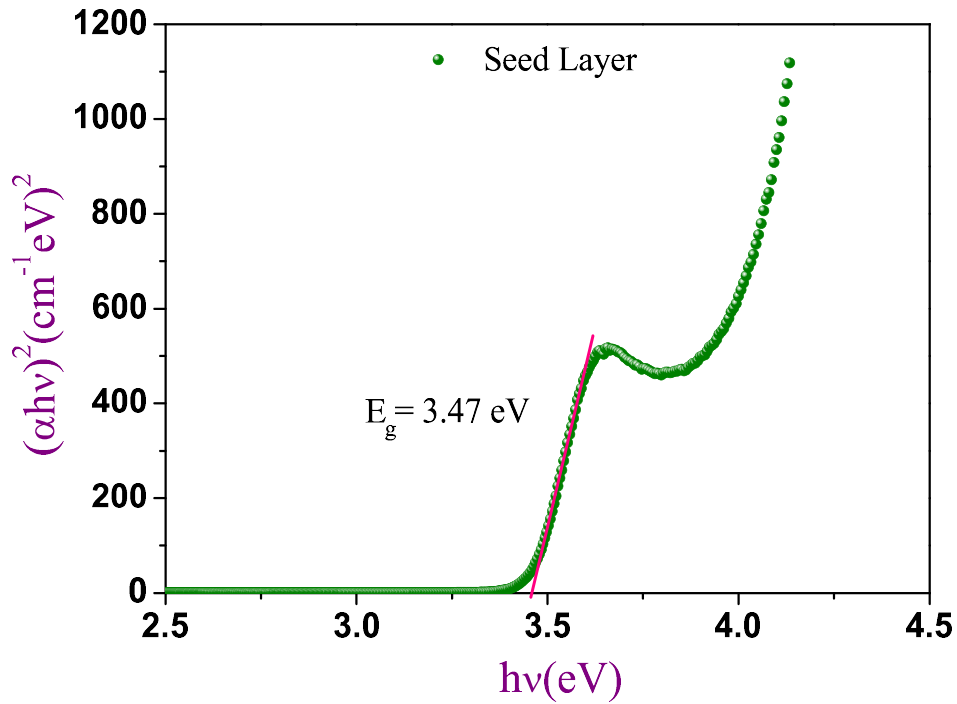


Figure 2.8: Tauc plot of AZO film deposited on Si substrate. The red line shows extraction of band gap by fitting a straight line.

2.5.2 Photoluminescence spectroscopy

Photoluminescence (PL) phenomenon is a consequence of radiative recombination of electron-hole pair between electronic bands, caused by an external optical excitation [26, 27]. In PL process, the optical excitation of energy $\hbar\omega_i \geq E_g$ are absorbed by the host material, causing the simultaneous ejection of electrons and holes of finite momenta (k) into the conduction and valance bands respectively. Once the electrons and holes are injected into respective bands, the excited electrons undergo the relaxation of energy by emitting Phonons of very short life time $\sim 100\text{fs}$ and accumulate at the bottom of conduction band, as shown by the cascade lines of figure 2.9(a), and finally by emitting photons, the annihilation of electron - hole pairs occur through the electronic transitions from the minima of conduction band to the maxima of valance

band. Figure 2.9 depicts a typical energy band diagram representation of PL process in a direct band gap semiconductor.

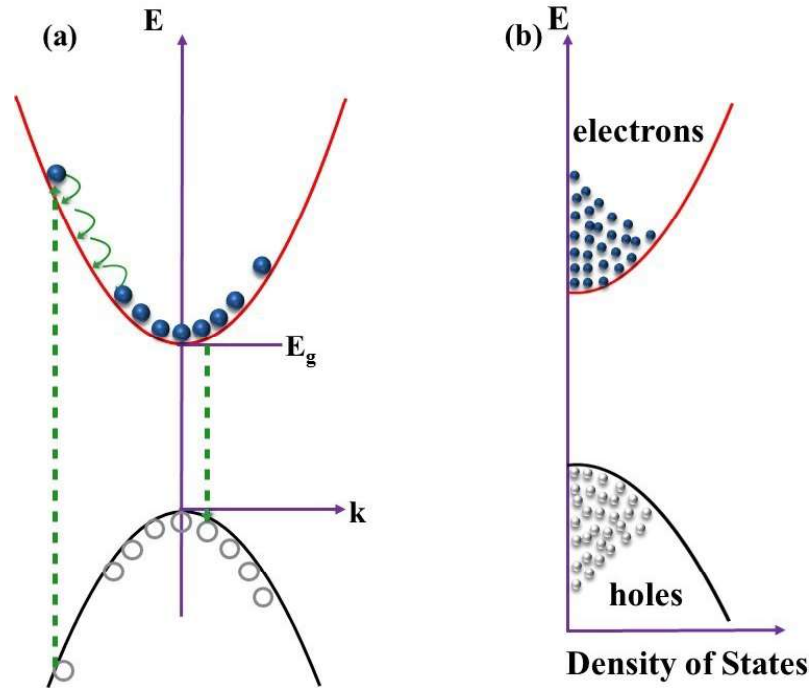


Figure 2.9: (a) schematic of PL process in a direct band gap semiconductor. The dotted green lines show electronic transition. (b) schematic for density of states occupancy of electrons and holes in corresponding states.

In a direct band gap semiconductor, optical transitions are governed by the dipole selection rules. During PL process, except band to band transitions some other electronic transitions like free to bound transition, donor-acceptor-pair (DAP) transition, free and bound exciton transitions may also take place, depending on the population strength and life time of respective states. In general, such additional electronic states are associated with various defect states like native point defects, and impurities. Absorbed molecular species also affect the luminescence of a material by creating different color centers. The intensity of direct band to band electronic transitions (near band edge emission) is expressed as:

$$I(\hbar\omega) = \sqrt{(\hbar\omega - E_g)} \left(\exp \frac{-(\hbar\omega - E_g)}{K_B T} \right) \quad (2.9)$$

Where $(\hbar\omega - E_g)^{1/2}$ factor arises from the joint density of states for the band to band transition and the second factor, from the Boltzmann statistics of the electrons and holes [26]. Figure 2.10 depicts the schematic representation of PL set-up used in this study (FLS 920, Edinburgh

Instruments) . A 325 nm He-Cd laser and a 355 nm laser were used as optical excitation sources. The low temperature PL measurements were carried out in liquid N₂ environment. In figure 2.10, the violet line represents the path of incident photons and the red line represents the emission from the sample. To prevent the detector from the incident light, different high pass filters are used as shown in figure. In setup, a neutral-density filter kept at beam entrance window endows the desired intensity of incident light for controlling the population of carriers. The objective lens placed in the path enables a precise probing of sample, as well as collection and focusing of emitted photons as consequence of luminescence of specimen.

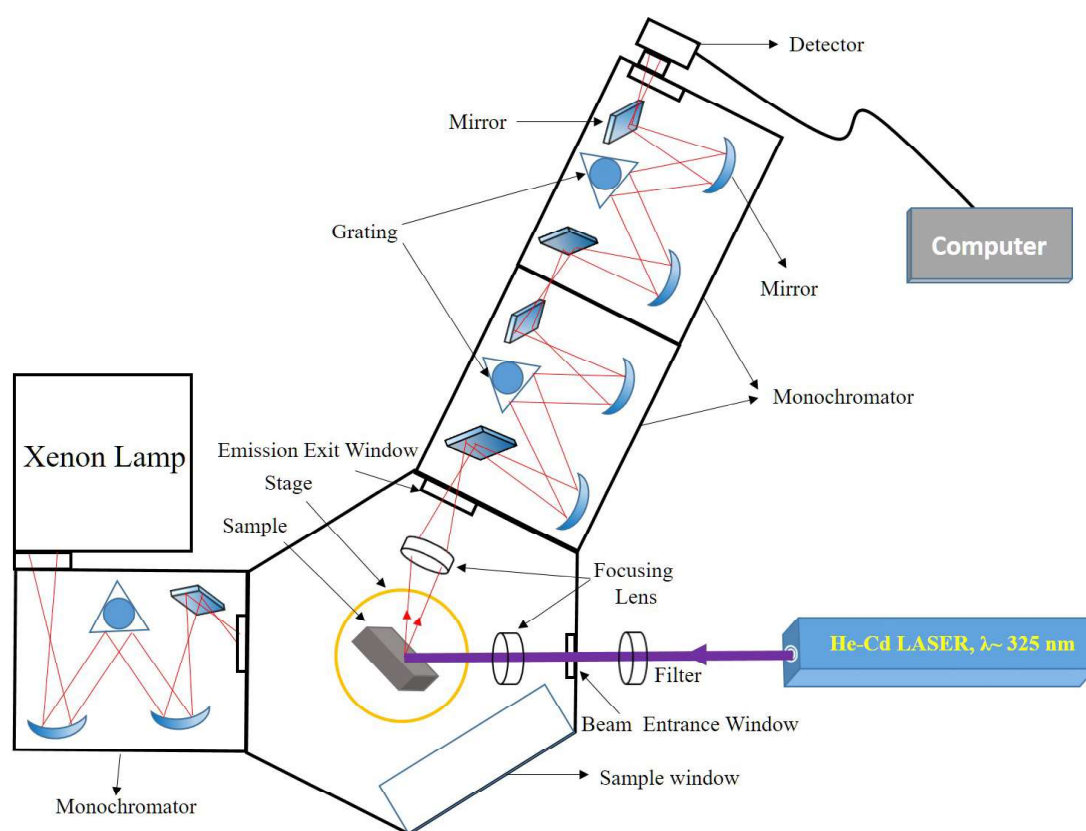


Figure 2.10: Schematic block diagram of PL set-up used in this study.

Temperature dependent PL mapping of twin nanorods was performed using alpha300 R Confocal Raman Imaging system from WITec, where a 355nm diode laser was used as an excitation source.

2.5.3 Raman spectroscopy

Raman spectroscopy is based on inelastic scattering process of photons, which is sensitive to the vibrational, rotational modes of atomic/molecular species. In this process, the electric field

of the electromagnetic radiation excites atomic/molecular species of the specimen either in the ground vibrational/rotational states or in the excited vibrational/rotational states depending on the energy of incident radiation. Upon excitation, the change in polarizability occurs and induces a dipole moment of the molecule, leading to inelastic scattering of photons (stokes or anti-stokes lines). The difference in energy between the initial vibrational/rotational state and final vibrational/rotational state leads to a shift in the frequency of emitted photons than the excitation frequency (Rayleigh line) and can be described as:

$$E_R = E_i - E_s \quad (2.10)$$

Where E_R , E_i and E_s are Raman energy shift, energy of incident photon and scattered photons respectively. Figure 2.11 shows the energy level diagram of Raman scattering process.

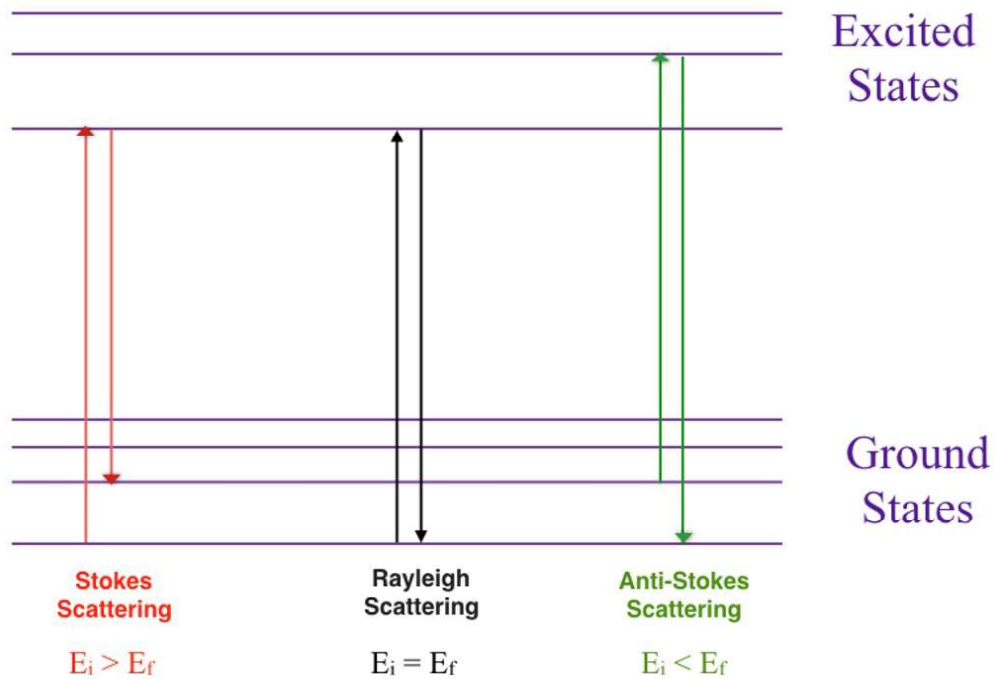


Figure 2.11: The energy level diagram of Raman scattering process.

In scattering process, the phonons are introduced to satisfy conservation of energy and momentum of incident and scattered photons, as described below.

$$\hbar\omega_i = \hbar\omega_s + \hbar\Omega \quad (2.11)$$

$$\hbar k_i = \hbar k_s + \hbar q \quad (2.12)$$

Where Ω and q are phonon frequency and phonon wave vector respectively. In our experimental setup, we used back-scattering geometry, where the scattered photons follow the path of the incident photons but in opposite direction and the max possible value of wave vector ($|q|$) is of the order of 10^7 m^{-1} [26], and in a crystal it is quite small compared to the size of the Brillouin zone (10^{10} m^{-1}). Thus, in back-scattering geometry the phonons of very small $q \sim 0$ are probed, due to which Raman scattering provides the frequencies of longitudinal optical (LO) and transverse optical (TO) phonon modes near the Brillouin zone center and very less information about the dispersion of the optical phonons. The non-destructive and contactless features of Raman spectroscopy make it more suitable over other techniques to characterize the materials. In addition, Raman spectroscopy is also used to observe the low frequency excitation of solids such as plasmons, magnons and superconducting gap excitation. For Raman spectroscopy, a setup from Horiba LabRAM HR was used. For excitation, a 532 nm green diode LASER was used as an excitation source and the Raman signals were recorded at a CCD.

2.5.4 Z-scan technique

The Z-scan technique is widely used in nonlinear optics to measure the non-linear refractive index(n_2) of the medium via close and open aperture methods.

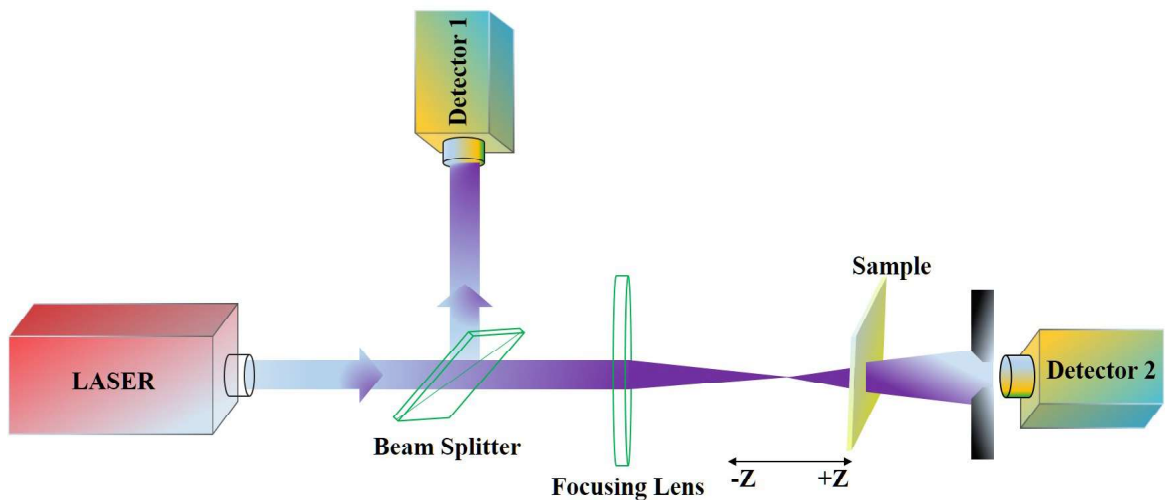


Figure 2.12: Schematic drawing of standard Z-scan technique [28].

As the name reflects, in this technique the change in transmittance of the sample is measured by translating the sample from $-Z$ to $+Z$ length scale. Figure 2.12 shows the sketch of the

experimental setup of Z-scan technique used in this study.

- **Theory**

In a linear medium the electric polarization depends on applied electric field and is expressed as:

$$\vec{P} = \epsilon\chi\vec{E} \quad (2.13)$$

Where, \vec{P} , ϵ , χ and \vec{E} are the polarization vector, permittivity of the medium, dielectric susceptibility of the medium and applied electric field, respectively. At large \vec{E} , the linear dependence of polarization vector on applied electric field breaks down and shows non-linear characteristics and it's Taylor series expansion about $\vec{E} = 0$ is expressed as:

$$\vec{P} = \epsilon\chi\vec{E} + \epsilon\chi^{(2)}\vec{E}^2 + \epsilon\chi^{(3)}\vec{E}^3 + \epsilon\chi^{(4)}\vec{E}^4 + \dots \quad (2.14)$$

Where

$$\vec{E} = (e/2)[A \exp(ikZ - i\omega t) + A^* \exp(-ikZ + i\omega t)] \quad (2.15)$$

For centrosymmetric medium ($-r = r$) $\vec{E}^2 = 0$, and polarization vector is modified as:

$$\vec{P} = \epsilon\chi\vec{E} + \epsilon\chi^{(3)}\vec{E}^3 + \dots \quad (2.16)$$

by simplifying above equation we obtain the relation between effective refractive index (n_{eff}) of the medium and polarization vector and is expressed below.

$$\vec{P} = \epsilon(n_{eff}^2 - 1)\vec{E} \quad (2.17)$$

with $n_{eff} = n + n_2$, and this phenomenon of change in refractive index is called optical kerr effect [29], Where n (cm^2/W) and n_2 (cm^2/W) are the linear and non-linear refractive index, respectively.

- **Experimental process**

In a typical Z scan technique, the LASER sources with Gaussian beam profile are used as source and transmittance of the sample is measured by using conventional photo-detectors. During experiments the position of detectors is fixed and the sample translates with respect to the focal point of a lens set at $Z = 0$. The measurement starts away from focus point ($-Z$), where the transmittance $T(Z)$ is relatively constant and sample keeps on translating towards the focal

point and then to the +Z as shown in figure 2.12. If the sample has $n_2 > 0$, the transmittance $T(Z)$ gives a valley followed by spire and vice versa for $n_2 < 0$. The beam narrows at the focal point, which results in the increased transmittance at the aperture. As defocusing occurs, the beam starts to broaden at the aperture and results in the decrease in the transmittance. The normalized transmittance is expressed as:

$$T(Z) = \frac{\int_{-\infty}^{\infty} P_T(\Delta\Phi_0(t)) dt}{S \int_{-\infty}^{\infty} P_i(t) dt} \quad (2.18)$$

where $P_i(t)$ is instantaneous input power in the sample, S is the aperture linear transmittance, $P_T(\Delta\Phi_0(t))$ is transmitted power. The $T(Z)$ is measured using mainly three different modes of aperture:

1. Closed aperture
2. Open aperture
3. Eclipsing aperture

Closed aperture

In this geometry, an aperture placed in the path of the transmitted light, which allows passing only the central region of the transmitted light reaching the detector, and blocks the rest of the radiation. This configuration allows the detector to measure only the focusing or defocusing that a sample may induce.

Open aperture

In this configuration, the aperture is either enlarged or completely removed from the path of the transmitted light and the entire transmitted light is reaching the detector. This configuration is used for measuring the nonlinear absorption coefficient ($\Delta\beta$) of the medium.

Eclipsing aperture

In this geometry a disk is placed at the place of aperture, which blocks the central region of transmitted light and passes the outer edges of the radiation reaching the detector.

To measure the $\Delta\beta$ and third order non-linear refractive index of a material, Z-scan technique is widely used due to its simplicity, accuracy and non destructive nature. In this study, we used a femto second (532nm) diode pumped solid state laser in a TEM₀₀ mode intensity profile. For the measurements the pulsed energy varied from 1 μ J to 125 μ J with pulse width $t_p \sim 0.7$ nS at 40 Hz repetition rate to minimize the impact of thermally induced optical nonlinearities.

2.6 Electrical properties measurement techniques

In this work, the influence of extended and point defects on electrical properties of ZnO nanorods were studied using field emission study, Atomic force microscopy (AFM), Kelvin probe force microscopy (KPFM) and Tunneling atomic force microscopy (TUNA).

2.6.1 Field emission study

The field emission is a quantum mechanical phenomenon, which occurs by the tunneling of electrons through a potential barrier at the solid-vacuum interface into the vacuum under an applied electrostatic field. The field emission process is highly efficient than the other emission processes like thermionic emission etc. However, for this process to take place high electric field ($\sim 10^7$ - 10^8 Vcm⁻¹) is required. The applied high electric field narrows the potential barrier at the metal-vacuum interface and the tunneling of electrons takes place by following Fowler-Northeim (F-N) mechanism [30]. Normally, the emission current density against applied electric field is described by the F-N equation which is as following:

$$J = A \left(\frac{\beta^2 E_{app}^2}{\Phi} \right) \exp \left(\frac{-B\Phi^{3/2}}{\beta E_{app}} \right) \quad (2.19)$$

Where, J (mA/cm²) and E(V/ μ m) are the emission current density and applied electric field respectively. $A = 1.56 \times 10^{-10}$ AeVV⁻², $B = 6830$ V/eV^{-3/2}/ μ m, β is field enhancement factor and Φ (eV) is the barrier height. However, the FE process from semiconductors is quite complicated, owing to their low carrier concentration in bulk compared to metal emitters. The F-N plot ($\ln(J/E^2)$ vs. $1/E$) provides the information about the emission characteristics of the emitting surface. The FE studies given in this thesis were carried out in a vacuum chamber at a base pressure of 4×10^{-7} mbar. The emission current density was recorded using a two electrode configuration (area ~ 0.05 cm²) made of copper as shown in figure 2.13. The samples were attached to the bottom cathode with a conducting copper tape (sheet resistance ~ 0.004 Ω /sq). The field induced emission current was recorded at a fixed separation of 100μ m between the sample and top cathode. A Keithley 2410 source meter was used for supplying the voltage and recording the emission current.

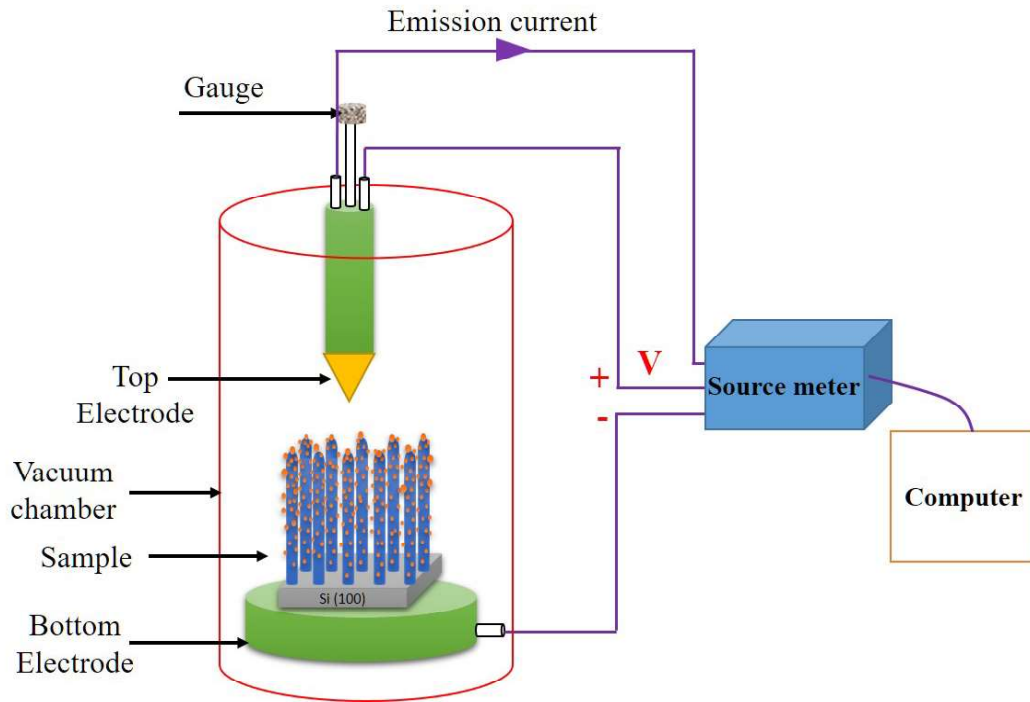


Figure 2.13: Schematic diagram of field emission unit.

2.6.2 Atomic force microscopy

The AFM is a localized real space imaging technique, which maps the tip-sample interaction due to the action of atomic forces between them. In an AFM, a platinum coated sharp tip of radius ~ 10 s of nm controlled by feedback loop is attached to the cantilever, which raster scans over the surface of the sample. During scanning over the surface, a LASER beam is focused on top of the cantilever [31]. The cantilever reflects the focused LASER beam to a photodiode, whereas the z-piezo movements re-adjust the bounced laser beam at the same position through a feedback loop, leading to the formation of the surface topography of the sample. Figure 2.14 shows a typical schematic of an AFM setup. The forces between AFM tip and sample have a direct impact on sample image and depend on deflection and stiffness of cantilever. The inter-atomic force versus distance curve between tip and sample is presented in figure 2.15. The point Z_0 , in figure, corresponds to the transition point between contact and non-contact mode of AFM. In a typical contact mode, both the tip and sample remains in close contact and tip experiences a strong repulsive force and while scanning over the surface of the sample the repulsive force causes bending of the cantilever as per change in the topography. In non-contact mode, as the name indicates, a separation between the AFM tip and sample is maintained and

the tip experiences an attractive force, due to which the sample cantilever starts vibrating near the surface of the sample without touching it.

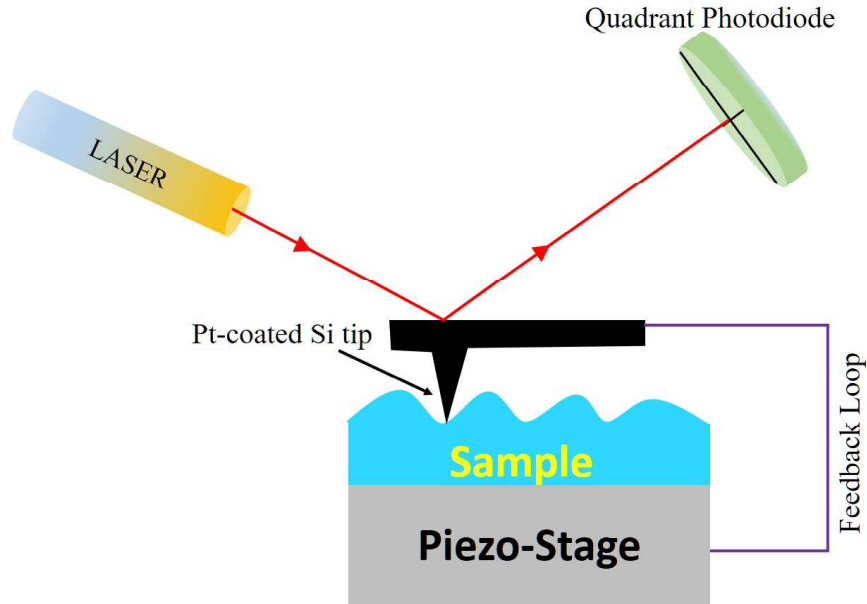


Figure 2.14: Schematic drawing of a conventional AFM setup.

In tapping mode (intermittent contact mode), the tip is oscillated (at its resonance frequency) very close to the sample surface and taps the surface only for a very small fraction of its vibration period. In tapping mode the lateral forces between the tip and the sample can be eliminated, which results into a better image resolution.

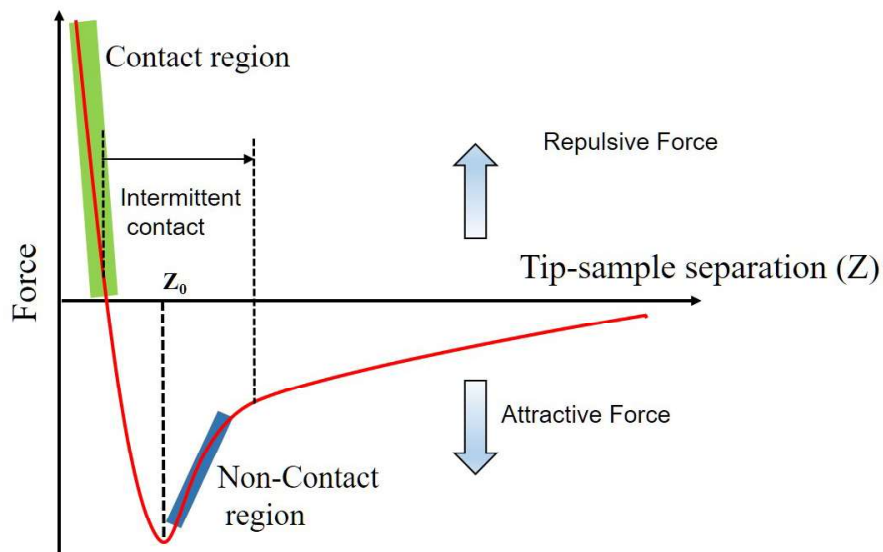


Figure 2.15: Inter-atomic force versus distance curve.

2.6.3 Kelvin probe force microscopy

The Kelvin probe force microscopy (KPFM) is a technique which enables nanometer-scale imaging of the surface potential of a material [32]. Unlike the typical AFM, KPFM operates in a non-contact mode, where the cantilever oscillates at its resonance frequency. The contact potential difference (V_{CPD}) between conducting AFM tip and a sample is described as:

$$V_{CPD} = \frac{\Phi_{tip} - \Phi_{sample}}{-e} \quad (2.20)$$

Where, Φ_{tip} and Φ_{sample} are barrier height of tip and sample respectively and e is the electronic charge. Figure 2.16 (a) shows the energy levels of AFM tip and the specimen surface when separated by a distance d and not electrically connected. Upon electrical contact between tip and sample surface, the Fermi levels of both the tip and sample (E_{ft} and E_{fs}) align through the electron current flow, as shown in figure 2.16 (b). The alignment of Fermi levels forms an apparent V_{CPD} , resulting in an electrical force on the contact area. An applied external DC bias (V_{DC}) with opposite polarity nullifies both the electrical force and surface charges on the contact area (figure 2.16 (c)). The amount of V_{DC} which nullifies this electrical force is equal to the work function difference between the tip and sample. In order to generate oscillating electrical forces between the AFM tip and specimen surface an additional AC voltage is applied to the AFM tip. In the present thesis, the KPFM measurements were performed using an AFM system (MFP-3D) from Asylum Research, with the spring constant 42 Nm^{-1} .

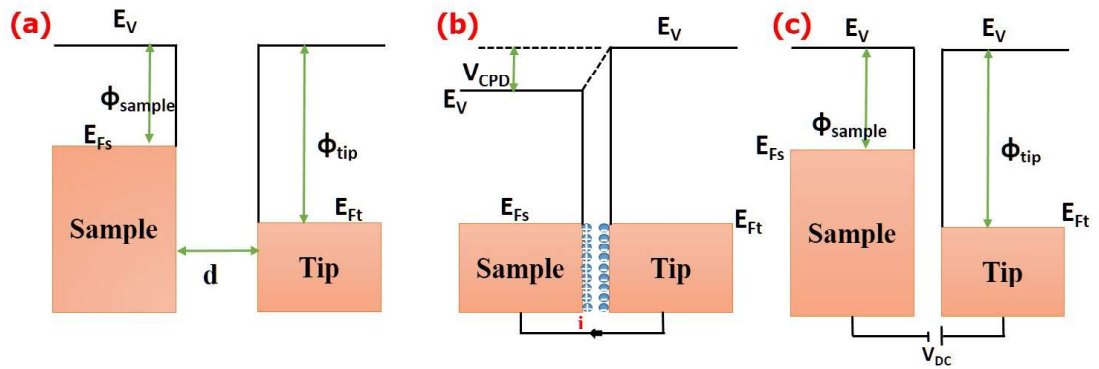


Figure 2.16: Schematic presentation of electronic energy levels of the sample and AFM tip for three different cases: (a) tip and sample are separated by distance d with no electrical contact, (b) tip and sample are in electrical contact, and (c) external bias (V_{dc}) is applied between tip and sample.

2.6.4 Tunneling atomic force microscopy

The TUNA is an AFM based dual pass technique, which allows measuring ultra-low current even from the low conducting surface. During measurements, in the first scan, tip scans the surface in contact mode and records the surface morphology, whereas in the second scan, the tip scans the surface in lift height mode by following the morphological information collected in the previous scan. In the second scan, a DC bias is applied between tip and sample resulting in a tunneling current, collected by a current amplifier [33]. The measurements of tunneling current with simultaneously following the morphological information provides a correlation between morphology and local conductance of the sample.

2.7 Summary

This chapter highlights experimental approaches used for the growth and characterization for different kind of ZnO nanorods. DC magnetron sputtering was used for the seed layer coating, and low temperature hydrothermal method was used for the growth of ZnO nanorods. Ion implantation in ZnO nanorods was carried out using low energy ion implanter facility. The structural characterization of ZnO nanorods were carried out using FESEM, TEM and XRD, XPS, XAFS techniques. Application potentials including phonon tunneling, nanothermometry, optical switching, reflection and transmission and current emission calibers were studied by techniques including Photoluminescence, Raman scattering, Z-Scan, UV-Visible spectroscopy, field emission, AFM, KPFM and TUNA respectively.

Bibliography

- [1] M. H. Huang, Y. Wu, H. Feick, N. Tran, E. Weber, P. Yang, *Adv.Mater.*, **2001**, 13, 113.
- [2] L. Vayssieres, *Adv.Mater.*, **2003**, 15, 464, .
- [3] T. Ma, Y. Wang, R. Tang, H. Yu, and H. Jiang, *J. Appl. Phys.*, **2013**, 113, 204503.
- [4] Z. W. Pan, Z. R. Dai, Z. L. Wang, *Science*, **2001**, 291, 1947.
- [5] W. I. Park, G. C. Yi, M. Kim and S. J. Pennycook, *Adv. Mater.*, **2002**, 14, 24.
- [6] C. S. Lao, P. X. Gao, R. S. Yang, Y. Zhang, Y. Dai, Z. L. Wang, *Chem. Phys. Lett.*, **2006**, 417, 358.
- [7] X. Y. Kong, Z. L. Wang, *Appl. Phys. Lett.*, **2004**, 84, 975.
- [8] Y. C. Chang, W. C. Yang, C. M. Chang, Hsu P. C. and L. J. Chen, *Crystal Growth & Design*, **2009**, 9, 3161.
- [9] Y. L. Liu, et al. *J. Chem. Phys.*, **2005**, 122, 174703.
- [10] H. Najafov, Y. Fukada, S. Ohshio, S. Iida, and H. Saitoh, *Jpn. J. Appl. Phys.*, **2003**, 42, 3490.
- [11] K. A. Alim, V. A. Fonoberov, and A. A. Balandin, *Appl. Phys. Lett.*, **2005**, 86, 053103.
- [12] F. Li, F. Gong, Y. Xiao, A. Zhang, J. Zhao, S. Fang, and D. Jia, *ACS Nano*, **2013**, 7, 10482.
- [13] A. Singh, K. Senapati, B. Satpati, M. Kumar and P. K. Sahoo, *Phys. Chem. Chem. Phys.*, **2015**, 17, 4277.
- [14] J. N. Wu and S. C. Liu *Adv. Mater.*, **2002**, 14, 215.

- [15] A. M. Morales and C. M. Lieber, *Science*, **1998**, 279, 208.
- [16] Y. W. Heo, V. Varadarajan, M. Kaufman, K. Kim, D. P. Norton, F. Ren, and P. H. Fleming, *Appl. Phys. Lett.*, **2002**, 81, 3046.
- [17] J. H. Choi, H. Tabata, and T. Kawai, *J. Cryst. Growth*, **2001**, 226, 493.
- [18] Qiu, X. Li, W. He, Se-Jeong Park, H.K. Kim, Y.H. Hwang, J.H. Lee and Y.D. Kim. *Nanotechnology*, **2009**, 20, 155603, .
- [19] L. Rayleigh, *Philos. Mag.*, **1879**, 8, 261.
- [20] J. I. Goldstein, D. E. Newbury, P. Echlin, D. C. Joy, C. E. Lyman, E. Lifshin, L. Sawyer, J. R. Michael, **2003**, ISBN: 0-306-47292-9.
- [21] D. B. Williams, C. B. Carter, **2009**, ISBN 978-0-387-76502-0.
- [22] W.H. Bragg, W.L. Bragg, *Proc R. Soc. Lond. A.*, **1913**, 88, 428.
- [23] F. L. Forgerini and R. Marchiori, *Biomatter.*, **2014**, 4, 28871.
- [24] P. Kubelka, F. Munk, *Zeits. f. Techn. Physik*, **1931**, 12, 593 .
- [25] J. Tauc, R. Grigorovici, A. Vancu, *Physica status solidi (b).*, **1966**, 15, 627.
- [26] M. Fox, Oxford University Press, **2001**, ISBN 0-19-850613-9.
- [27] P. Y. Yu, M. Cardona, Springer, **2010**, ISBN 978-3-642-00710-1.
- [28] M. S. bahae, A. A. Said, and E. W. Van Stryland, *OPTICS LETTERS*, **1989**, 14, 955.
- [29] J. Kerr, *Philosophical Magazine.*, **1875**, 50, 337.
- [30] R.H. Fowler, L. Nordheim, *Proceedings of the Royal Society A*, **1928**, 119, 173.
- [31] G. Binnig, C. F. Quate, C. Gerber, *Phy. Rev. Lett.*, **1986**, 56, 930.
- [32] W. Melitz, J. Shen, A. C. Kummel, S. Lee, *Surface Science Reports*, **2011**, 66, 1.
- [33] P. De Wolf, E. Brazel, A. Erickson, *Materials Science in Semiconductor Processing*, **2001**, 4, 71.

Chapter 3A

**Synthesis and Biochemical Evaluation of Alanyl
Thymine Triphosphate (Ala-TTP)**

Chapter 3A

Synthesis and Biochemical Evaluation of Alanyl Thymidine Triphosphate

(Ala-TTP)

Contents

3A. 1 Introduction	120
3A 1.1 Hypothesis and design	121
3A.2 Results and discussion	122
3A.2.1 Synthesis of alanyl thymidine triphosphate	122
3A.2.2 Biochemical evaluation of alanyl thymidine triphosphate	124
3A.2.3 Liquid Chromatography –Mass Spectrometry (LC-MS) Studies	127
3A.2.4 Self-assembly study of alanyl-thymidine ester (3)	128
3A. 3 Conclusion	132
3A.4 Experimental section	132
3A. 5 Refeerences	137
3A.6 Appendix	139

3A. 1 Introduction

Deoxyribose nucleic acid (DNA) is the genetic material and exists as double helical structure.¹ DNA has the phosphate back bone which is negatively charged. Due to the biological significance of DNA the structural analogues of DNA have been developed. Peptide nucleic acid (PNA) has emerged as potential DNA analogues which backbone is peptide oligomer from rationally designed aminoethylglycinate (*aeg*) amino acid (Figure 3A.1).² However the backbone of this peptide is acyclic and achiral, unlike deoxyribose sugar ring of DNA. In course of structurally modified PNA, Didersion and co-workers have reported alanyl-PNA containing alanine amino acid derivative as backbone, which is emerged a potential chiral PNA analogue.^{3,4} Importantly, alanyl-PNA has less distance between nucleobase for increasing the π - π interactions and stabilizing PNA-PNA duplex/tetraplex structures.^{5,6} However duplex structure from alanyl-PNA are unable to form perfect duplex structure, unlike DNA duplex, due to short distance between nucleobases and poor flexibility in the backbone. Further consecutive repeated cytosine rich sequence as TC₈ are reportedly formed stable i-motif tetraplex type of structure.⁷ Alanyl nucleobases are also incorporated into protein.⁹ Further a modified PNA as alanyl Peptides nucleic acid (PNA) have been explored as the formation of stable i-motif tetraplex¹² structure and other biological applications

Moreover similar analogue as glycerol nucleic acid (GNA) are synthesized and studied in the formation /stabilizing of DNA duplex type of structure. GNA oligomers/homo oligomer are synthesized from its phosphoramidites using DNA synthesizer.^{8,9} GNA units are also biosynthetically introduced into DNA primer from

its triphosphate analogue as glycerol triphosphate in presence of template DNA and DNA polymerase enzyme and however it is found to be poor substrate of various DNA polymerases.^{10,11} Further alanyl nucleobase are incorporated into Peptides nucleic acid binds strongly to RNA and DNA.¹² Alanyl nucleobases incorporated into protein are synthesized and used as probe for DNA binding protein.¹³

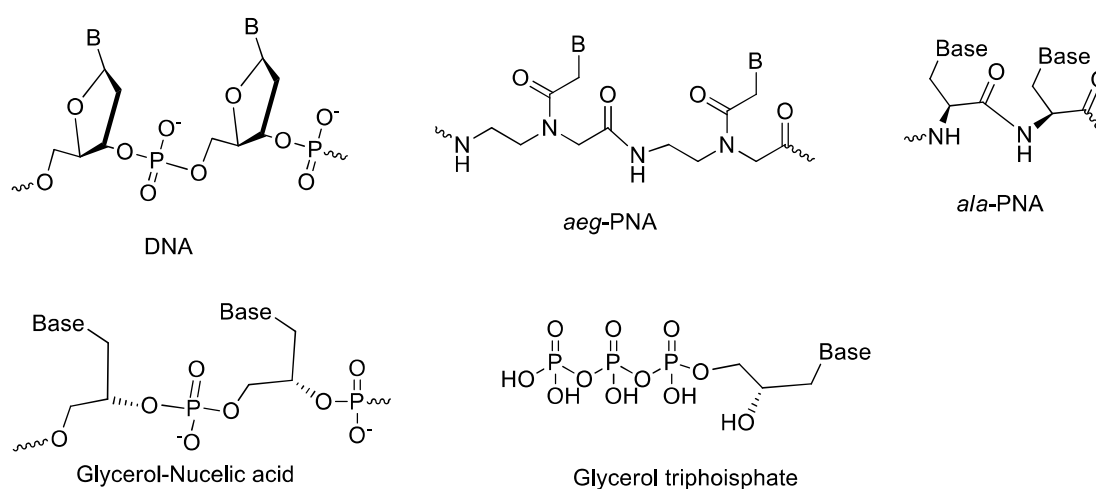
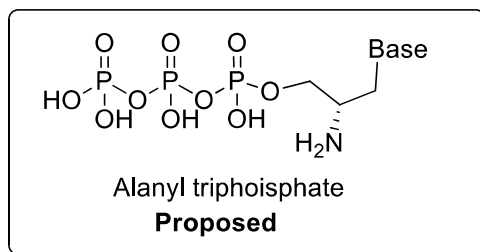


Figure 3A. 1 Structure of *aeg*-PNA, Ala-PNA, glycerol nucleic acid, and glycerol triphosphate.

3A 1.1 Hypothesis and objectives

Since *alanyl*-PNA is neutral acyclic chiral PNA analogue which encourage us to design its triphosphate analogue and incorporate into DNA primer enzymatically. This chapter describe the synthesis of rationally designed *alanyl*-nucleoside triphosphate analogue and its biochemical evaluation as enzymatic incorporation into DNA primer with DNA polymerases.



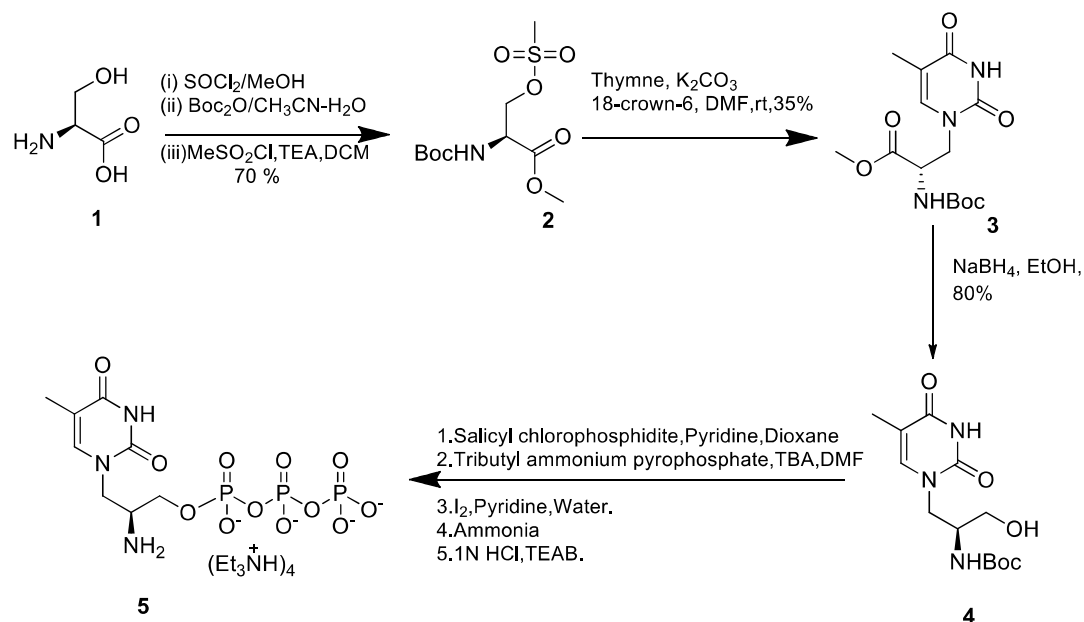
3A.2 Results and discussion

3A.2.1 Synthesis of alanyl thymidine triphosphate

The synthetic scheme of alanyl triphosphate analogue is described in Scheme 3A.1. Herein the synthesis of alanyl thymidine triphosphate was started from the naturally occurring amino acid L-serine (**1**). The carboxylic acid and amine groups were protected as methyl ester and *N*-Boc respectively. The hydroxyl group of protected *N*-Boc-Aminoacid-ester was modified as active mesylate derivative (**2**) with mesyl chloride. This mesyl derivative (**2**) was treated with nucleobase thymine under basic conditions (K_2CO_3/DMF) and isolated as desired *N*-Boc-thyminyl-alanyl methyl ester (**3**) after purification by column chromatography. In next, the methyl ester group of nucleoside (**3**) was reduced into alcohol as compound **4** with versatile reducing agent $NaBH_4$. This nucleoside alcohol (**4**) was phosphorylated with phosphorylating reagents by treating with salicylchlorophosphidite, tributylammonium pyrophosphate followed by oxidation with iodine pyridine/water solution then hydrolysed the cyclic triphosphate to triphosphate. Finally then *N*-Boc group was deprotected with aq. HCl (1.0N). As resultant the desired compound as *N*-Boc-alanyl-thymidine triphosphate (ala-TTP, **5**) was isolated in moderate yield and purified by Sephadex-Gel column and

HPLC methods. All new intermediates of this scheme are well characterized by NMR ($^1\text{H}/^{13}\text{C}/^{31}\text{P}$) and ESI-Mass techniques.

Scheme 3A. 1 synthesis of Alanyl thymidine triphosphate



The nucleobases are known in hydrogen bonding and self-assembled with unique pattern. Thus we desired to obtain any self-assembly structure in alanyl-thymidine nucleoside for structural organizations. Thus we attempted to get single crystal from alanyl-thymidine nucleoside ester (**3**)/alcohol (**4**)/ triphosphate (**5**). However we got crystal of only alanyl nucleoside ester (**3**) in solid state after many attempts. The single crystal of nucleoside (**3**) was analysed by single X-ray diffractometer and its data are deposited to Cambridge crystallographic data centre (CCDC) with 1568315. number.

3A.2.2 Biochemical evaluation of alanyl thymidine triphosphate

The biochemical evaluation as examination of genuine substrate of DNA is studied with primer extension reaction method. In comparison, the known substrates of DNA, dTTP & ddTTP, are employed as control studies with following DNA polymerases: *Taq*, *Vent exo*, *Deep vent-exo*, *Bst* and *Therminator*. The DNA primers (**P1/FAM-P1**) and DNA template (**T1/T2**) are used for incorporation of *ala*-TTP or/& control dTTP/ddTTP under primer extension reactions. The sequence of DNA primer and templates are following: primer (**P1**) 5'-TGTA AACGACGGCCAGT-3'; labelled primer (**FAM-P1**) Fam-5'TGTA AACGACGGCCAGT-3'; Template (**T1**) 3'ACATTTTGCTGCCGGTCAA*GTCGAGGCAT-5'; template (**T2**) 3'ACATTTTGCTGCCGGTCAAAAAAAAAAAAAAA-5. The underline sequence are complementary to primers.

For gel electrophoretic studies, the FAM labeled primer (5'**FAM-P1**) as **FAM-5'**TGTA AACGACGGCCAGT-3' was treated with alanyl-TTP and enzyme (DNA polymerase) in presence of DNA template (T1) at 55⁰C. The labelled DNA and its incorporated products, after primer extension reactions were visualized by denaturing PAGE. Their gel images are depicted in Figure 2. In Figure 2 A, the gel-band of L1 belongs to labelled DNA primer. While the gel-bands of L2/L3/L4 belong the extended labelled primer with respective dTTP,/ddTTP/*ala*-TTP with *therminator* DNA polymerase (Figure 2A). The remarkable gel-bands shift of FAM-DNA primer are visualized with *ala*-TTP as like control (dTTP & ddTTP). However with dTTP the shift is comparatively more than ddTTP and *ala*-TTP. In literature, the multiple incorporations of dNTP into primer are reported with high fidelity DNA polymerase.¹⁴

Since ddTTP is well known as terminator of DNA synthesis after single incorporation into DNA primer. In case of also the gel-shift band of extended labelled primer is closely matched with that of ddTTP. These gel-shift band analysis strongly support the only single incorporation of alanyl-TTP into DNA primer with highly efficient DNA *Therminator* polymerase. With *vent-exo* & *Taq* DNA polymerases, the similar gel-shifts of DNA primer (**FAM-P1**) are noticed with *ala*-TTP and control ddTTP (Figure 3A, 2.A L4 & L5).

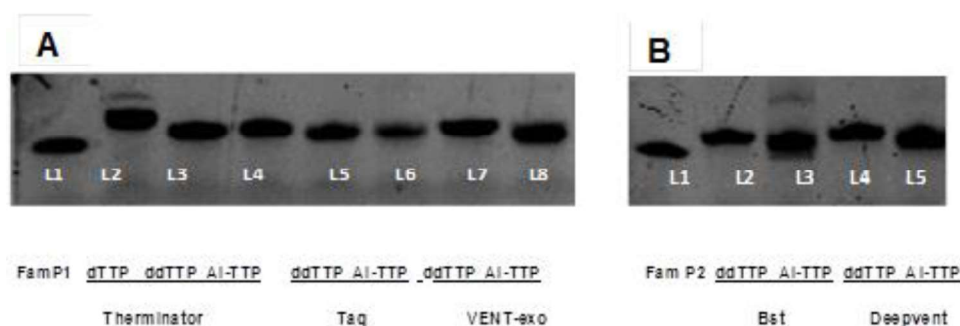
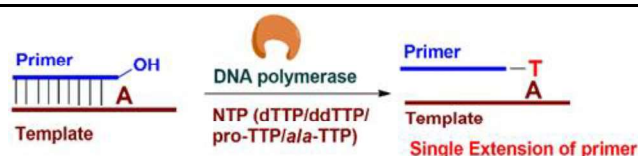


Figure 3A. 2 PAGE analysis of primer extension reactions of Ala-TTP with DNA polymerases (A) L1 FAM P1, L2, L3 and L4 extended primer with dTTP, ddTTP and Ala-TTP by *Therminator* DNA polymerase, L5 and L6 extended primer with ddTTP and Ala-TTP by *Taq* DNA polymerase, L7 and L8 extended primer with ddTTP and Ala-TTP by *Vent exo*-DNA polymerase (B) L1 FAM P1, L2 and L3 extended primer with ddTTP and Ala-TTP by *Bst* DNA polymerase, L4 and L5 extended primer with ddTTP and Ala-TTP by *Deep vent* DNA polymerase

With *Bst* & *Deepvent* DNA polymerases, the gel-shifts of DNA primer (**FAM-P1**)'s gel-band are consistently similar. (Figure 3A.2B; Lane 2-5). These gel studies strongly support the single incorporation of *ala*-TTP into DNA primer as like control

ddTTP with other DNA polymerases too. The incorporation of dTTP/ddTTP/alanyl-TTP into labeled primer with DNA polymerase are also summarized in Table 3A.1. As like control dTTP and ddTTP, alanyl-TTP is also get easily incorporated into DNA with all given DNA polymerase. Hence *ala*-TTP is another terminator of enzymatic DNA synthesis after single incorporation.

Table 3A. 1 DNA polymerase activity of *alanyl*-TTP & control (dNTP & ddNTP) reaction results



Sr. No	DNA Polymerase	dTTP	ddTTP	ala-TTP
1	Bst	✓	✓	✓
2	Deepvent	✓	✓	✓
3	Taq	✓	✓	✓
4	Vent-Exo	✓	✓	✓
5	Therminator	✓	✓	✓

Further to investigate for multiple incorporations of *ala*-TTP into primer, we designed a template (**T2**) which could incorporate multiple thymidine triphosphate. Herein, we performed primer extension reactions with designed primer/template and *ala*-TTP and control dTTP by gel-electrophoretic methods. Their gel-shifts are depicted in Figure 3. In case of dTTP, the synthesis of multiple dTTP incorporated DNA, almost full

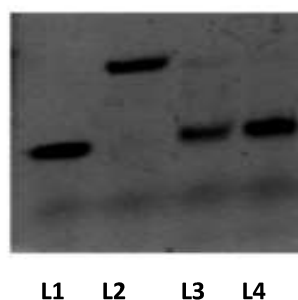


Figure 3A. 3 PAGE analysis of primer extension reactions of *ala*-TTP/dTTP/ddTTP with DNA polymerase L1 FAM P1, L2, L3 and L4 extended primer with dTTP, ddTTP and Ala-TTP by Therminator DNA polymerase

length DNA sequence were noticed (Figure 3, L2). However, with *ala*-TTP, gel-shift band (Figure 3A. 3, L3) is almost equal to that of ddTTP (Figure 3A. 3, L4). Hence *ala*-TTP also could not extend the synthesis of DNA after single incorporation like ddTTP. In literature, glycerol NTP is known for single incorporation into DNA.

3A.2.3 Liquid Chromatography –Mass Spectrometry (LC-MS) Studies

Finally the incorporation of *ala*-TTP into DNA primer was analyzed by LC-ESI-Mass analyses. We recorded the mass spectra of DNA primer (**P1**) and Template (**T1**) before and after treatment with *ala*-TTP/ddTTP in presence of one of the enzyme, *Therminator* DNA polymerase. The mass spectra of primer/extended primer with *ala*-TTP and control ddTTP are provided in Appendix of this chapter. The mass spectrum of DNA primer **P1** exhibited a prominent peak at 1381.99 (m/z) which belong to molecular mass ion (M_p) of primer as $[M_p-4H]^4+$, while the mass of template(**T1**) as $[M_T-6H]^6-$ is appeared at 1483.57 In presence of therminator polymerase and *ala*-TTP,

the mass of DNA primer (P1) is increased and appeared at 1447.28 (m/z) (Figure 3A.4) which belong to the

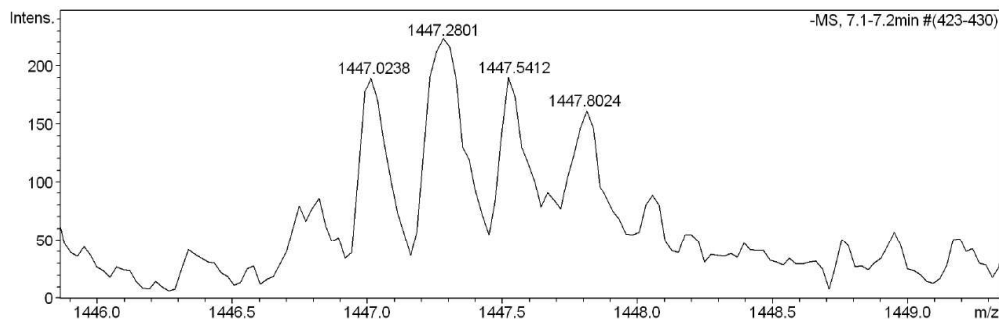


Figure 3A. 4 Mass spectra of extended mass of primer with *ala*-TTP

molecular mass ion of single *ala*-TTP extended DNA primer (M_p^*) as $[M_p^* - 4H]^{4-}$. However, with control sample, ddTTP, the mass of DNA primer P1 is also increased and appeared at 1454.16 (m/z) as $[M_p^* - 4H]^{4-}$ under similar primer extension reaction conditions which belongs to the mass of single ddTTP extended DNA primer. Hence these mass results confirm the single enzymatic incorporation of *ala* TTP into DNA primer in presence of DNA Template and DNA polymerase.

3A.2.4 Self-assembly study of alanyl-thymidine ester (3)

Importantly we got single crystal of *alanyl* nucleoside ester (3), precursor of *ala*-TTP (5), and studied by X-ray diffractometer which confirmed the chemical structure of nucleoside ester (3) in solid state. The X-ray data is deposited to Cambridge crystallographic data center (CCDC) with reference CCDC 1568315. The ORTEP diagram of compound 3 are depicted in Figure 3A.5.

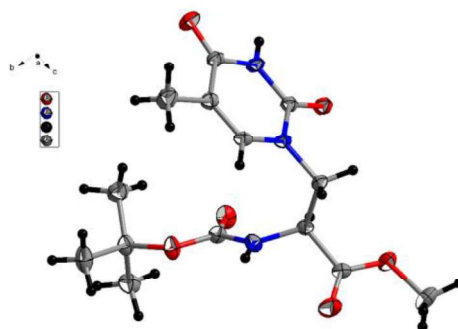


Figure 3A. 5 ORTEP diagram and Phase data of ala-thymidine ester (3): Space-group P 1 21/c 1 (14) – monoclinic; Cell a=5.2456(3) Å b=26.0994(15) Å c=12.1838(7) Å $\beta=99.467(4)^\circ$; V=1645.33(16) Å³

After the confirmation of ala-thymidine ester (3) crystal structure, we attempted to find its (compound 3) supramolecular assembly in solid state. Using crystal visualizing software Diamond 3.2, the packing arrangement of thymidine ester **3** was obtained (Figure 3A.6, top left). The viewing from one axis ‘b’ indicate two thymidine ester (3) are assembled by an unusual hydrogen bonding pattern between their thymidine residues in plane’s axis ‘a’ and ‘c’ (Figure 3A .6, top right). Herein a unique type of nucleobase pairs, Thymine: Thymine (T:T) are noticed by two hydrogen bonding between two thymine residues as following: N³-H of one thymine (T) with O=C² of other thymine (T) and vice versa. In literature too, such type of hydrogen bonding are called as reverse Watson-Crick hydrogen bonding which are noticed in the supra molecular assemblies of Ferrocene linked Thymine/Uracil conjugated compounds.^{15,16} However, Watson-Crick and Hoogsteen types of hydrogen bonding are found in nucleobase supramolecular self-assembly in many modified nucleosides.¹⁷⁻²¹ In addition further the side view of ala-Thymidine ester supramolecular assembly are depicted in Figure 3A.6 (bottom left) which indicate the

formation of *anti-parallel self-duplex* type of structure. Each strand of this duplex is formed by hydrogen bonded backbone as $\text{-C=O}\cdots\cdots\text{HN}$ of Boc- group of ester **3**. Interesting unique π - π interactions are noticed between thymine residues of one strand with that of other strand and further stabilized that self-duplex structure of *alanyl* nucleoside in solid state. The distance of hydrogen bonds and π - π interactions are extracted from the supramolecular structure of alanyl ester (**3**) (Figure 3A. 6, bottom right). The hydrogen bond distances between two thymine are 2.0Å; hydrogen bond distances between two Boc groups are 2.4Å; the distance of π - π interactions in thymine are 3.7Å; the distance between two strands of that duplex are 10Å, and distance between two units of each strand are 5.2Å (Figure 3A.6, bottom right). 6, bottom right).

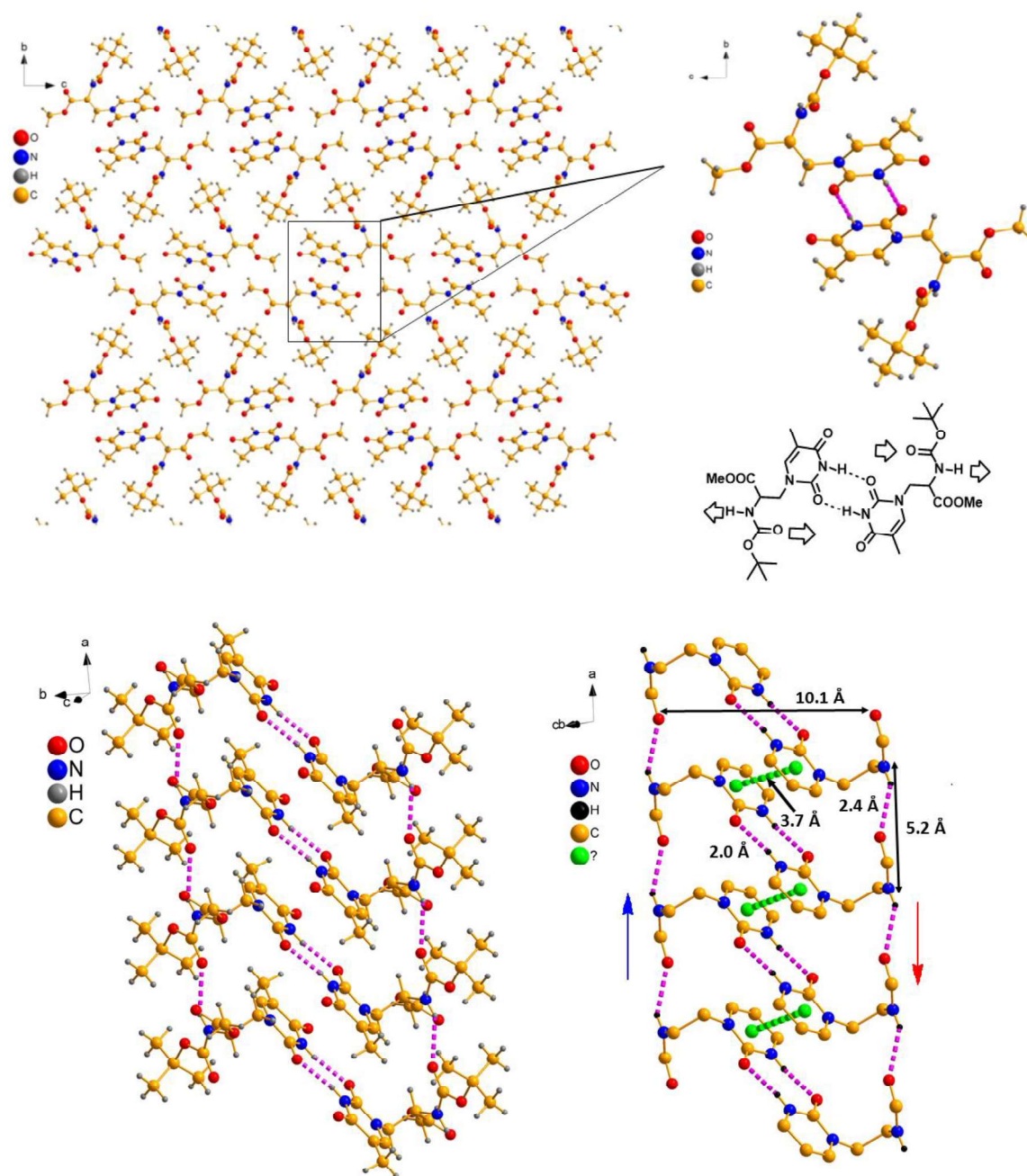


Figure 3A .6 Structural studies of single crystal of Boc-N-alanylthymidine methylate (3) by X-analyse: (a) Packing diagram (top left); (b) diagram of selected region (top right); (c) Hydrogen bonding pattern (bottom left) and (d) Detail of distance for hydrogen bonding and π - π interaction (Bottom right)

3A.3 Conclusion

We have successfully synthesized alanyl thymidine triphosphate (*ala*-TTP), and performed its biochemical evaluation with various DNA polymerases in presence of DNA primer and DNA templates. The alanyl thymidine triphosphate is a substrate of several DNA polymerases. The *ala*-TTP involves in primer extension reaction and incorporated one could extend the primer only one extension like glycerol NTP due to its flexible backbone and rotational degrees of freedom. The *ala*-thymidine triphosphate can be used to synthesize the 3'-amino functionalized DNA. We have also studied the self-assembly of crystal structure of *ala*-thymidine ester. The compound shows self-assembly and duplex type of structure aided by hydrogen bonding and pi-pi interactions.

3A.4 Experimental section

All chemicals and reagents purchased from commercial sources and used as received. Oilgo nucleotide purchased from IDT. All enzymes purchase from NEB .DMF and DCM distilled over CaH₂ and stored on molecular sieves. THF and dioxane dried over Sodium benzophenone and stored over sodium. Pyridine distilled over potassium hydroxide and stored on CaH₂. Triethyl ammonium bicarbonate (TEAB) prepared by passing CO₂ gas into 2M aqueous triethylamine solution and stored at 4°C. HPLC performed on Waters semipreparative HPLC using sunfire column(C18 ,4.6X150 mm) using 20mM TEAB and Acetonitile (0-10 % 30 min). LC-MS experiments performed on Bruker microTOF-Q II coupled with a Waters Acquity UPLC auto sampler .Primerextension reaction products(25 µl) were diluted with 25 µl Milli-Q water and 10.0 µl from this mixture injected by auto sampler by following programme

at a flow rate 0.2ml/minute linear gradient.0-10 min80% A gradient, 10-12 min 30% A gradient, at 12- 13 min30% A isocratic, 13-14min 100% A gradient, at 14-15 min 100% A isocratic. A C-18 RP UPLC column (2.1 x 5.0 mm, 1.7 μ m, Acquity Waters) used for LC-MS experiments. Column temperature maintained at 30 $^{\circ}$ C during the experiments (buffer A: 5mM ammonium acetate (pH 7.0) and buffer B: methanol)

Primer extension reactions for LC-MS analysis were carried out with 5 μ M of primer and template, 100 μ M ala-TTP or ddTTP in a total reaction volume of 25 μ l with 2 units of Vent exo- DNA polymerase

All primer extension reactions performed with 1 μ M FAM labelled primer, 1 μ M template 100 μ M NTP in 10.0 μ l with reaction buffer provided by the supplier. All reactions performed at 55 $^{\circ}$ C for 60 minutes. 2 units of each terminator, Vent exo- and Deep Vent exo- DNA polymerases were used in 10.0 μ l reactions .Bst and Taq DNA polymerases were used 8.0 units and 10.0 units in 10.0 μ l reactions.

Gel experiments performed with 20% PAGE (29: 1 Acrylamide ,bis acrylamide) and 7M urea .Gels prepared and ran in 1x TBE and visualised under trans UV using Bio-Rad gel doc system.

Experimental procedures for the synthesis of compounds 2-5

(S)-methyl 2-((*tert*-butoxycarbonyl)amino)-3-((methylsulfonyl)oxy)propanoate (**2**): Boc serine ester (2.0 g, 9.13 mmol) dissolved in anhydrous pyridine (10 ml) and stirred at 0°C under nitrogen atmosphere. Mesylchloride (1.06 ml, 13.7 mmol) was added dropwise with a syringe and the reaction stirred at 0°C for one hour. The reaction mixture concentrated in roto and extracted with water and DCM. The DCM layer washed with sodium bicarbonate solution followed by brine solution, dried with anhydrous sodium sulphate and concentrated followed by purification using ethyl acetate and hexanes on silica gel gave 1.89 g of oily compound in 70% yield. ¹H NMR (400MHz, CDCl₃) δ ppm 1.36 (9H, s), 2.95 (3H, s), 3.71(3H, s), 4.39-4.42(1H, m), 4.47-4.53(2H, m), 5.53-5.55(1H, m) ¹³C NMR (100MHz, CDCl₃) δ ppm 28.11, 37.17, 52.89, 53.01, 68.99, 80.43, 155.07, 169.15. HRMS (ESI-TOF) Calculated (C₁₀H₁₇O₇N S +Na) 320.0774, Measured 320.0775

(S)-methyl 2-((*tert*-butoxycarbonyl)amino)-3-(5-methyl-2,4-dioxo-3,4-dihydropyrimidin-1(2H)-yl)propanoate (**3**): Thymine (0.2g, 1.58 mmol) dissolved in anhydrous DMF (5 ml), K₂CO₃ (0.328 g, 2.38 mmol) and 18-Crown-6 (0.083 g, 0.31mmol) added and stirred under nitrogen atmosphere for 10 minutes. Mesyl derivative (compound **2**) (0.471 g, 1.58mmol) was added to the reaction and stirred at room temperature overnight under nitrogen atmosphere. The reaction mixture concentrated followed by purification on silica gel using methanol and dichloromethane as solvents gave 0.181 g white solid in 35% yield. ¹H NMR (400MHz, DMSO-D₆+CD₃OD) δ ppm 1.27 (9H, s), 1.72 (3H, s), 3.54-3.60(1H, m), 3.63(3H, s),

4.18-4.23 (1H, m), 4.44-4.46 (1H, m), 7.18(1H, m). ^{13}C NMR (100 MHz, DMSO- D_6 + CD_3OD) δ ppm 11.23, 27.49, 49.19, 51.78, 51.88, 79.40, 109.05, 142.20, 151.43, 156.01, 165.26, 17.42 HRMS (ESI-TOF) Calculated ($\text{C}_{14}\text{H}_{21}\text{O}_6\text{N}_3 + \text{Na}$) 328.1503, Measured 328.1509.

(S)-*tert*-butyl (1-hydroxy-3-(5-methyl-2,4-dioxo-3,4-dihydropyrimidin-1(2H)-yl)propan-2-yl)carbamate (**4**): Thymine ester (0.15 g, 0.45 mmol) dissolved in anhydrous ethanol, stirred under nitrogen atmosphere for 10 minutes followed by addition of sodium borohydride (0.05 g, 1.37 mmol) and stirred overnight under nitrogen atmosphere at room temperature. The reaction mixture concentrated and extracted with ammonium chloride and ethylacetate. Ethylacetate layer washed with brine solution, dried with anhydrous sodium sulphate and concentrated. The crude compound purified on silica gel column using methanol and dichloromethane to obtain 0.11 g of white solid in 80% yield. ^1H NMR (400MHz, DMSO- D_6) δ ppm 1.29 (9H, s), 1.72 (3H, s), 3.23-3.29(1H, m), 3.34-3.41(2H, m), 3.74-3.80(1H, m), 3.95-4.00(1H, m), 4.80-4.83(1H, m), 6.54-6.57(1H, m), 7.31(1H, s), 11.12(1H, s) ^{13}C NMR (100 MHz, DMSO- D_6) δ ppm 12.51, 28.52, 49.98, 51.18, 61.90, 78.25, 107.90, 142.58, 151.43, 155.72, 164.81. HRMS (ESI-TOF) Calculated ($\text{C}_{13}\text{H}_{21}\text{O}_5\text{N}_3$) 300.1554, Measured 300.1556.

Triethylammonium (*S*)-2-amino-3-(5-methyl-2,4-dioxo-3,4-dihydropyrimidin-1(2H)-yl)propyl triphosphate (**5**): Triphosphorylation was performed by following reported literature.¹ Compound **4** (0.04 g, 0.13 m mol) taken in a 25 ml round bottom flask dissolved in 3 ml of anhydrous pyridine and dried in roto followed by drying in a vacuum desiccator at ambient temperature for one hour. Descicator opened under argon atmosphere and closed with septum. All the further steps performed under argon

pressure. Salicylchlorophosphidite (0.03g, 0.160mmol) dissolved in dry dioxane (1.0 ml) was added and stirred at room temperature for 10 minutes. Immediately a cock tail containing tri- butylammonium pyrophosphate (0.14 g, 0.26 mmol) and tri-butylamine (0.26 mL, 1.07 mmol) in anhydrous dimethylformamide (DMF) (1ml) injected into the flask and stirred for 10 minutes followed by the addition of Iodine in pyridine/water solution (1% in pyridine/water 98/2). After 10 minutes 10 ml of 100 mM TEAB buffer (pH 8.0) was added and stirred for one hour followed by lyophilization. The reaction mixture dissolved in 10 ml water and extracted with ethyl acetate. Aqueous layer lyophilized followed by anion exchange column (DEAE Sephadex A-25) chromatography eluted with TEAB buffer (0.1M-1.0M) compound containing fractions were pooled and concentrated followed by boc deprotection with 1N HCl. The reaction was quenched with aqueous ammonia and concentrated followed by HPLC purification and lyophilization of the HPLC purified samples gave Ala-TTP as a white powder dissolved in nuclease free water and used for primer extension reactions. ^1H NMR (400 MHz, D_2O) δ 7.57 (s, 1H), 4.41 (dd, $J = 6.7, 3.1$ Hz, 1H), 4.26 (dd, $J = 14.7, 7.3$ Hz, 1H), 4.20 – 4.04 (m, 2H), 3.94 (s, 1H), 1.94 (s, 3H). ^{31}P NMR (162 MHz, D_2O): (-22.13, t, 1P, P_β), (-11.16, -11.04, d, 1P, P_γ), (-10.4, -10.16, d, 1P, P_α) ($J_{\alpha\beta} = 19.44\text{Hz}$, $J_{\beta\gamma} = 19.44\text{Hz}$) HRMS, ^1H NMR ESI-TOF calcd for $[\text{C}_8\text{H}_{15}\text{NO}_{12}\text{P}_3(\text{M}-\text{H})]$ m/z 437.9863, found m/z 437.9969.

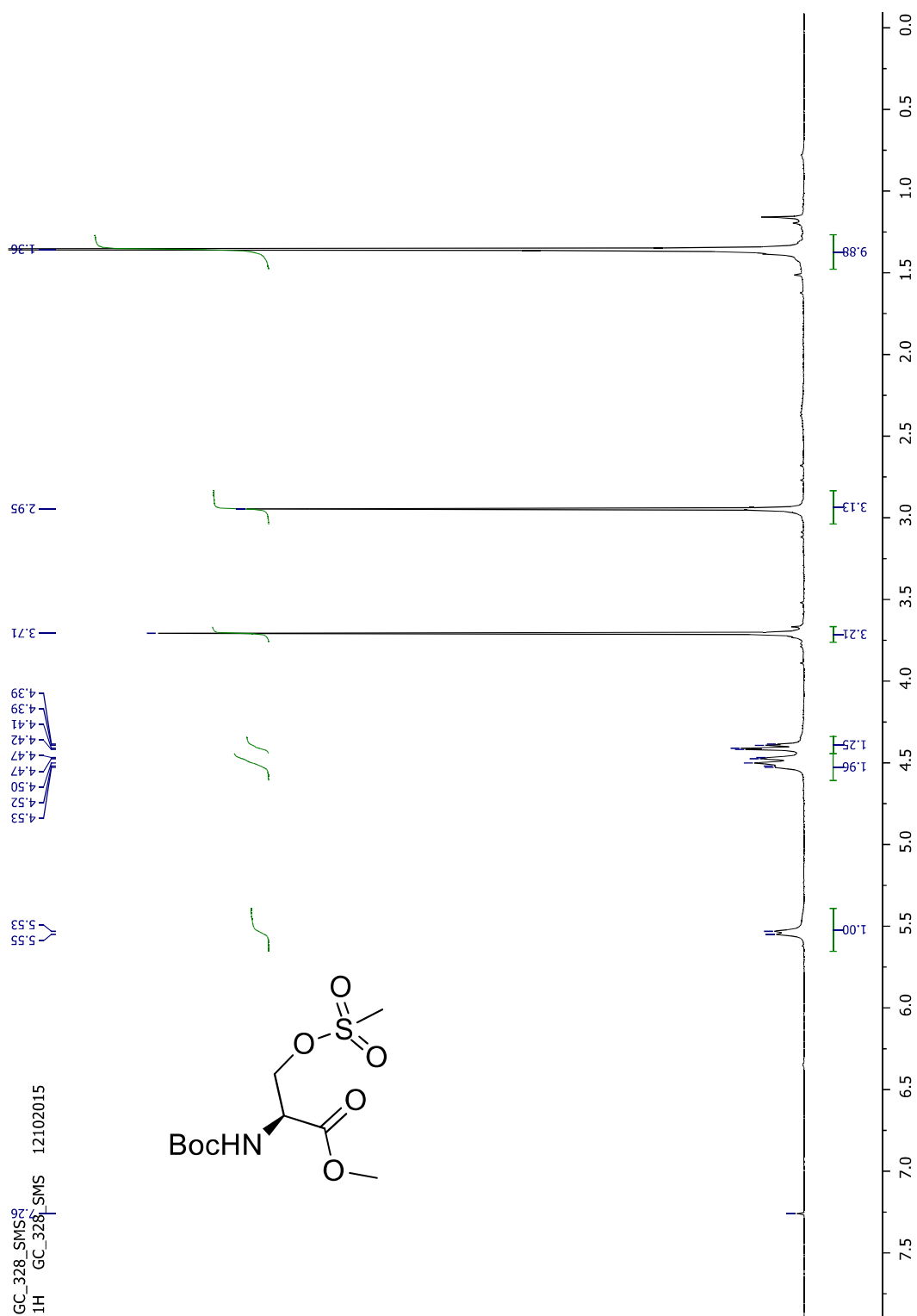
3A. 5 Reefeerences

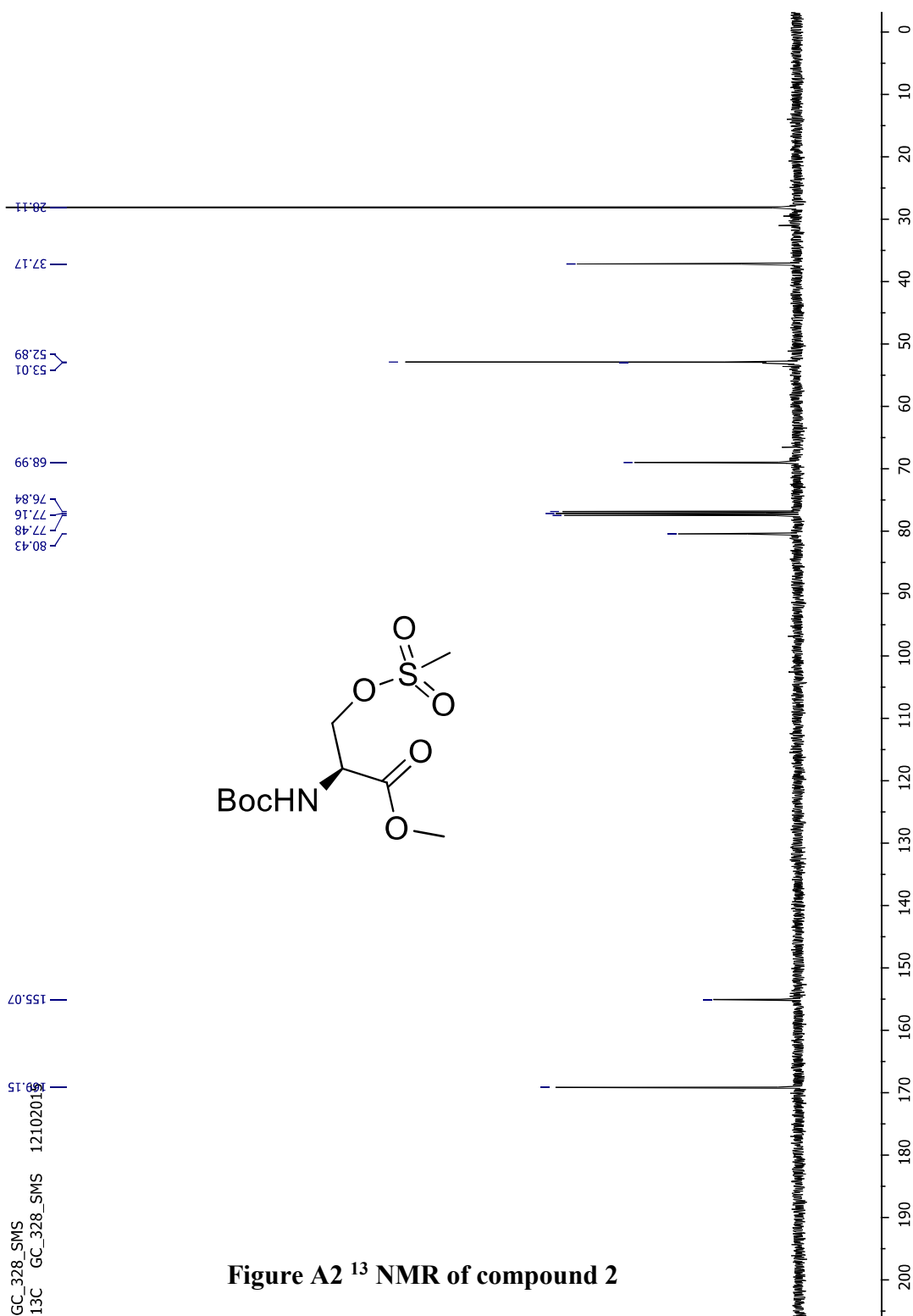
- (1) Watson, J. D.; Crick, F. H. *Nature* **1953**, *171*, 737.
- (2) Nielsen, P. E.; Egholm, M.; Berg, R. H.; Buchardt, O. *Science* **1991**, *254*, 1497.
- (3) Diederichsen, U. *Bioorganic & medicinal chemistry letters* **1998**, *8*, 165.
- (4) Diederichsen, U.; Weicherding, D.; Diezemann, N. *Organic & biomolecular chemistry* **2005**, *3*, 1058.
- (5) Diederichsen, U. *Angew. Chem. Int. Ed.* **1996**, *35*, 445.
- (6) Diederichsen, U. *Angew. Chem. Int. Ed.* **1997**, *36*, 1886.
- (7) Diederichsen, U. *Angew. Chem. Int. Ed.* **1998**, *37*, 2273.
- (8) Zhang, L.; Peritz, A.; Meggers, E. *J. Am. Chem. Soc.*, **2005**, *127*, 4174.
- (9) Meggers, E.; Zhang, L. *Acc. Chem. Res* **2010**, *43*, 1092.
- (10) Horhota, A. T.; Szostak, J. W.; McLaughlin, L. W. *Org. Lett.* **2006**, *8*, 5345.
- (11) Chen, J. J.; Tsai, C.-H.; Cai, X.; Horhota, A. T.; McLaughlin, L. W.; Szostak, J. W. *PLoS One* **2009**, *4*, e4949.
- (12) Bose, T.; Kumar, V. A. *Bioorg. Med. Chem* **2014**, *22*, 6227.
- (13) Talukder, P.; Dedkova, L. M.; Ellington, A. D.; Yakovchuk, P.; Lim, J.; Anslyn, E. V.; Hecht, S. M. *Bioorg. Med. Chem.* **2016**, *24*, 4177.
- (14) Hu, G. *DNA and cell biology* **1993**, *12*, 763.
- (15) Patwa, A. N.; Gonnade, R. G.; Kumar, V. A.; Bhadbhade, M. M.; Ganesh, K. *N. J. Org Chem.* **2010**, *75*, 8705.
- (16) Patwa, A. N.; Gupta, S.; Gonnade, R. G.; Kumar, V. A.; Bhadbhade, M. M.; Ganesh, K. N. *J. Org. Chem.* **2008**, *73*, 1508.
- (17) Pedireddi, V.; Ranganathan, A.; Ganesh, K. N. *Org. Lett* **2001**, *3*, 99.

- (18) Perumalla, S. R.; Pedireddi, V. R.; Sun, C. C. *Cryst. Growth. Des.* **2013**, *13*, 429.
- (19) Sanjayan, G. J.; Pedireddi, V.; Ganesh, K. N. *Org. Lett.* **2000**, *2*, 2825.
- (20) Verma, S.; Mishra, A. K.; Kumar, J. *Acc.Chem. Res* **2009**, *43*, 79.
- (21) Sivakova, S.; Rowan, S. J. *Chem.Soc. Rev.* **2005**, *34*, 9.

3A.6 Appendix

NMR and HRMS spectra of compounds 2-5

Figure A1 ^1H NMR of compound 2



Generic Display Report

Analysis Info

Analysis Name D:\Data\FEB-2017\NKS\gcl22022017_NKS_GC_SMS-3.d
Method Pos_tune_low.m
Sample Name Bruker micro TOF -Q II
Comment

Acquisition Date 2/22/2017 5:41:40 PM
Operator G.C.Reddy.
Instrument micrOTOF-Q II

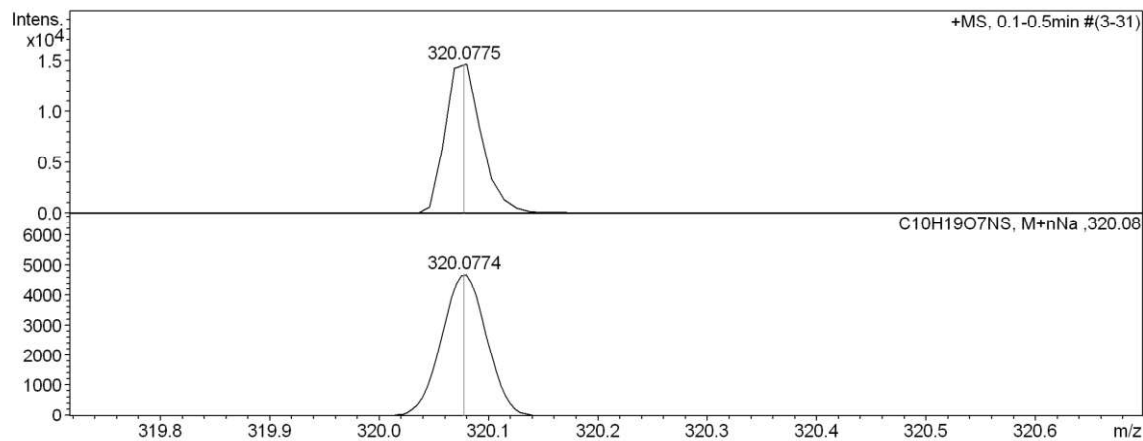
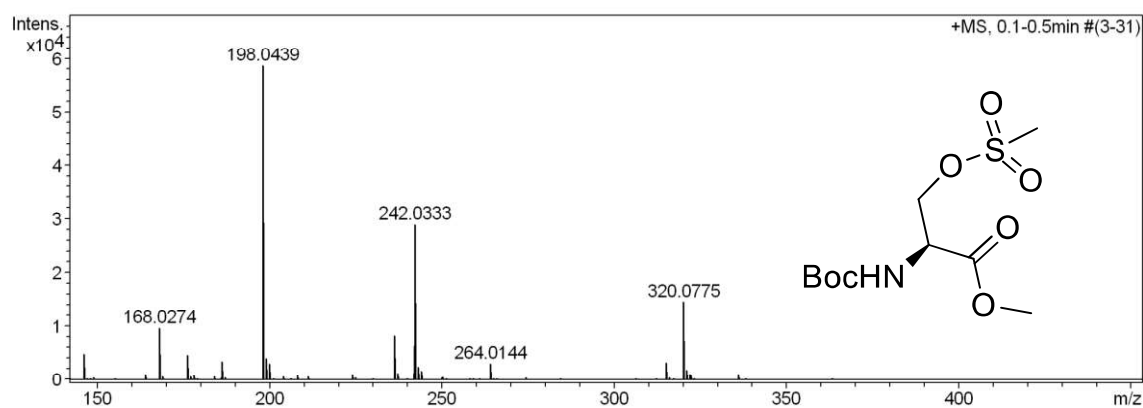
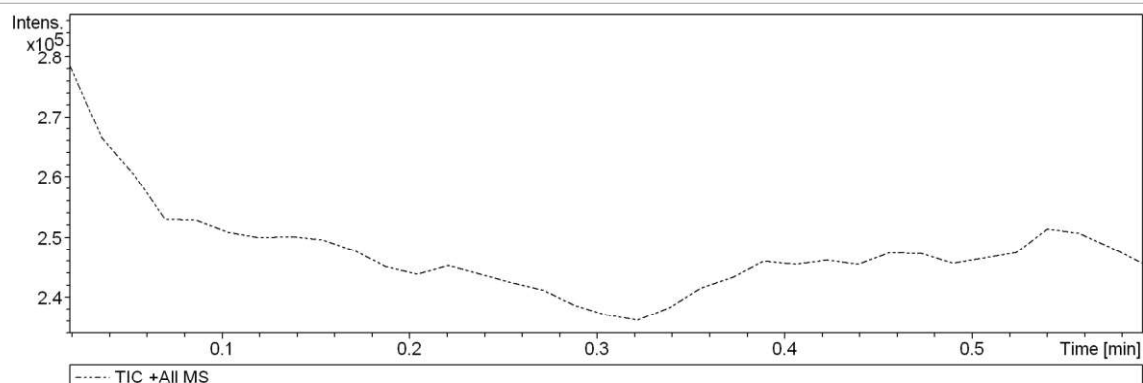
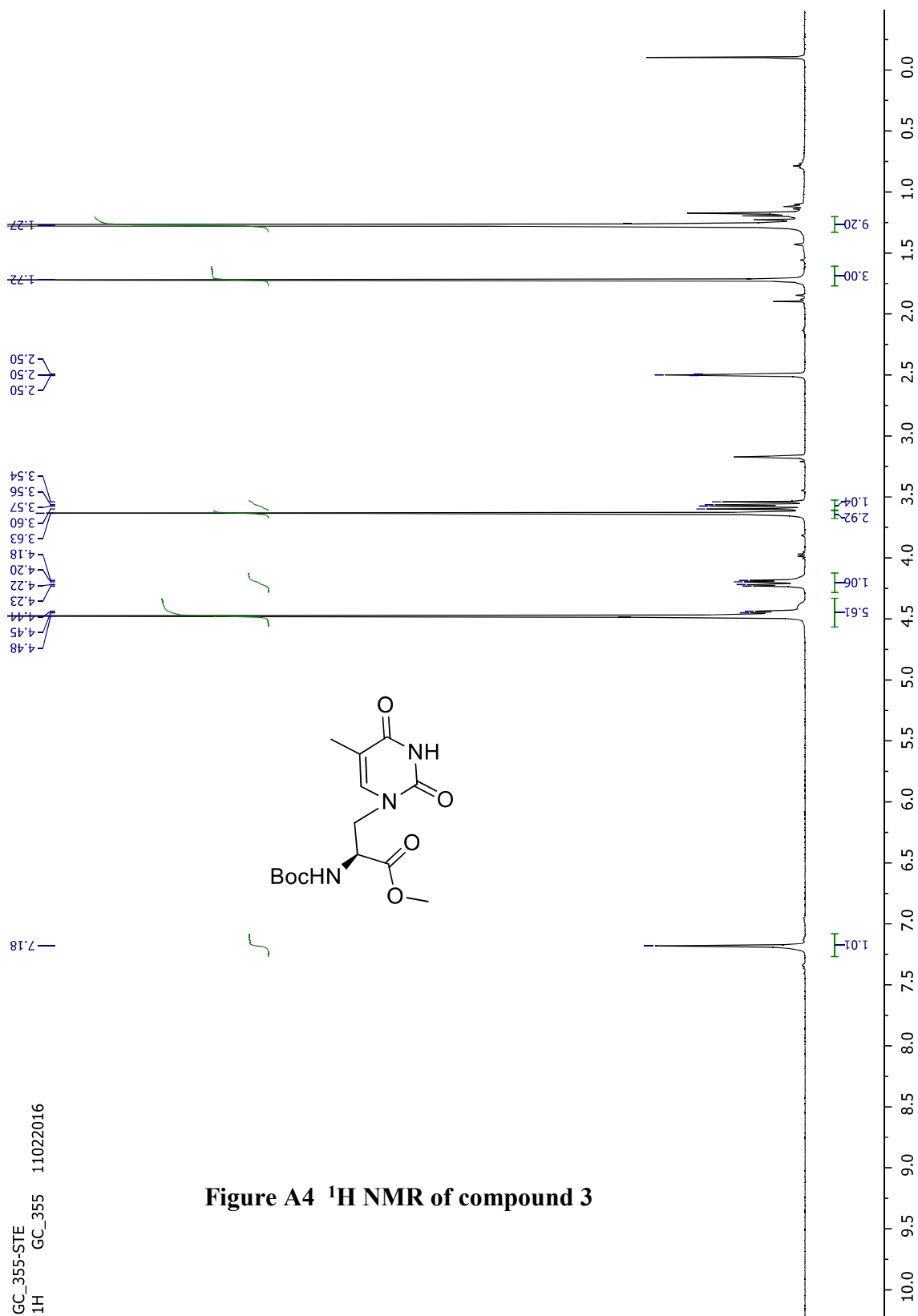
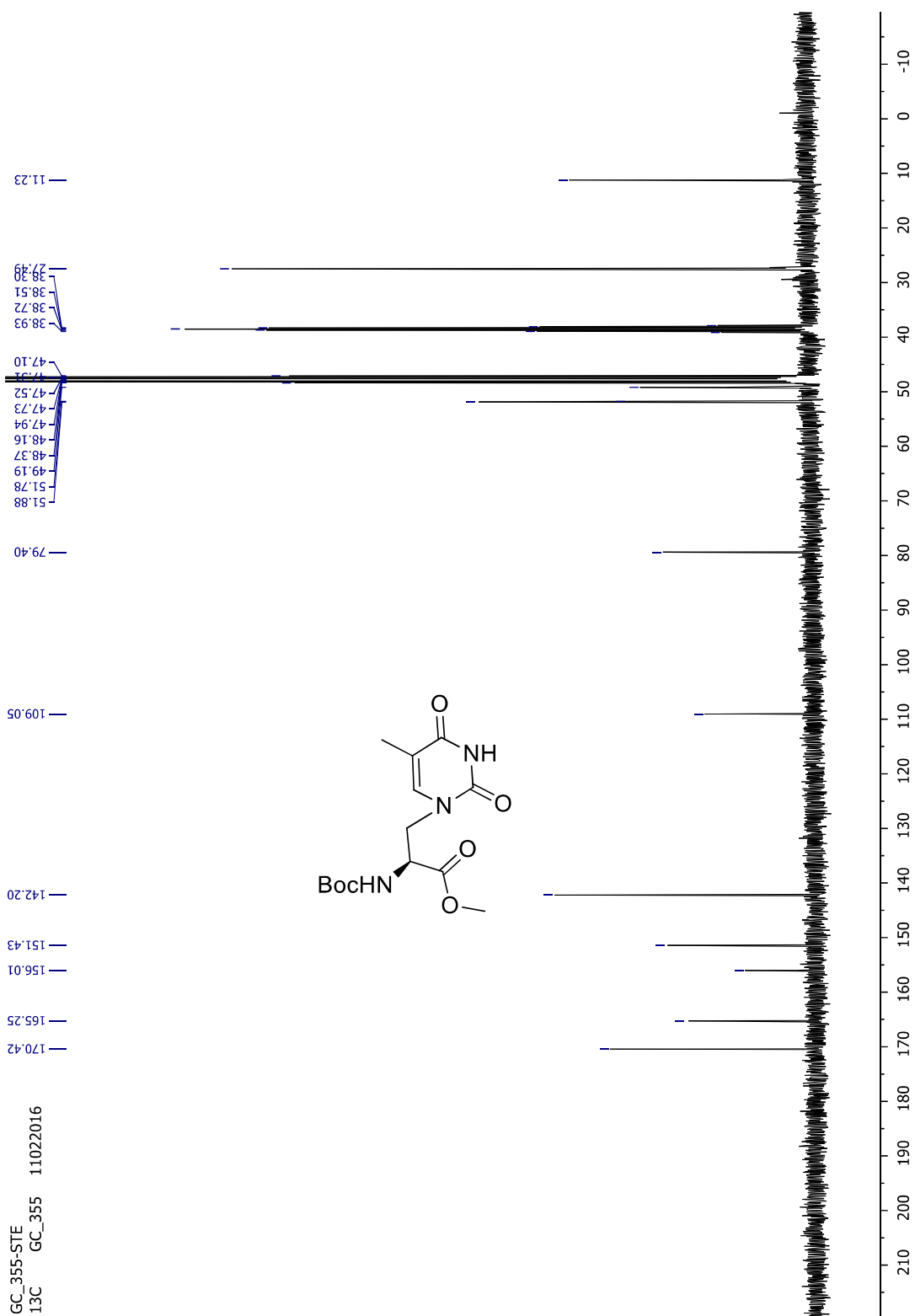


Figure A3 HRMS of compound 2

Figure A4 ^1H NMR of compound 3

Figure A5 ^{13}C NMR of compound 3

Generic Display Report

Analysis Info

Analysis Name D:\Data\FEB-2017\NKS\gc\22022017_NKS_GC_STE.d
Method Pos_tune_low.m
Sample Name Bruker micro TOF -Q II
Comment

Acquisition Date 2/22/2017 5:54:21 PM

Operator G.C.Reddy.
Instrument microTOF-Q II

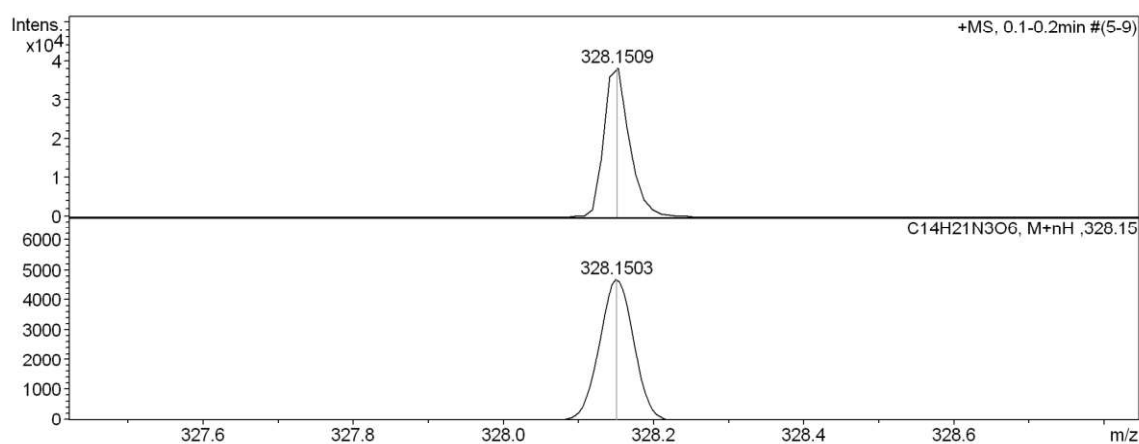
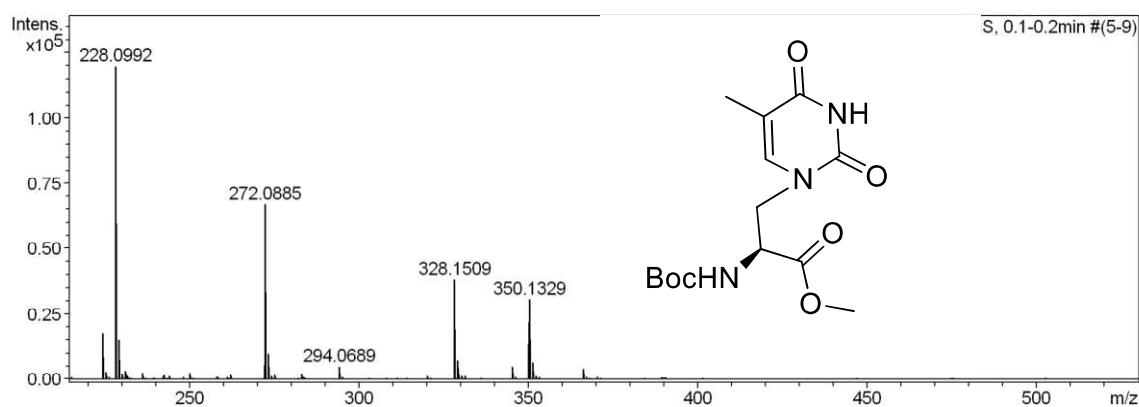
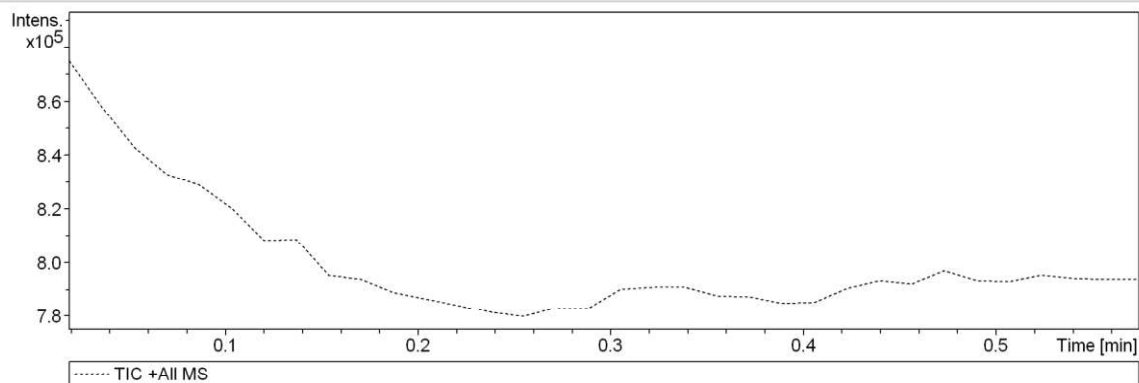
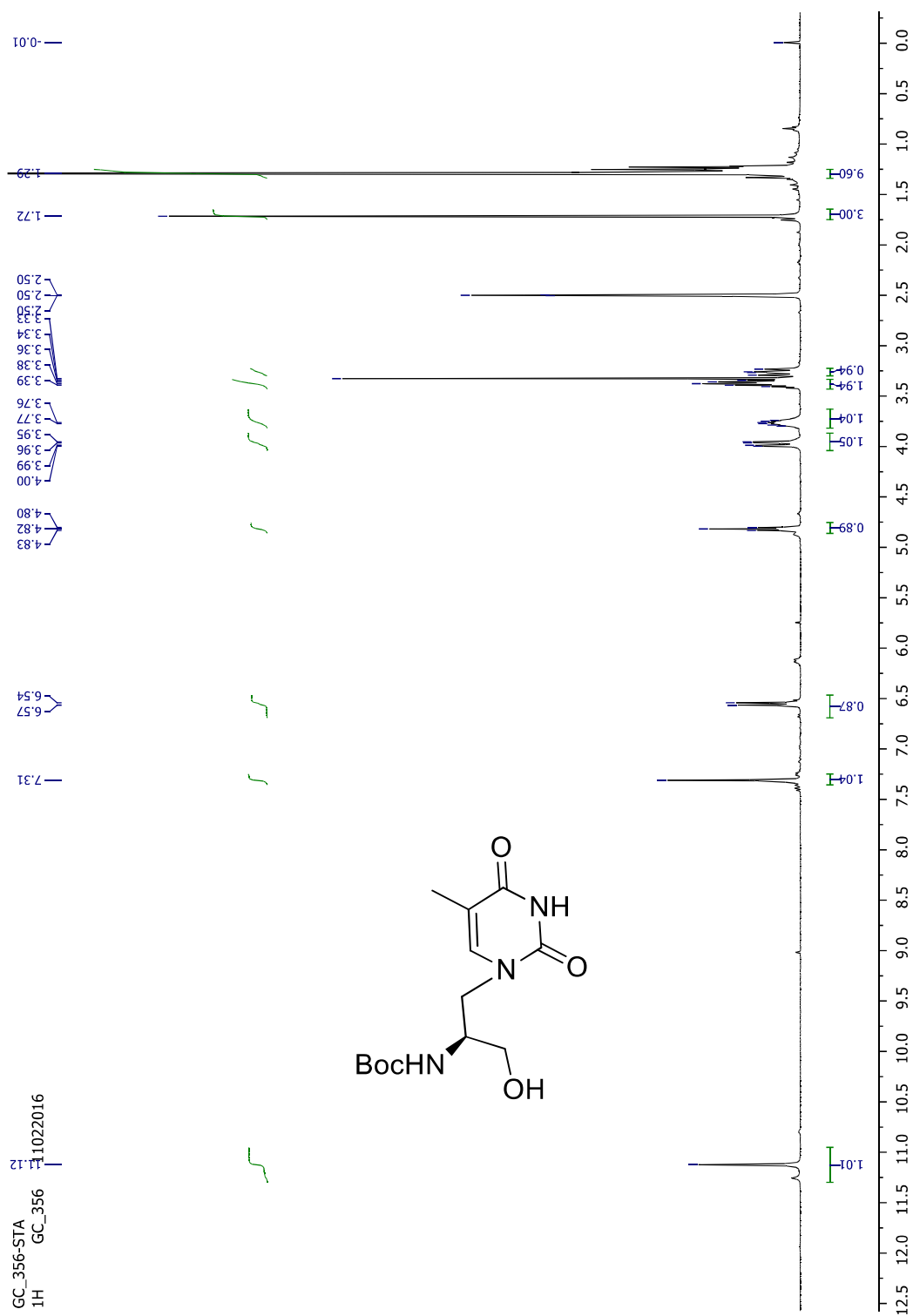
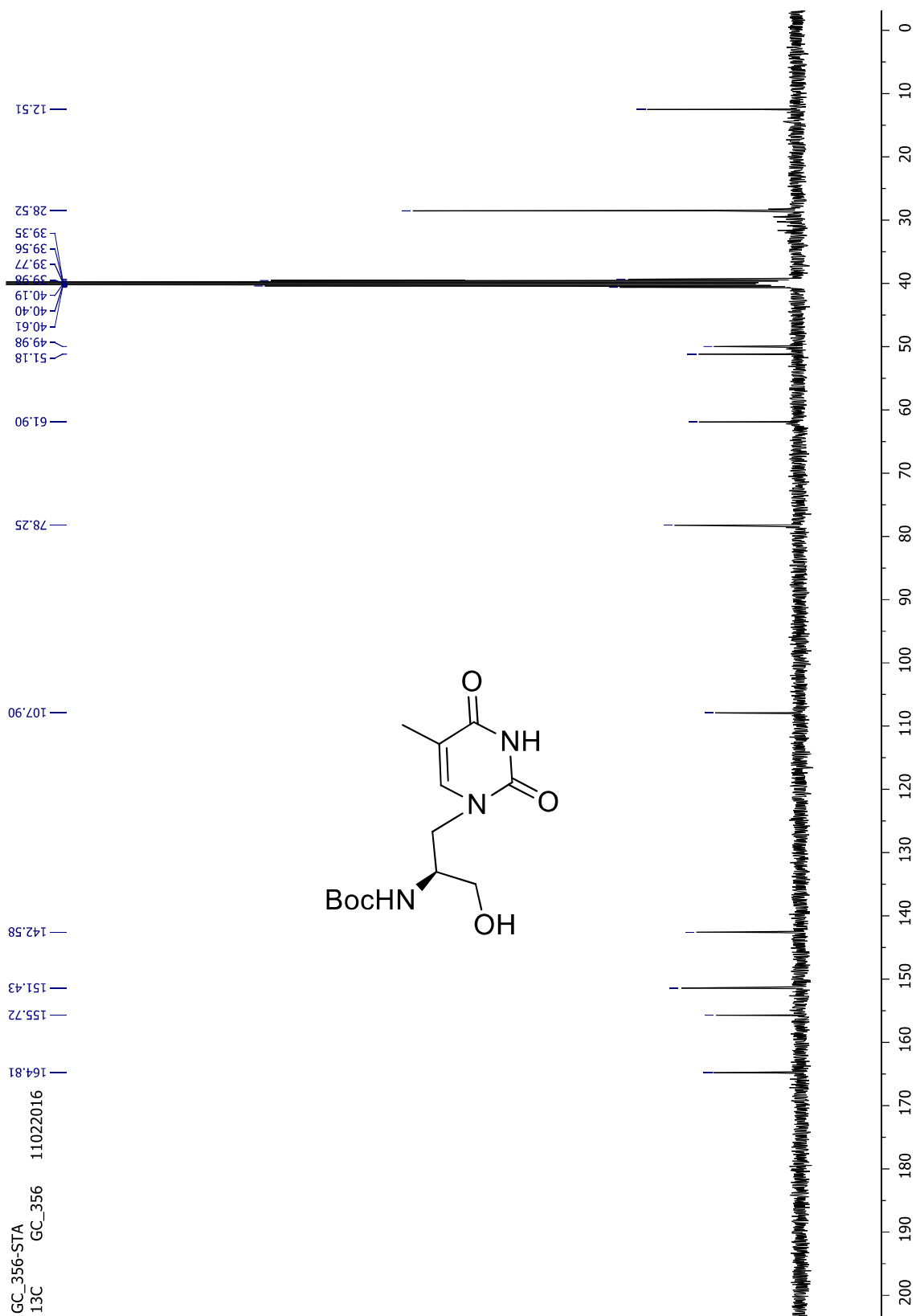


Figure A6 HRMS of compound 3

Figure A7 ^1H NMR of compound 4

Figure A8 ^{13}C NMR of compound 4

Generic Display Report

Analysis Info

Analysis Name D:\Data\FEB-2017\NKS\gc\22022017_NKS_GC_STOL.d
Method Pos_tune_low.m
Sample Name Bruker micro TOF -Q II
Comment

Acquisition Date 2/22/2017 6:04:14 PM

Operator G.C.Reddy.
Instrument micrOTOF-Q II

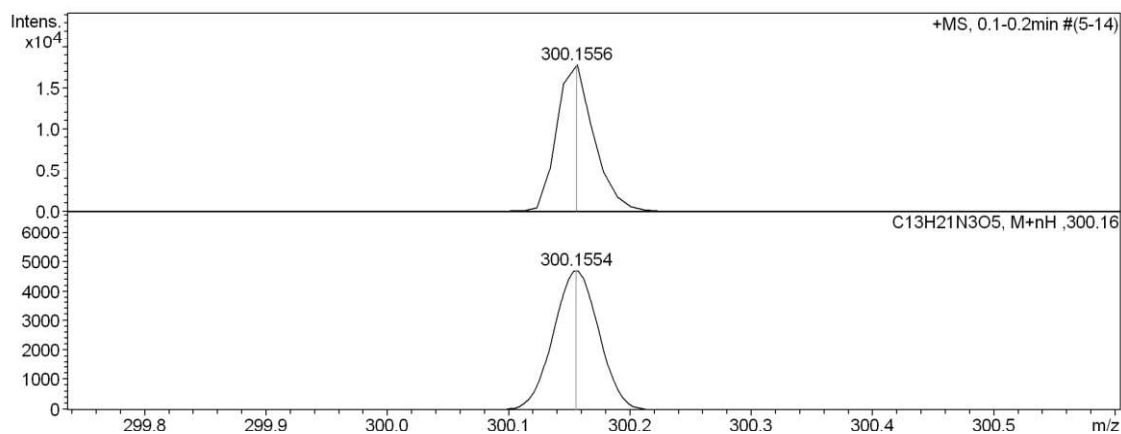
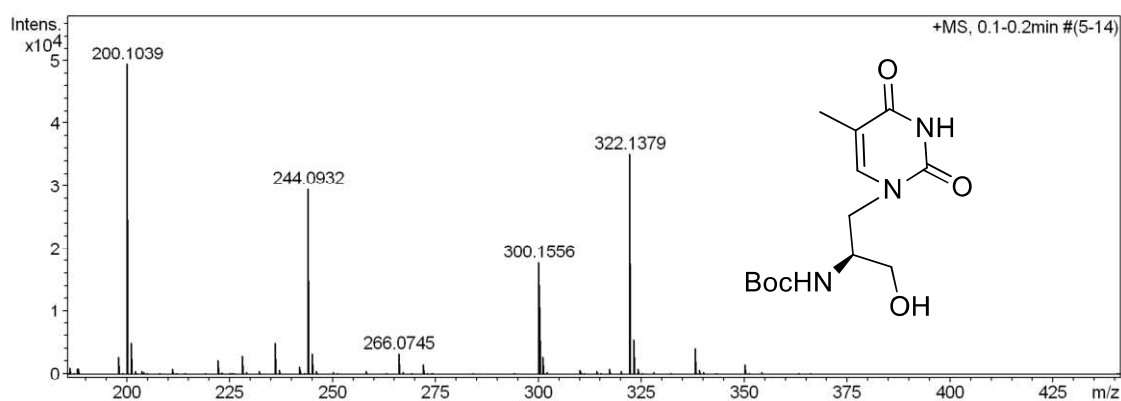
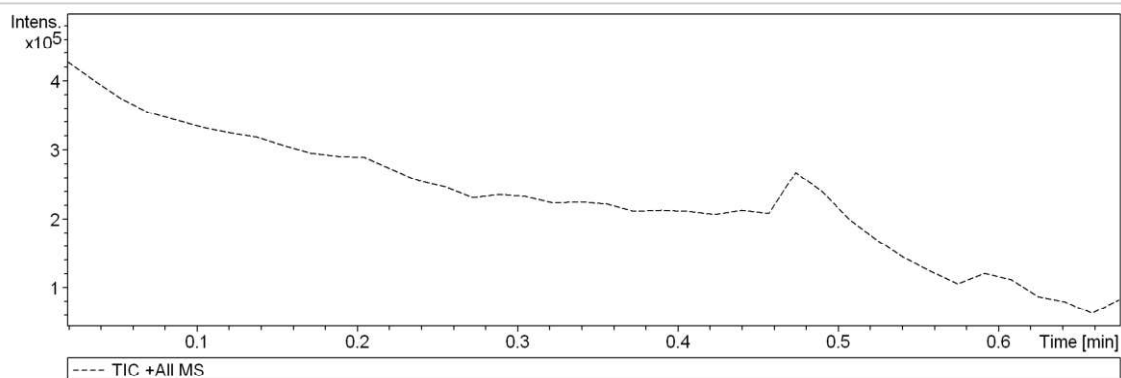
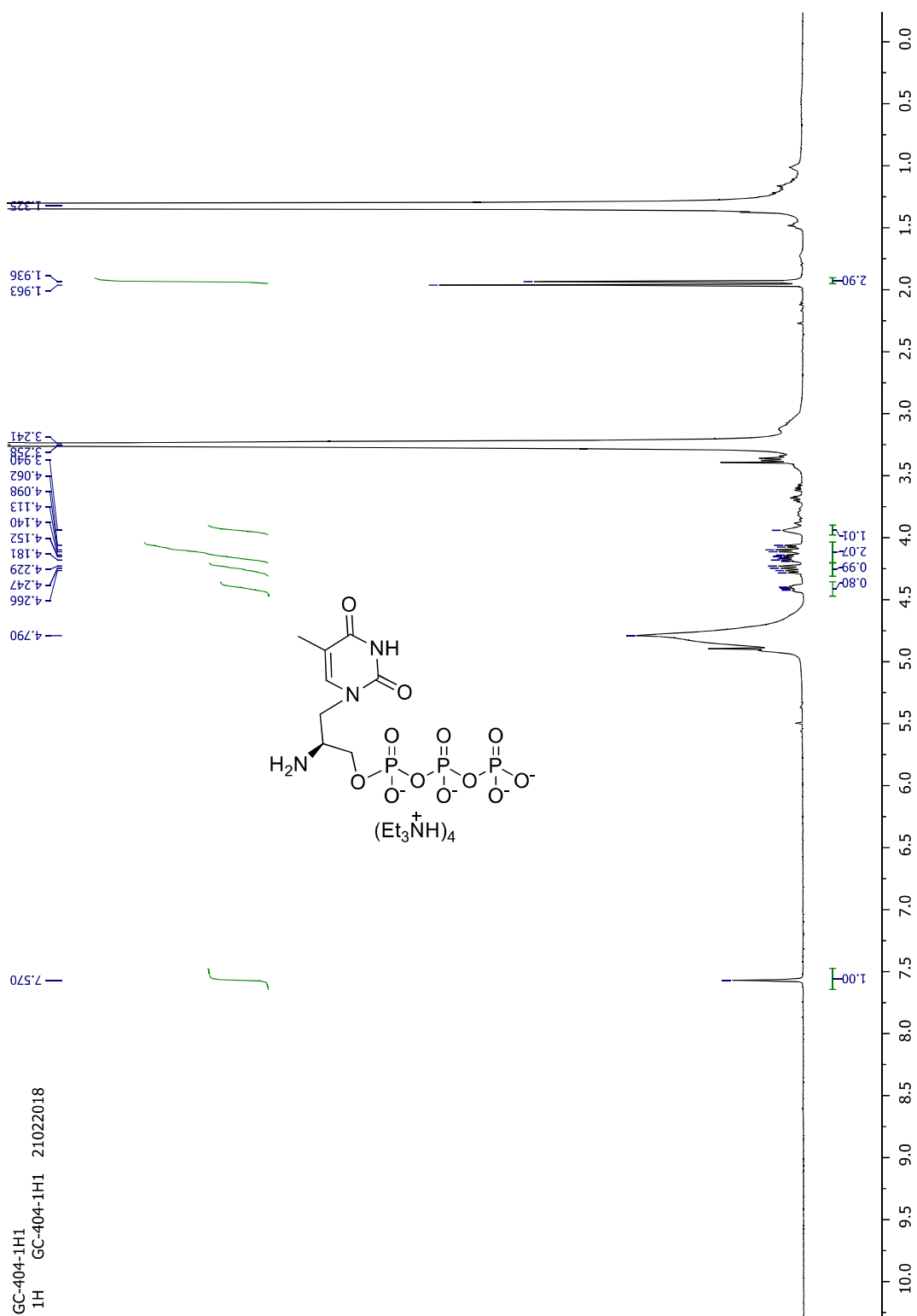


Figure A9 HRMS of compound 4

Figure A11 1H NMR of compound 5

Generic Display Report

Analysis Info

Analysis Name D:\Data\DEC-2016\NKS\02122016_NKS_GC_404.d
Method neg_tune_low.m
Sample Name Bruker micro TOF -Q II
Comment

Acquisition Date 12/2/2016 6:21:56 PM

Operator Amit S.Sahu
Instrument micrOTOF-Q II

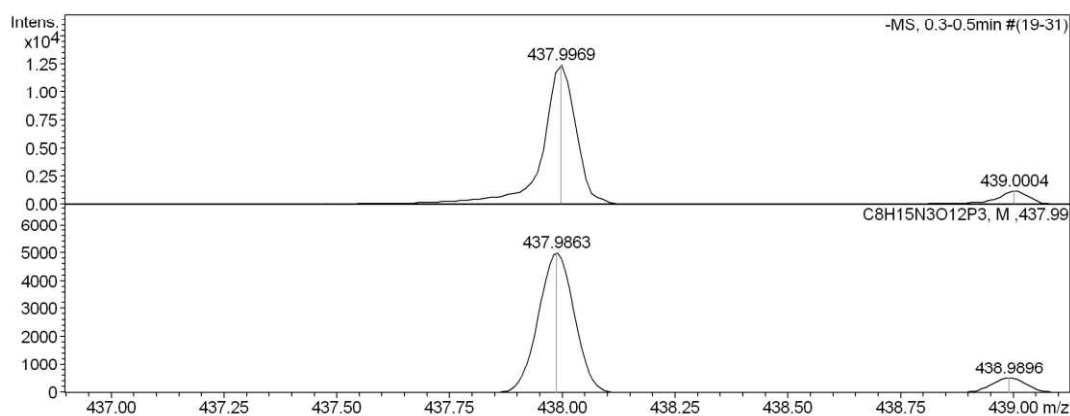
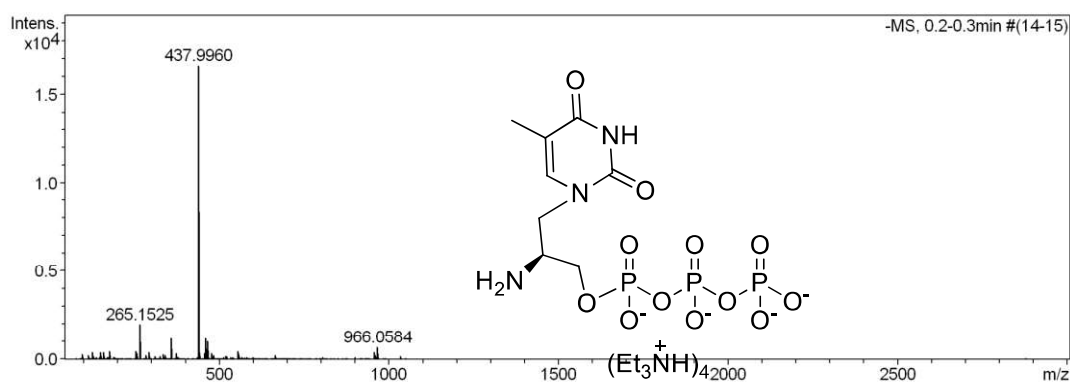
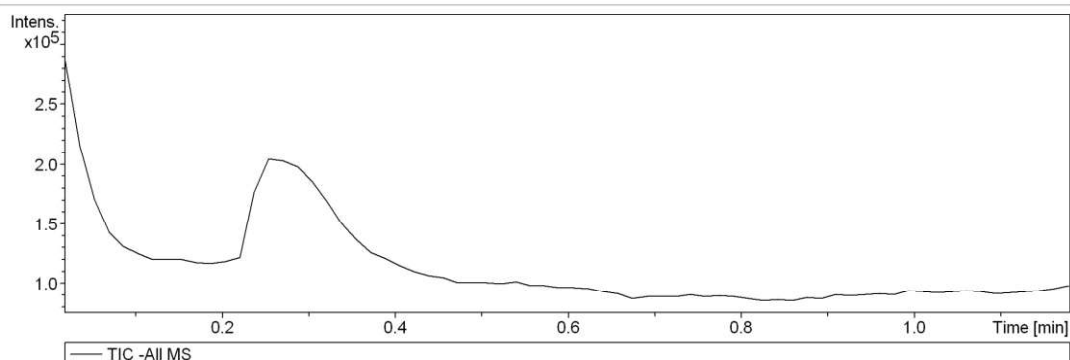
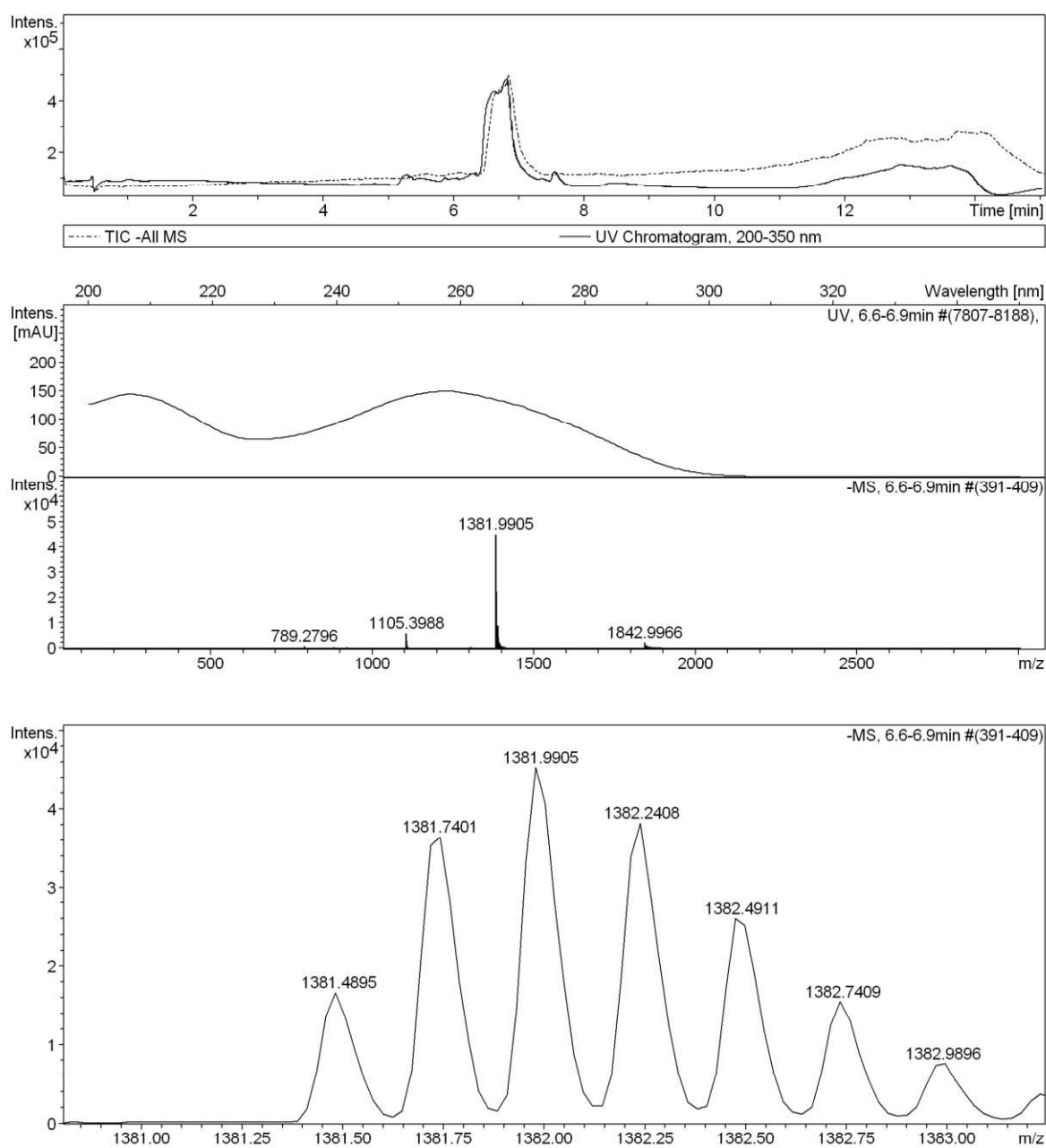


Figure A12 HRMS of compound 5

LC-MS of primer, template and extended primer with ala-TTP and ddTTP



TGTAAAACGACGGCCAGT Mass =5532.676

Calculated, (M-4H)⁴⁻= 1382.16, observed 1381.99

Figure A13 LC-MS of primer

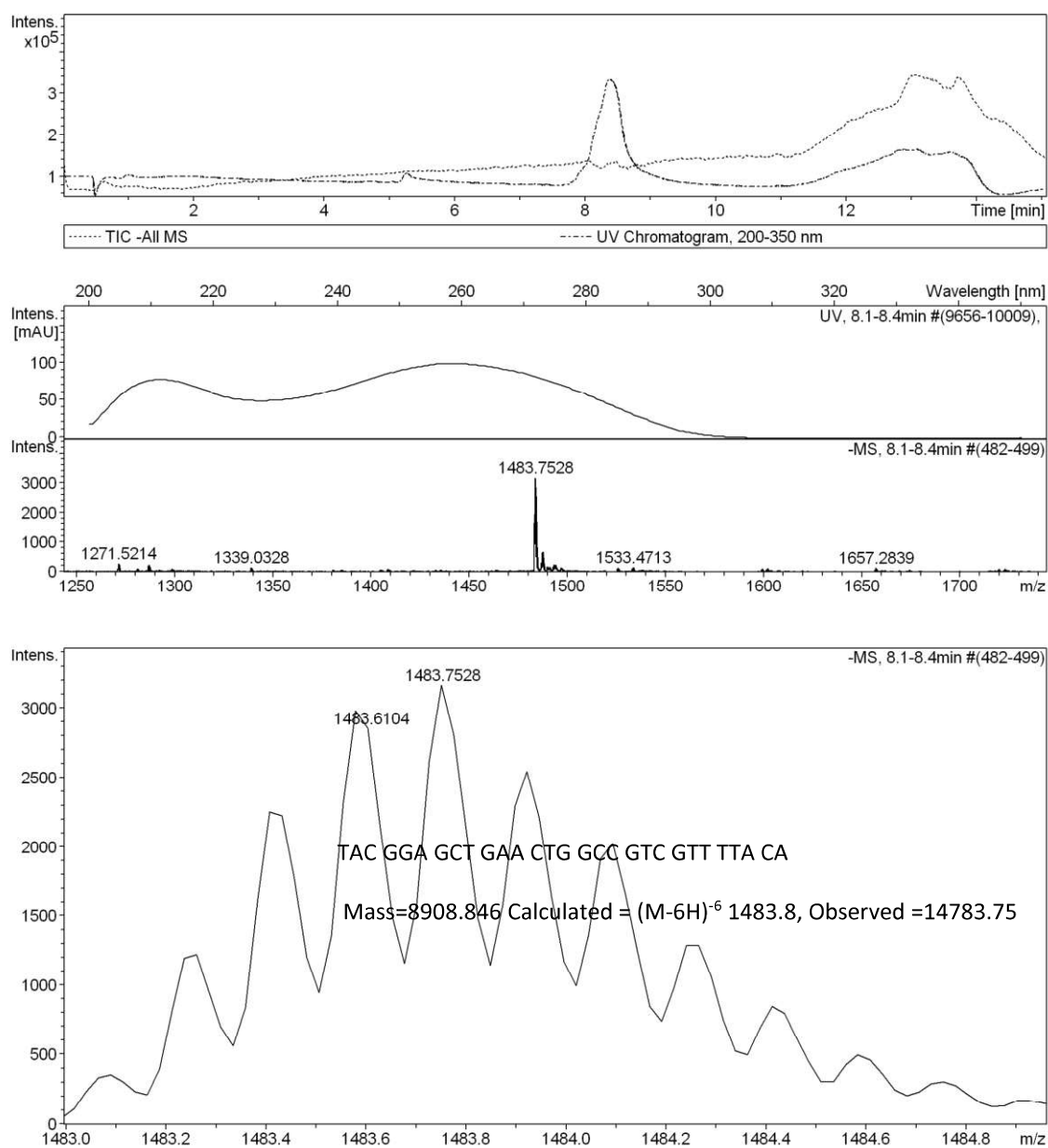


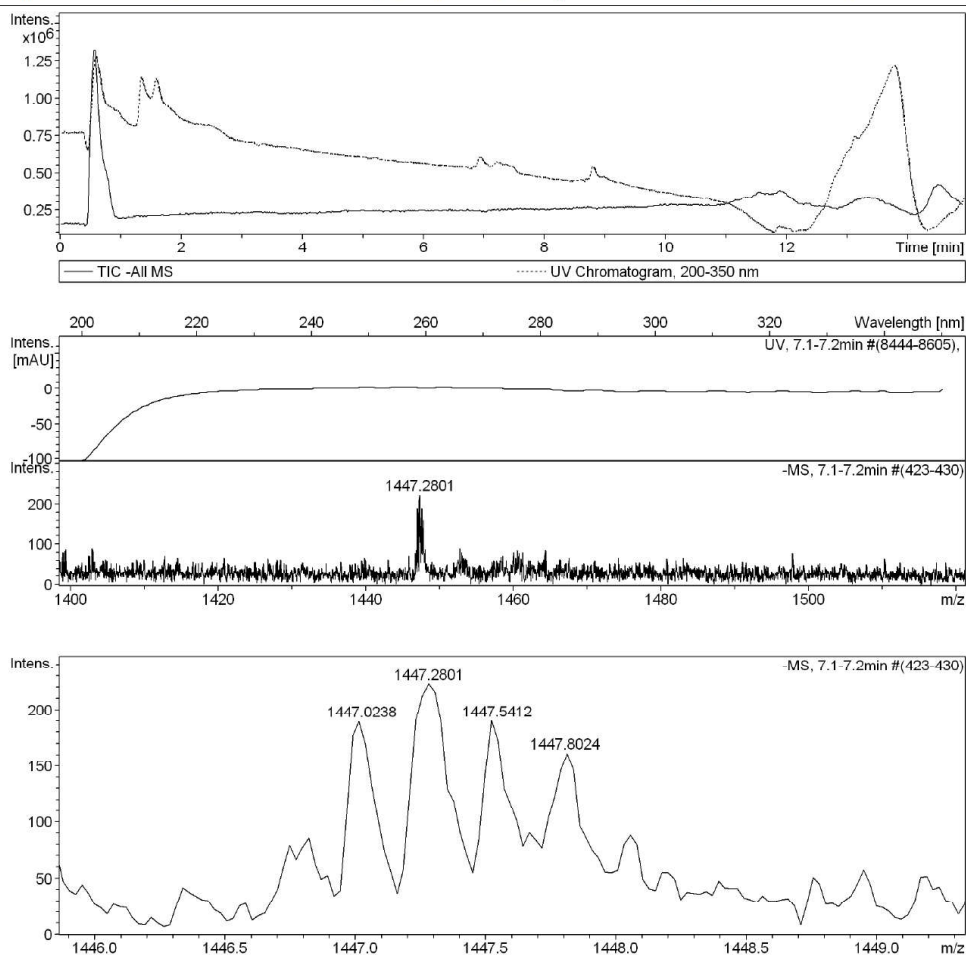
Figure A14 LC-MS of template

Display Report

Analysis Info		Acquisition Date	3/29/2017 8:11:26 PM
Analysis Name	D:\Data\AUG-2016\NKS\GC\29032017_NKS_GC_212-2_2-D_6_01_626.d	Operator	GCSREDDY.
Method	cafeine-no-uv.m	Instrument	micrOTOF-Q II 10337
Sample Name	29032017_NKS_GC_212-2		
Comment			

Acquisition Parameter

Source Type	ESI	Ion Polarity	Negative	Set Nebulizer	1.7 Bar
Focus	Not active	Set Capillary	2800 V	Set Dry Heater	220 °C
Scan Begin	50 m/z	Set End Plate Offset	-500 V	Set Dry Gas	7.0 l/min
Scan End	3000 m/z	Set Collision Cell RF	2100.0 Vpp	Set Divert Valve	Waste



Bruker Compass DataAnalysis 4.0

printed: 11/29/2017 7:53:48 PM

Page 1 of 1

TGTAACGACGGCCAGTT Mass =5,789

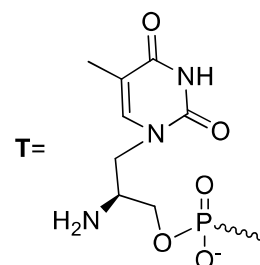
Calculated, (M-4H)⁴⁻ = 1447.25, observed =1447.28

Figure A15 LC-MS of extended primer with Ala-TTP and Vent exo-

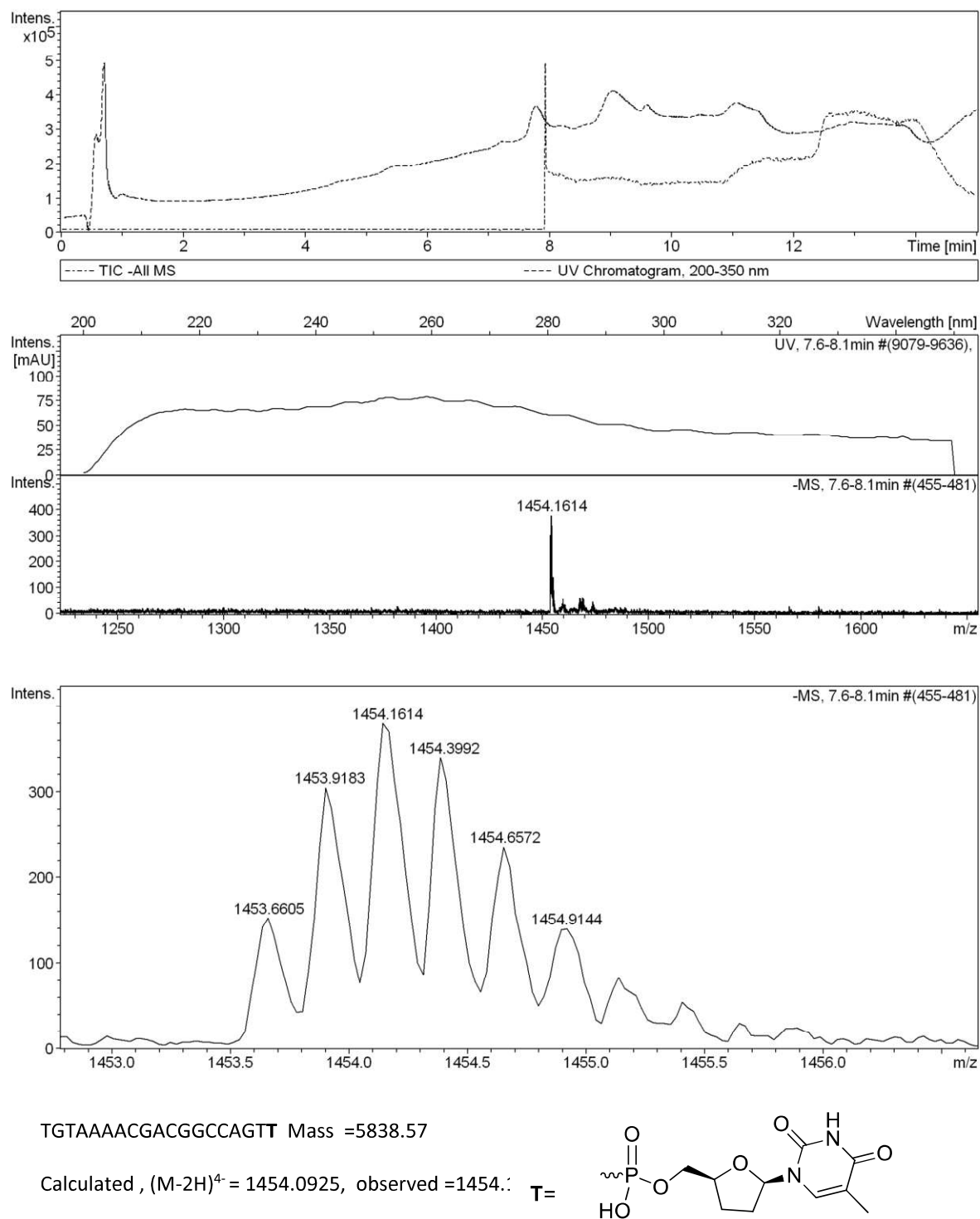


Figure A16 LC-MS of extended primer with dd-TTP and Vent exo-

Chapter 3B

**Synthesis and Biochemical Evaluation of Prolamide
Thymidine/Uridine Triphosphate Analogues**

Chapter 3B

Synthesis and Biochemical Evaluation of Prolamide Thymidine/Uridine Triphosphate Analogues

Contents

3B.1 Introduction	158
3B.1.1 Hypothesis and rational of present work	159
3B.2. Results and discussion	159
3B.2. 1 Synthesis of prolamide thymidine/uridine triphosphates.....	159
3B.2. 2 Biochemical evaluation of prolinol acetyl thymidine/uridine triphosphates	160
3B.2. 3 Self-assembly prolinol acetyl thymine/uracil	161
3B.2.4 Self-assembly study by scanning electron microscopy (SEM).....	165
3B.2.5 ESI-MS studies	167
3B.3 Conclusion	170
3B.4 Experimental section	170
3B.5 References	174
3B.6 Appendix	177

3B.1 Introduction

Dideoxy nucleoside triphosphates (ddNTP) are the sequence terminators developed by Sanger.¹ After Sanger's report researchers have been developed alternate ddNTP analogues. Amino ethyl glycyl (*aeg*) Peptide nucleic acids (PNA) are nucleic acid analogues where phosphate back bone is replaced by neutral amide backbone. *Aeg* derived triphosphate analogues have been synthesized and studied as ddNTP analogues.^{2,3} *Aeg* PNA are the acyclic and flexible molecules. Proline derived conformationally constrained PNA analogues have been synthesized and their binding properties with complementary DNA/RNA have been studied (Figure 3B.1).⁴⁻⁶ We have synthesized and studied the biochemical properties of 4-hydroxy proline derived pyrrolidine nucleoside triphosphates (Pr-NTPs) as ddNTP analogues.⁷ PNA analogues with prolinol acetyl nucleobase have been synthesized and incorporated in PNA at terminal and interior positions which stabilized the duplex with complementary DNA.^{8,9 10,11}

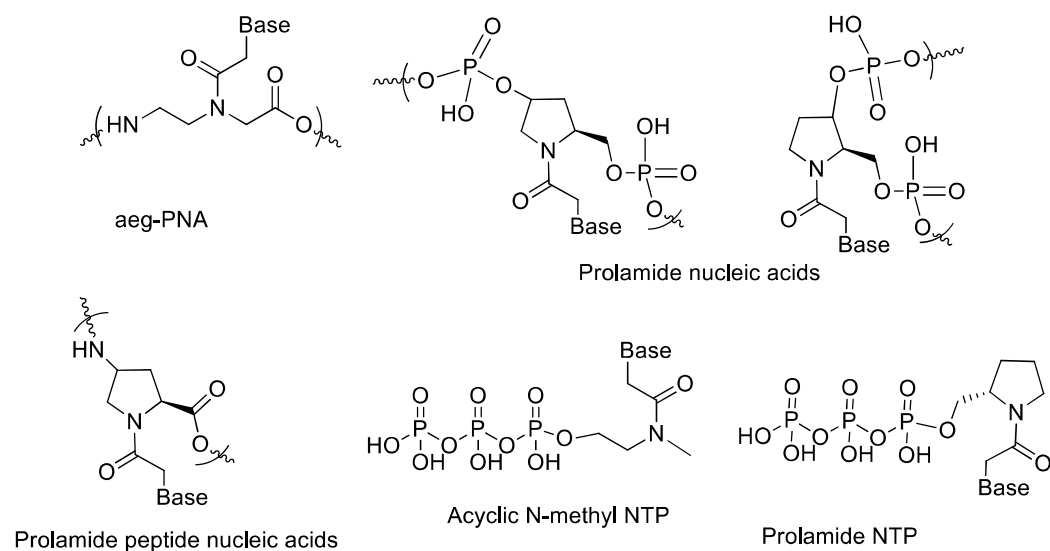


Figure 3B. 1. Structure of *aeg*-PNA, Prolamide nucleic acids, Prolamide PNA, Acyclic N-methyl NTP and Prolamide NTP

The 4-hydroxy /3-hydroxy prolinol acetyl nucleobase modified phosphoramidates have been synthesized and studied the stability of the hybrid duplex with complimentary DNA/RNA.¹²⁻¹⁴

3B.1.1 Hypothesis and rational of present work

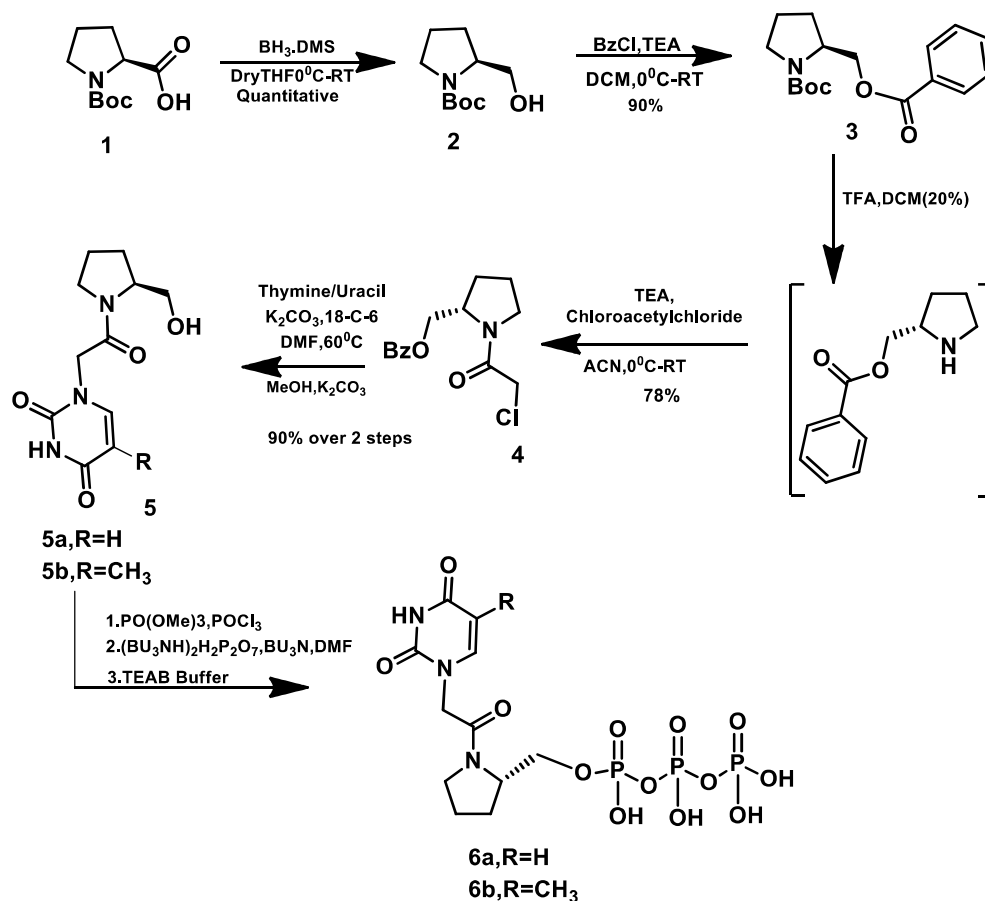
As prolinol acetyl nucleobase nucleic acid analogues forms stable duplexes with complementary DNA/RNA we hypothesized to synthesize nucleoside triphosphates derived from prolinol acetyl thymine/ uracil and study the biochemical activities of with DNA polymerase as alternate ddNTP analogues.

3B.2. Results and discussion

3B.2. 1 Synthesis of prolamide thymidine/uridine triphosphates

We started the synthesis of prolinol acetyl thymine/ uracil form N-Boc proline (**1**). N-Boc proline was treated with borane dimethyl sulphide to obtain N-Boc prolinol (**2**). The alcohol was protected as benzoate (**3**).The N-Boc proline benzoate was treated with 20% TFA/DCM to remove the boc group and insitu it is treated with chloroacetyl chloride to afford chloro derivative (**4**). The chloro derivative treated with thymine/uracil in dimethylformamide using potassium carbonate to obtain the benzoyl protected nucleoside analogue which was treated with potassium carbonate in methanol to obtain the nucleoside alcohols (**5a&5b**).Nucleosides **5a** & **5b** were characterized by single crystal X-ray diffraction. The nucleoside alcohols (**5a** & **5b**) phosphorylated by Yoshikawa's method. The alcohol treated with phosphoryl chloride in trimethylphosphate followed by treatment with tributylammonium pyrophosphate to obtain thymine/uracil triphosphate analogues.The synthetic steps are depicted in scheme 3B.1

Scheme 3B. 1: Synthesis of prolamide thymidine/uridine triphosphate



3B.2. 2 Biochemical evaluation of prolamide thymidine/uridine triphosphate analogues

The synthesized analogues were tested with many DNA polymerases *therminator*, *taq*, *vent*, *deepvent*, *bst*, and *klenow* DNA polymerases to study the primer extension reaction. Both the thymine and uracil analogues are the substrates for none of these enzymes.

3B.2. 3 Self-assembly prolinol acetyl thymine/uracil

The single crystal structure analysis of nucleosides show the helical self-assembly by hydrogen bonding interactions. Helix is the spiral symmetrical arrangement of molecules by supramolecular interactions. Helix is the supramolecular structure with coiled topology present in biological systems.¹⁵ The helical supramolecular assemblies are formed by hydrogen bonding interaction originated in intra or inter molecular fashion as seen in alpha-helix of proteins¹⁶ and double helix of DNA.¹⁷ The helices assemble to supramolecular structure by interaction with other molecules to form coil-coiled structure, DNA-protein, super helices of DNA structures to form functional supramolecular system which are vital for life and involved in many biological function such as ion-transport, molecular recognition, catalysis and genetic information storage.¹⁸ Hydrogen bonding is the key element in the formation and maintenance of the supramolecular structures in biomolecules.¹⁹ Chemists used many strategies to make artificial helical systems to mimic the nature. Foldamers, small molecules, oligomers, double stranded helical polymers have been synthesized to mimic the helix topology.²⁰⁻²² Nucleic acids attain different conformations under given physiological condition to adopt a secondary structure which play crucial role in biological systems.²³ Many nucleic acid based supramolecular structures have been developed. Small molecule based supramolecular self-assembled systems have been developed and studied their structural features by X-ray crystallography and other techniques²⁴. The supramolecular self-assembly of molecules at nucleobase level have been studied by designing small molecules based on homo or hetero dimerization

/self-assembly of nucleobase derivatives.^{25 26} Adenine nucleobase derivatives forms supra molecular structures by hydrogen bonding^{27,28} or metal mediated²⁹ self-assembled structures. Guanosine derivatives self-assemble to supramolecular structure by Hoogsteen hydrogen bonding.^{30 31} Hemi protonated cytosine and its derivatives self-assemble to form supra molecular structures by hydrogen bonding.³² Ferrocene linked Thymine/Uracil conjugates forms supra molecular assemblies by Watson-Crick/reverse Watson-Crick hydrogen bonding.^{33,34} Thymine/uracil N-acetyl prolinol derivatives have been synthesized and incorporated in DNA/PNA analogues and their binding properties have been studied. We are interested to study the supramolecular self-assembly formed by Thymine/uracil N-acetyl prolinol derivatives. Herein we describe the synthesis, self-assembly study of Thymine/uracil N-acetyl prolinol derivatives by X-ray crystallography, ESI-MS studies and SEM image techniques.

Helical self-assembly of prolinol acetyl uracil: The crystal structure of prolinol acetyl uracil is depicted in (Figure 3B .2). The supramolecular helical self-assembly in prolinol acetyl uracil originated from the hydrogen bonding interactions between the alcohol OH and carbonyl group. The helix formation from the hydrogen bonding interactions is explained here by taking 3 residues of prolinol acetyl uracil. The single crystal X-ray structure of prolinol acetyl uracil shows the arrangement of alcohol and carbonyl groups oriented in such a way that the carbonyl group can accept the hydrogen from another molecule in upward direction and the alcohol group can donate the proton to carbonyl group of another molecule in downward direction. This continuous arrangement of the residues by hydrogen bonding interactions build a helix around a pseudo axis. The puckered conformation of proline ring facilitated

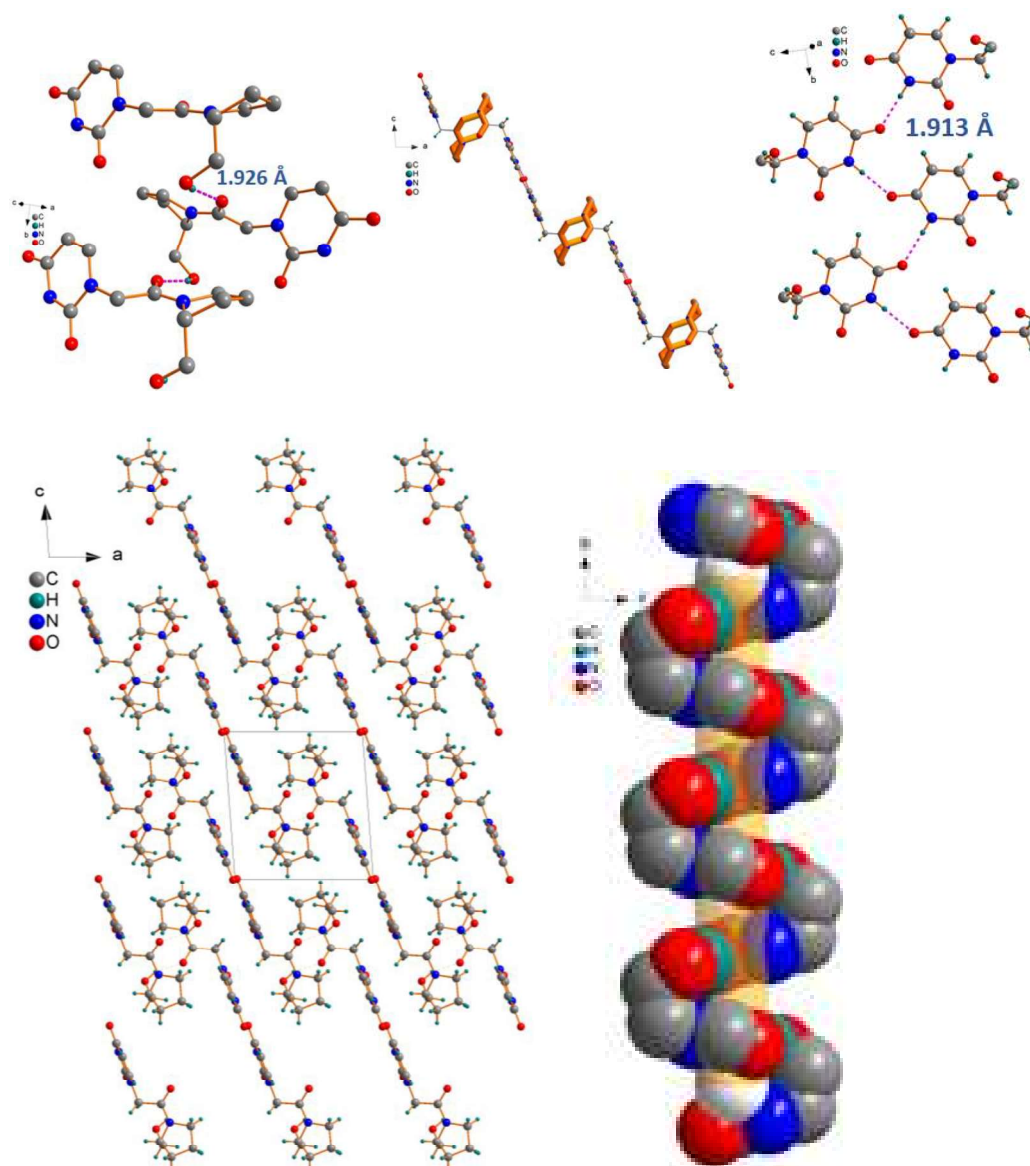


Figure 3B. 2 Crystal structure and self-assembly of prolinol acetyl uracil

such an arrangement of donor-acceptor to make stable helix. The uracil units flanked around the helix provides further supra molecular interaction with the uracil units of adjacent helices. An uracil moiety donates its N3 H to O 4 of uracil in downward direction and accepts hydrogen form N3 H to its O4 in upward direction. The hydrogen bonding distance between the alcohol OH and carbonyl group is 1.926 Å

and the distance between N3 H and O4 is 1.913 Å both are strong hydrogen bonding interactions.

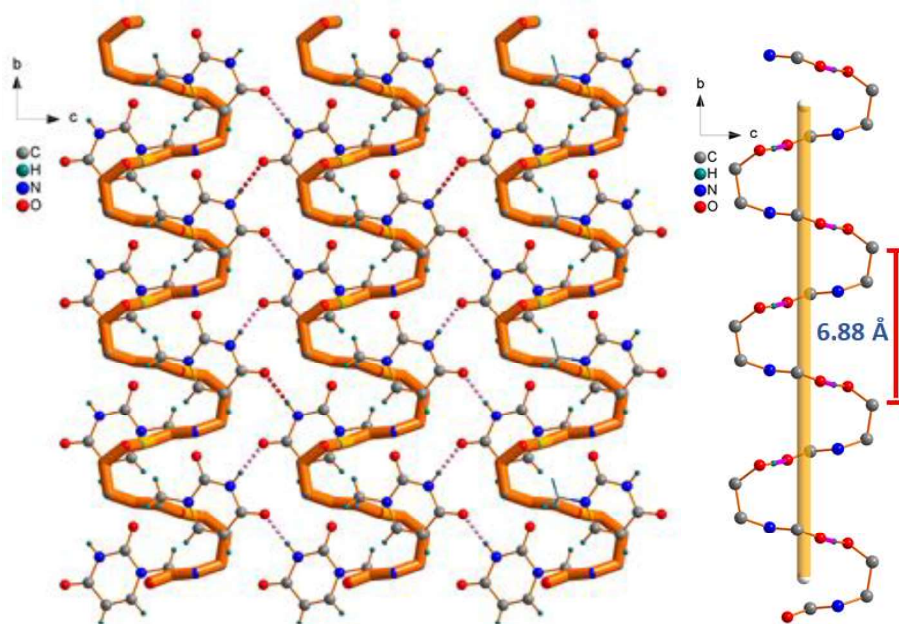


Figure 3B. 3 Crystal structure and self-assembly of prolinol acetyl uracil

Helical self-assembly of prolinol acetyl thymine: Prolinol acetyl thymine also forms helical supramolecular self-assembled structure. The crystal structure of prolinol acetyl thymine illustrated in Figures 3B.4 and 3B.4 In contrast to the prolinol acetyl uracil in thymine analogue with same backbone the carbonyl group of acetyl unit is not involved in the hydrogen bonding but here thymine take part in the helix formation and the alcohol acts as both donor by donating hydrogen to the carbonyl of thymine O 4 and acceptor by taking hydrogen from the N3 of thymine. Here the thymine residues are arranged in such a way that O4 accepts hydrogen from upward direction of alcohol and N3 accepts hydrogen from the alcohol from down ward direction and the

repeating units makes helix. Hydrogen bond distance of N3-H and alcohol oxygen is 1.902 Å and OH and O4 of thymine is 1.723 Å both are strong hydrogen bonds.

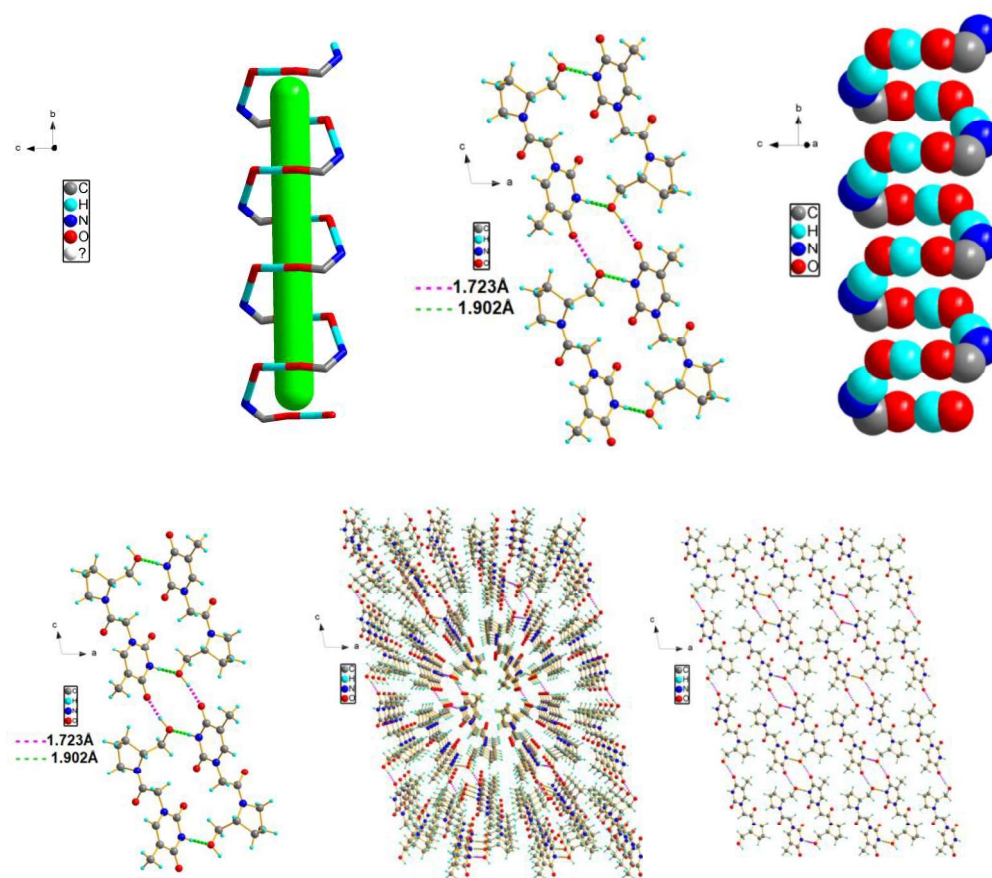


Figure 3B. 4 Crystal structure and self-assembly of prolinol acetyl Thymine

3B.2.4 Self-assembly study by scanning electron microscopy (SEM)

We recorded SEM images of prolinol acetyl thymine/uracil to study the morphology of self-assembled structures. The SEM image of prolinol acetyl thymine show rod like structures (Figure 3B.5). The rods are in nanometer size. At micrometer size also we observed the rod like structures and some aggregation. The SEM image of prolinol acetyl uracil (Figure 3B.5) show high aggregation in comparison to the thymine analogue. The crystal structure of prolinol acetyl uracil (Figure 3B. 2) show the helical self-assembly formed by the hydrogen bonding interactions of alcohol OH and

carbonyl oxygen. The flanking uracil units around helix connects other helices by hydrogen bonding interaction with adjacent uracil units forming a high aggregation. The crystal structure of prolinol acetyl thymine show that thymine residue is involved in the helix formation along with alcohol OH of proline ring where as in uracil case the carbonyl oxygen of acetyl group and alcohol OH of proline ring are involved in helix formation and uracil units take part in the connection of helices by hydrogen bonding interactions. Due to extension of aggregation of helices by joining uracil units a high aggregation seen in uracil analogue (Figure 3B.6). In thymine analogue thymine residue involves in helix formation and not available to extend the attachment of helices as like in uracil. Due to this a symmetrical rod like structure are observed in thymine case.

Overall the SEM studies support the self-assembly of prolinol acetyl thymine/uracil and also provide an evidence to understand the nature of aggregation as seen in crystal structures.

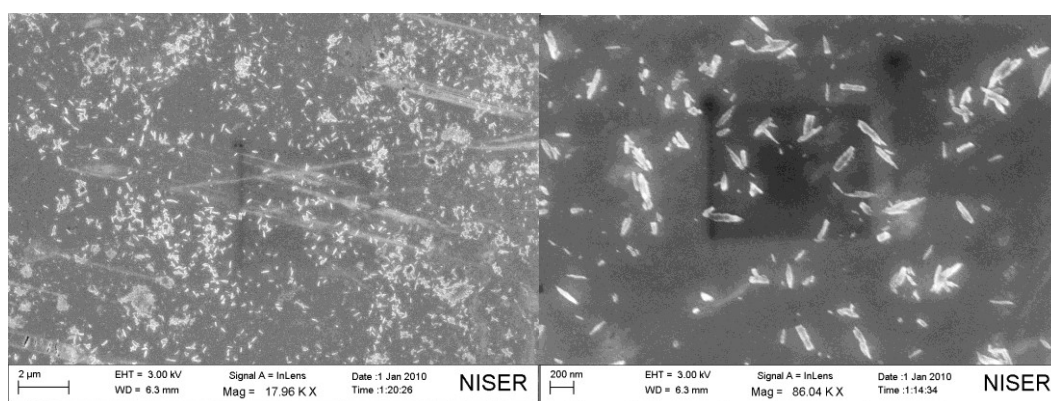


Figure 3B. 5 SEM image of prolinol acetyl thymine

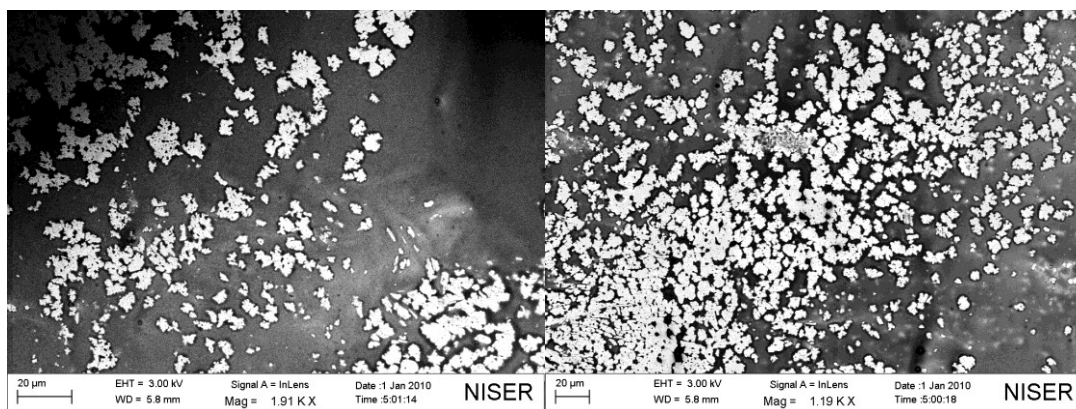


Figure 3B. 6 SEM image of prolinol acetyl uracil

3B.2.5 ESI-MS studies

The self-assembly of nucleobase/nucleosides derivative have been studied by ESI-MS. For example Guanine nucleosides forms G-quartets which formed by the self-assembly four guanine units in presence of metal ion. 5-substituted thymine and uracil derivatives also forms pentameric structures in presence of metal-ions have been studied by ESI-MS studies. As our helical structures are formed by the self-assembly we are interested to study the self-assembly by ESI-MS. We recorded the ESI-MS of thymine and uracil derivatives (Figure 3B.7& 3B8). In both cases the monomer is predominate and the dimer and trimers were also observed with less intensity. A tetramer also observed with less intensity. The higher order aggregates are not stable in ESI conditions. However ESI-MS results support the self-assembly of these analogues though they not stable enough to determine the high order self-assembled structures.

Display Report

Analysis Info
Analysis Name D:\Data\NOV-2017\NKS\04112017_NKS_GC_PUA-3.d
Method pos tune_low_16102017.m
Sample Name ESI-MS
Comment
Acquisition Date 11/4/2017 6:33:52 PM
Operator GCREDDY
Instrument micrOTOF-Q II 10337

Acquisition Parameter
Source Type ESI
Focus Not active
Scan Begin 50 m/z
Scan End 3000 m/z
Ion Polarity Positive
Set Capillary 4500 V
Set End Plate Offset -500 V
Set Collision Cell RF 300.0 Vpp
Set Nebulizer 0.4 Bar
Set Dry Heater 180 °C
Set Dry Gas 4.0 l/min
Set Divert Valve Source

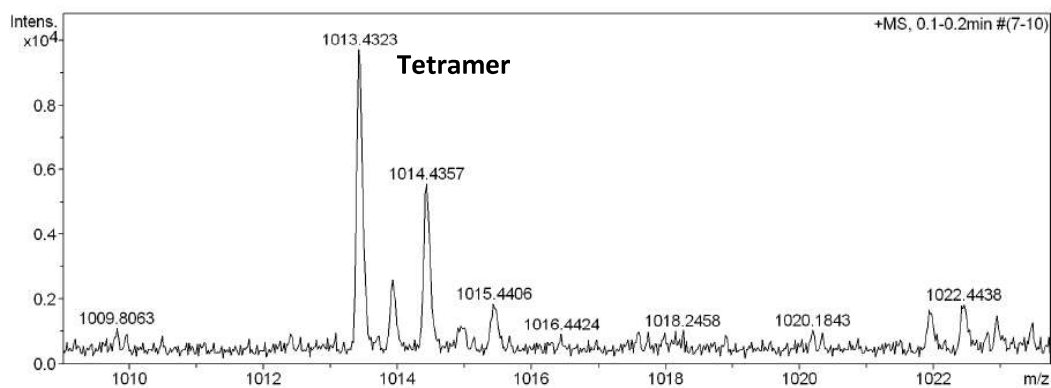
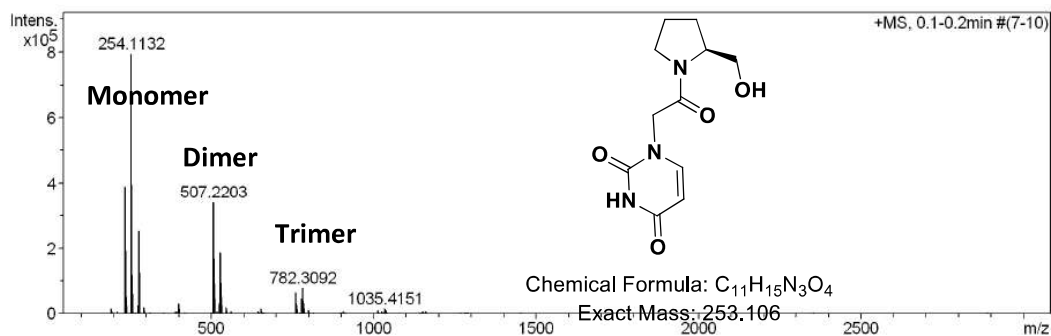
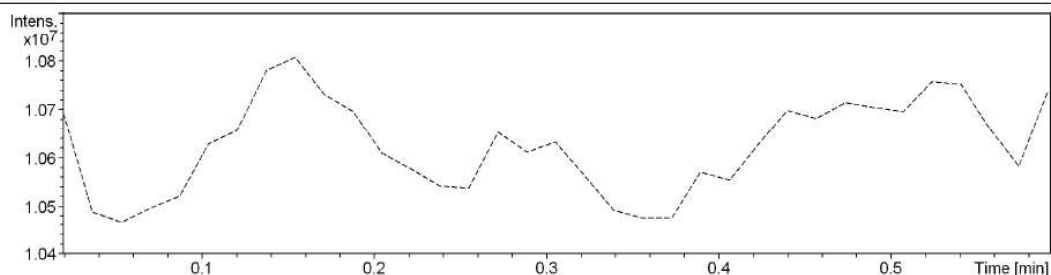


Figure 3B.7. ESI-MS of prolinol acetyl uracil

Display Report

Analysis Info

Analysis Name D:\Data\NOV-2017\NKS\04112017_NKS_GC_PTA2.d
 Method pos tune_low_16102017.m
 Sample Name ESI-MS
 Comment

Acquisition Date 11/4/2017 6:40:01 PM

Operator GCREDDY
 Instrument micrOTOF-Q II 10337

Acquisition Parameter

Source Type	ESI	Ion Polarity	Positive	Set Nebulizer	0.4 Bar
Focus	Not active	Set Capillary	4500 V	Set Dry Heater	180 °C
Scan Begin	50 m/z	Set End Plate Offset	-500 V	Set Dry Gas	4.0 l/min
Scan End	3000 m/z	Set Collision Cell RF	300.0 Vpp	Set Divert Valve	Source

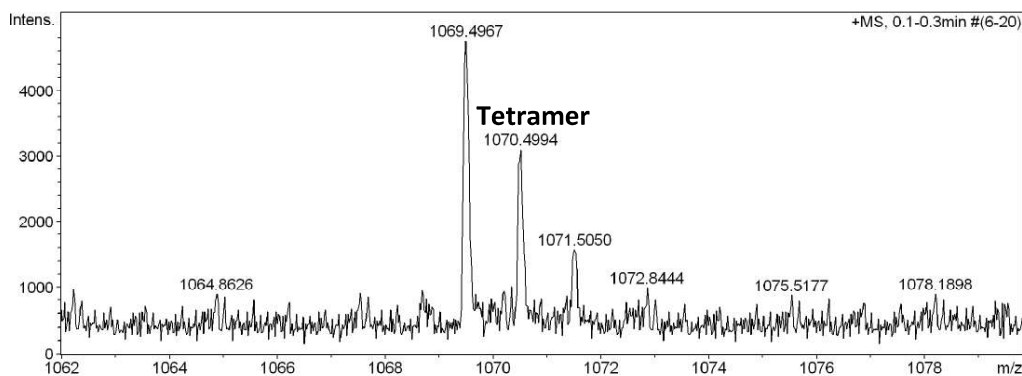
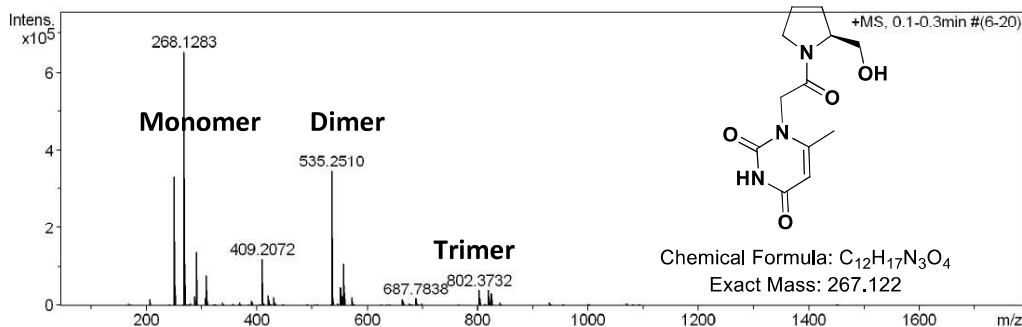
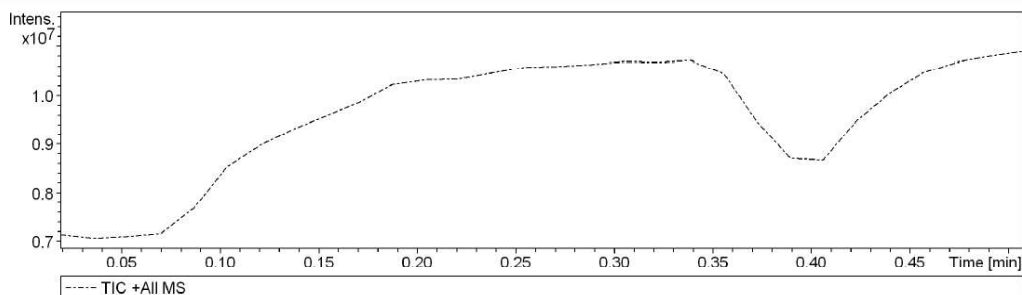


Figure 3B. 8. ESI-MS of prolinol acetyl uracil

3B.3 Conclusion

In conclusion we synthesized prolinol acetyl thymine/uracil triphosphates and studied their biological activity with DNA polymerase. The triphosphate analogues are not substrates of DNA polymerase. We have studied the self-assembly of prolinol acetyl thymine/uracil by single crystal X-ray Diffraction. The two analogues form supramolecular helical self-assembly by hydrogen bond interactions as shown crystal structure. Importantly the puckered nature of prolinol acetyl moiety plays crucial role in the orientation of helix structure. The systems can help to understand and design the helical self-assembled structures.

3B.4 Experimental section

(S)-*tert*-butyl 2-(hydroxymethyl)pyrrolidine-1-carboxylate (**2**) 4.0g (18.6mmol) boc proline was dissolved in 30 ml dry THF and stirred at 0°C for 10 minutes under nitrogen atmosphere, borane dimethyl sulphide (5M in diethyl ether) 3.71ml (18.6mmol) was added drop wise with syringe at 0°C. After 10 minutes the reaction mixture warmed to room temperature and stirred for 6 hours. The reaction mixture evaporated to dryness and coevaporated with methanol (2x30 ml) and extracted with water and ethylacetate. Ethyl acetate layer washed with brine solution and dried with anhydrous sodium sulphate and concentrated at reduced pressure. White solid 3.73 g obtained in quantitative yield used directly in next step without any purification. TLC DCM R_f = 0.43 ^1H NMR (400MHz in CDCl_3) δ 1.45(s,9H), 1.84-1.85(m, 3H), 1.95-2.04(m, 2H), 3.26-3.32(m, 1H), 3.41-3.49(m, 1 H), 3.54-3.62(m, 2H), 3.85-3.94(m, 1H) 4.74(s, 1H) ^{13}C NMR (100M HZ in CDCl_3) δ 24.18, 28.57, 28.22, 47.66, 60.30, 67.78, 80.33, 157.26 HRMS (ESI-TOF) Calcd for $(\text{C}_{10}\text{H}_{19}\text{NO}_3 + \text{Na})^+$ 224.1257 found 224.1231

(S)-tert-butyl 2-((benzyloxy)methyl)pyrrolidine-1-carboxylate (3)

To a solution of Boc prolinol 3.6 g (18.15mmol) in dry DCM (30ml), triethylamine 5.0ml(36.3mmol) was added at 0°C followed by addition of benzoyl chloride 3.1 ml (27.2 mmol) drop wise and the reaction was stirred at room temperature overnight. 50 ml water was added to the reaction mixture and stirred for 10 min and organic layer was separated. Aqueous layer extracted with DCM (2x50 ml) .Combined organic layer washed with brine solution and dried with anhydrous sodium sulphate ,concentrated at reduced pressure and purified by silica gel column chromatography (ethylacetate and hexane) to afford 4.9 g of white solid in 90% yield. TLC DCM R_f =0.32 ^1H NMR (400MHz CDCl_3) δ 1.45(s,9H),1.85-2.0(m,4H), 3.29-3.53(br, 2H) 4.10-4.42(m,3H),7.43(t,2H 8hz),7.55(t,1H 8hz),8.03(d ,2H 8hz). ^{13}C NMR(100 MHz CDCl_3) δ 23.30,23.98, 28.05,28.59,29.00, 46.62,48.5, 55.79, 65.20,65.39, 79.55,79.92,128.50, 129.74, 130.18, 133.16, 154.61, 166.51. HRMS Calcd for $(\text{C}_{17}\text{H}_{23}\text{NO}_4+\text{Na})^+$: 328.1519 found 328.1542.

S-(1-(2-Chloroacetyl)pyrrolidine-2-yl)methyl benzoate (4): 530 mg (1.73mmol) of compound **3** was treated with 10 ml of TFA.DCM (20%) at room temperature. After 3hours the reaction mixture was evaporated to dryness and diluted with 5ml dry acetonitrile, triethylamine 0.48 ml(3.47mmol) was added at 0° C under N_2 atmosphere followed by chloroacetyl chloride 0.20 ml (2.6mmol) at 0° C and stirred overnight at room temperature .The reaction mixture concentrated and extracted with ethylacetate and water .Ethyl acetate layer washed with brine solution, dried with anhydrous sodium sulphate and concentrated followed by purification on silica gel column chromatography to obtain colourless oily compound 380 mg in 78% yield. TLC DCM

$R_f = 0.64$ ^1H NMR (400MHz CDCl_3) δ 1.96-2.13(m,4.3H), 3.57-3.64(m,2H), 4.04(s,1.42H), 4.12-4.17(m,0.45H),4.29-4.74(m, 3H), 7.44(t,2H, $J = 8$ HZ),7.56 (t,1H $J = 8$ HZ) 8.01(d,2H $J = 8$ HZ) ^{13}C NMR (100MHz , CDCl_3) δ 21.16, 24.40, 27.39, 28.89, 41.62, 42.36, 46.33, 47.32, 56.25, 56.96, 63.93, 65.13, 128.48, 128.66, 129.33, 129.61, 129.96, 133.13, 133.57, 165.49, 165.76, 166.32, 166.36. HRMS (ESI-TOF) Cald for $(\text{C}_{14}\text{H}_{15}\text{O}_3\text{NCl}+\text{H})^+$: 282.0891 found 282.0889.

(S)-1-(2-(2-(hydroxymethyl)pyrrolidin-1-yl)- 2-oxoethyl) -5-methylpyrimidine 2,4(1H,3H)-dione(**5a**)

0.126 g (1.00mmol) of thymine dried under high vacuum at room temperature for 2 hours and dissolved in 4 ml anhydrous DMF followed by addition of 0.2g (1.5mmol) anhydrous potassium carbonate and 18-crown-6, 52mg (0.2mmol) and stirred at 60⁰c for 20 minutes under N_2 atmosphere followed by addition of anhydrous DMF solution (2.8ml) of compound **5** 0.28g (1.0mmol) by a syringe and stirred over night at 60⁰c .The reaction mixture was concentrated to dryness and extracted with water and ethyl acetate. Ethylacetate layer dried with anhydrous sodium sulphate and concentrated to get white pluffy compound which was dissolved in methanol, stirred at room temperature for 10 minutes followed by addition of 0.276 g (2.0 mmol) of potassium carbonate and stirring was continued for 24 hours at room temperature, the reaction mixture was concentrated and purified by silica gel column chromatography using DCM/MeOH to obtain a white solid 0.262 g in 95% yield. TLC 10 % MeOH/DCM $R_f = 0.56$ ^1H NMR (400 MHz CD_3OD) 1.88(s, 3H), 1.93-2.11(m,4H),3.41-3.66(m,4.0H),4.08-4.18(m, 1H),4.50-4.71(m, 2H),7.32(s,1H) ^{13}C NMR (CDOD_3 100MHz) δ 12.33, 22.54, 25.09, 28.01, 29.14, 60.42, 61.21, 62.92,

64.48, 110.79, 110.96, 143.74, 143.99, 153.18, 166.97, 167.84, 168.34 HRMS (ESI-TOF) Calcd for (C₁₇H₁₂N₃O₄Na) 268.1292 found 268.1290

(S)-1-(2-(2-(hydroxymethyl)pyrrolidin-1-yl)-2-oxoethyl)pyrimidine-2,4(1H,3H)-dione

(5b): 0.112 g (1.0 mmol) of uracil used to synthesize the compound **5b** in a similar procedure to obtain 0.24 g **5b** in 95% yield as white solid. TLC 10 % MeOH/DCM R_f = 0.43 ¹H NMR (400 MHz CD₃OD) 1.69-2.27 (m, 4H) 3.28 (m, 2H), 3.61-3.85 (m, 3H), 4.30 (s, 1H) 4.56 (s, 1H), 5.64-5.70 (m, 1H) 7.49-7.60 (m, 1H) (CD₃OD, 100 MHz) 22.67, 24.38, 25.21, 28.13, 29.72, 60.55, 61.31, 63.12, 64.57, 102.21, 102.36, 148.13, 148.38, 153.27, 167.05, 167.91, 168.35. HRMS Calcd for C₁₁H₁₅N₃O₄Na 276.0955 Found 276.0970.

((S)-1-(2-(5-methyl-2,4-dioxo-3,4-dihydropyrimidin-1(2H)-yl)acetyl)pyrrolidin-2-yl)methyl trihydrogen triphosphate **(6a)**

Compound **5a** 0.03 g (0.112 mmol) dried in high vacuum at room temperature for 2 hours, dissolved in 3 ml trimethyl phosphate and stirred under nitrogen atmosphere at -20 °C for 10 minutes. 0.03 ml (0.33 mmol) of phosphorous oxy chloride was added and stirred at -5 °C for 2 hours followed by injection of a cocktail containing 154 mg (0.28 mmol) tributylammonium pyrophosphate and 0.21 ml (0.89 mmol) of tributylamine in 2 ml of anhydrous DMF and stirred at room temperature for 30 minutes. 5 ml of 100 mM TEAB buffer added and stirred at room temperature for one hour the hydrolysis step was monitored by mass spectrometry after one hour another 5 ml TEAB buffer added and stirred for 30 minutes. The reaction mixture lyophilized and purified by DEAE sephadex column using ammonium bicarbonate as eluent (0.1 M - 1.0 M). The compound further purified by HPLC using 10 mM TEAB buffer (A) and acetonitrile (B). ¹H NMR (400 MHz D₂O)

δ 2.01-2.11(m,1H), 3.36-3.40(m,1H), 3.53-3.67(m,2H) 3.97-4.13(m,1H),4.29-4.44(m,3H), 4.91-5.0(m,1H), 5.87-5.89((m,1H), 7.60-7.71(m,1H) ^{31}P NMR (162MHz,D₂O): δ -22.05,-22.79 (br ,1P,), -9.91(br, 2P) HRMS: Calcd for C₁₂H₁₉N₃O₁₃P₃ 506.0125 Found 506.0178

((S)-1-(2-(2,4-dioxo-3,4-dihydropyrimidin-1(2H)-yl)acetyl)pyrrolidin-2-yl)methyl trihydrogen triphosphate **6b**

Compound 5b 0.03 g (0.11 mmol) phosphorylated as described above to obtaine prolamiode uridine triphosphate (**6b**) ^1H NMR (400 MHz D₂O) 2.01-2.11(m ,4H), 3.50-3.71(m,2H), 3.94-4.17 (m,2H), 4.28(br,1H), 4.44 (br,1H), 5.83-5.89(m,1H), 7.60-7.70 (m,1H), ^{31}P NMR(162MHz,D₂O): δ -22.05,-22.44 (br ,1P,), -10.34(br, 2P) HRMS: Calcd for C₁₁H₁₇N₃O₁₃P₃ 499.9969 Found 499.9918

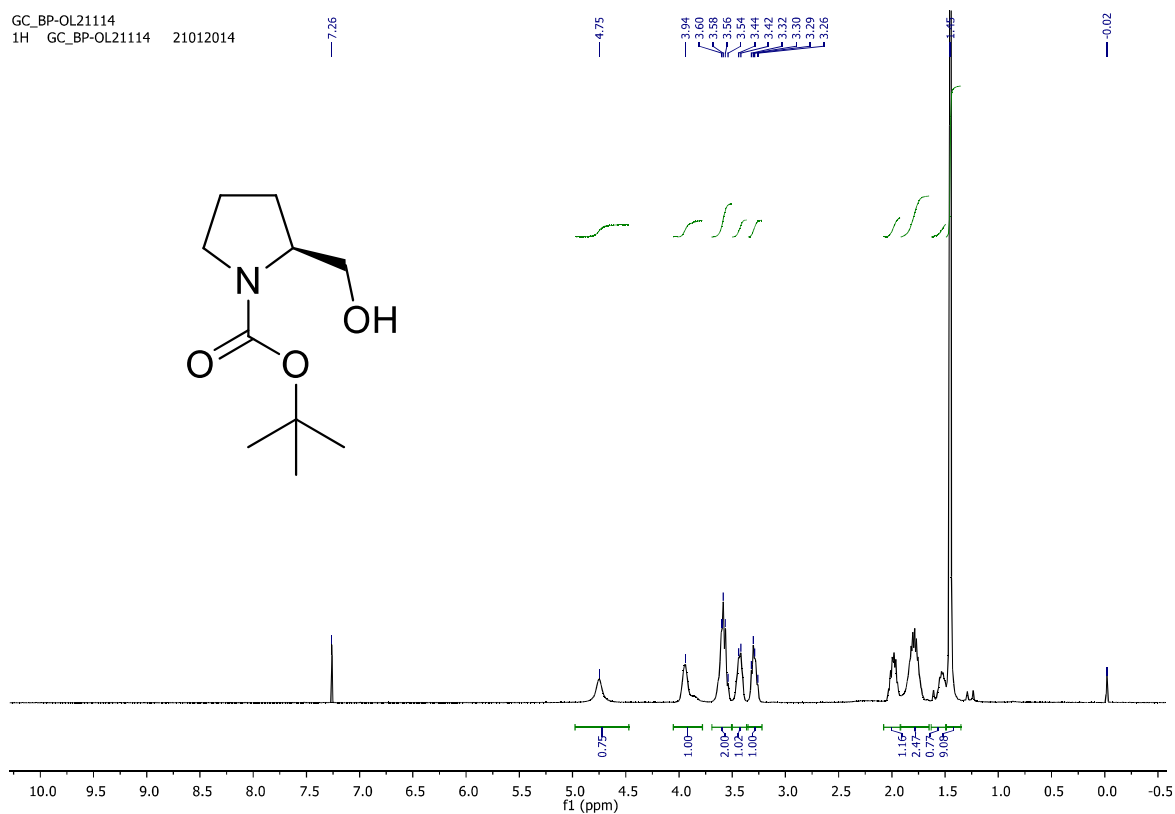
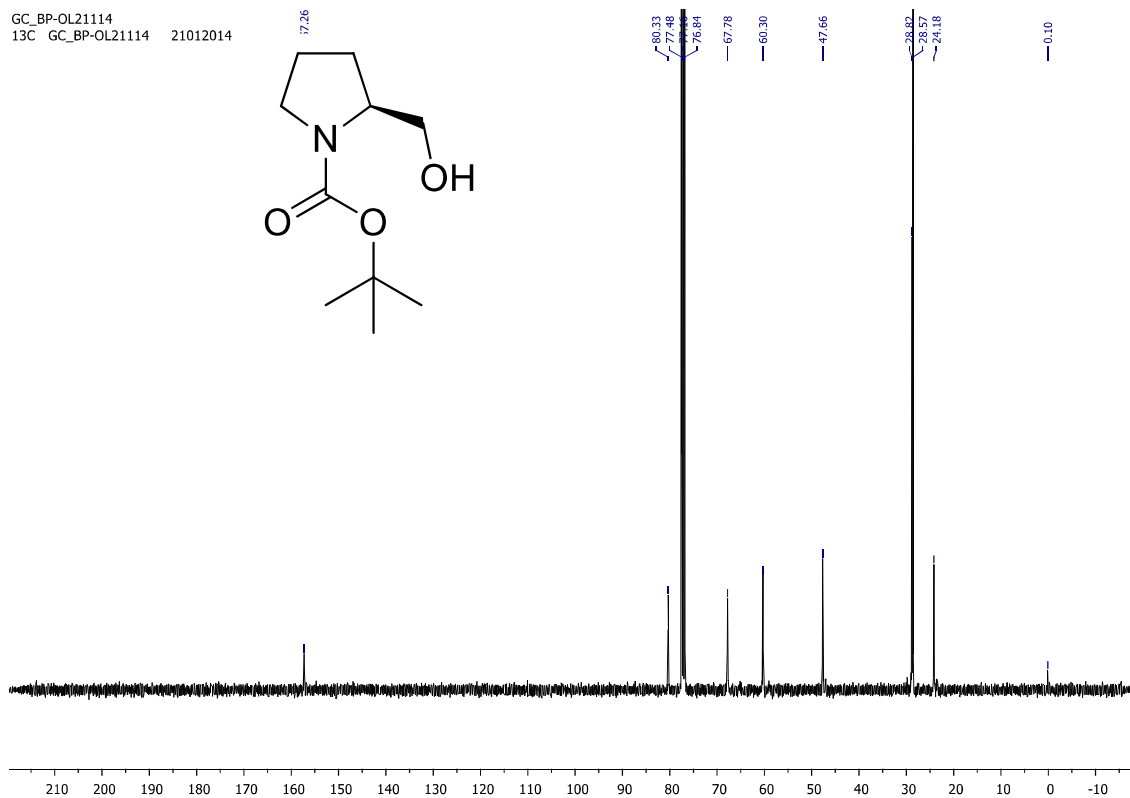
3B.5 Refferences

- (1) Sanger, F.; Nicklen, S.; Coulson, A. R. *Proc Natl Acad Sci U S A* **1977**, *74*, 5463.
- (2) Martinez, C. I.; Ali Ansari, M.; Gibbs, R.; Burgess, K. *Bioorg Med Chem Lett* **1997**, *7*, 3013.
- (3) Martinez, C. I.; Thoresen, L. H.; Burgess, K.; Gibbs, R. A. *Nucleic Acids Research* **1999**, *27*, 1271.
- (4) Vilaivan, T. *Acc. Chem. Res.* **2015**, *48*, 1645.
- (5) Kumar, V. A.; Ganesh, K. N. *Acc Chem Res* **2005**, *38*, 404.
- (6) Efimov, V. A.; Klykov, V. N.; Chakhmakhcheva, O. G. *Nucleosides, Nucleotides, and Nucleic Acids* **2007**, *26*, 1595.
- (7) Gade, C. R.; Dixit, M.; Sharma, N. K. *Bioorg.Med.Chem.* **2016**, *24*, 4016.

-
- (8) Gangamani, B. P.; Kumar, V. A.; Ganesh, K. N. *Tetrahedron* **1996**, *52*, 15017.
- (9) Gangamani, B. P.; Kumar, V. A.; Ganesh, K. N. *Tetrahedron* **1999**, *55*, 177.
- (10) Gangamani, B. P.; Decosta, M.; Kumar, V. A.; Ganesh, K. N. *Nucleosides and Nucleotides* **1999**, *18*, 1409.
- (11) Farrera-Sinfreu, J.; Avino, A.; Navarro, I.; Aymamí, J.; Beteta, N. G.; Varon, S.; Pérez-Tomás, R.; Castillo-Avila, W.; Eritja, R.; Albericio, F. *Bioorg. Med. Chem. Lett.* **2008**, *18*, 2440.
- (12) Ceulemans, G.; Van Aerschot, A.; Wroblowski, B.; Rozenski, J.; Hendrix, C.; Herdewijn, P. *Chem. Eur. J.* **1997**, *3*.
- (13) Efimov, V.; Aralov, A.; Chakhmakhcheva, O. *Russ. J. Bioorg. Chem.* **2010**, *36*, 663.
- (14) Ceulemans, G.; Van Aerschot, A.; Rozenski, J.; Herdewijn, P. *Tetrahedron* **1997**, *53*, 14957.
- (15) Yashima, E.; Ousaka, N.; Taura, D.; Shimomura, K.; Ikai, T.; Maeda, K. *Chem. Rev* **2016**, *116*, 13752.
- (16) Pauling, L.; Corey, R. B.; Branson, H. R. *Proc. Natl. Acad. Sci. U. S. A* **1951**, *37*, 205.
- (17) Watson, J. D.; Crick, F. H. *Nature* **1953**, *171*, 737.
- (18) Yashima, E.; Maeda, K.; Iida, H.; Furusho, Y.; Nagai, K. *Chem. Rev* **2009**, *109*, 6102.
- (19) Atwood, J. L.; Steed, J. W. *Encyclopedia of supramolecular chemistry*; CRC Press, 2004; Vol. 1.
- (20) Hill, D. J.; Mio, M. J.; Prince, R. B.; Hughes, T. S.; Moore, J. S. *Chem. Rev.* **2001**, *101*, 3893.
-

-
- (21) Gellman, S. H. *Acc.Chem.Res.* **1998**, *31*, 173.
- (22) Hecht, S.; Huc, I. *Foldamers: structure, properties and applications*; John Wiley & Sons, 2007.
- (23) Choi, J.; Majima, T. *Chem.Soc. Rev.* **2011**, *40*, 5893.
- (24) Zhao, H.; Guo, X.; He, S.; Zeng, X.; Zhou, X.; Zhang, C.; Hu, J.; Wu, X.; Xing, Z.; Chu, L. *Nat. Commun.* **2014**, *5*.
- (25) Pedireddi, V.; Ranganathan, A.; Ganesh, K. N. *Org. Lett* **2001**, *3*, 99.
- (26) Sanjayan, G. J.; Pedireddi, V.; Ganesh, K. N. *Org. Lett.* **2000**, *2*, 2825.
- (27) Chakraborty, S.; Sharma, S.; Maiti, P. K.; Krishnan, Y. *Nucleic Acids Res.* **2009**, *37*, 2810.
- (28) Saha, S.; Bhatia, D.; Krishnan, Y. *small* **2010**, *6*, 1288.
- (29) Verma, S.; Mishra, A. K.; Kumar, J. *Acc.Chem. Res.* **2009**, *43*, 79.
- (30) Davis, J. T.; Spada, G. P. *Chem.Soc. Rev.* **2007**, *36*, 296.
- (31) Davis, J. T. *Angew. Chem. Int. Ed* **2004**, *43*, 668.
- (32) Perumalla, S. R.; Pedireddi, V. R.; Sun, C. C. *Cryst. Growth Des.* **2013**, *13*, 429.
- (33) Patwa, A. N.; Gonnade, R. G.; Kumar, V. A.; Bhadbhade, M. M.; Ganesh, K. N. *J.Org.Chem.* **2010**, *75*, 8705.
- (34) Patwa, A. N.; Gupta, S.; Gonnade, R. G.; Kumar, V. A.; Bhadbhade, M. M.; Ganesh, K. N. *J.Org.Chem.* **2008**, *73*, 1508.

3B.6 Appendix

GC_BP-OL21114
1H GC_BP-OL21114 21012014Figure A 1 ¹H NMR of compound 2GC_BP-OL21114
13C GC_BP-OL21114 21012014Figure A 2 ¹³C NMR of compound 2

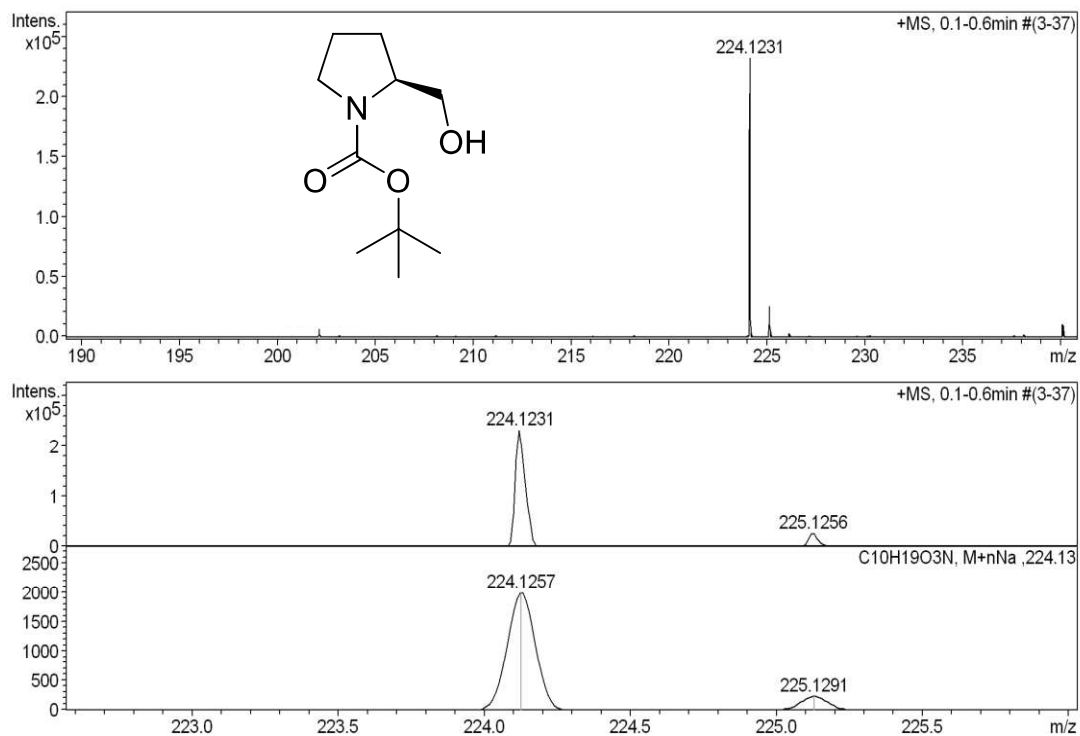
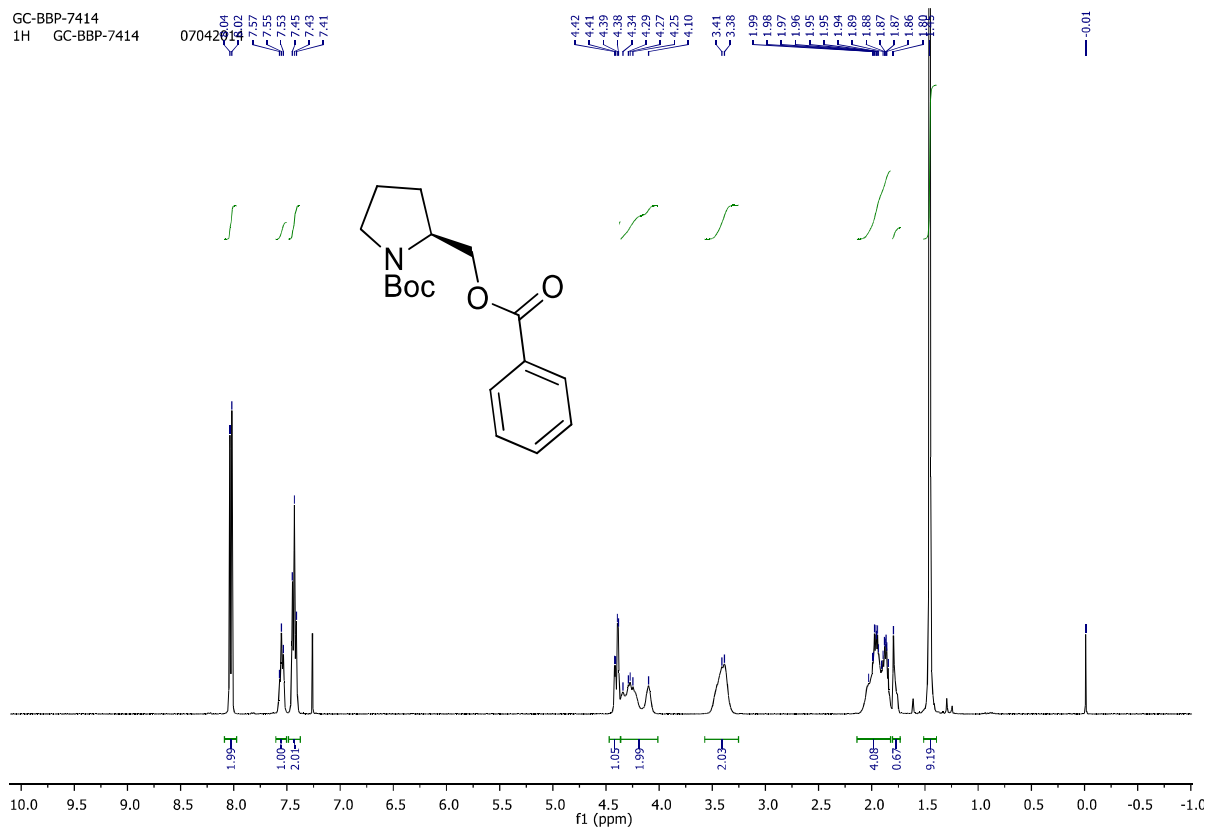


Figure A 3 HRMS of compound 2

Figure A 4 ¹H NMR of compound 3

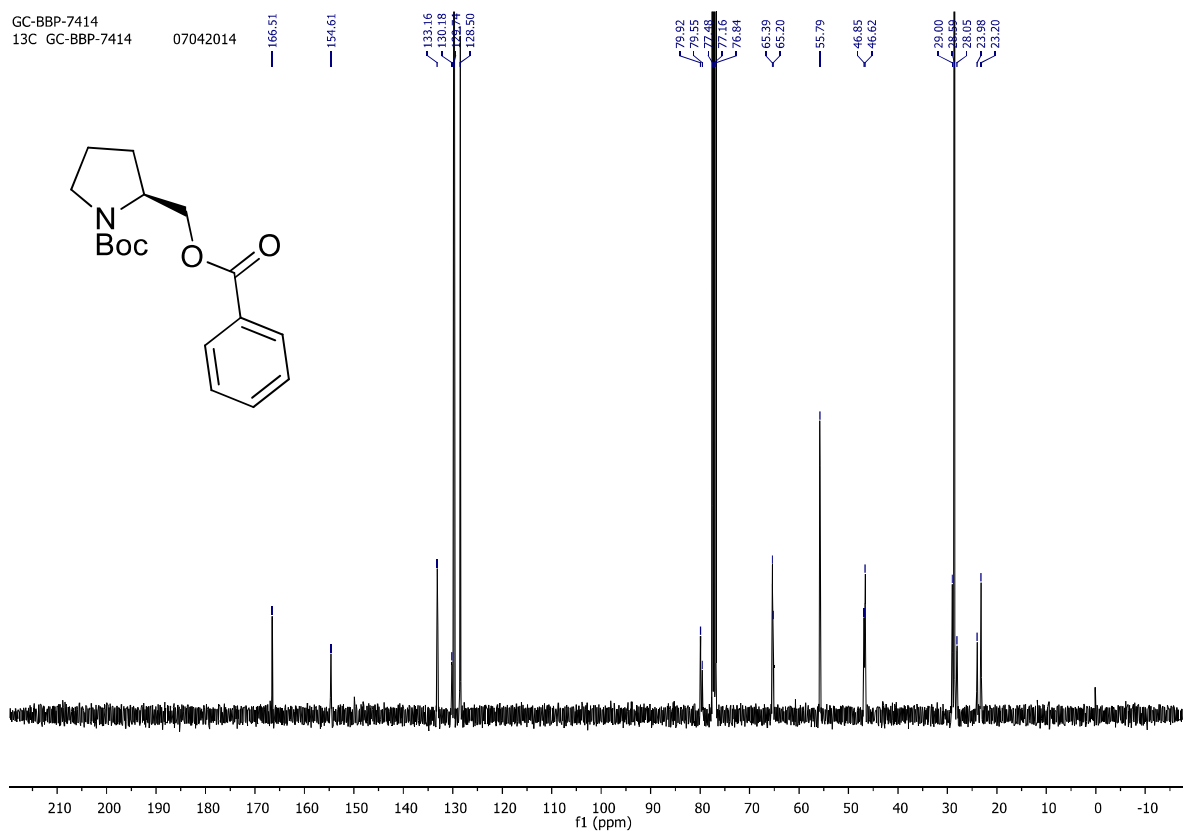
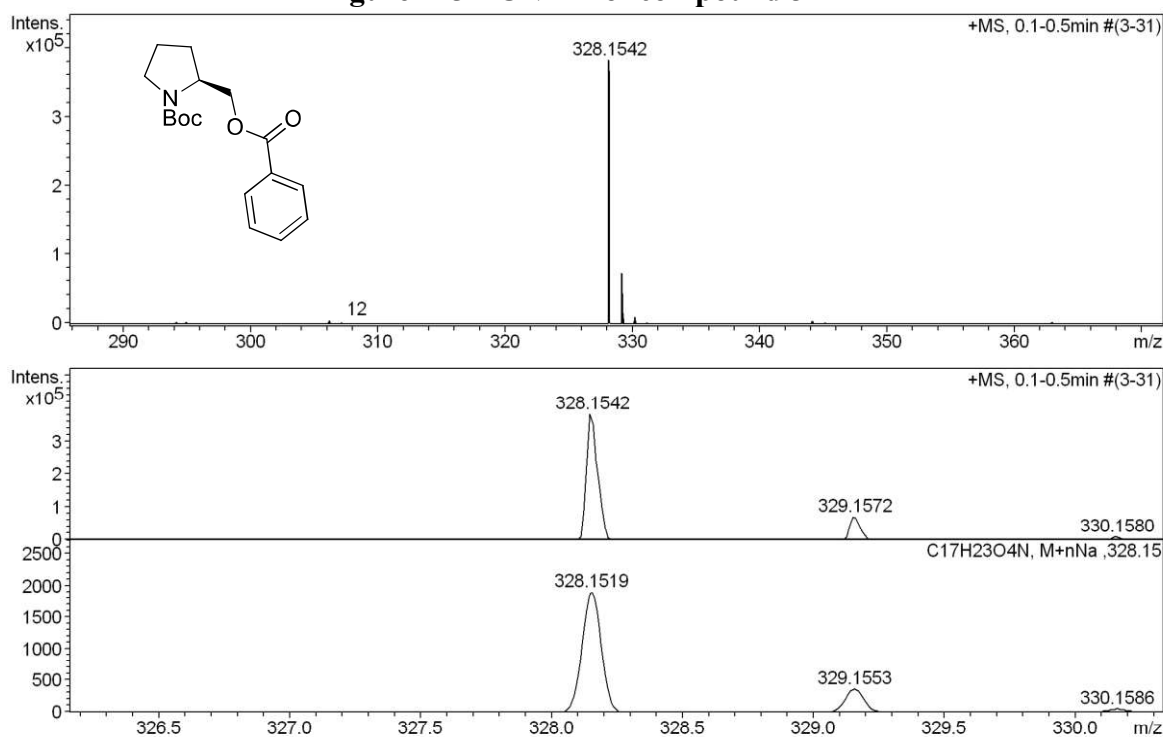
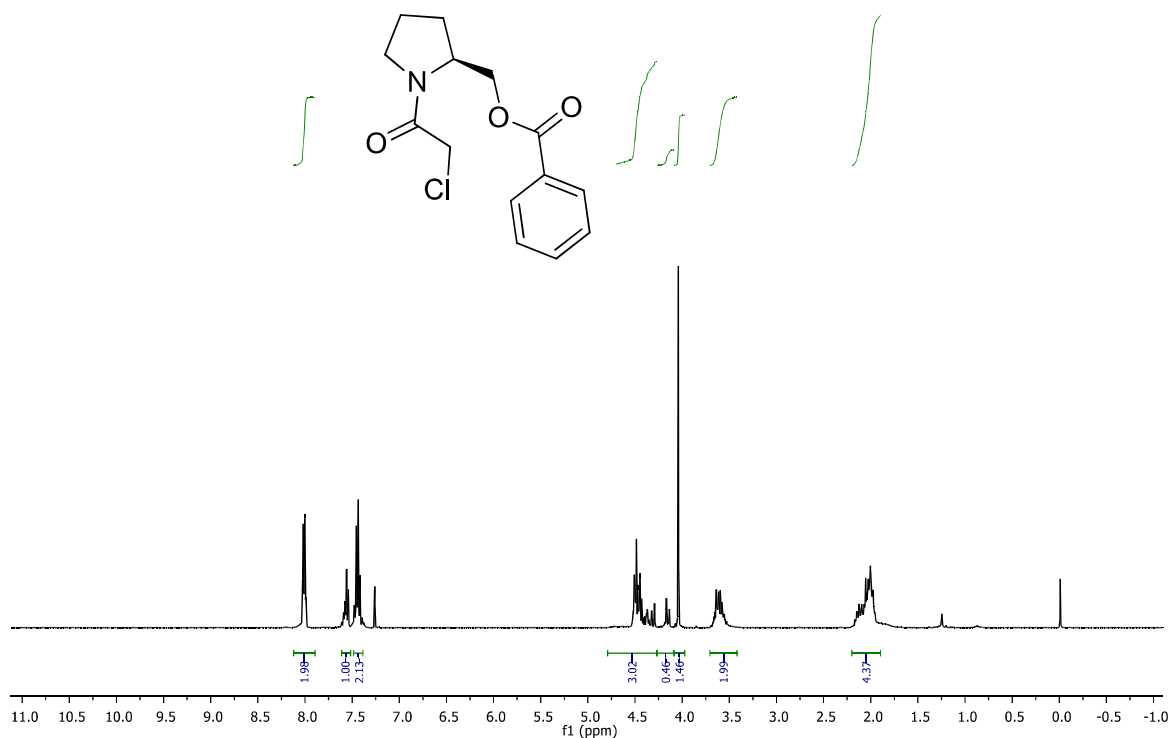
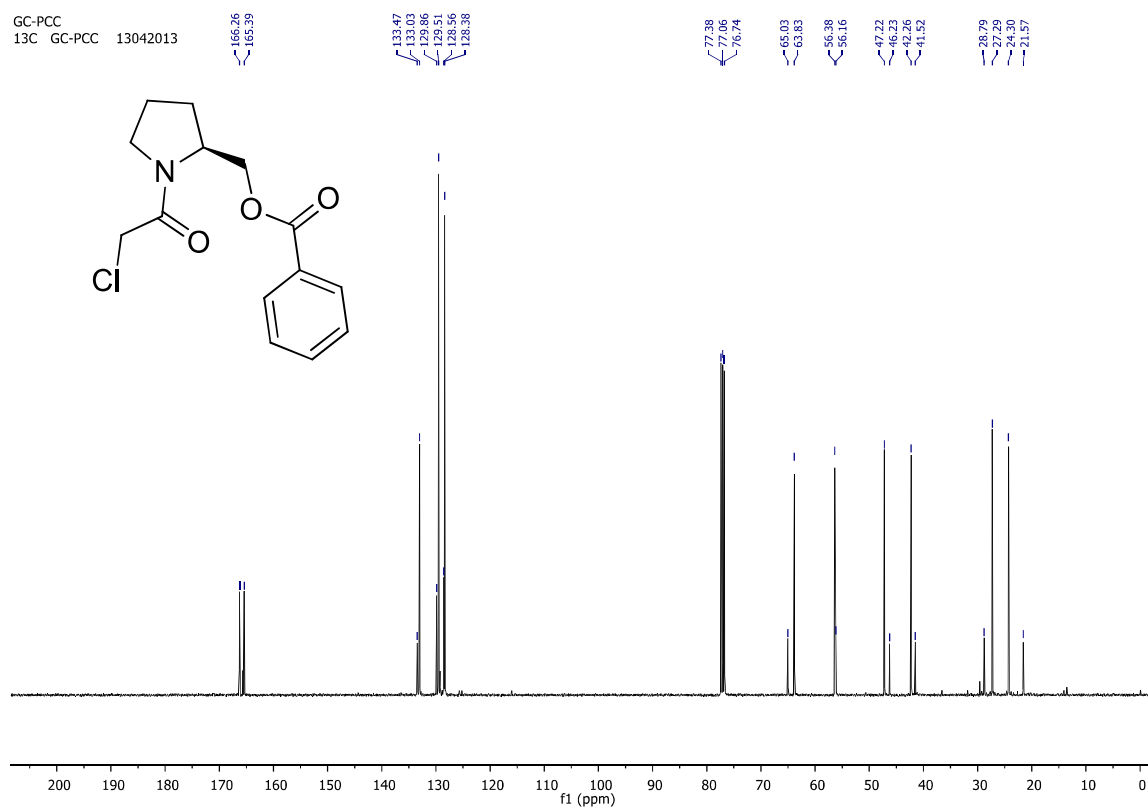
Figure A 5 ¹³CNMR of compound 3

Figure A 6 HRMS of compound 3

GC_PCC_21114
 1H GC_PCC_21114 21012014



GC-PCC
 13C GC-PCC 13042013



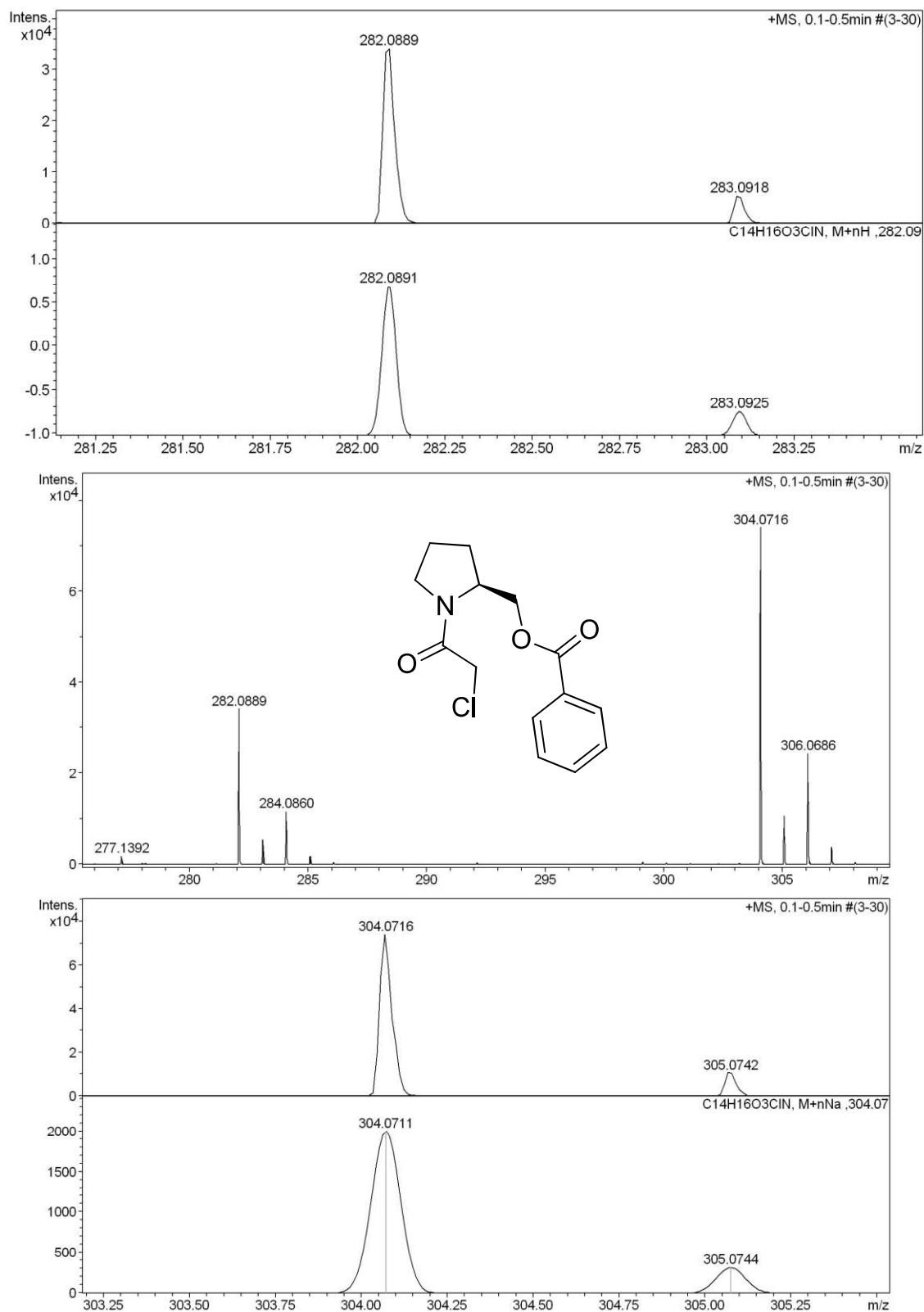
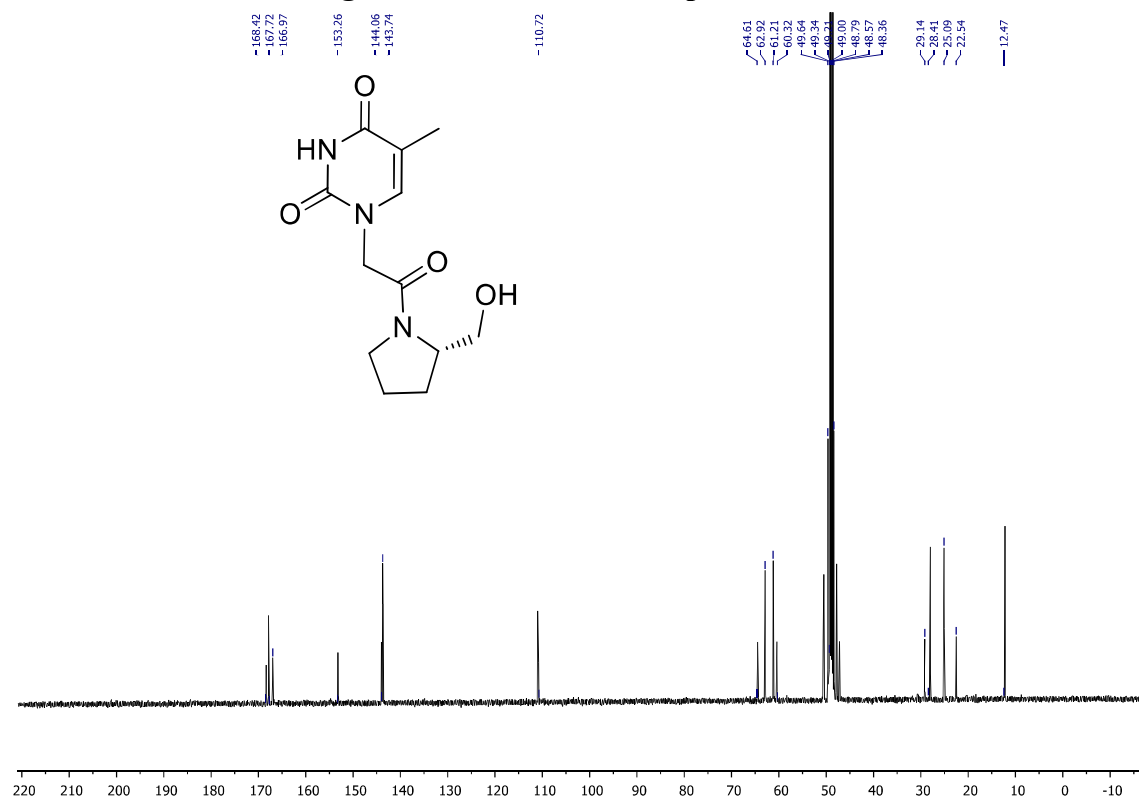
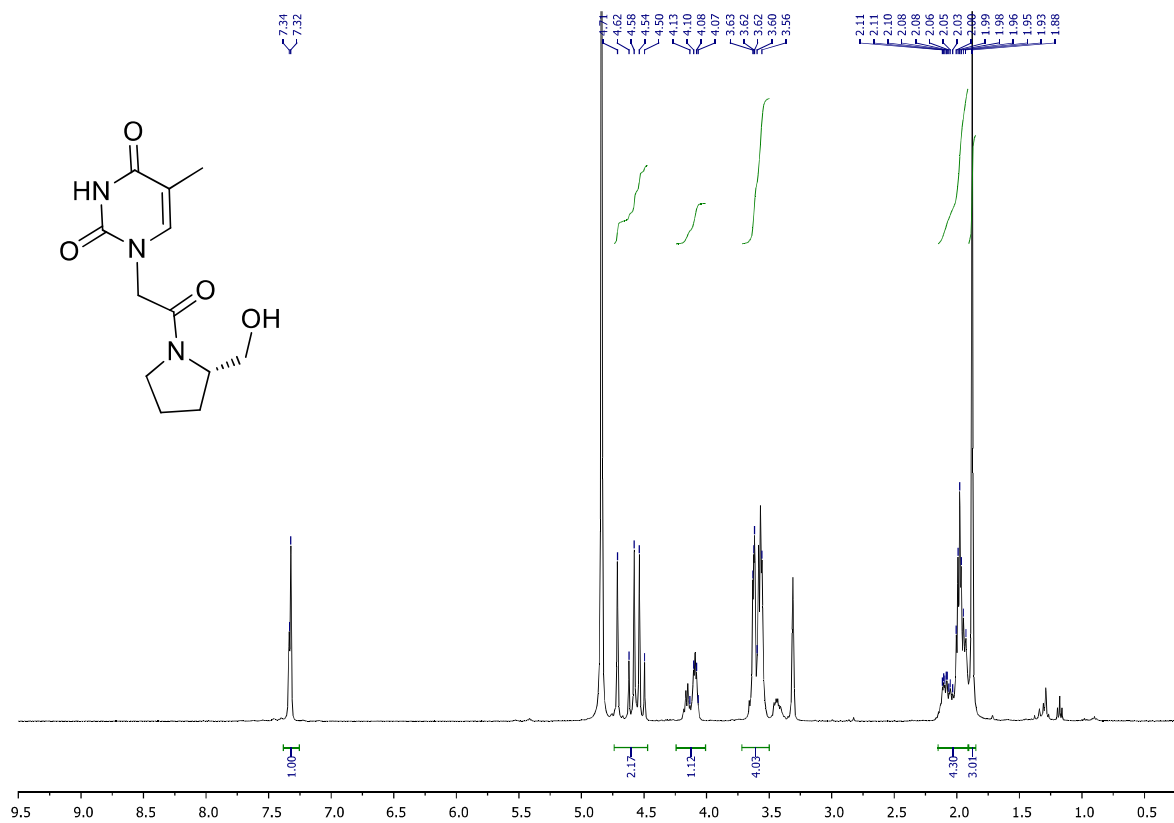


Figure A 8 HRMS of compound 4



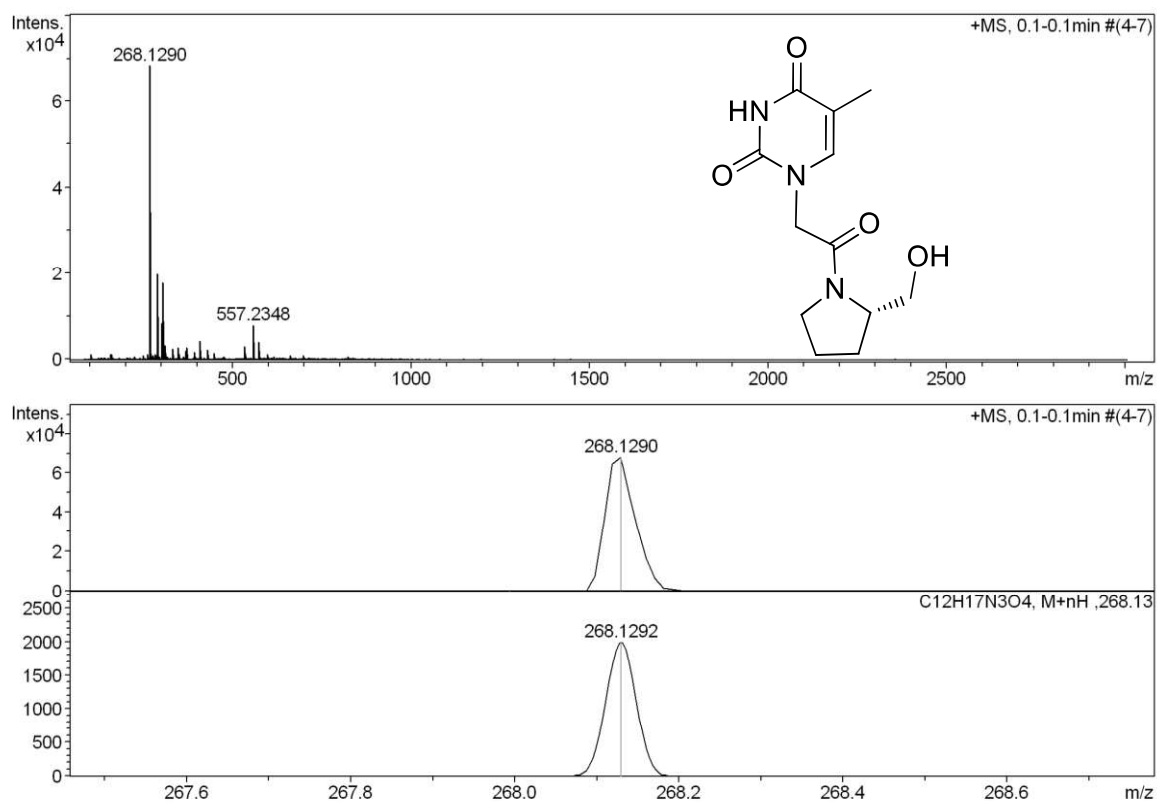
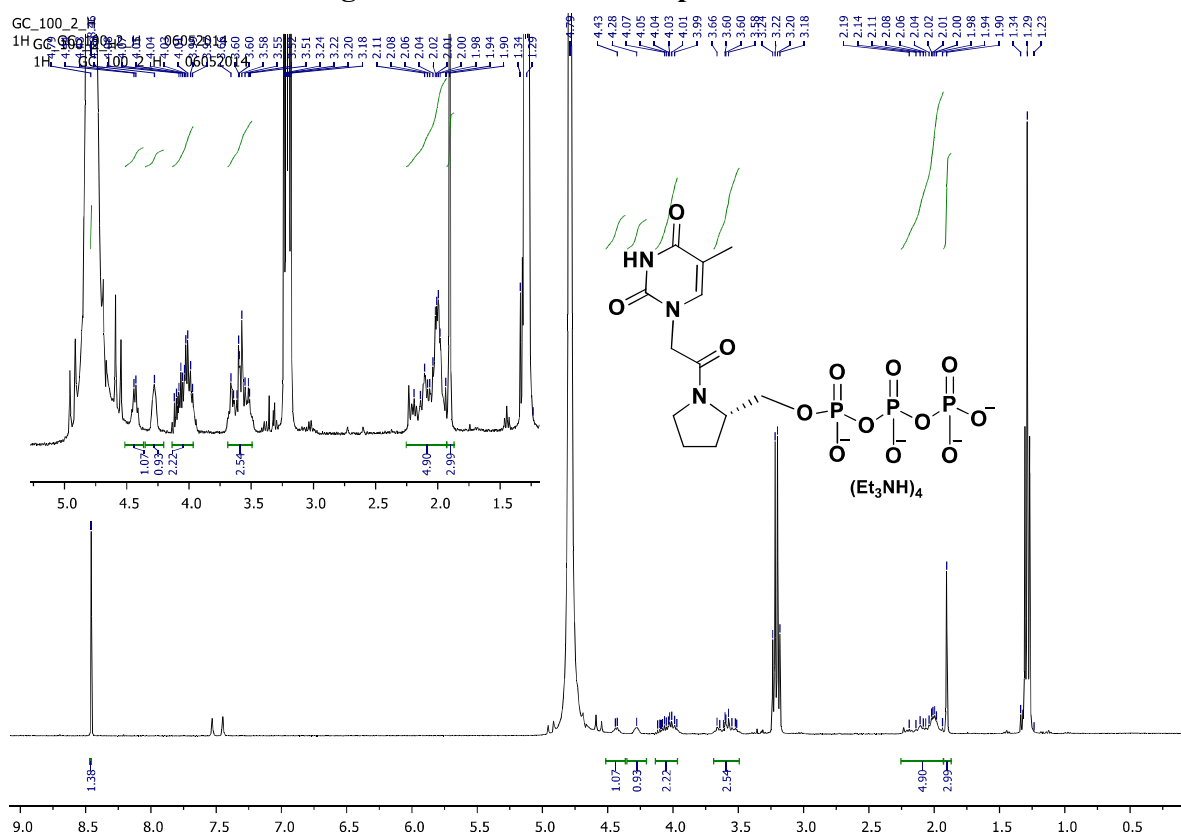


Figure A 11 HRMS of compound 5a

Figure A 12 ¹H NMR of compound 5a

GC_100_2_REF
31P GC_100_2 06052014

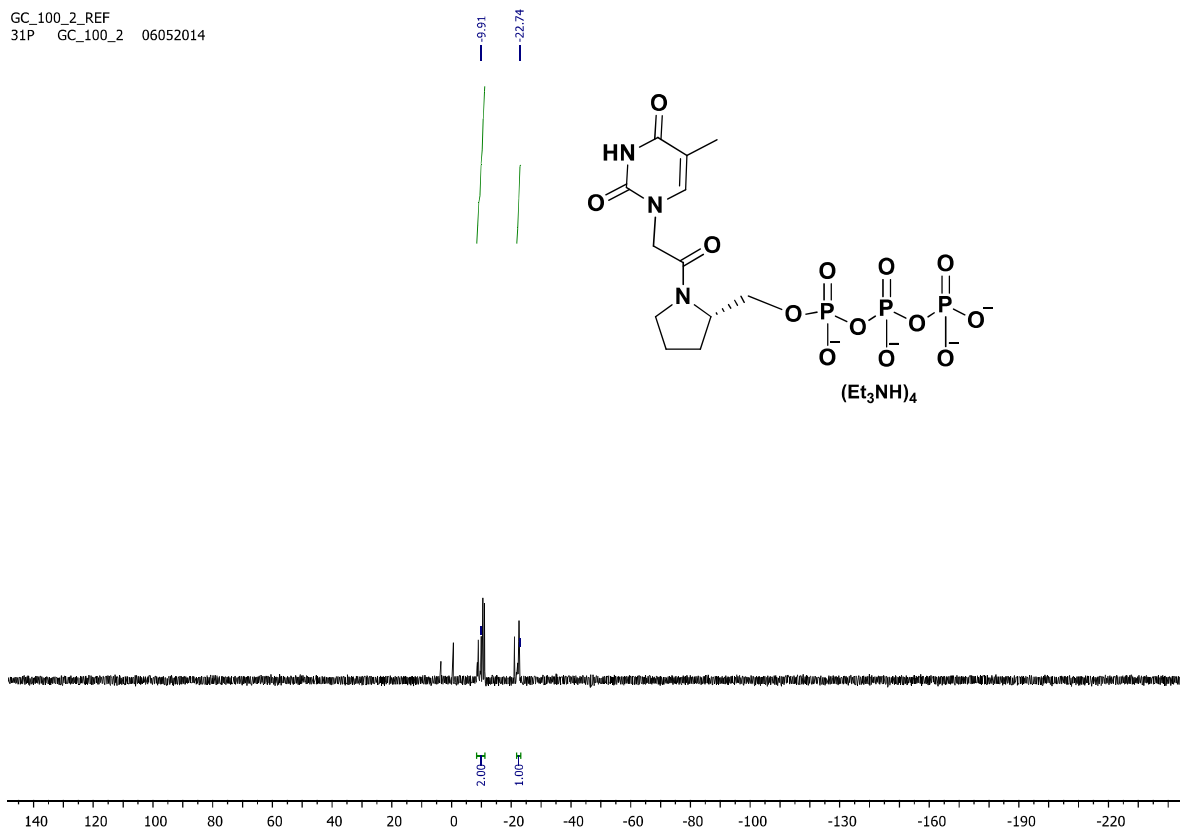


Figure A 13 ^{31}P NMR of compound 5a

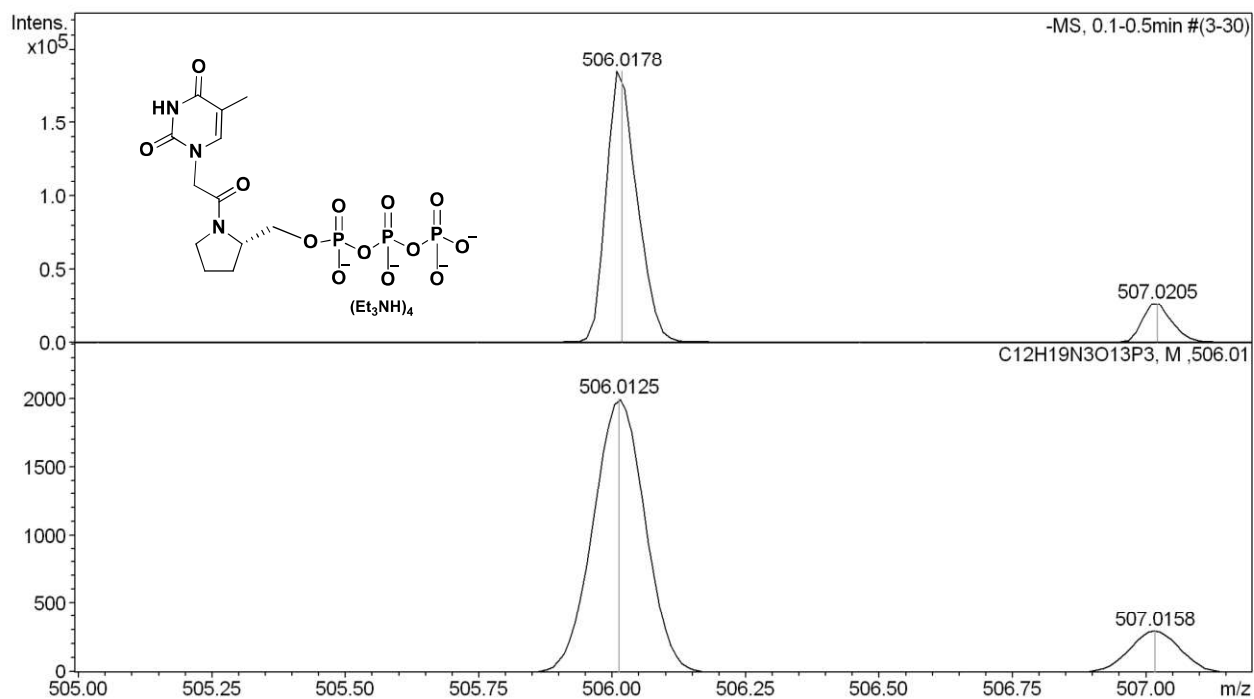
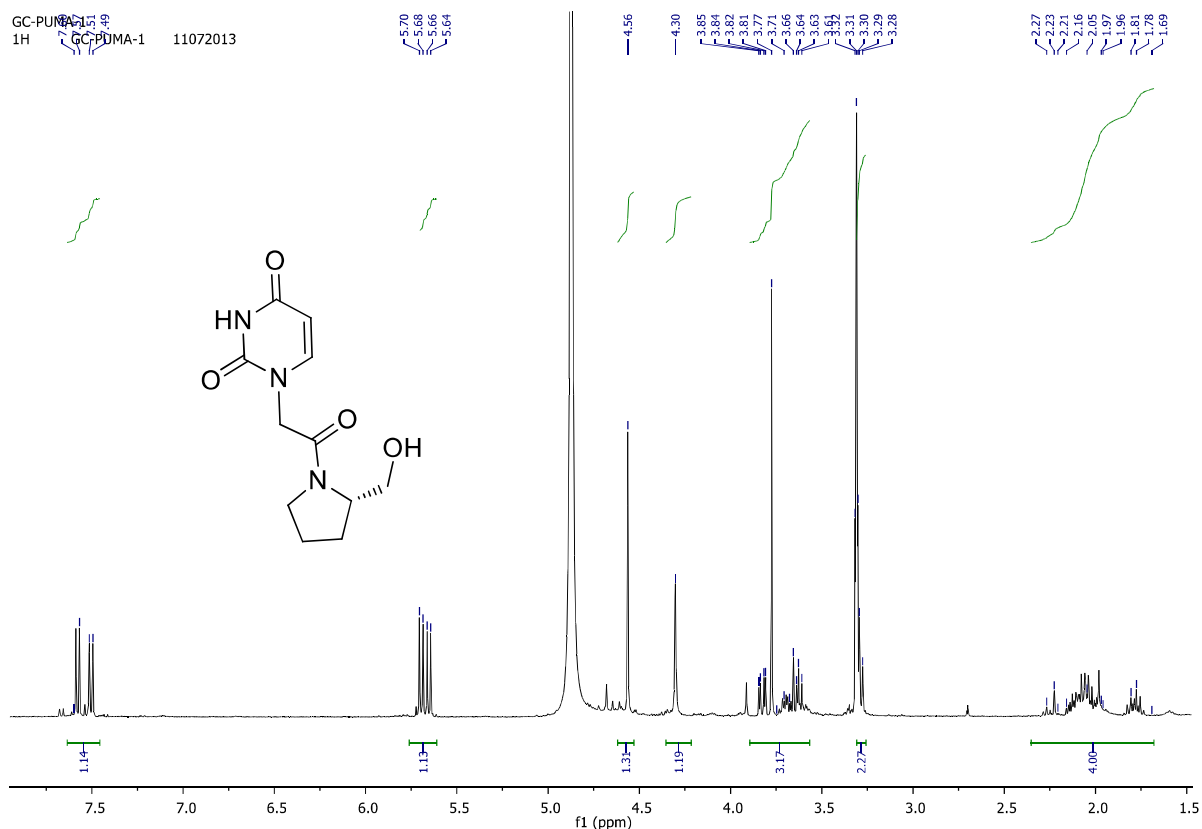
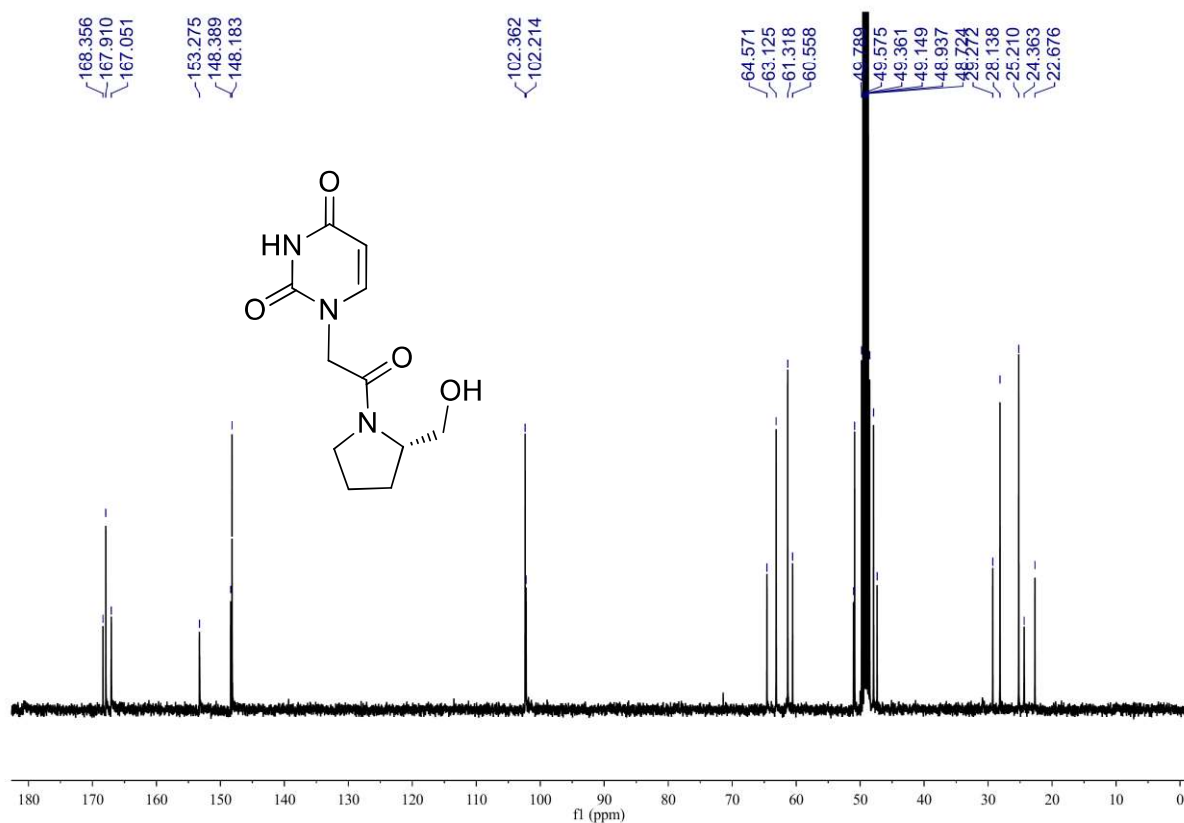


Figure A 14 HRMS of compound 5a

Figure A 15 ^1H NMR of compound 5bFigure A 16 ^{13}C NMR of compound 5b

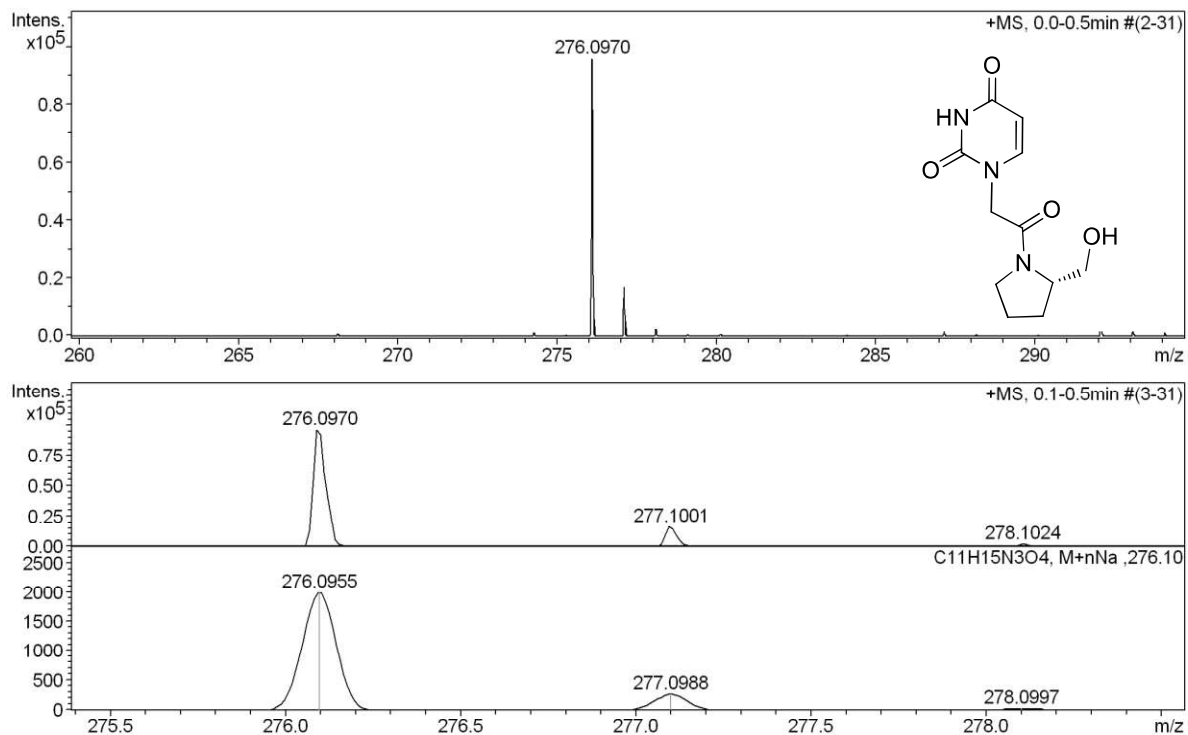
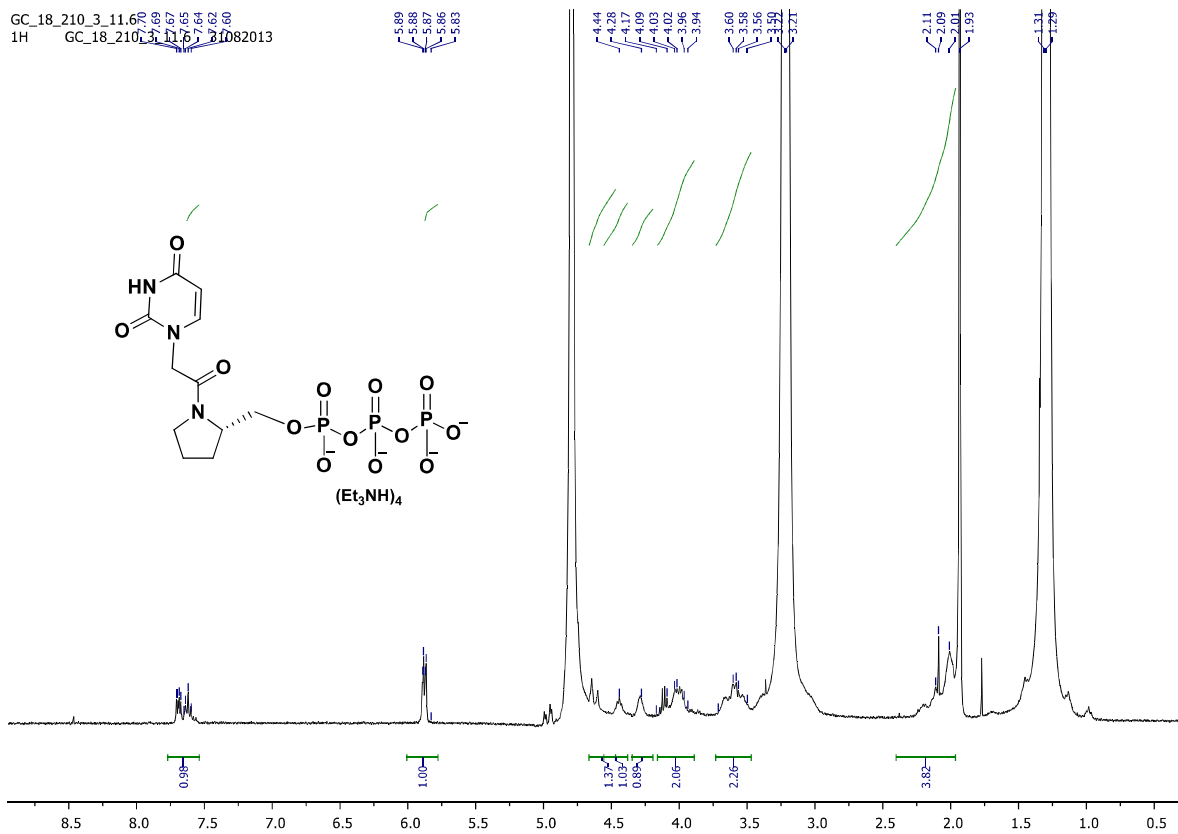


Figure A 17 HRMS of compound 5b

Figure A 18 ¹H NMR of compound 6b

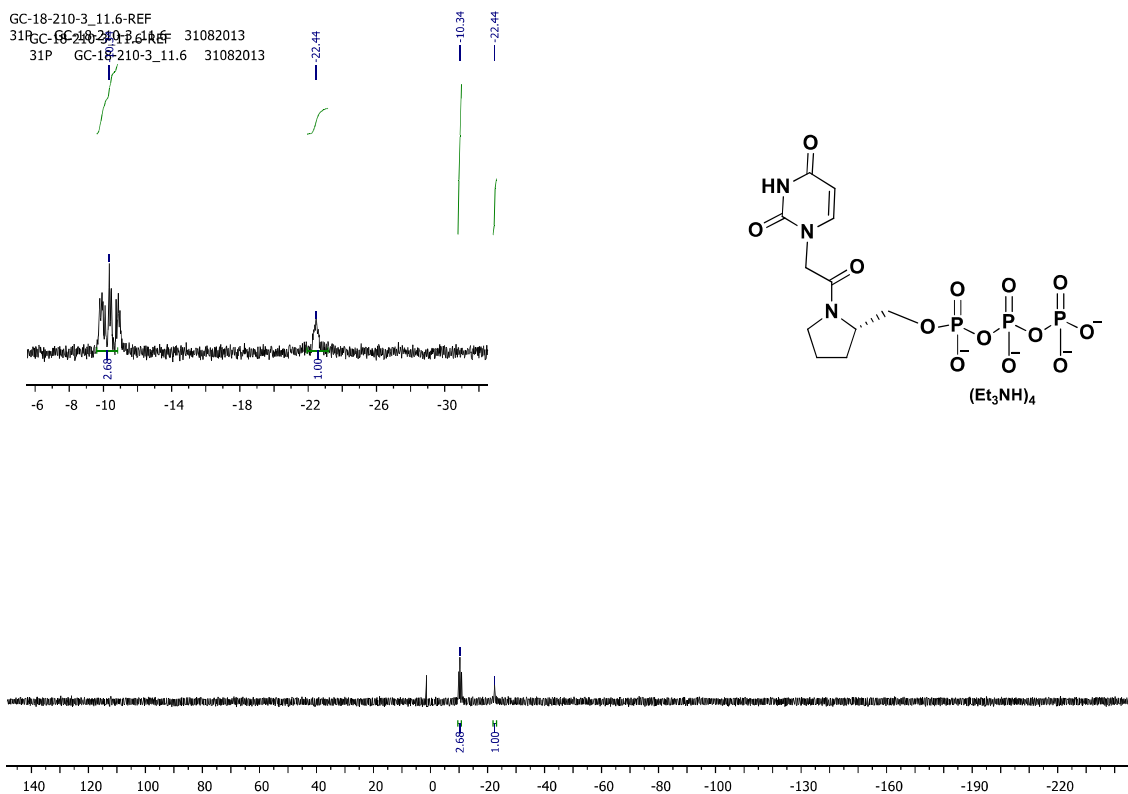
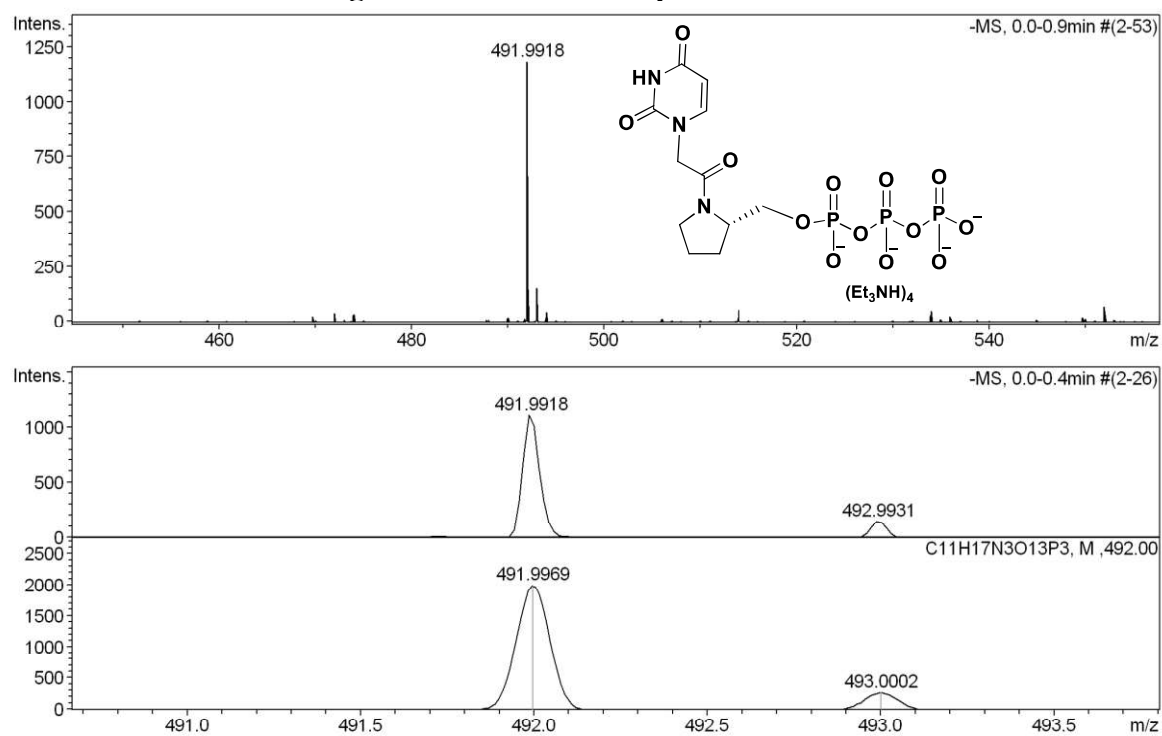
Fig S19 ³¹P NMR of compound 6b

Figure A 20 HRMS of compound 6b

Generic Display Report

Analysis Info

Analysis Name D:\Data\AUG2014\NKS\LCMS\1982014_NKS_GC_100-4_2-B,4_01_48.d

Acquisition Date 8/19/2014 7:03:38 PM

Method caffeine-no-uv.m

Operator RAJKUMAR

Sample Name 1982014_NKS_GC_100-4

Instrument

micrOTOF-Q II

Comment

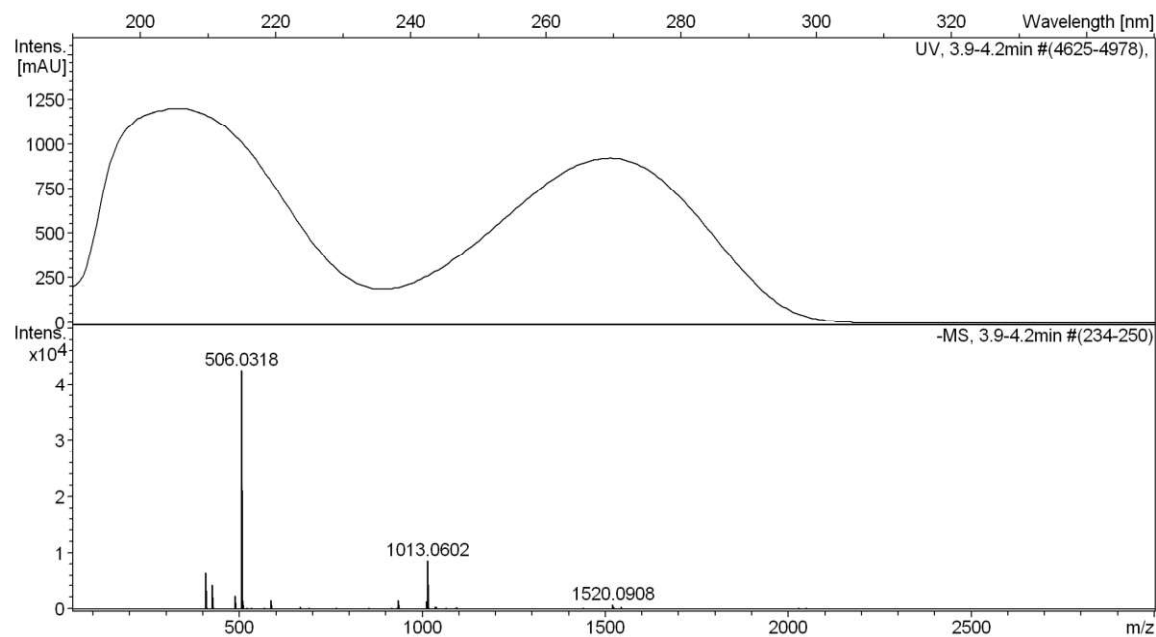
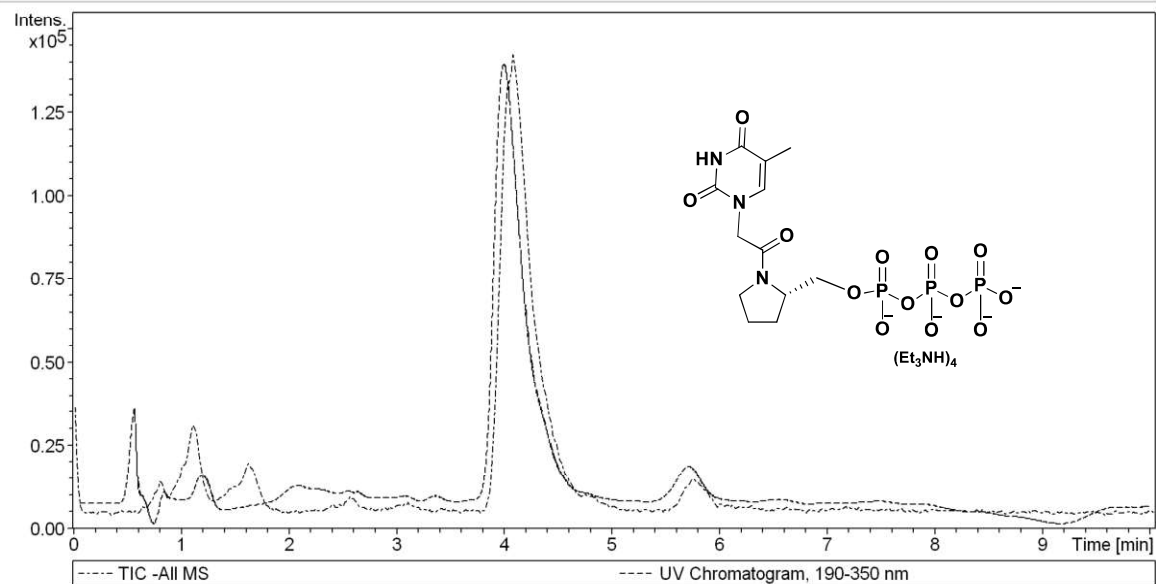


Figure A21 LC-MS of compound 6

Chapter 4

Au decoration on ZnO nanotapers for field emission applications

One-dimensional nanostructures with tailored morphology and desirable surface properties have gained attention owing to their nanoelectronic applications like flat panel displays, field effect transistors, solar cell applications. From device application perspective, cold-cathode electron field emitters have emerged as a potential candidate for next-generation electronic devices like electron microscopes, microwave amplifiers, field emission displays, x-ray sources [1–6]. For device fabrication, materials having high thermal stability and mechanical strength, low electron affinity and high oxidation resistivity properties all together are desired. In this prospect, ZnO has been considered as a suitable candidate. Several studies on field emission behavior of various ZnO nanostructures including nanowires [7], nanoneedles, nanocavities, bottle shaped [8], branched nanowires [9], and nanowires on carbon cloths [11] have been carried out. However, a better control over the vertical alignment of nanostructures, and difficulties in achieving high emission current density with low turn-on field and long stability are the bottleneck for fabricating field emission based devices.

The field emission (FE) characteristics of materials are explained by the Fowler-Nordheim (FN) theory, which describes that both the field enhancement factor (β) and work function (Φ) of the material strongly affect their FE characteristics. The factor β is defined as the ratio of local electric field to the applied electric field, in which the local field is directly associated with the geometry of the emitter and is 1 for flat surface whereas large for tip kind geometries. The Φ associated with the electronic structure of the material can be tuned by modifying the electronic structure. Except for the modifications made in the architecture of ZnO nanostructures as mentioned in above paragraph, several attempts have been taken to modify the electronic struc-

ture of ZnO nanostructures using various methods like hydrogen plasma treatment [12], n-type doping [13], annealing in different ambiances [14], coating them with noble metal nanoparticles like Au, Pt [15, 16]. Among all the adopted methods, the coating of metallic nanoparticles on the surface of ZnO is widely accepted because in metal-semiconductor junctions, the interface formed between metallic nanoparticles and ZnO may modify the electronic structure in two possible ways: Thermal equilibrium of Fermi levels of both the metallic nanoparticles and ZnO, or metal-induced midgap states at the interface of metal-ZnO. The relatively low-temperature growth of ZnO nanostructures may induce near-surface defect states like oxygen vacancies (V_O), Zinc interstitial (Zn_i) [17–19], depending on growth conditions, and the presence of such surface states can be more suitable environment for the formation of metal-induced midgap states than the alignment of Fermi levels at the interface. Such midgap states are likely to play a significant role in modifying the electronic structure at the surface and may change the Φ of ZnO. In this chapter, the influence of corrugated Au decoration induced midgap states (at Au-ZnO interface) on the work-function of ZnO nanotapers is studied using Kelvin probe force microscopy. This decoration of Au on the surface of ZnO introduces extended defects at Au-ZnO interface, which may play an important role to change the electronic properties. The obtained results showed that as a consequence of the reduction in work-function as a function of the thickness of Au, the field emission characteristics of Au decorated nanotapers is significantly enhanced.

4.1 Methodology and growth of ZnO nanotapers

For this study, ZnO nanotapers were grown using standard aqueous growth method [20]. The aqueous solution of precursors zinc nitrate and hexamethylenetetramine (HMT) was prepared in a molar ratio of 1:1. After filling the aqueous solution in glass bottles, substrates placed on a glass slide, were dipped into the solution in a lateral way as shown in figure 4.1, followed by subsequent placing of bottles into the preheated water bath (at 90°C) in a laboratory oven for three different durations 1, 3 and 6 hours. The nanotapers grown for 1hour duration were of very short length, whereas for 6 hours duration the nanotapers tend to attain the nanorod architecture. The samples grown for 3hours were of tip geometry, as shown in next section and are used in this thesis work. The Si (100, p-type) substrates were coated with a thin seed layer of ZnO film ($\sim 30\text{nm}$) using pulsed DC magnetron sputtering system, which effectively lowers

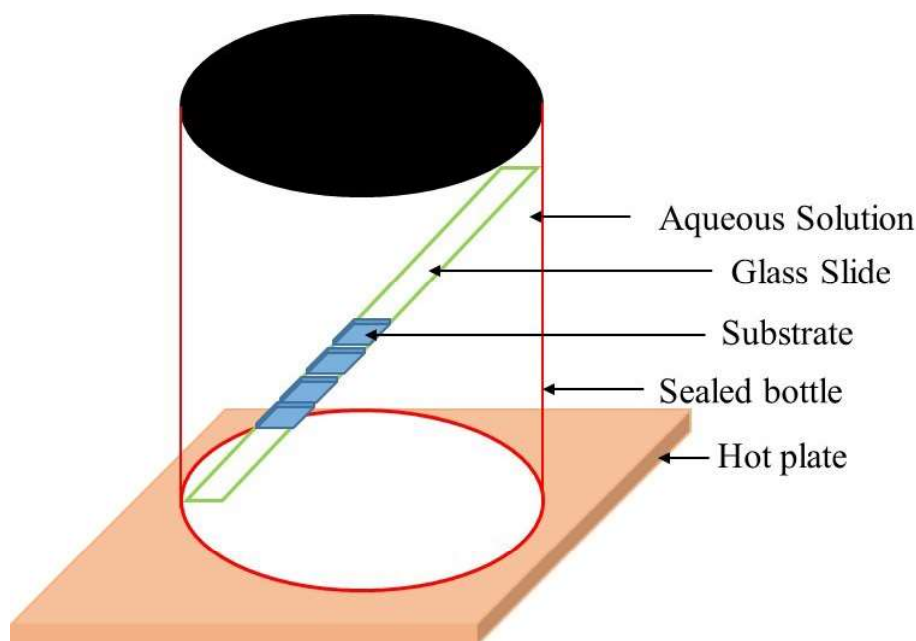


Figure 4.1: A schematic for the sample preparation unit.

the interface energy between ZnO nucleation points and substrates, and initiates vertical growth of nanopapers of smaller diameter [21]. Here it is worthwhile to mention that the pre-heating of water bath provides sufficient thermal energy for the crystallization in the reaction medium, and initiates the growth of ZnO as well. During nucleation, the HMT a non-polar chelating agent attaches to the non-polar facets of initially grown crystalline ZnO and initiates the growth along (0001) direction. With increasing the growth duration, the epitaxial growth of crystalline ZnO leads to vertically aligned ZnO nanopapers. Post-growth, samples were rinsed with de-ionized water to remove residuals. The corrugated Au films of five different thickness of $\sim 1, 2, 3, 4$ and 5 nm were coated on nanopapers using electron beam evaporation technique, in a vacuum chamber while maintaining the base pressure at 2×10^{-7} mbar. The KPFM and field emission characteristics were studied on some selective samples: as-grown, 3 and 5 nm Au decorated.

4.2 Morphological and structural studies

4.2.1 SEM and XRD study

Figure 4.2 (a, b) depict the cross-sectional FESEM images (tilted at 10°) of nanopapers decorated with Au of two different thickness of 3 and 5 nm, respectively. The inset of figure 4.2 shows top view of as-grown nanopapers. In both of these samples, bright spots on nanopapers are observed, which indicate that Au is coated on nanopapers in the form of the islands. The

uneven surface of samples as seen in FESEM images and substrate rotation (20 rpm) drove the formation of Au islands on all faces of nanotapers. For confirming the presence of Au on

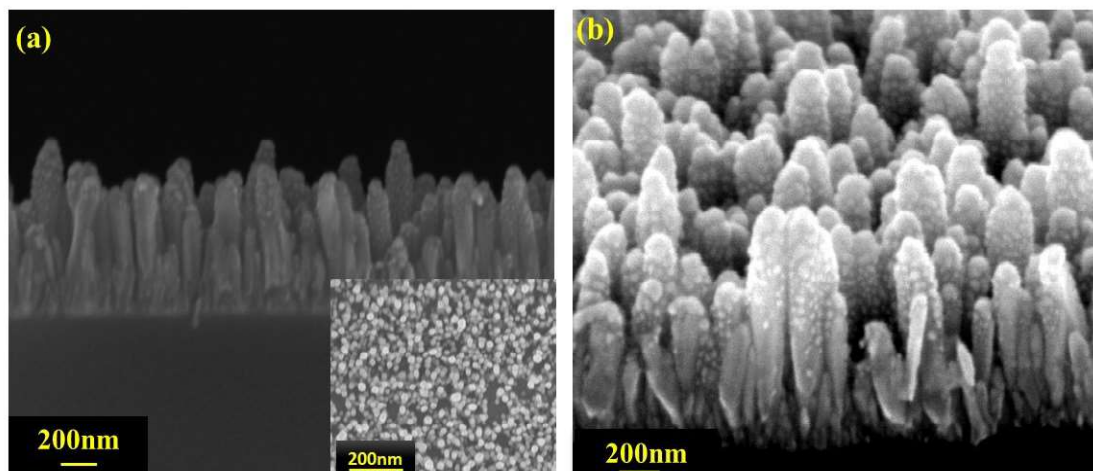


Figure 4.2: Cross-sectional FESEM images of nanotapers decorated with Au of thickness (a) 3 nm and (b) 5 nm. The inset of (a) shows top view FESEM micrograph of as-grown ZnO nanotapers.

ZnO nanotapers, the EDX spectroscopy was employed on both the 3 and 5 nm Au decorated samples. The appearance of Au signal along with the Zn and O signals in the EDX spectra of both samples indicates the decoration of Au on nanotapers. As an evidence the EDX spectrum recorded from 3 nm Au coated sample is shown in figure 4.3 (a). The structural characterization of nanotapers was carried out using synchrotron radiation based X-ray diffraction (XRD) technique of wavelength 0.8293 \AA . The XRD patterns of as-grown and Au-coated (3 & 5nm) nanotapers are shown in figure 4.3 (b), where the (002) Bragg diffracted peaks of ZnO dominate over (101) peaks. The dominating (002) Bragg peak indicates the preferential orientation of nanotapers along the c-axis, initiated by the minimum surface free energy along (002) and are parallel to the basal plane of Si substrate. We notice that in XRD patterns of Au decorated samples, an additional peak is apparent between the 38 to 40 2θ values, which is associated with the (111) plane of Au. The appearance of Au signal further confirms our FESEM and EDX results.

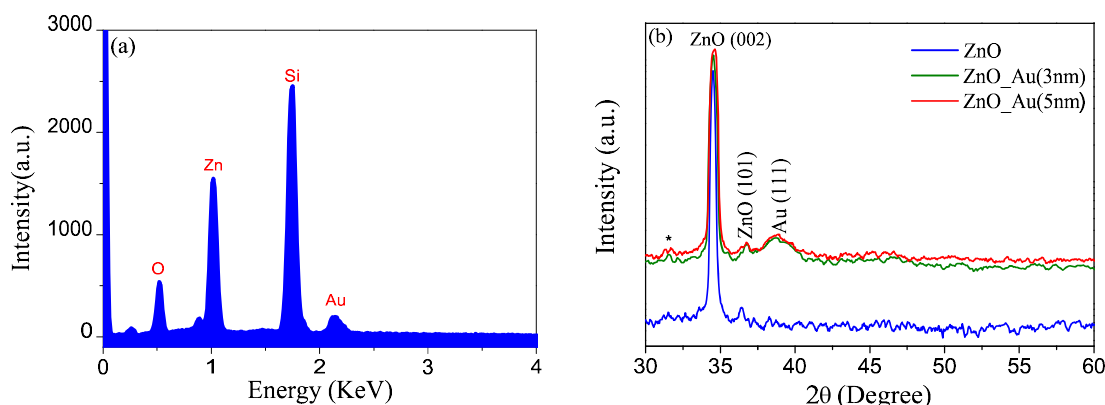


Figure 4.3: EDX spectrum acquired from 3 nm Au coated ZnO nanotapers (a) and X-ray diffraction patterns of as-grown and Au coated nanotapers.

4.2.2 TEM study

Figure 4.4 (a) shows annular dark field (ADF) STEM image of ZnO nanotaper decorated with 5nm Au, where the difference in color contrast confirms the presence of Au particles on the surface of nanotaper. In order to investigate the local electronic structure the EELS measurements were performed across the Au-ZnO interface (green line shown in STEM image) and the obtained results are shown in figure 4.4 (b).

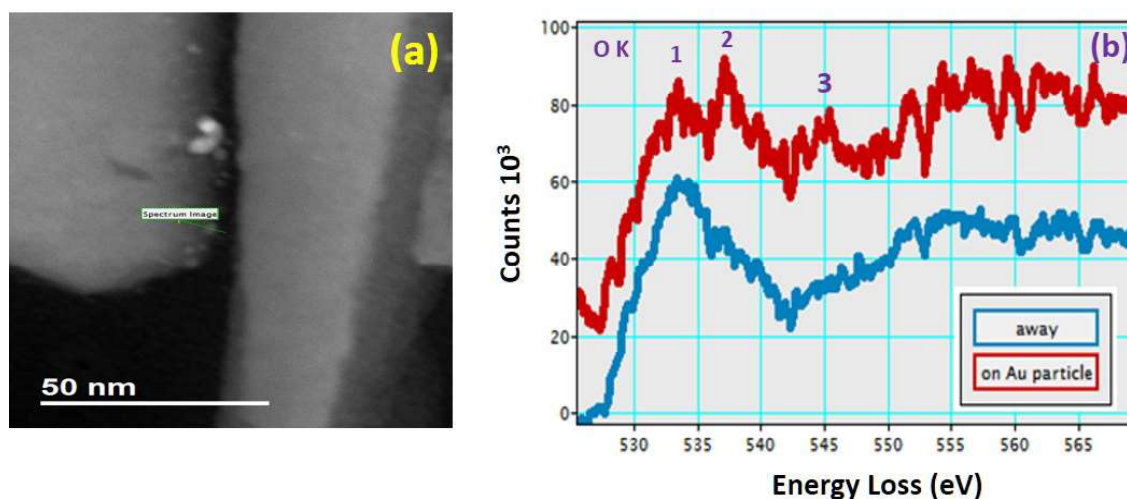


Figure 4.4: (a) ADF STEM image of 5nm Au decorated ZnO nanotapers. The Au particles on the surface can be easily seen. (b) O-K edge EELS spectra extracted across the Au-ZnO interface and away along the green line as shown in panel (a).

Significant changes in EELS spectra are observed, in particular the peaks marked as 2 and 3

are much more defined than those in the spectrum recorded on the ZnO surface away from the Au particles. Dileep et al. showed that the typical O-K edge EELS peak appearing at 535eV (labeled as 1) is associated with the transition from p unoccupied levels of O hybridized with 4s levels of Zn [22]. The additional peaks at 537eV and 545eV (labeled as 2 and 3) appearing in EELS spectrum of Au-ZnO interface are associated with the $O_{i:oct}$ and $O_{i:tet}$ respectively [23]. The appearance of these additional peaks in EELS spectrum of Au-ZnO interface clearly indicate that Au decoration onto the surface of nanopapers modifies the surface states and Zn-O bonding, which can modify the optical and electrical properties of nanopapers.

4.2.3 X-ray absorption fine structure study

The X-ray absorption fine structure (XAFS) spectroscopy endow the local crystal environment of a material at the atomic scale, by measuring the X-ray absorption coefficient around a selected element present in the sample [24]. The XAFS spectra were recorded from all the samples including as-grown and 1 - 5 nm Au decorated. Figure 4.5 summarizes the results of XAFS measurements for as-grown and 3 & 5 nm Au coated ZnO nanopapers. Figure 4.5 (a) shows the normalized XAFS spectra of ZnO and Au decorated (3 & 5 nm) ZnO nanopapers, around the Zn-K edge. Noticeably, for all the samples, no change in XANES region is observed as shown in Figure 4.5 (a) (Shaded region). In order to investigate Au induced changes in the local crystal structure of ZnO nanopapers, the normalized X-ray absorption spectra were analyzed using FEFF 6.0 code [25]. This includes the background reduction followed by Fourier transform (FT) of each spectrum and generation of the theoretical EXAFS spectra starting for an assumed crystallographic structure. Finally the experimental data is fitted with the obtained theoretical spectra using ARTEMIS software [26]. In figure 4.5 (b), (c) and (d), the dotted lines show the FT transformed EXAFS oscillations of as-grown, 3 and 5 nm Au coated ZnO nanopapers respectively, and the solid lines represent theoretical fitting of corresponding EXAFS oscillations for k-range from 2.5 - 9.5 \AA^{-1} . In a pure ZnO crystal, Zn is coordinated by four oxygen atoms at about 1.98 \AA^{-1} distance in first coordination shell, whereas the next-nearest-neighbor Zn is surrounded by 12 Zn atoms at 3.21 \AA^{-1} distance, and by considering all these facts, the fittings were performed in R-space in the range 1 - 3.21 \AA^{-1} . For fitting, the coordination numbers were kept fixed to those of crystalline ZnO. The mean value of inter-atomic distance and Debye-Waller factor (σ^2) were fitted as free parameters. The obtained fitting parameters for all the samples are tabulated in table 4.1. The fitting parameters reveal that, around the Zn-edge,

the Au decoration affects the local crystal structure in both the Zn-O shell and the Zn-Zn shell and further supports our EELS results. The change in the local crystal structure may affect the electronic structure and electrical properties of nanotapers.

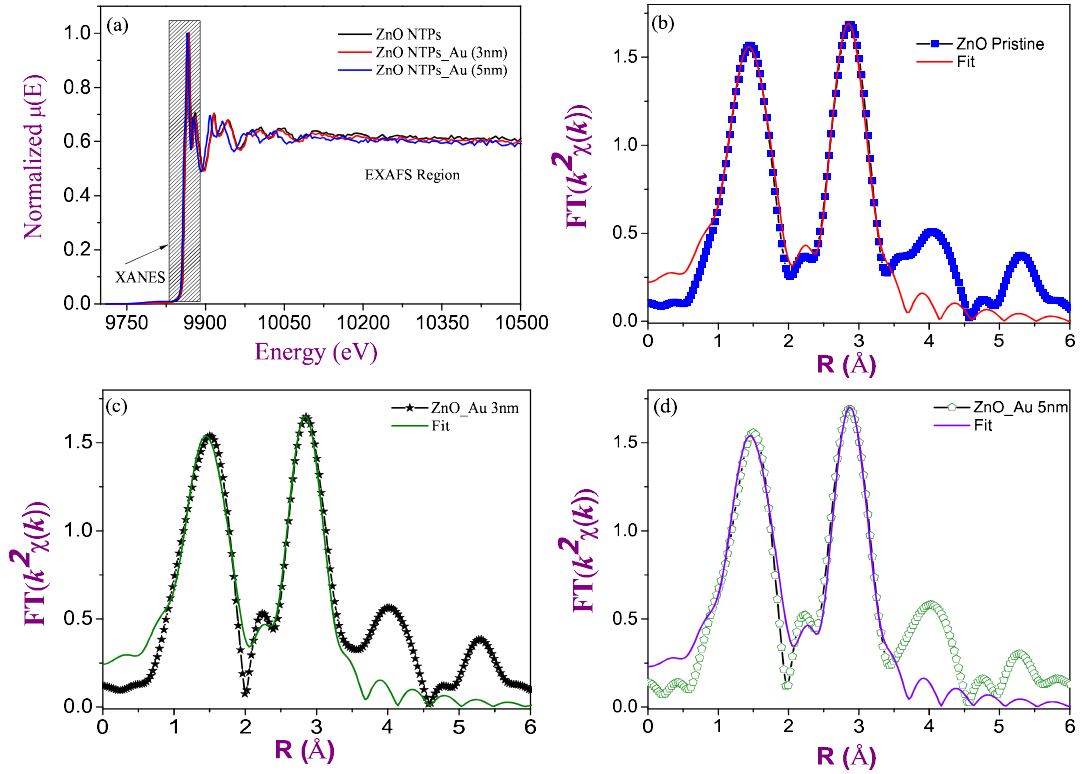


Figure 4.5: Normalized X-ray absorption spectra of as-grown and Au coated samples (a) and (b - d) around Zn K-edge, Fourier transform of k^2 -weighted EXAFS spectra of as-grown, 3 and 5 nm Au decorated ZnO nanotapers respectively.

Table 4.1: Extracted EXAFS fitting parameters

Sample	R_{Zn-O} (Å)	σ^2 (Å ²)	R_{Zn-Zn} (Å)	σ^2 (Å ²)
As-grown nanotapers	1.944 (1)	0.0087 (2)	3.205 (2)	0.0105 (2)
1 nm Au decorated	1.945 (3)	0.0096 (2)	3.228 (5)	0.0098 (3)
2 nm Au decorated	1.942 (2)	0.0102 (3)	3.224 (4)	0.0095 (2)
3 nm Au decorated	1.949 (3)	0.0095 (3)	3.196 (5)	0.0107 (3)
4 nm Au decorated	1.951 (1)	0.0094 (4)	3.212 (2)	0.0106 (3)
5 nm Au decorated	1.954 (2)	0.0093 (2)	3.216 (4)	0.0104 (2)

4.3 Absorption characteristics

The optical absorption characteristics of as-grown and Au decorated nanopapers is presented in figure 4.6 (a) - (f). Figure 4.6 (a) represents the absorption spectrum of as-grown sample, and

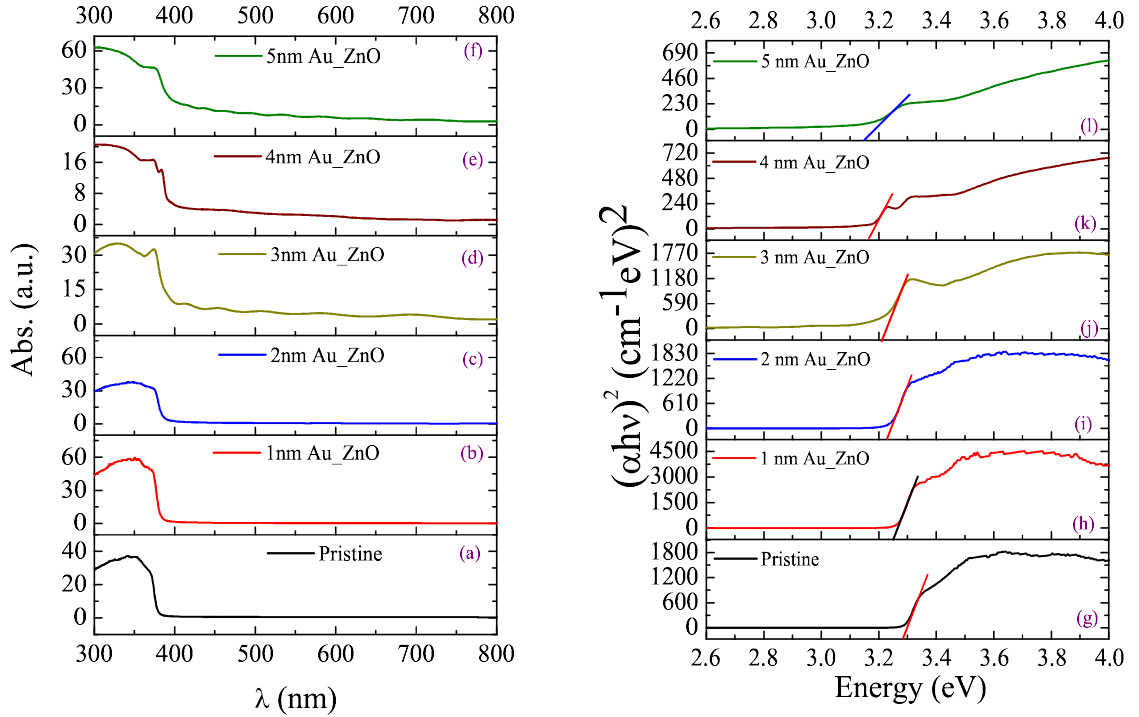


Figure 4.6: (a) - (f) RT absorption spectra of as-grown and 1-5 nm Au decorated samples, respectively. Their corresponding Tauc plots are shown in (g) - (l) respectively.

figure 4.6 (b) - (f) are from the 1-5 nm Au decorated samples, respectively. We notice that with Au decoration the absorption spectra exhibit redshift as a function of thickness of Au, indicating the influence of Au decoration on absorption edge of nanopapers. Here, it is worthwhile to mention that no signature of surface plasmons characteristics is seen in the absorption spectra of Au decorated samples, which normally appears between 500nm to 600nm [27]. In order to find the absorption edge (bandgap), each absorption spectrum was converted into the Tauc plot using Tauc relation (as described in chapter 3) and are shown in figure 4.6 (g)-(l). The Tauc plot of the as-grown sample is shown in figure 4.6 (g), and for Au decorated samples are shown in panel (h) (l), respectively. At the $h\nu$ turning point, the Tauc plots of Au decorated samples exhibit remarkable shift towards the lower energy as a function of the thickness of Au, compared to the as-grown nanopapers. The absorption edge of samples was extracted by fitting a straight line in

a similar way as described in chapter 3. For clarity, the extracted bandgap of all the samples is plotted in figure 4.7 with respect to the thickness of Au. In plot, the bandgap narrowing characteristics is apparent. The bandgap narrowing of Au decorated nanopapers is attributed to the interface coupling between Au and ZnO by the electron transfer between Au and ZnO and alignment of their Fermi levels [28]. The observed bandgap narrowing characteristics supports our argument of modification in the electronic structure at the Au-ZnO interface, as already shown by EELS and XAFS study.

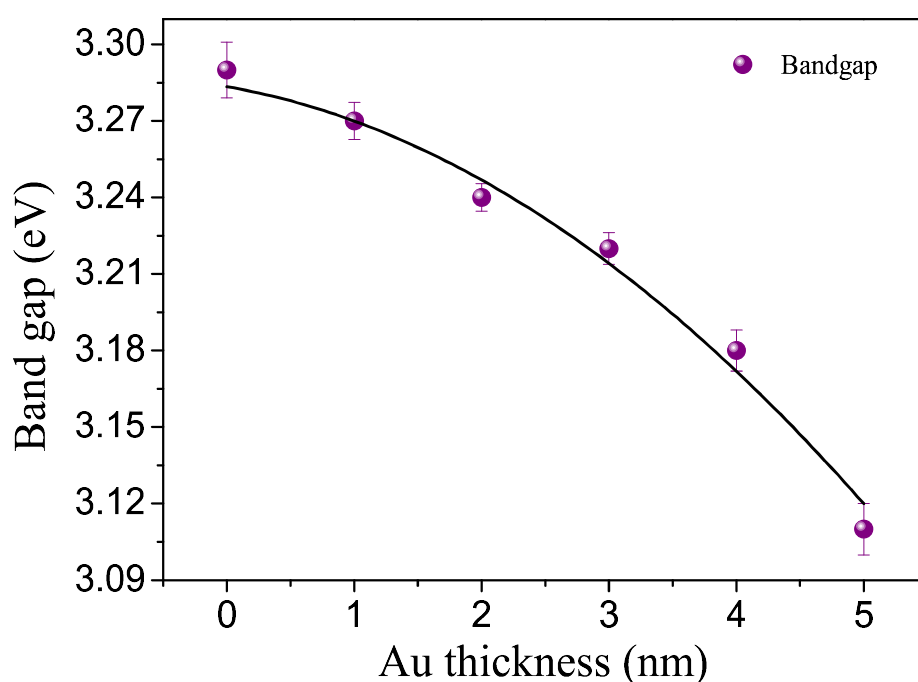


Figure 4.7: Extracted bandgap of nanopapers vs thickness of Au. The error bars were obtained from the straight line fitting of Tauc plots.

4.4 Field emission characteristics

The field emission (FE), also known as field electron emission, is quantum tunneling of surface electrons from a solid into the vacuum. In this process, the emission of surface electrons is induced by an external electric field (E_{appl}). Ralph H. Fowler and Lothar Wolfgang Nordheim (F-N) proposed the theory of FE from bulk metals [29]. In this theory, F-N derived a couple of equations named as "Fowler-Nordheim equations" which describe the characteristics of emission current. However, the F-N equations are applicable for bulk materials but are often used

at the nanoscale, as a rough approximation of emission current. The FE results of as-grown and Au coated ZnO nanotapers are summarized in figure 4.8. The emission current density (J) versus applied electric field (E) plots for as-grown (sample a), 3 and 5 nm Au coated ZnO nanotapers (samples b and c) are shown in figure 4.8 (a). Here it is worthwhile to mention that,

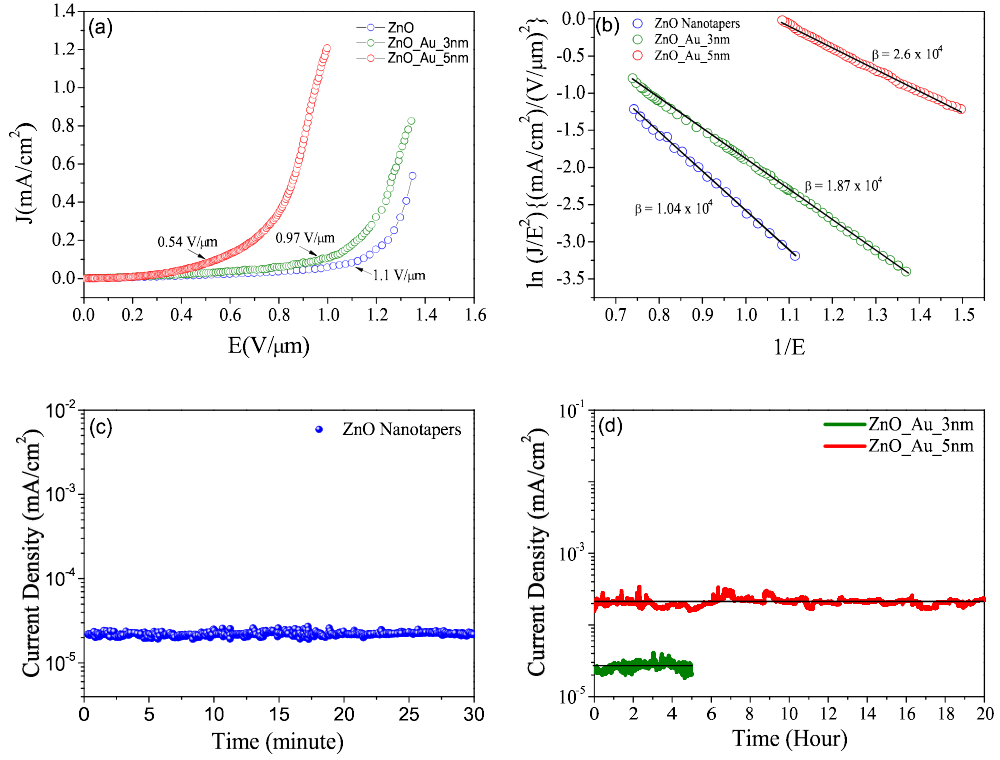


Figure 4.8: (a) Emission current density vs applied electric field, (b) F-N plots of samples a, b and c. (c - d) emission stability plots of as-grown nanotapers, 3 and 5nm Au-decorated ZnO nanotapers, respectively.

to establish an abiding emission current density, each data was recorded by applying 10 bias cycles. The Au decoration on ZnO nanotapers has shown a strong influence on its current density profile, as shown in figure 4.8 (a). At a fixed emission current density $J \sim 100$ A/cm², the turn-on field of samples b and c were found ~ 0.97 V/ μ m and ~ 0.54 V/ μ m, respectively compared to ~ 1.1 V/ μ m of sample a. The threshold field, a measure of quality parameter of field emitters, are found to be ~ 1.24 V/ μ m, ~ 1.12 V/ μ m, and ~ 0.7 V/ μ m at a fixed $J \sim 0.2$ mA/cm² for samples a, b and c respectively, which are lower than the existing values 2V/ μ m, and 3.5 & 5.6V/ μ m [30, 31]. For the analysis of FE characteristics of samples, we have employed FN theory [29], which establishes a relation between tunneling current density and applied electric

field.

$$J = A \left(\frac{\beta^2 E_{app}^2}{\Phi} \right) \exp \left(\frac{-B\Phi^{3/2}}{\beta E_{app}} \right) \quad (4.1)$$

Where, J (mA/cm²) and E (V/ μ m) are the emission current density and applied electric field respectively. $A = 1.56 \times 10^{-10}$ AeVV⁻², $B = 6830$ V/eV^{3/2} μ m, β and Φ (eV) are field enhancement factor and barrier height (work function), respectively [30]. The slope of F-N plots shown in figure 4.8 (b) yield the field enhancement factor β for respective samples and equation 2 describes the essential relation between their slope and β [32]:

$$S_{FN} = \frac{-B\Phi^{3/2}}{\beta} \quad (4.2)$$

In order to calculate the slope, we have plotted F-N plots of each sample as $1/E$ vs $\ln(J/E^2)$ followed by fitting with a straight line and are shown in figure 4.8(b). The blue, green and red dotted curves in figure 4.8(b) show the F-N plots of samples a, b and c respectively, where, the solid lines represent the linear fits. The linear fits to F-N plots imply the applicability of F-N mechanism for emission of electrons from the surface of as-grown and Au-coated ZnO nanotapers. For samples a, b and c, the extracted slopes from the linear fits, are found around -7.561, -4.0426 and -2.0987 respectively. However, to calculate β of each sample, the work function of the respective sample is required. In this context, the average Φ for each sample was calculated from their 2D contact potential difference measured using Kelvin probe force microscopy (KPFM). The average Φ values of samples a, b, and c were found to be 5.1 ± 0.3 eV, 4.96 ± 0.07 eV, and 3.98 ± 0.02 eV, respectively. Here, we notice that the experimentally calculated Φ of as-grown nanotapers is consistent with the standard Φ of ZnO (5.3eV) [33], whereas it decreases from 5.1 eV to 4.96 and 3.98eV for the samples b and c, respectively. The decrease in Φ and mapping process will be discussed in detail in the succeeding paragraph. The substitution of the values of S_{FN} and Φ of the individual samples a, b, and c in the equation 4.2 provided the β for samples a, b and c, as 1.04×10^4 , 1.87×10^4 , and 2.6×10^4 , respectively. The calculated β values for Au coated samples are higher than the as-grown nanotapers and for sample c it is almost 2 times than the sample a, which implies that Au decoration on the surface of nanotapers improves the field emission characteristics of ZnO nanotapers [30]. Figure 4.8 (c) and (d) show the emission stability plots for samples a, b and c, respectively. In figure 4.8 (d), the green and red curves represent the emission stability plots for samples b and c, respectively. Notice, nanotapers showed enhanced emission stability behavior with increasing the thickness of Au, whereas the as-grown nanotapers showed temporal stability. Sample b was found to be

stable only for 5 hours, compared to sample c (20 hours) and due to which in figure 4.8 (d) the green plot is plotted only up to 5 hours.

4.5 Work function calculations using Kelvin probe force microscopy

Figure 4.9 summarizes the KPFM results of samples a, b, and c. Panels (a), (c) and (e) show the AFM images of samples a, b, and c, respectively from where the V_{CPD} values were mapped, and their corresponding 2D V_{CPD} maps are shown in panels (b), (d) and (f), respectively.

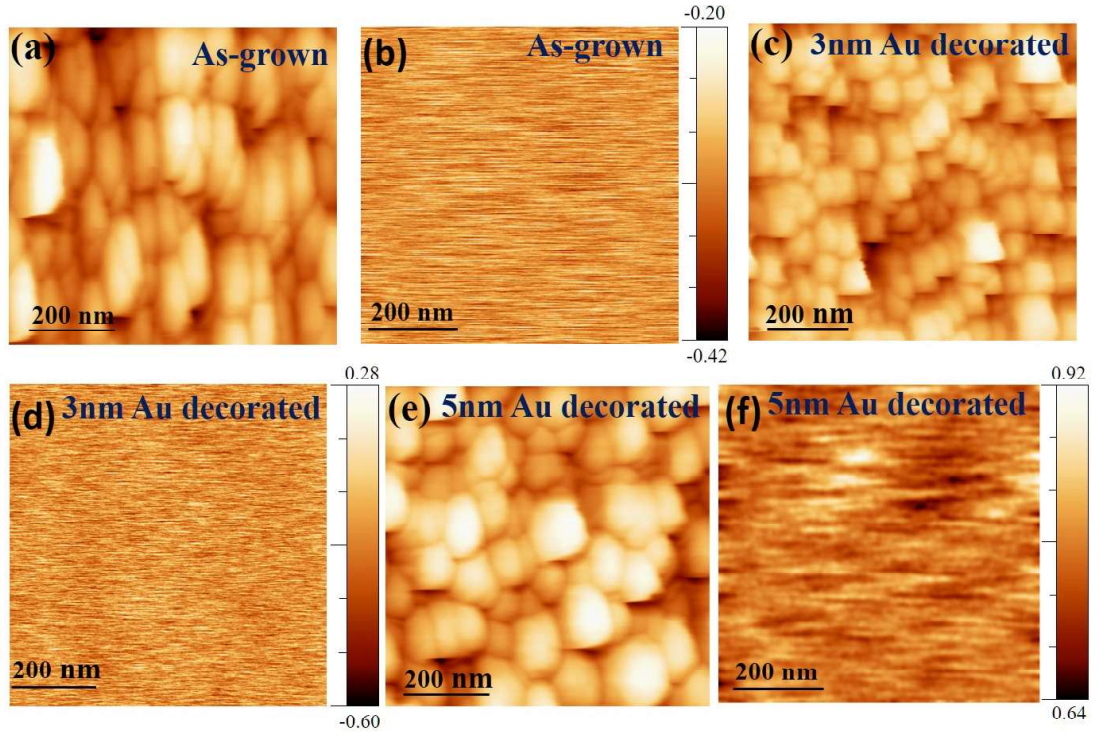


Figure 4.9: (a), (c) and (e) The AFM images of samples a, b, and c, respectively from where the V_{CPD} values were mapped. (b), (d) and (f) 2D maps of V_{CPD} of samples a, b, and c, respectively.

Each 2D map was analyzed to calculate the average V_{CPD} value of the respective samples. The average work-function of each sample was calculated by substituting their average V_{CPD} value into the expression 4.3 which describes a relation between V_{CPD} value and sample work function.

$$\Phi_{sample} = \Phi_{tip} - qV_{CPD} \quad (4.3)$$

where q is the electronic charge, Φ_{sample} , and Φ_{tip} are the sample and tip work functions (4.85eV), respectively [34]. The average local work function of samples a, b and c calculated by using above equation are found to be 5.1 ± 0.3 eV, 4.96 ± 0.07 eV, and 3.98 ± 0.02 eV respectively. Since both the FESEM and STEM images show that on the surface of ZnO nanotapers the Au is deposited in islands like morphology (discontinuous), and don't cover the entire surface of the nanotapers, we believe that the calculated values of average work-function of samples a, b, and c, are contribution from the entire surface of Au-ZnO. The thin metallic films effectively modify the interface properties of metal-semiconductor contacts [35–38]. The most widely accepted mechanism behind such effects is the metal-induced sub-gap states, induced at the metal-semiconductor interface, which leads to band bending. Heine et. al. [35] showed that such band bending can reduce the effective work function of the semiconductor leading to the enhanced electronic activity of the semiconductors in response to external stimulus. Subsequent calculations and experiments by Nakato et al. [37, 38] have shown that nanoscale metallic islands on a semiconductor surface, as seen in our case, can also result in very effectively band bending in the metal-free part of the surface. By considering the EELS & XAFS results, bandgap narrowing characteristics, and KPFM measurements, we attribute the reduction of effective work function to a similar band bending in the metal free zone of nanotapers.

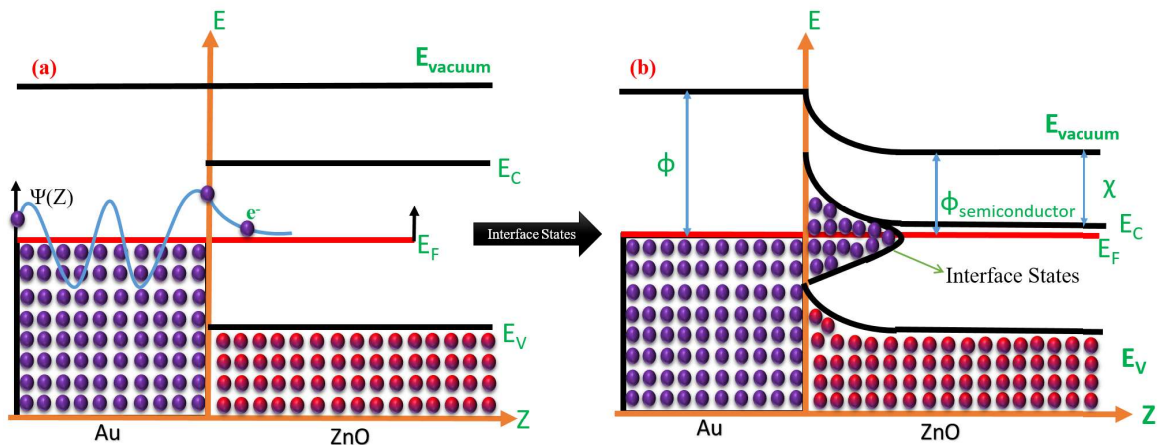


Figure 4.10: (a) The continuum of Au Bloch state leaking into the ZnO forbidden gap and representation of reduced work function, (b) Au induced gap states (interface states) caused by leaking of Bloch states.

A schematic representation of band-bending is shown in figure 4.10, where panel (a) represents the continuum of Au metal states leaking into the induced gap states of ZnO and (b) shows

the formation of interface states and band-bending leading to reduction of work-function. Our experimental findings are in good agreement with latest progress on field emission based studies of ZnO nanostructures. For comparison, a detailed list of recent updates in this area, is presented in table 4.2.

Table 4.2: Summary of recent updates on field emission characteristics of ZnO nanostructures

ZnO samples	E (V/ μm)	J ($\mu\text{A}/\text{cm}^2$)	Φ (eV)	Ref.
Nanorod arrays	6.00	50	-	[7]
Nano-needles	2.40	10	-	[9]
N-implanted nanowires	2.40	0.1	-	[10]
Nano-pins	1.92	0.1	-	[13]
Au capped nanowires	0.86	100	5.04 ± 0.05	[19]
Triangular nanoflakes	0.52	100	4.7 ± 0.1	[19]
Au-coated nanowires	2.00	0.1	-	[30]
Pure Nanowires	4.90	10	-	[31]
In-doped Nanowires	2.40	10	-	[31]
Tetrapod-like	1.60	1.0	-	[39]
N-doped nanobullet	2.90	10	-	[40]
ZnO on rough-Si Rods	2.90	10	-	[41]
Tailored nanorods	1.80	0.1	-	[42]
Urchin-like	3.70	10	-	[43]
In doped-nanorods	4.70	10	-	[44]
Nanorods on seed layer	20-27	10	-	[45]
V ₂ O ₅ nanoparticles coated	3.25-4	100	-	[46]
ZnO NWs/MgO buffer	3.9	100	-	[47]
ZnO nanotapers	1.1	100	5.1 ± 0.03	[48]
Au decorated ZnO nanotapers	0.97, 0.54	100	$4.96 \pm 0.07, 3.98 \pm 0.02$	[48]

4.6 Study of local conductance using tunneling atomic force microscopy

Figure 4.11 summarizes the obtained TUNA results of as-grown, and Au decorated (3 & 5 nm) ZnO nanotapers. Figure 4.11 (a) shows the surface morphology of sample a. TUNA mapped 2D tunneling current images of samples a, b and c are shown in figure 4.11 (b), (c) and (d) respectively. The insets of figure 4.11 (c) and (d) depict the surface morphology of the respective samples. For each sample, the 2D map of tunneling current was recorded at a DC bias of 3V applied between the tip and sample. The current image of sample a exhibits a non-uniform and low-intensity current. The current maps of samples b and c show a very uniform and relatively high-intensity tunneling current profile. If we notice carefully, a significant difference

is observable even between the current profiles of samples b and c. This implies that the Au-decoration on ZnO nanotapers modify the surface states and provides additional free electrons to participate in conduction with an applied potential, and causes the improvement of the local conductance of nanotapers. The very uniform and intense tunneling current profiles of Au decorated ZnO nanotapers indicate their applicability for large-scale device applications.

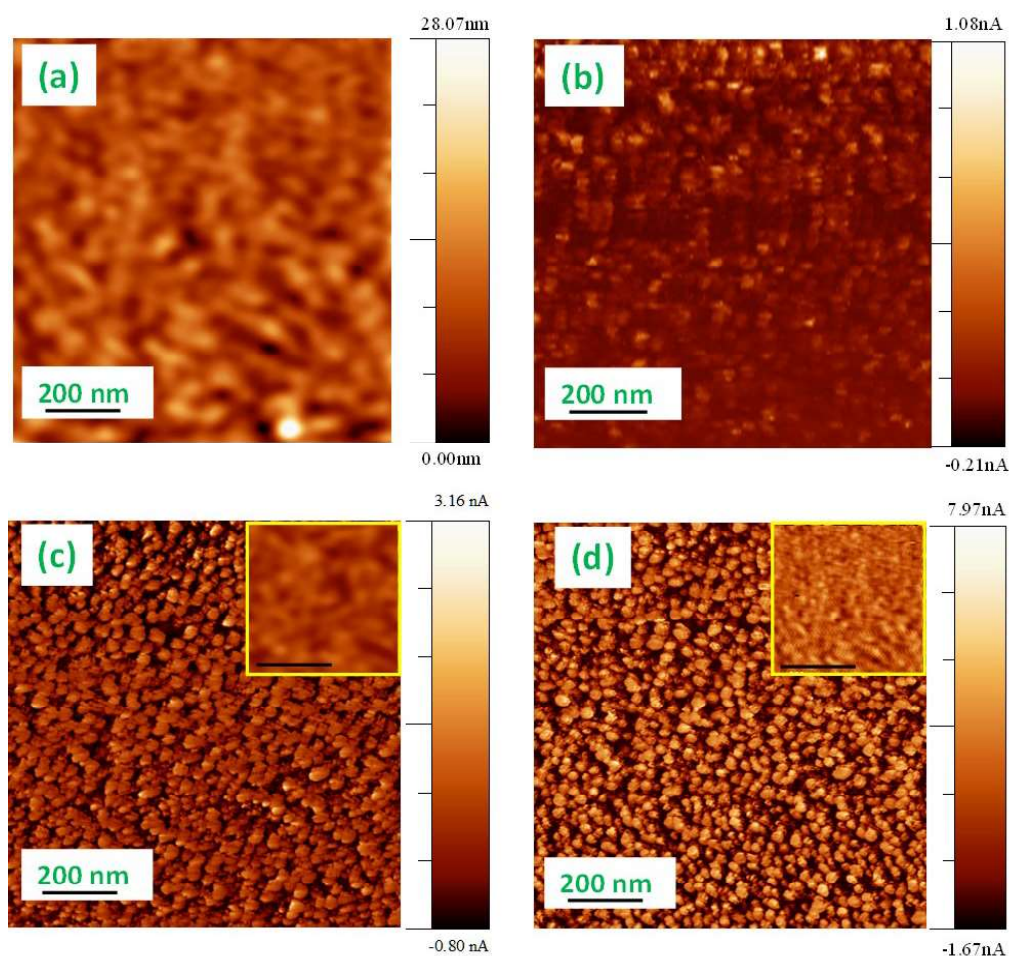


Figure 4.11: (a) C-AFM image of as-grown ZnO nanotapers. (b - d) 2D tunneling current maps of as-grown, 3 nm and 5 nm Au-decorated ZnO nanotapers respectively. The inset of (c) and (d) show C-AFM images of 3 nm and 5 nm Au-decorated nanotapers respectively.

4.7 Summary

Vertically aligned ZnO nanotapers were grown on seed layer coated Si substrates using the wet chemical route. Nanotapers were coated with Au layers of five different thickness 1-5 nm, using e-beam evaporation technique. For their characterization, field emission scanning electron microscope, EDX, EELS spectroscopy and synchrotron radiation based XRD techniques

were employed. The FESEM images showed corrugated decoration of Au on ZnO nanotapers. The presence of Au particles on the surface of ZnO nanotapers shown in ADF-STEM image confirms the Au-decoration. In addition, the appearance of Au signal in both the EDX spectrum and XRD patterns further confirmed the Au-decoration on ZnO nanotapers. The EELS spectrum recorded at Au-ZnO interface exhibits distinct features compared to the spectrum acquired from the ZnO surface. This is the evidence that interaction with the Au particles modifies the ZnO surface. The local crystal structure of as-grown and Au-decorated nanotapers were studied by XAFS technique, where no change in XANES region was observed. However, the fitting of Fourier transformed EXAFS oscillations showed modifications in the local crystal structure of Au-decorated nanotapers compared to the as-grown nanotapers, which implies fine modifications in the electronic structure of the samples. The bandgap narrowing characteristics of Au-decorated nanotapers were consistent the results of EELS and EXAFS, regarding the modification in electronic structure. The ZnO nanotapers showed efficient field emission characteristics with low turn-on field by a corrugated decoration of Au, especially of thickness 5 nm. The TUNA results showed a very uniform and efficient tunneling current profile for Au-decorated nanotapers. A direct mapping of effective work-function using Kelvin probe force microscopy displayed a drop of 0.14 eV and 1.1 eV in the effective work-function of 3 and 5 nm Au decorated ZnO nanotapers compared to as-grown nanotapers. On the basis of our experimental findings, we believe that Au decoration on ZnO nanotapers modifies the electronic structure by forming metal induced mid-gap states at Au-ZnO interface. This results in the observed low turn-on field, as a consequence of the drop in the effective work-function of Au decorated ZnO nanotapers.

Bibliography

- [1] Z. Zhang, G. Meng, W. Qiang, H. Zheng, J. Chen, Q. Xu, F. Zhou, Nature Sci. Rep., **2014**, 4, 4676.
- [2] I. Brodie and C. A. Spindt, Adv. Electron. Electron Phys., **1992**, 83, 1.
- [3] C. Hernandez-Garcia, M. L. Stutzman and P. G. O'Shea Phys. Today, **2008**, 61, 44.
- [4] F. M. Charbonnier, J. P. Barbour, L. F. Garrett, W. P. Dyke, Proc. IEEE, **1963**, 51, 991.
- [5] J. Chen, Y. Y. Dai, J. Luo, Z. L. Li, S.Z. Deng, J. C. She, N. S. Xu, Appl. Phys. Lett., **2007**, 90, 253105.
- [6] B. Singer, H.D. Doolittle, J. Appl. Phys., **1965**, 36, 2002.
- [7] V. Semet, V. T. Binh, Th.Pauporte, L. Joulaud, F. J. Vermersch, J. Appl. Phys., **2011**, 109, 54301.
- [8] Q. Zhao, H. Z. Zhang, Y. W. Zhu, S. Q. Feng, X. C. Sun, J. Xu, D. P. Yu, Appl. Phys. Lett., **2005**, 86, 203115.
- [9] R. P. Sugavaneshwar, K. K. Nanda, Appl. Phys. Lett., **2014**, 104, 22104.
- [10] Q. Zhao et al., Nanotechnology, **2010**, 21, 095701.
- [11] D. Banarjee, S. H. Jo, Z.F. Ren, Adv.Mater., **2004**, 16, 2028.
- [12] J. B. You et al., Appl. Phys. Lett., **2009**, 94, 262105.
- [13] C. X. Xu, X. W. Sun and B. J. Chen, Appl. Phys. Lett., **2004**, 84, 1540.
- [14] Q. Zhao, X. Y. Xu, X. F. Song, X. Z. Zhang, D. P. Yu, C. P. Li and L. Guo Appl. Phys. Lett., **2006**, 88, 033102.

- [15] C. Ye, Y. Bando, X. Fang, G. Shen and D. Golberg, *J. Phys. Chem. C*, **2007**, 111, 12673.
- [16] Y. M. Chang, M. L. Lin, T. Y. Lai, H. Y. Lee, C. M. Lin, Y. C. S. Wu and J. Y. Juang, *ACS Appl. Mater. Interfaces*, **2012**, 4, 6676.
- [17] J. Wang, Z. Wang, B. Huang, Y. Ma, Y. Liu, X. Qin, X. Zhang and Y. Dai, *ACS Appl. Mater. Interfaces*, **2012**, 4, 4024.
- [18] D. C. Look, G. C. Farlow, P. Reunchan, S. Limpijumnong, S. B. Zhang and K. Nordlund, *Phys. Rev. Lett.*, **2005**, 95, 225502.
- [19] A. Ghosh et al., *Nanotechnology*, **2016**, 27, 125701.
- [20] L. Vayssieres, *Adv. Mater.*, **2003**, 15, 464.
- [21] J. Qiu, X. Li, W. He, S. J. Park, H. K. Kim, Y. H. Hwang, J. H. Lee, Y. D. Kim, *Nanotechnology*, **2009**, 20, 155603.
- [22] K. Dileep, L. S. Panchakarla, K. Balasubramanian, U. V. Waghmare, and R. Datta, *J. Appl. Phys.*, **2011**, 109, 063523.
- [23] Y. Sato, T. Mizoguchi, F. Oba, M. Yodogawa, T. Yamamoto, and Y. Ikuhara, *Appl. Phys. Lett.*, **2004**, 84, 5311.
- [24] G. Bunker, Cambridge University Press, **2010**.
- [25] S. I. Zabinsky, J. J. Rehr, A. Ankudinov, R. C. Albers, and M. J. Eller, *Phys. Rev. B*, **1995**, 52, 2995.
- [26] B. Ravel and M. Newville, *J. Synch. Rad.*, **2005**, 12, 537.
- [27] Y. K. Mishra, S. Mohapatra, R. Singhal, D. K. Avasthi, D. C. Agarwal, and S. B. Ogale, *Appl. Phys. Lett.*, **2008**, 92, 043107.
- [28] N. L. Tarwal, R. S. Devan, Y. R. Ma, R. S. Patil, M. M. Karanjkar, P. S. Patil, *Electrochim Acta.*, **2012**, 72, 32.
- [29] R. H. Fowler, L. Nordheim, *Proceedings of the Royal Society A*, **1928**, 119, 173.

- [30] B. Cui, C. P. Daghljan, U. J. Gibson, R. Pusche, P. Geithner, L. Ley, *J. Appl. Phys.*, **2005**, 97, 044315.
- [31] M. Ahmad, H. Sun, J. Zhu, *ACS Appl. Mater. Interfaces*, **2011**, 3, 1299.
- [32] V. S. Kale, R. R. Prabhakar S. S. Pramana, M. Rao, C. H. Sow, K. B. Jinesh, S. G. Mhaisalkar, *Phys. Chem. Chem. Phys.*, **2012**, 14, 4614.
- [33] A. A. Al-Tabbakh, M. A. More, D. S. Joag, I. S. Mulla, V. K. Pillai, *ACS Nano*, **2010**, 4, 5585.
- [34] Y. Lv, J. Cui, Z.M. Jiang, X. Yang, *Nanoscale Res. Lett.*, **2012**, 7, 659.
- [35] V. Heine, *Phys. Rev. A*, **1965**, 138, 1689.
- [36] M. W. Allena, S. M. Durbin, *Appl. Phys. Lett.*, **2008**, 92, 122110.
- [37] Y. Nakato, H. Tsubomura, *J. Photochem.*, **1985**, 29, 257.
- [38] Y. Nakato, H. Tsubomura, *Electrochim. Acta*, **1992**, 37, 897.
- [39] Q. Wan, K. Yu, T.H. Wang, C.L. Lin, *Appl. Phys. Lett.*, **2003**, 83, 2253.
- [40] U. K. Gautam et al., *Adv. Funct. Mater.*, **2009**, 19, 131.
- [41] H. C. Wu, T. Y. Tsai, F. H. Chu, N. H. Tai, H. N. Lin, H. T. Chiu, C. Y. Lee, *J. Phys. Chem. C*, **2010**, 114, 130.
- [42] H. Zeng, X. Xu, Y. Bando, U. K. Gautam, T. Zhai, X. Fang, B. Liu, D. Golberg, *Adv. Funct. Mater.*, **2009**, 19, 3165.
- [43] H. Jiang, J. Hu, F. Gu, C. Li, *Nanotechnology*, **2009**, 20, 055706.
- [44] T.H. Fang, S.H. Kang, *Curr. Appl. Phys.*, **2010**, 10, 1076.
- [45] Y. Liu et al., *Appl. Surf. Sci.*, **2015**, 331, 497.
- [46] H. Yina, C. Songa, Z. Wanga, B. Guo, K. Yu, *Appl. Surf. Sci.*, **2015**, 345, 256.
- [47] S. Chen, J. Chen, J. Liu, J. Qi, Y. Wang, *Appl. Surf. Sci.*, **2016**, 387, 103.
- [48] A. Singh, K. Senapati, M. Kumar, T. Som, A. K. Sinha, P. K. Sahoo, *Appl. Surf. Sci.*, **2017**, 411, 117.

Chapter 5

Point defects in vertically aligned ZnO nanorods by O^+ ion implantation

In general, the ZnO nanostructures exhibit strong room temperature UV emission with large exciton binding energy and long exciton diffusion length, which enable them for various optoelectronic, and photonic applications [1–4]. However, their utilization is not limited only to these applications, and can be used further as multifunctional nanostructures by modifying their physical properties. In literature, various methods including the chemical doping [5–7], coating of metallic nanoparticles [8, 9], ion implantation [10, 11] etc. have been reported for the modification of the optical and electrical properties of ZnO. Nevertheless, the modifications in these physical properties completely depend on the management of defects inside the host matrix. In present research on ZnO, the controlled production of defects and their management inside the matrix is the main focus. Among all above-mentioned techniques, ion implantation is an effective technique to introduce controlled defect states into a material and has been used in ZnO as well [10, 11]. Meanwhile, among various reports on tailoring the optical and electrical properties, it is to be noticed that for realizing the ZnO based electrical devices, high p-type conductivity in ZnO is essentially required and is still under debate. Its inherent n-type conductivity hinders the fabrication of ZnO based electrical devices. Theoretical calculations by Zhang et al. [12] propound that the n-type conductivity in ZnO occurs from the presence of intrinsic defects in the crystal, which include Zn interstitial (Zn_i), Oxygen vacancies (V_O), V_O complexes, residual impurities, the deep acceptor levels, and low dopant solubility. These intrinsic defects and low dopant solubility are the bottlenecks for the p-type conductivity in ZnO. In literature, several experimental efforts have been made to obtain p-type conductivity in ZnO nanostructures by various methods like doping of group V elements (P, N, Li, and

As), and the growth of ZnO nanostructures in the Oxygen-rich environment using wet chemical method [13–21]. The reports by Butkhuzi et al. [22] and Georgobiani et al. [23] claim intrinsic p-type conductivity in ZnO thin films deposited by radical-beam gettering epitaxy by heat-treating ZnO in an oxygen ambient. In a similar way, a report by Ilyas et al. claims [21] p-type conductivity in ZnO thin films grown using wet chemical method and PLD. In their report, the ZnO thin films were deposited on Si (100) substrates using PLD technique, for which the ZnO targets (pellets) were synthesized by wet chemical route. The experimental investigations showed that high-temperature annealing in air, the dynamic recovery of defects resulted in the synthesis of O rich thin films. The produced acceptor levels of O_i (O rich) contributed maximum p-type conductivity at 700°C. In another report Oh et.al. [19] also claimed p-type conductivity in ZnO thin films deposited using PLD technique, when oxygen pressure changed from 6×10^{-5} to 3×10^{-4} Torr. Despite several reports on the p-type conductivity in ZnO nanostructures, the reproducible and stable p-type conductivity is still under debate. The point defects may significantly alter the conductivity of ZnO by changing the stoichiometry. However, it strongly depends on the distribution and nature of the defects. Hence, in this context, during doping, both the dopant concentration and control over a range of doping become an important and challenging task as well. The ion implantation technique provides an advantage over the other techniques owing to its ion selectivity, selected areal doping and precise depth distribution features.

This chapter deals with the incorporation of point defects in vertically aligned ZnO nanorods, at different depth and their influence on physical properties of vertically aligned ZnO nanorods. For this purpose this chapter is subdivided into two parts. The first part describes the influence of ion fluence (Φ) of O^+ ions of energy 100 keV on the structural and optical properties of ZnO nanorods. After considering the literature that O-rich environment in ZnO produces p-type conductivity, we tried to create an oxygen-rich environment in ZnO nanorods by implantation of O^+ ions. Since the O^+ ions of different energies have a different projectile range (R_p) in the ZnO matrix, which enables this technique as doping range selective. The different R_p of O^+ ions at different energies can create an O-rich environment in ZnO nanorods at different depths, which can fabricate oxygen-rich/n-type environment in a single vertically aligned ZnO nanorod. However, the energy loss processes involved during the ion-matter interaction also determines the number of defects inside the crystal, and one has to select an appropriate energy for implantation for creating an O-rich environment in ZnO nanorods. During ion im-

plantation, the charged projectile collides with the target material through both the elastic and inelastic collision processes and is stopped inside the material (if the projectile range is less than the thickness of the target) by transferring its energy to the atoms of the target material. In this process the inelastic collisions contribute to the electronic energy loss (S_e), whereas elastic collisions nuclear energy loss (S_n).

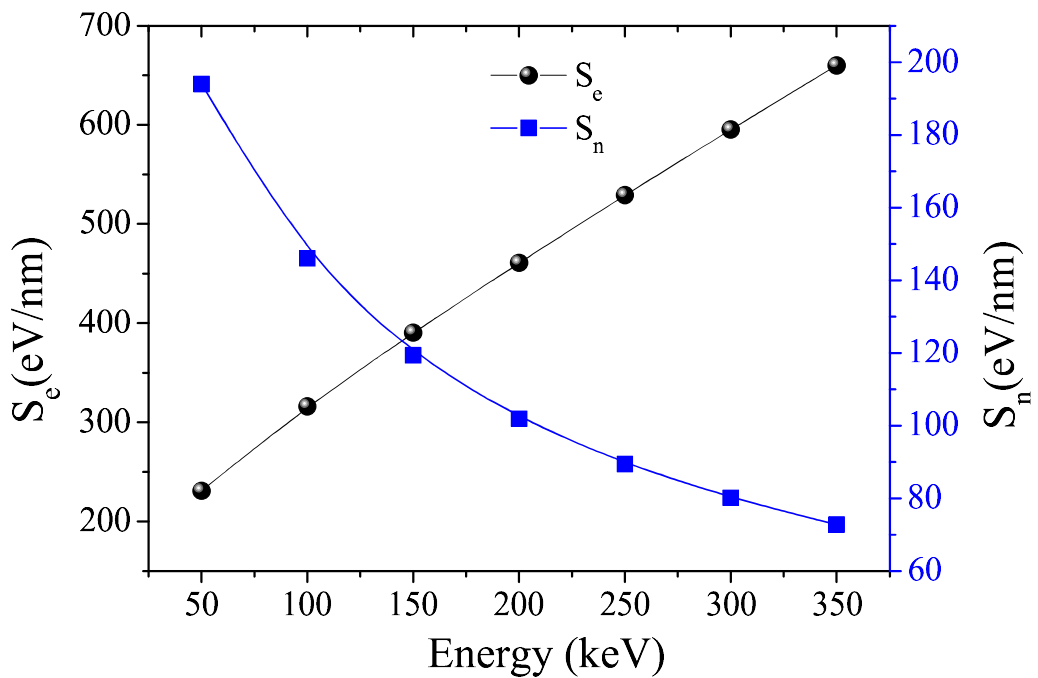


Figure 5.1: Simulated electronic and nuclear energy losses of O^+ ions in ZnO with respect to different energies.

The S_e contributes to both the ionization and atomic excitation as well, whereas the S_n contributes to the formation of atomic displacements (vacancies). The relative contribution from the S_e and S_n is dependent on the mass of the projectile ion, its kinetic energy, charge state, and density of the target material. Remarkably, stopping and Range of Ions in Matter (SRIM) simulated S_e and S_n values plotted in figure 5.1 show that with increasing O^+ ion energy, the S_e dominates over S_n . As the ions travel into the nanorods they are slowed down by losing their kinetic energy resulting in the domination of S_n , which can create vacancies in nanorods [24]. The SRIM simulations shown in figure 5.1 showed that for O^+ implantation in ZnO the nuclear energy loss decreases monotonically with increasing energy, whereas the electronic energy loss increases with increasing energy. From the SRIM results we expect

that implantation of ZnO nanorods with 350keV energy may create O-rich environment in the nanorods. In this context, the second part includes the successive O⁺ ion implantation in nanorods of two different energies 50 and 350 keV at a fixed Φ of 5×10^{16} ions/cm² in the same sample. The modifications in optical properties were investigated using room temperature PL, UV-visible, and Raman techniques. The C-AFM technique was employed for the study of their electrical properties.

5.1 Growth methodology and O⁺ ion implantation in vertically aligned ZnO nanorods

For this study, vertically aligned ZnO nanorods were grown on p-type Si (100) substrates using standard hydrothermal process [25]. Prior to growth, substrates were coated with a thin seed layer of ZnO deposited. Here, it is worthwhile to mention that the vertically aligned nanorods were grown for 6 hours growth duration, for which the entire experimental procedure remained similar to the growth of nanotapers as described in the previous chapter. The inclusion of both the seed layer and HMT induces the growth of closely packed and vertically aligned ZnO nanorods. After subsequent growth of nanorods, samples were characterized using FESEM, XRD and XPS techniques. The optical properties of nanorods were studied using UV-visible spectroscopy, PL, and Raman techniques, and the electrical properties were investigated using C-AFM measurements. In order to create point defects vertically aligned ZnO nanorods, samples were implanted with O⁺ ions in two sets. In the first set of samples, the O⁺ ions were implanted at a fixed energy of 100keV, but at three different Φ 5×10^{14} ions/cm², 5×10^{15} ions/cm², and 5×10^{16} ions/cm². In the second set of samples, two successive energies of 50 keV and 350 keV at a fixed Φ of 5×10^{16} ions/cm² were implanted successively in the same sample to create the O-rich/as-grown/O-rich/as-grown environment in a single nanorod, which we called p-n-p-n tandem junction. Post-implantation, the samples were annealed at 500^oC for 3 hours, in vacuum at a base pressure of 5×10^{-4} mbar.

5.2 Simulated projectile range

Since, in a material, the ion species have different projectile range, depending on their kinetic energy, and for the appraisal of the R_P of O⁺ ions in ZnO, at different energies used in this thesis, the SRIM simulation was performed, which is a computational tool for the study of

ion matter interactions in a material [26]. Figure 5.2 represents the R_P of O^+ ions in ZnO at three different energies of 50keV, 100keV, 150keV, 250keV and 350keV. We notice that for each energy the R_P of O^+ ions is different and the maxima of R_P of 50 and 350keV energies are separated by around 400 nm, indicating that the successive O^+ ion implantation creates O-rich/as grown/O-rich/as-grown tandem patterns in ZnO nanorods. The inset in figure 5.2 represents the schematic of an ideal p-n-p-n type tandem pattern in a single nanorod.

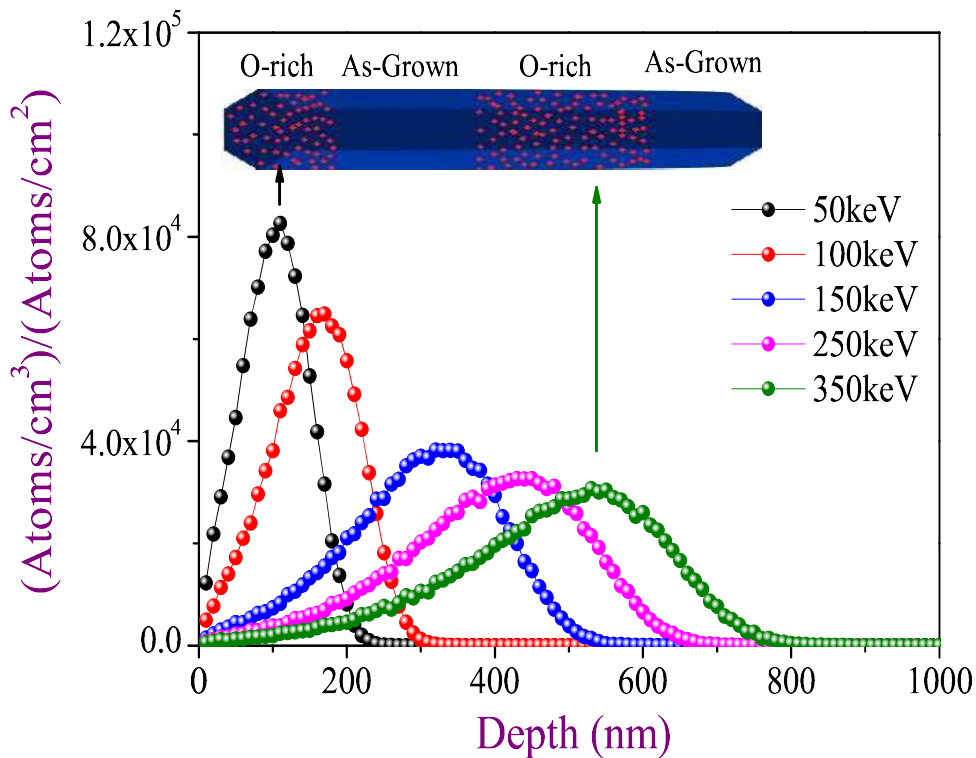


Figure 5.2: The simulated projectile range profile of O^+ ions in ZnO for different energies 50, 100, 150, 250, and 350 keV respectively. The inset shows the schematic diagram for the distribution of oxygen ions of two different energies of 50 and 350keV in a single ZnO nanorod.

5.3 Morphological and structural studies

5.3.1 SEM and XRD study

Figure 5.3 (a) shows the cross-sectional FESEM micrograph (Tilted at an angle of 12°) of as-grown ZnO nanorods (Sample A), where closely packed nanorods appear vertically aligned having hexagonal shape [27]. The vertically aligned nanorods are suitable nanostructures for

the 1D based device fabrication. Figure 5.3 (b) & (c) shows the top view FESEM images of ZnO nanorods implanted with O^+ ions of energy 50 keV (Sample B) and successively 50 and 350 keV (Sample C), respectively. The post-annealed FESEM images of samples A, B, and C are shown in figure 5.3 (d), (e) and (f), respectively. The FESEM images reveal that the morphology of nanorods remained unaffected after ion implantation and high-temperature annealing as well, which is essential for device fabrication and their sustainability. The grazing

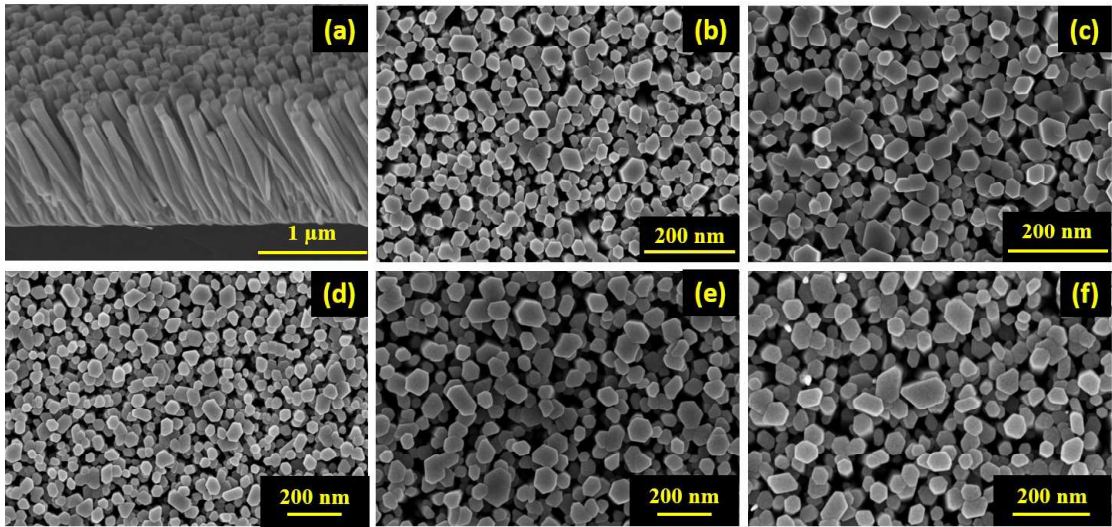


Figure 5.3: (a) Cross sectional FESEM image of as-grown ZnO nanorods (sample A). (b - c) Top-view FESEM images of ZnO nanorods implanted with 50 (sample B) and gradual 50 & 350 keV (sample C), respectively. (d - f) Post-annealed FESEM images of samples A, B and C (called as samples D, E and F) respectively.

angle X-ray diffraction patterns of two different set of samples are presented in figure 5.4. The influence of Φ at a fixed energy 100keV on crystal structure of ZnO nanorods is shown in panels (a) - (c) of figure 5.4. Panels (a), (b) and (c) show the XRD patterns of nanorods implanted at three different Φ 5×10^{14} ions/cm², 5×10^{15} ions/cm², and 5×10^{16} ions/cm², respectively. Figure 5.4 (d), (e), and (f) represents the XRD patterns of samples A, B and C respectively. Here we observe that the both sets of samples show a sharp and strong Bragg diffracted peak marked as (002). In all the diffraction patterns, the appearance of (002) Bragg peaks associated with the wurtzite structure of ZnO, and the absence of any other phase of ZnO is exhibiting the preferential growth along the c-axis (as seen in FESEM images) and good quality crystalline nature of the nanorods as well. The perseverance of the wurtzite structure of nanorods against implantation ensures the properties of ZnO associated with its crystal structure and indicates their applicability in device fabrication.

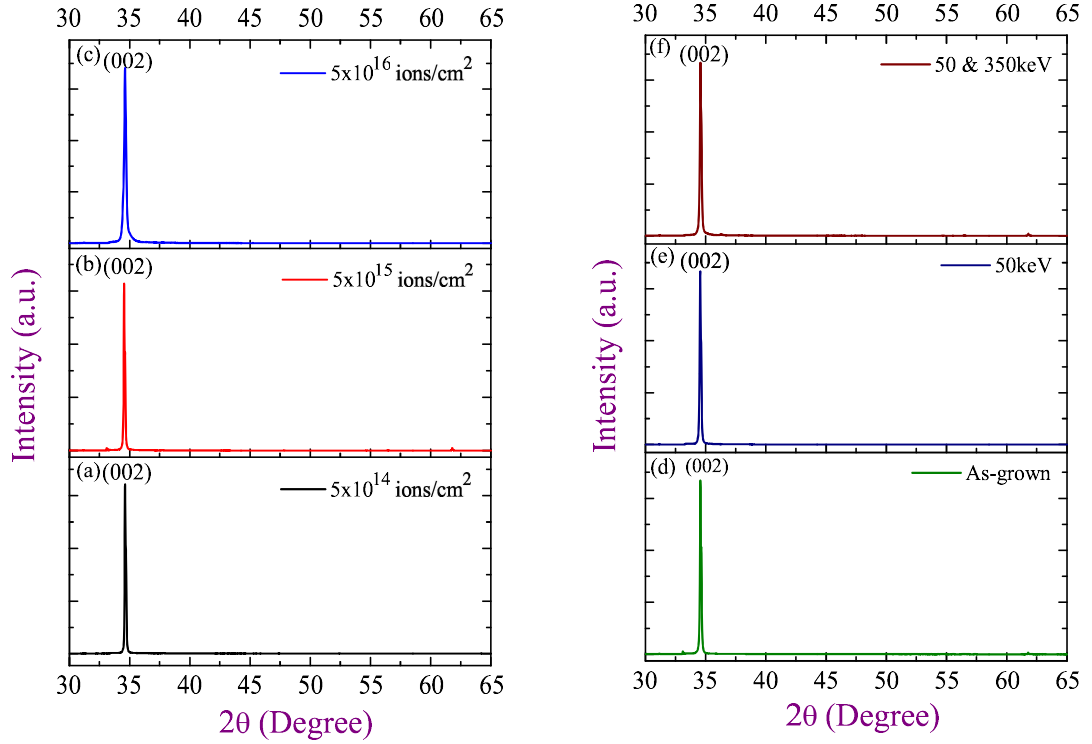


Figure 5.4: (a) - (c) Grazing angle X-ray diffraction patterns recorded from the samples implanted with $\Phi 5 \times 10^{14}$ ions/cm², 5×10^{15} ions/cm², and 5×10^{16} ions/cm², respectively. (d), (e) & (f) XRD patterns of samples A, B and C, respectively.

5.3.2 XPS study

The XPS results of as-grown, and 100keV O⁺ ions implanted samples are summarized in figure 5.5 & figure 5.6. Figure 5.5 compares the Zn core levels of implanted samples (at 100keV and three different $\Phi 5 \times 10^{14}$, 5×10^{15} , and 5×10^{16} ions/cm²) with the as-grown sample. At Zn core, each XPS spectrum consists of two distinct peaks corresponding to Zn2p_{3/2} (1021.57eV) and Zn2p_{1/2} (1044.67 eV), with the spin-orbital splitting of 23.08eV. The spin-orbital splitting (Δ metal) of Zn peaks is a signature of +2 oxidation state of Zn atoms [28]. Except for the Zn core level, the electronic states and chemical stoichiometry at O1s level were also carefully investigated by deconvoluting the O1s spectra of as-grown and implanted samples. Each deconvoluted spectrum consisted of three different Gaussian peaks, labeled as O²⁻ (530.12), O_V(531.26) and O_C(532.46eV). The peaks O²⁻, O_V, and O_C represent the lattice oxygen (Zn-O) of the wurtzite structure of ZnO, oxygen vacancy (O_V) and OH molecule attached to the surface of ZnO nanorods, respectively [29]. Figure 5.6 (a) plots the O 1s core level XPS spec-

trum of the as-grown sample, where the black dotted curve shows the experimentally obtained data. The O1s XPS spectra of samples implanted with three different Φ (fixed energy 100keV) 5×10^{14} , 5×10^{15} , and 5×10^{16} ions/cm² are shown in panels (b), (c), and (d), respectively. In order to investigate the influence of implantation, the composition concentration of all the three states in the O 1s level were calculated and are presented in Table 5.1. The table shows that with increasing Φ the concentration of V_O increases and the concentration of O^{2-} decreases.

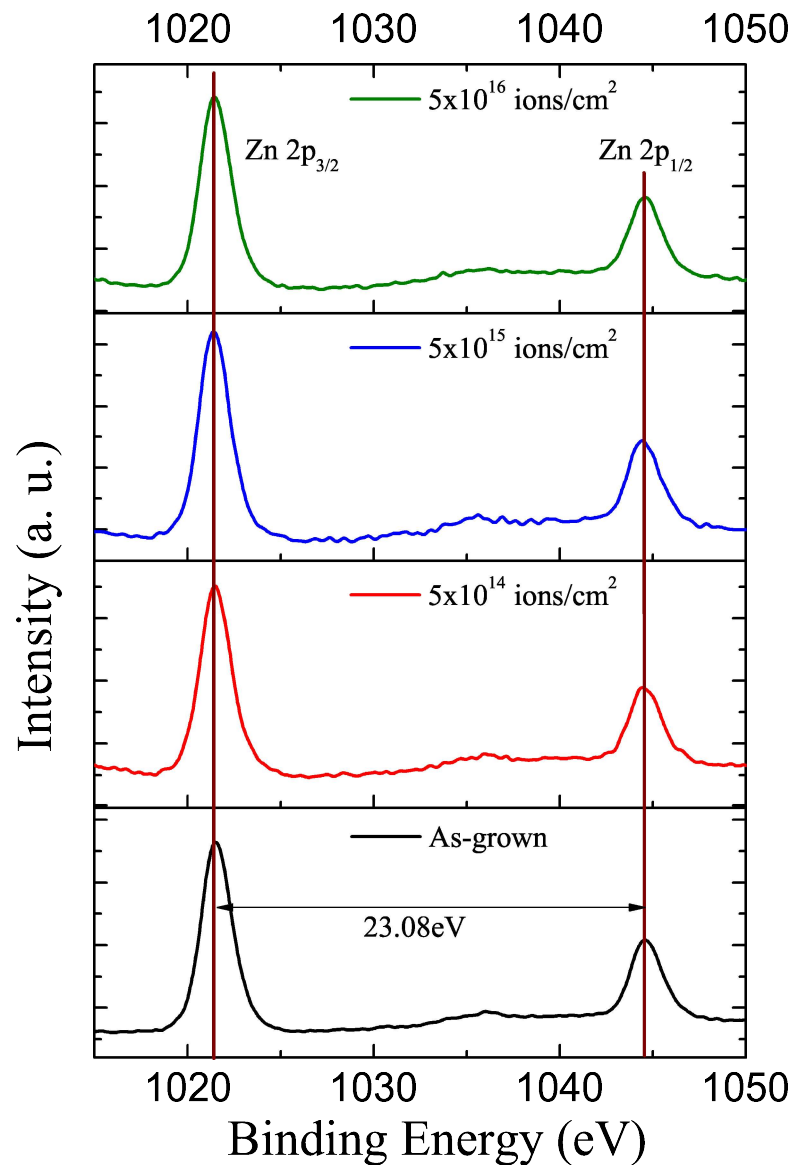


Figure 5.5: Zn 2p core level XPS spectra recorded from the as-grown and 100keV O^+ ions implanted samples. The spectra from implanted samples were recorded from the samples implanted with Φ 5×10^{14} ions/cm², 5×10^{15} ions/cm², and 5×10^{16} ions/cm², respectively.

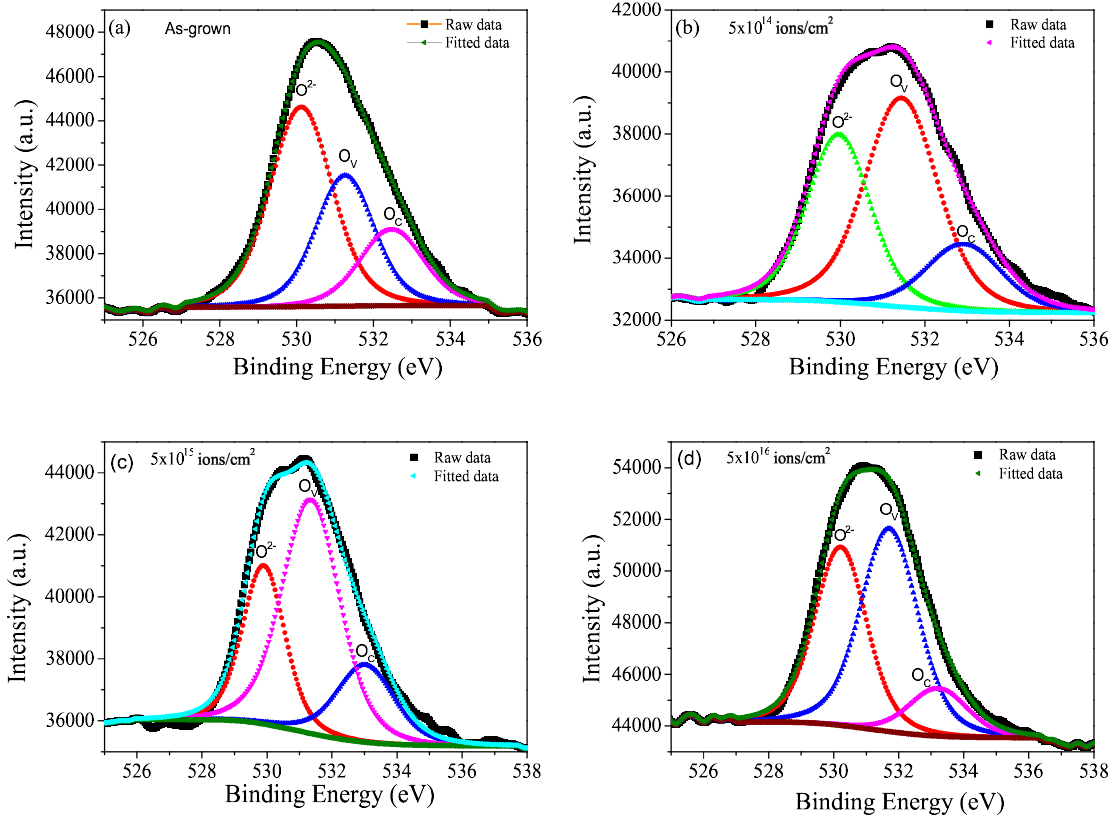


Figure 5.6: (a) O 1s XPS spectrum of as-grown sample. (b) - (d) O 1s core level XPS spectra of nanorods implanted with O^+ ions with Φ 5×10^{14} ions/cm², 5×10^{15} ions/cm², and 5×10^{16} ions/cm², respectively.

Remarkably, at Φ of 5×10^{16} ions/cm², the concentration of V_O drops (47.24%), whereas the concentration of O^{2-} rises (34.67%). For clarity, the ratio of V_O/O^{2-} is also tabulated in the table. This characteristic indicates that at 5×10^{16} ions/cm² Φ , the concentration of V_O in nanorods saturates and incoming ions replace the vacancies, which may create oxygen rich environment in nanorods [30, 31].

Table 5.1: Concentration variation of O^{2-} , O_V , and O_C states.

Sample	O^{2-} (%)	V_O (%)	O_C (%)	V_O/O^{2-}
As-grown	57.36	25.94	16.69	0.45
5×10^{14} ions/cm ²	34.14	49.46	16.40	1.45
5×10^{15} ions/cm ²	27.12	54.76	18.12	2.02
5×10^{16} ions/cm ²	34.67	47.24	18.09	1.36

5.4 Optical studies

Room temperature (RT) optical properties of ZnO nanorods were studied using UV-visible, PL and Raman spectroscopy and the obtained corresponding results are presented in respective sections.

5.4.1 Room temperature UV-visible spectroscopy:

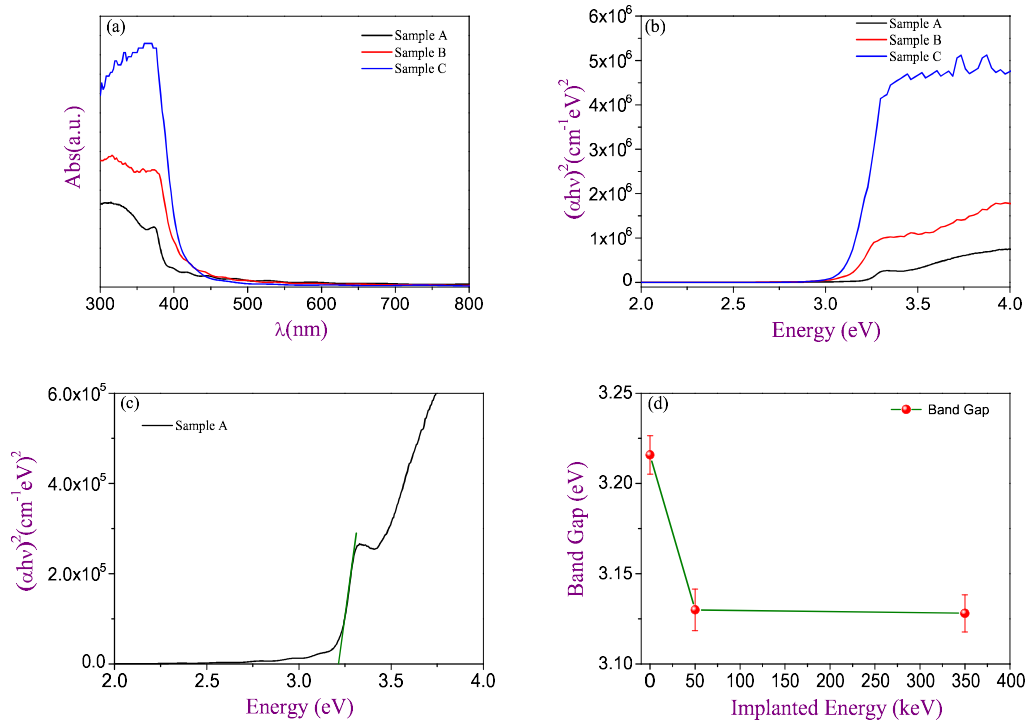


Figure 5.7: (a - b) Absorption and Tauc plots of samples A, B and C, respectively. (c) Demonstration of band gap extraction from the Tauc plot of sample A by fitting a straight line. (d) A plot for extracted band gap of samples A, B, and C, where the solid line is a guide for the eyes. The error bars were obtained from the fitting of a straight line in the Tauc plots.

Figure 5.7 encapsulates the results of UV-visible spectroscopy. The absorption spectra of samples A, B and C are shown in figure 5.7 (a). Remarkably, as a function of energy of implanted ions, the absorption shows a blueshift of 0.09 eV. For extracting the optical band gap, we converted each absorption spectrum into Tauc plots by using Tauc relation [32].

$$\alpha h\nu = \sqrt{[\beta(h\nu - E_g)]} \quad (5.1)$$

Where α , β , $h\nu$ and E_g are interband transition absorption coefficient, constant term, incident Photon energy and optical gap, respectively. The Tauc plots of the absorption spectra of samples

A, B, and C are shown in figure 5.7(b), where the optical transitions from the valence band to conduction band for samples B and C differ from the as-grown nanorods (sample A). Figure 5.7(c) shows the image of extracting bandgap (3.22eV) from the Tauc plot of sample A by fitting a straight line (green line). The optical band gap for samples B and C were extracted by following the same procedure. The extracted band gap of samples A, B and C are plotted in figure 5.7 (d), where both the samples B and C showed a drop of $\sim 0.1\text{eV}$ compared to the sample A. The blueshift in the band gap is consistent with the fact that oxygen vacancies induced by O^+ ion implantation are responsible for that [33].

5.4.2 Photoluminescence spectroscopy

In order to investigate the influence of point defects created by O^+ ion implantation on the luminescent characteristics of ZnO nanorods, room temperature PL measurements were performed and the data is shown in Figure 5.8. The PL spectra of samples A, B and C are shown in figure 5.8 (a) [27], where for the as-grown nanorods only a strong UV emission is present. This UV emission arises from the annihilation of band edge electron-hole pairs. Interestingly, we observe that after implantation the NBE emission is completely suppressed (samples B and C), unlike the sample A. In literature, a report by Chen et al. [34] attributes the suppression of NBE emission to the formation of competing nonradiative recombination transition centers influenced by the ion implantation. Authors claimed that upon post-annealing treatment recovered the NBE emission. However, except for the temperature, the recovery of NBE emission depends on other parameters like environment, ambient pressure and annealing time also. In this work, we annealed the samples in vacuum at relatively low temperature (500°C) compared to other reports [10, 34], and the post-annealed PL spectra of samples A, B and C (named as samples D, E, and F respectively) are shown in figure 5.8 (b) [27]. For all samples, the post-annealing treatment recovered the NBE emission along with a broad DLE band. Here we notice that for implanted samples the broad DLE band dominates over NBE emission, whereas its vice versa for sample D. As compare to sample D, a significant decrease in the intensity of NBE emission of samples E and F are also noticed. In order to find out the origin of DLE, we deconvoluted each PL spectrum, and simultaneously the positions of deconvoluted peaks were corrected by following the approach suggested by Bebb and Williams [35].

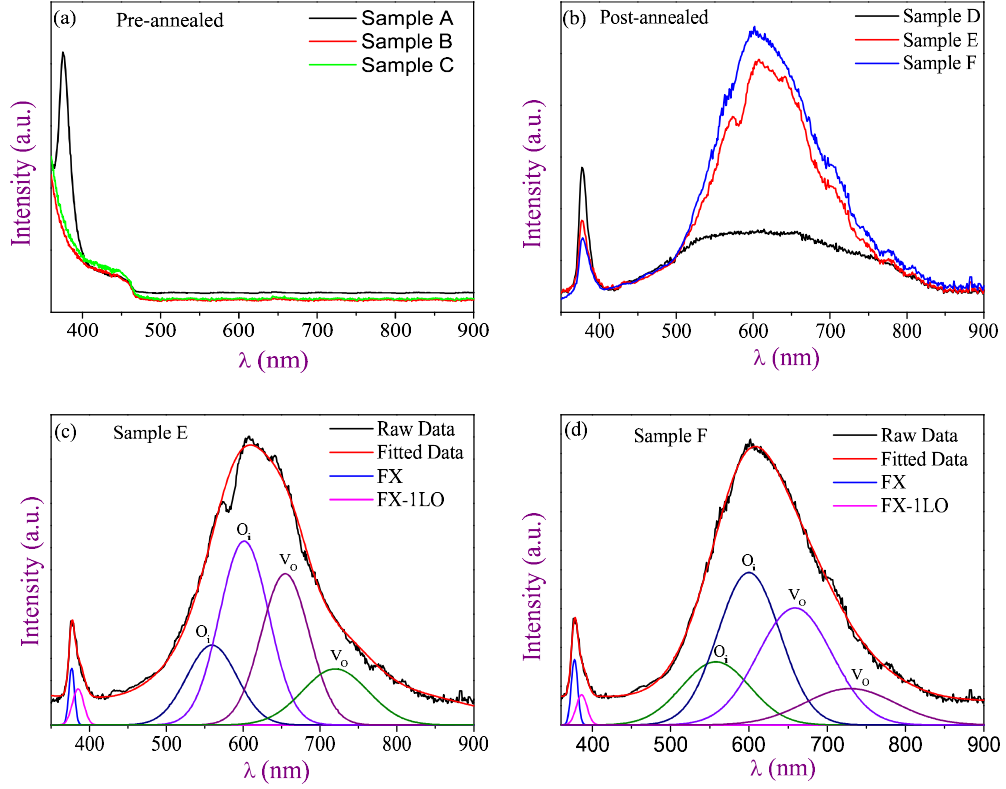


Figure 5.8: (a - b) Pre-annealed and post-annealed room temperature PL spectra of samples A, B and C, respectively. (c - d) Deconvoluted PL spectra of samples E and F respectively [27].

The deconvoluted spectra of samples E and F are shown in figure 5.8 (c) and (d), respectively. In both figures, the NBE emission peak is fitted by two peaks associated with FX emission and FX-1LO phonon mode and the broad DLE band is best fitted with four peaks centered around 555nm, 610nm, 655nm, and 710nm. The deconvoluted PL spectrum of sample D is shown in figure 5.9 (a), in which, like the deconvolution of samples E and F, the NBE and DLE emission bands are best fitted with two and four peaks, respectively. The peaks originating at 555nm, 610nm, 655nm and 710nm are attributed to optical transitions from the conduction band to O_i , Zn_i to O_i , conduction band to V_O and V_O to the valance band respectively [36–38]. Here, it is to be noticed that the integrated intensity of NBE band is large for sample D as compared to both the samples E and F, whereas the integrated intensity of DLE bands of samples E and F is higher than the sample D. In figure 5.9 (b), we have plotted the ratio of the total integrated intensity of $I_{Defectstates}/I_{FX}$ for samples D, E and F. From the plot, we observe that for the samples E and F, the ratio of integrated intensity of I_{O_i}/I_{FX} is almost double to the ratio of the integrated intensity of I_{V_O}/I_{FX} , and for sample D the I_{V_O}/I_{FX} is higher than the I_{O_i}/I_{FX} .

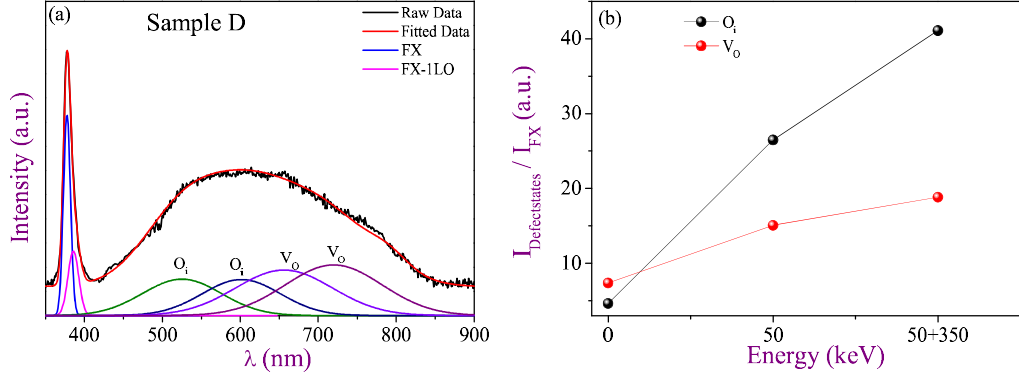


Figure 5.9: (a) Deconvoluted PL spectrum of sample D, (b) Plots the integrated intensity ratio of $I_{\text{Defectstates}}/I_{\text{FX}}$ peaks for the samples D, E and F.

The enhancement in the area under the curve of O_i over V_O is consistent with the fact that at above certain value of Φ the concentration of V_O saturates and the excess of incoming O^+ ions (5×10^{16} ions/cm²) concentration of O_i increases. During high-temperature annealing treatment of samples, some of the interstitials may significantly annihilate the V_O , whereas few of them may remain attach at the interstitials sites leading to dominating optical emissions over emissions associated with V_O . We attribute the decrease in intensity of NBE emissions of samples E and F to the nonradiative carrier transfer from the conduction band to the defect centres. From the results of PL measurements, we expect that the oxygen-rich environment in ZnO nanorods can be created by annealing the O^+ ion implanted nanorods, where O_i may act as acceptor levels and provide the p-type conductivity in ZnO nanorods as reported earlier [21].

5.4.3 Raman spectroscopy

In ionic crystal/polar semiconductors, the optical transitions are mainly governed by Frolich interactions [39,40], in which the relaxation of excited charge carriers occurs through the transition from the excited state to the ground state accompanied by the phonons. The Raman scattering measurement is a well-suited tool to obtain information about the sample quality in wide bandgap semiconductors [41–43] as well as to analyze more specific aspects of the lattice dynamics such as isotopic effects [44,45] and phonon lifetimes [46,47]. In group theory, the wurtzite structure ZnO belongs to the C^4_{6v} space group with two formula units in the primitive cell, and consists of eight zone-center(Γ) optical phonon modes and are described as:

$$\Gamma = 2A_1 + 2E_1 + 2E_2 + 2B_1 \quad (5.2)$$

These phonon modes are classified as Raman active ($2A_1 + 2E_1 + 2E_2$), infrared active ($2A_1 + 2E_1$), and silent ($2B_1$) modes. The room temperature Raman spectra of samples implanted with energy 100 keV (at three different Φ values) and samples A, B and C are shown in figure 5.10 (a) and (b), respectively. Two Raman peaks centered at 438 and 520cm^{-1} are appearing in the Raman spectrum of sample A, whereas in the Raman spectra of all the implanted samples (100keV and Samples B, and C) these two Raman modes are accompanied by an additional peak centred at 575cm^{-1} . The Raman peaks centered at 438 and 520cm^{-1} are associated with E_2 mode of wurtzite structure of ZnO and Si substrate, respectively. The additional Raman peak centered at 575cm^{-1} is assigned to the $A_1(\text{LO})$ mode [48, 49]. The appearance of additional $A_1(\text{LO})$ phonon mode is a characteristic of incorporation of defect states by O^+ ion implantation [49].

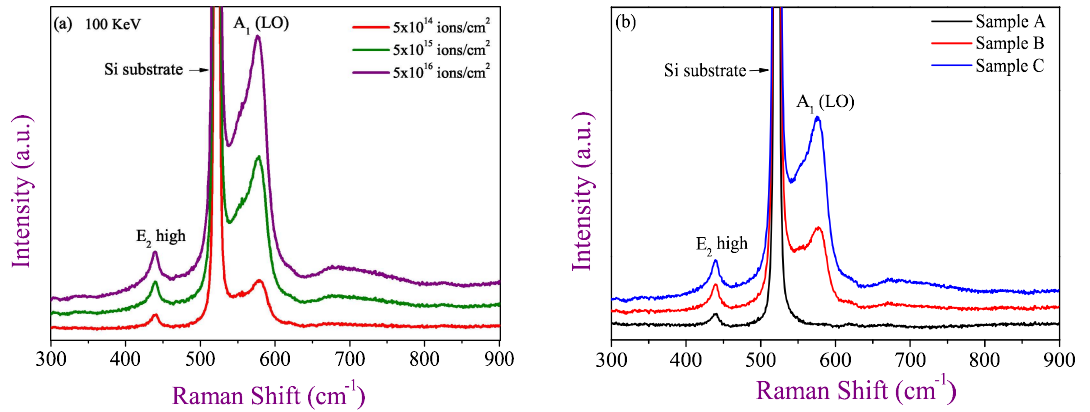


Figure 5.10: (a) and (b) RT Raman spectra of samples implanted with 100 keV energy, and samples A, B, and C, respectively.

5.5 Local electrical transport studies

The C-AFM technique was employed to address the influence of O^+ ion implantation on local electrical transport properties of ZnO nanorods. Figure 5.11 summarizes the pre-annealing and post-annealing treatment on the local electrical transport characteristics of implanted samples. The AFM images of the first derivative of local current maps of samples A - F were recorded at a fixed tip voltage $V_{tip} = +5\text{V}$, and are shown in panels (a) - (f), respectively. The inset of figure 5.11(a) shows the topography of as-grown nanorods. It is seen that the current maps of samples A, B, and C, and their respective post-annealed maps differ from each other. Here it is

worthwhile to mention that the first derivative of the current maps locates the current extrema. The points where the current derivative reaches its extrema correspond to the situations when the current changes its behavior from rising to decay or vice versa [50]. The figure 5.12 (a) and

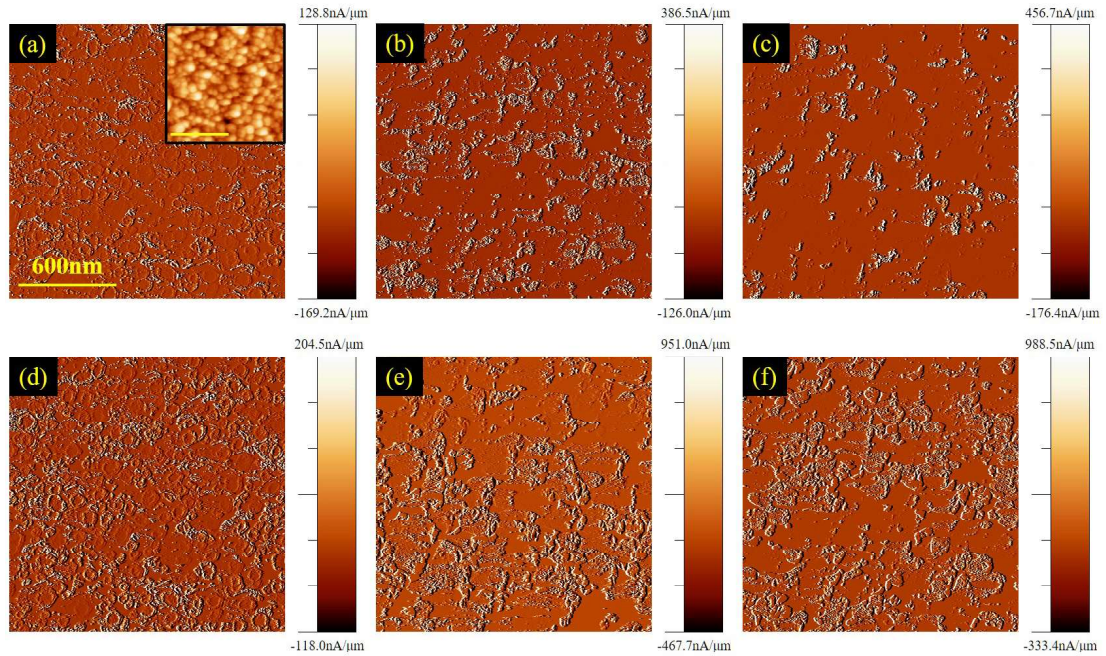


Figure 5.11: (a - c) First derivative 2D current map of sample A, B and C respectively. The inset of (a) shows topography of corresponding sample. (d - f) Post-annealing First derivative 2D current map of sample A, B, and C, respectively. The spatial scale in topography image and all current maps is kept fixed at 600nm.

(b) represents the magnified 2D current map of samples A and B, respectively. Panel (a) reveals a number of clear bursts coming from the side planes of the ZnO NRs. The current maps of the samples B and C exhibit more localized and intense current bursts compare to sample A (shown in figure 5.12 (b)), and we attribute it to the trapping of charge carriers in defect states present in the samples. A similar behavior is seen for the samples E and F, where samples E and F show more localized and intense current bursts compared to sample D. The high surface conductivity, and presence of various adsorbates on the surface of nanorods can be two different possibilities for such burst of current from the side facets of nanorods [51, 53]. Here, for the presence of various adsorbates to be a possible mechanism for such burst of current, the samples B and C must show improved current maps compared to samples D, E, and F because the high-temperature annealing eliminates the surface adsorbates. The post-implantation first derivative 2D current maps of samples B and C (figure 5.11 (b) and (c)) exhibit localized current burst indicating lowering the surface conductivity by trapping of free charge carriers

into defect states. The localization of current bursts suggests that high surface conductivity can

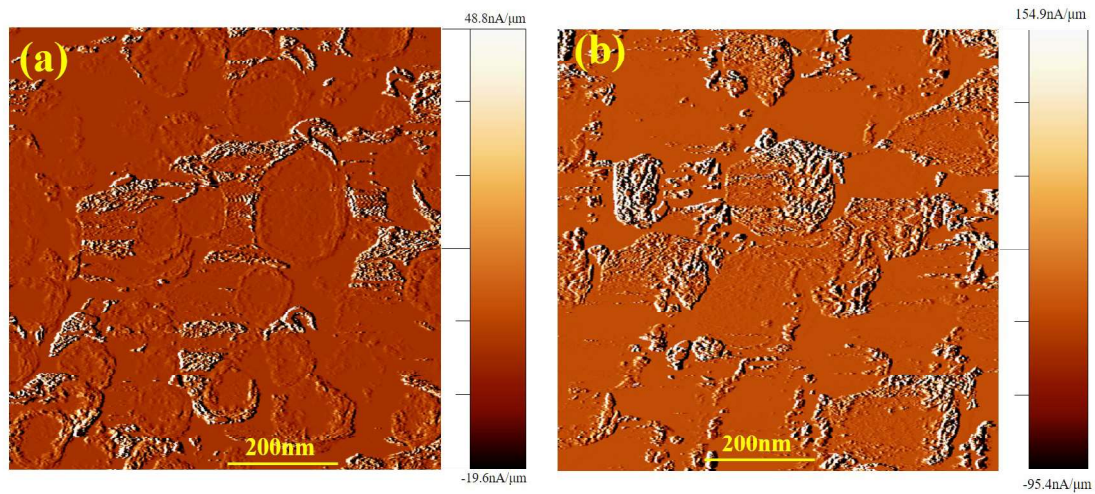


Figure 5.12: (a) and (b) Magnified view of first derivative 2D current map of samples A and B, respectively.

be a possible mechanism for the current from the side facets of sample A. As we have seen in figure 5.9 (b) that after annealing the samples at high temperature, the relative concentration of O_i increases (favored by excess of O^+ ions), which may be responsible for the modified local electrical transport characteristics of samples E, and F [52]. However, the calculations of charge carrier concentration by direct techniques like Hall measurements may provide in-depth insights about the influence of O^+ ion implantation on p-type conductivity in ZnO nanorods.

5.6 Summary

In summary, vertically aligned ZnO nanorods were grown on seeded Si substrates using the wet chemical method. The contributions from stopping energies (S_e and S_n) were simulated using SRIM simulation. The obtained results indicate that in ZnO matrix the electronic energy loss increases with increasing the energy of incident oxygen ions, whereas the nuclear energy loss decreases. As a result of this process, at low energies, the oxygen ions contribute mainly to the formation of vacancies, whereas at higher energies where S_e dominates over S_n the incident ions may create oxygen interstitials. The results of SRIM simulations showed that the projectile range of oxygen ions in ZnO matrix varies according to their energies. The FESEM and XRD measurements reveal the c-axis oriented hexagonal structure of ZnO nanorods and remain preserved even after implantation. The XPS results show that concentration of V_O is

lowest for the ion fluence of 5×10^{16} ions/cm² compared to other Φ values. We attribute it to the saturation of V_O and excess of O^+ ions in the ZnO nanorod matrix. Post-implantation, the optical absorption edge of samples showed a drop of $\sim 0.1e$. This we attribute to the V_O induced by O^+ ion implantation. Pre-annealing PL studies exhibit formation of nonradiative transition centers leading to complete suppression of NBE emission of ZnO nanorods. The post-annealing treatment in a vacuum, exhibit recovery of NBE emission followed by deep level emissions. The post-annealed PL spectra of implanted samples showed strong and dominating DLE band, whereas the post-annealed PL spectrum of as-grown nanorods showed dominating NBE emission over DLE band. The deconvoluted DLE band peaks are associated with O_i , and V_O . The strength of these transitions was found few orders of magnitude higher than the DLE transitions in as-grown sample confirming the formation of O^+ ion implantation induced point defects in nanorods. The analysis of deconvoluted PL spectra exhibited that with increasing energy (at a fixed Φ 5×10^{16} ions/cm²) the transitions from O_i dominate over the transitions associated with V_O , indicating O-rich environment in ZnO nanorods. Such characteristics are consistent with the fact that at higher Φ values (here Φ 5×10^{16} ions/cm²) the concentration of V_O saturates and the excess of O^+ ions may not only annihilate them at high-temperature annealing but also may create O_i . By considering previous reports, we expect that the dominating point defects associated with O_i in ZnO nanorods may form shallow acceptor levels, leading to the p-type conductivity in samples. However, measurements of majority carrier concentration using techniques like Hall effect measurement will provide in-depth insights about the p-type conductivity in ZnO nanorods by creating an O- rich environment using O^+ ion implantation. The first derivative 2D current map of as-grown nanorods exhibits current burst from the side facets of nanorods, whereas it is more localized for implanted samples. The high surface conductivity of ZnO is responsible for such burst from side facets, whereas the defect states created by implantation may be responsible for the localization of current bursts. The post-annealing treatment improved the local electrical transport characteristics of the samples compared to the pre-annealing treatment of their counterparts. The findings suggest that ion implantation facilitates defects formation up to the desired depth in nanorods by choosing appropriate energy. The excess of O^+ ions increases the concentration of point defects associated with O_i in the specific regions. Such depth selective defects can be utilized for the fabrication of p-n junction/p-n-p-n tandem junction in a single ZnO nanorod.

Bibliography

- [1] R. F. Service, *Science*, **1997**, 276, 895.
- [2] Z. K. Tang, G. K. L. Wong, P. Yu, M. Kawasaki, A. Ohtomo, H. Koinuma, and Y. Segawa, *Appl. Phys. Lett.*, **1998**, 72, 3270.
- [3] D. C. Look, *Mater. Sci. Eng.*, **2001**, B 80, 383.
- [4] J. S. Hwang, F. Donatini, J. Pernot, R. Thierry, P. Ferret and L. S. Dang, *Nanotechnology*, **2011**, 22, 475704.
- [5] J. Zhang, W. Que, *Sol. Energy Mater. Sol. Cells*, **2010**, 94, 2181.
- [6] S. Phadke, J. Y. Lee, J. West, P. Peumans, A. Salleo, *Adv. Funct. Mater.*, **2011**, 21, 4691.
- [7] N. Kouklin, *Adv. Mater.*, **2008**, 20, 2190.
- [8] H. Yin, C. Songa, Z. Wang, B. Guob, K. Yu, *Appl. Surf. Sci.*, **2015**, 345, 256.
- [9] A. Singh, K. Senapati, M. Kumar, T. Som, A. K. Sinha, P. K. Sahoo, *Appl. Surf. Sci.*, **2017**, 411, 117.
- [10] Q. X. Zhao, P. Klason, M. Willander, H. M. Zhong, W. Lu, and J. H. Yang, *Appl. Phys. Lett.*, **2005**, 87, 211912.
- [11] M. Wang, F. Ren, J. Zhou, G. Cai, L. Cai, Y. Hu, D. Wang, Y. Liu, L. Guo and S. Shen, *Scientific Reports*, **2015** 5, 12925.
- [12] S.B. Zhang, S.H. Wei, A. Zunger, *Phys. Rev. B*, **2001**, 63, 075205.
- [13] P. Wang, NuoFu Chen, and Z. G. Yin, *Appl. Phys. Lett.*, **2006**, 88, 152102.
- [14] G. Du, Y. Ma, Y. Zhang, and T. Yang, *Appl. Phys. Lett.*, **2005**, 87, 213103.

- [15] B. Chavillon et al., *J. Am. Chem. Soc.*, **2012**, 134, 464.
- [16] Y. J. Zeng, Z. Z. Ye, J. G. Lu, W. Z. Xu, L. P. Zhu, B. H. Zhao, and S. Limpijumnong, *Appl. Phys. Lett.*, **2006**, . 89, 042106.
- [17] D. C. Look, G. M. Renlund, R. H. Burgener, and J. R. Sizelove, *Appl. Phys. Lett.*, **2004**, 85, 5269.
- [18] Y. Ma et al., *J. Appl. Phys.*, **2004**, 95, 6268.
- [19] M. S. Oh, S. H. Kim, and T. Y. Seong, *Appl. Phys. Lett.*, **2005**, 87, 122103.
- [20] Y. Y. Liu, H. J. Jin, and C. B. Park, *Trans. Electr. Electron. Mater.*, **2009**, 10, 24.
- [21] U. Ilyas, R. S. Rawat, T. L. Tan, P. Lee, R. Chen, H. D. Sun, Li Fengji, and S. Zhang, *J. Appl. Phys.*, **2011**, 110, 093522.
- [22] T. V. Butkhuzi, A. V. Bureyev, A. N. Georgobiani, N. P. Kekelidze, and T. G. Khulordava, *J. Cryst. Growth*, **1992**, 117, 366.
- [23] A. N. Georgobiani, M. B. Kotlyarevskii, V. V. Kidalov, L. S. Lepnev, and I. V. Rogozin, *Inorg. Mater.* , **2001**, 37, 1287.
- [24] S. Chattopadhyay et al., *J. Appl. Phys*, **2010**, 107, 113516.
- [25] L. Vayssieres, *Adv.Mater.*, **2003**, 15, 464.
- [26] J. P. Biersack, L. Haggmark, *Nucl. Instrum. Methods*, **1980**, 174, 257. (also refer to www.srim.org).
- [27] A. Singh, K. Senapati, D.P. Datta, R. Singh, T. Som, S. Bhunia, D. Kanjilal, P. K. Sahoo, *Nucl. Instrum. Meth. Phys. Res. B*, **2017**, 409, 143.
- [28] Y. Sun, J. H. Seo, C. J. Takacs, J. Seifter, and A. J. Heeger, *Adv. Mater.*, **2011**, 23, 1679.
- [29] K. K. Banger, et al., *Nat. Mater.*, **2011**, 10, 45.
- [30] E. Wendler et al., *Nuc. Inst. Meth. Phys. Res. B*, **2009**, 267, 2708.
- [31] Z. Q. Chen, M. Maekawa, A. Kawasuso, S. Sakai, H. Naramoto, *Physica B*, **2006**, 722, 376.

- [32] J. Tauc, R. Grigorovici, A. Vancu, *Physica status solidi (b)*, **1966**, 15, 627.
- [33] J. Wang, Z. Wang, B. Huang, Y. Ma, Y. Liu, X. Qin, X. Zhang, and Y. Dai, *Appl. Mater. Interfaces*, **2012**, 4, 4024.
- [34] Z. Q. Chen, A. Kawasuso, Y. Xu, H. Naramoto, X. L. Yuan, T. Sekiguchi, R. Suzuki, and T. Ohdaira, *J. Appl. Phys.*, **2005**, 97, 013528.
- [35] H. B. Bebb and E. W. Williams, ed. R. K. Willardson and A. C. Beer, Academic, New York, **1972**, 8, 181.
- [36] B. Lin, Z. Fu and Y. Jia, *Appl. Phys. Lett.*, **2001**, 79, 943.
- [37] N. H. Alvi, K. U. Hasan, O. Nur, M. Willander, *Nanoscale Research Letters*, **2011**, 6, 130.
- [38] C. H. Ahn, Y. Y. Kim, D. C. Kim, S. K. Mohanta, and H. K. Cho, *J. Appl. Phys.*, **2009**, 105, 013502.
- [39] H. Frohlich, H. Pelzer, S. Zienau, *Phil. Mag.*, **1950**, 41, 221.
- [40] H. Frohlich, *Adv. Phys.*, **1954**, 3, 325.
- [41] N. Hasuike, H. Fukumura, H. Harima, K. Kisoda, H. Matsui, H. Saeki, and H. Tabata, *J. Phys. Condens. Matter*, **2004**, 16, S5807.
- [42] W. Limmer, W. Ritter, R. Sauer, B. Mensching, C. Liu, and B. Rauschenbach, *Appl. Phys. Lett.*, **1998**, 72, 2589.
- [43] D. Pastor, R. Cusc, L. Arts, G. Gonzalez-Daz, S. Fernandez, and E. Calleja, *Semicond. Sci. Technol.*, **2005**, 20, 374.
- [44] A. Gbel, T. Ruf, C.-T. Lin, M. Cardona, J.-C. Merle, and M. Joucla, *Phys. Rev. B*, **1997**, 56, 210.
- [45] J. M. Zhang, T. Ruf, M. Cardona, O. Ambacher, M. Stutzmann, J.-M. Wagner, and F. Bechstedt, *Phys. Rev. B*, **1997**, 56, 14399.
- [46] J. Serrano, F. J. Manjn, A. H. Romero, F. Widulle, R. Lauck, and M. Cardona, *Phys. Rev. Lett.*, **2003**, 90, 055510.

- [47] L. Bergman et al., Phys. Rev. B, **1999**, 59, 12977.
- [48] J. M. Calleja and M. Cardona, Phys. Rev. B, **1977**, 16, 3753.
- [49] R. Cusco, E. A. Llado, J. Ibanez, L. Artus, J. Jimenez, B. Wang, M. J. Callahan, Phys. Rev. B, **2007**, 75, 165202.
- [50] I. Beinik et al., J. Appl. Phys., **2011**, 110, 052005.
- [51] H. J. Krusemeyer, Phys. Rev., **1959**, 114, 655.
- [52] S. M. Hatch, J. Briscoe, A. Sapelkin, W. P. Gillin, J. B. Gilchrist, M. P. Ryan, S. Heutz, and S. Dunn, J. Appl. Phys., **2013**, 113, 204501.
- [53] G. Sberveglieri, Sens. Actuators B, **1995**, 23, 103.

Chapter 6

Nonlinear optical properties of Mn-doped ZnO nanorods

The materials possessing noncentrosymmetry (absence of inversion symmetry) exhibit second-order non-linear characteristics, whereas, the third-order nonlinear optical process may occur for both centrosymmetric and noncentrosymmetric materials. In the era of quantum electronics, materials of large third order susceptibility are of immense interest owing to their applications in high-speed nonlinear optical devices like optical switches, self-phase modulators [1, 2]. In recent years, the nonlinear optical studies on ZnO have gained wide attention for its special properties like non-centrosymmetric crystal symmetry, direct and wide band gap with large exciton binding energy and a wide range of sub-wavelength nanostructures. In ZnO based sub-wavelength structures, the structural resonance effects significantly enhanced optical nonlinear characteristics compared to their bulk counterpart [3, 4]. In addition, the resonant excitonic transitions from defect states and the inbuilt polar potential with unequal atomic radii also significantly contribute to enhancing their nonlinear characteristics [5–7]. However, the structural arrangement and spatial atomic arrangement strongly depend on their growth process [8]. Interestingly, the magnetization induced modifications in nonlinear optical (NLO) susceptibilities can improve the NLO characteristics remarkably. In literature, the ferromagnetic ordering in ZnO sub-wavelength structures is achieved by doping of impurities like Mn, Co, Ni, and Fe [9–12]. Among these dopants, Mn doping in ZnO has gained wide attention owing to its high thermal solubility, isovalent bonding nature, match of the ionic radius ($\text{Mn}^{2+} = 0.8\text{\AA}$) with Zn ($\text{Zn}^{2+} = 0.76\text{\AA}$) and fine lattice-matching with the ZnO lattice constant [3, 13]. The theoretical calculations predict the max solubility of Mn in ZnO matrix about 35% while keeping wurtzite structure of ZnO, which limits the doping of Mn into ZnO at higher concentration [3].

In literature, it reported that Mn doping in ZnO stabilizes an oxygen-deficient Mn_xO_y secondary phase, resulting in an exchange interaction between magnetic moments localized at Mn sites mediated by free charge carriers. Such exchange interactions lead to a resultant magnetization which can contribute in enhancing nonlinear susceptibilities ($\chi_{(ijk)}^{(2)}$, $\chi_{(ijk)}^{(3)}$ etc.) as stated above. By considering all the above facts, one can expect that the Mn doping in ZnO sub-wavelength structures may incorporate additional electric-dipole contribution from structural resonance and magnetization-induced effects, which may considerably differ their NLO characteristics from bulk ZnO and/or thin films. However, despite numerous studies on NLO characteristics of ZnO [14–17], detailed investigations on third-order NLO properties of Mn-doped ZnO based sub-wavelength structures still need to be accomplished. In this chapter comprehensive investigations on nonlinear refractive-index (NLR) and two-photon absorption (TPA) coefficient for different molar fractions of Mn-doping in ZnO nanorods grown by the aqueous growth method are presented.

6.1 Experimental specification

As mentioned in chapter 2, commercially purchased glass substrates coated with a thin layer (500 nm) of Indium Tin Oxide (ITO), were used for the growth of ZnO nanorods. Prior to growth, substrates were cleaned in solution of $3HCl + HNO_3$ followed by cleaning in deionized water. The details of substrate cleaning are described in chapter 2. For the growth of nanorods, the wet chemical single-step hydrothermal method was employed, where the Mn ions were doped into nanorods at four different molar percentages of 0.5%, 1.5%, 2.0%, and 2.5%. For this purpose, an appropriate amount manganese chloride tetrahydrate was added in aqueous solutions of precursor zinc nitrate hexahydrate and HMT [5] and followed by heating the solution in a laboratory oven at $90^{\circ}C$ for 6 hours. The rest of the process remained similar to the growth of vertically aligned nanorods described in chapter 5. The morphological and structural characterization of Mn-doped nanorods were carried out using FESEM and XRD techniques. For the confirmation of Mn-doping, the elemental analysis of nanorods was performed using energy dispersive X-ray spectroscopy (EDX), attached with the FESEM system. The impact of Mn-doping on optical absorption edge and NBE emissions of nanorods were investigated using UV-Visible and PL spectroscopy, respectively. The Z-scan technique was employed for the study of the influence of Mn-doping on NLO characteristics of nanorods,

where a Q switched diode-pumped solid-state (DPSS) laser emitting linearly-polarized, sub-nanosecond pulses in a TEM_{00} mode intensity profile was used as an excitation source [5]. During experiments, the pulse energy varied from $1 \mu\text{J}$ to $125 \mu\text{J}$ with pulse width $t_p \sim 0.7\text{ns}$ at 40 Hz repetition rate, to minimize the impact of thermally induced optical nonlinearities. Using a converging lens of focal length 150mm the beam was focused with a spot size $w_0=45\mu\text{m}$, resulting in Rayleigh length ($z_0 = \pi w_0^2 / \lambda$) $\sim 12\text{mm}$. This Rayleigh length ensures negligibly small sample plus substrate thicknesses compared to z_0 . Throughout the measurements, the samples have translated a distance of 100 mm across the focal point followed by measuring the transmitted power both in open-aperture (OA) and closed-aperture (CA) configuration using a fast photodiode sensor (Model S120C, Thorlabs Inc.). The experimental setup of the Z-scan technique is shown in chapter 2.

The outcomes of influence of point defects on structural and optical (Nonlinear) properties are discussed in following sections.

6.2 Morphological and structural studies

6.2.1 SEM and XRD study

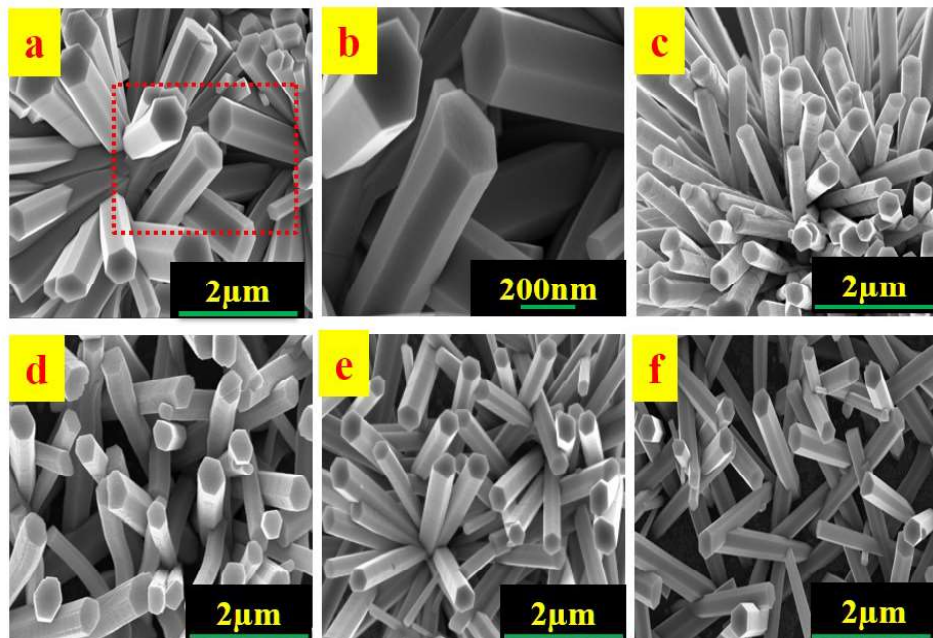


Figure 6.1: (a) FESEM micrograph of undoped ZnO nanorods, (b) enlarge view of red marked area of panel (a). (c - f) FESEM images of Mn-doped ZnO nanorods at molar concentration 0.5%, 1.5%, 2.0% and 2.5% respectively [5].

The morphological evolution of undoped and Mn-doped ZnO nanorods is presented in figure 6.1, where panel (a) shows the FESEM micrograph of undoped ZnO nanorods, and the images of nanorods doped with Mn at molar concentrations 0.5%, 1.5%, 2.0% and 2.5% are shown in panels (c - f) respectively. Figure 6.1 (b) shows the magnified view of the rectangular area (red marked) of the panel (a). From FESEM images it is clear that on ITO coated glass substrates, nanorods are randomly oriented unlike the vertically aligned nanorods shown in chapter 5. However, the hexagonal shape of ZnO nanorods remains preserved even after Mn doping. The dimensional analysis of nanorods carried out using software ImageJ [18] reveal that nanorods were of average length $\sim 2 - 4 \mu\text{m}$ and diameter $\sim 400 - 600\text{nm}$. In order to ensure the Mn doping in ZnO nanorods, energy dispersive spectroscopy was employed. Figure 6.2 shows the EDX elemental mapped results of sample doped with 2.0% & 0.5% molar concentration of Mn. Panel (a) represents the EDX image of 2.0% Mn-doped nanorods from which a single nanorod was selected (Red-marked area) for the elemental mapping. Panels (b), (c) and (d) show the elemental maps of Zn, O, and Mn respectively. A combined mapping of all these elements is

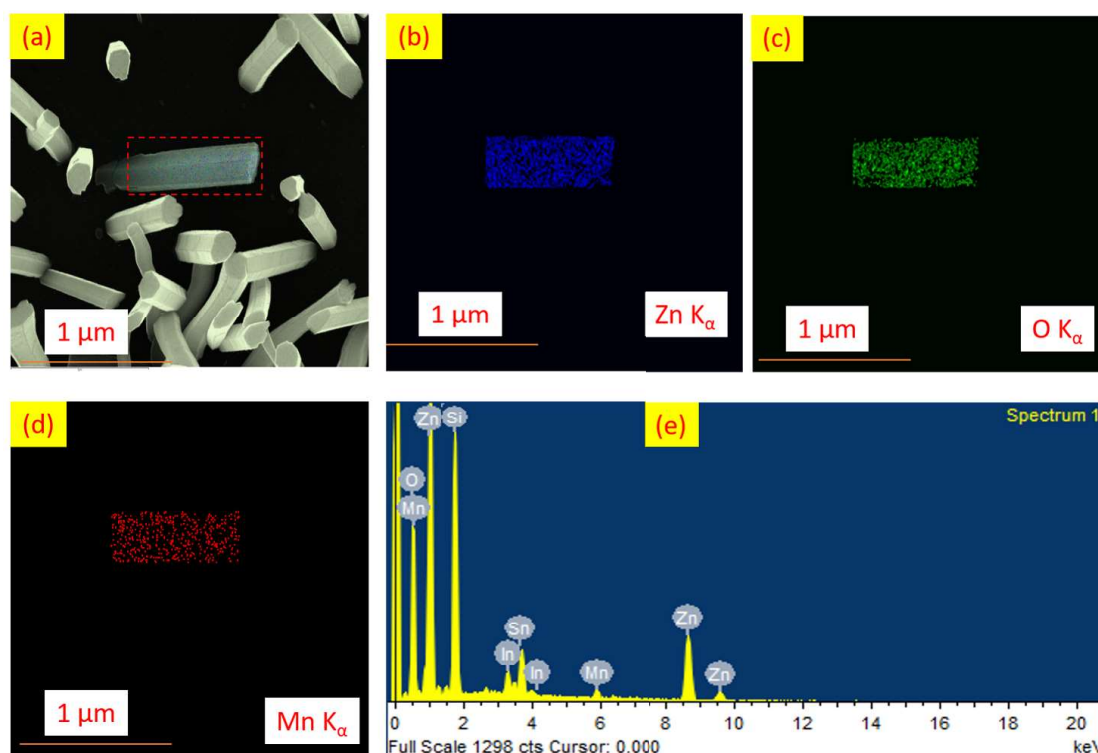


Figure 6.2: (a) EDX image of the nanorods doped with 2.0% of Mn. The red-marked zone represents the area from where the elemental mapping was performed. (b), (c) and (d) EDX mapped elemental maps of Zn, O, and Mn signals, respectively. (e) EDX spectrum acquired from the 0.5% Mn-doped ZnO nanorods.

shown in the Red-marked zone of panel (a), where the presence of Mn maps confirms the Mn-doping in nanorods. In addition, an EDX spectrum recorded from the sample doped with 0.5% Mn is shown in panel (e), where the presence of Mn signal further confirms doping in nanorods even at low concentration. Typical glancing angle (0.5°) X-ray diffraction patterns of undoped and 2.5% Mn-doped ZnO nanorods are shown in figure 6.3 (a). The sharp and intense (002) Bragg diffracted peak in both XRD patterns exhibit the preferential growth of nanorods along the c-axis with wurtzite hexagonal phase. The appearance of hexagonal phase of nanorods is consistent with the FESEM results.

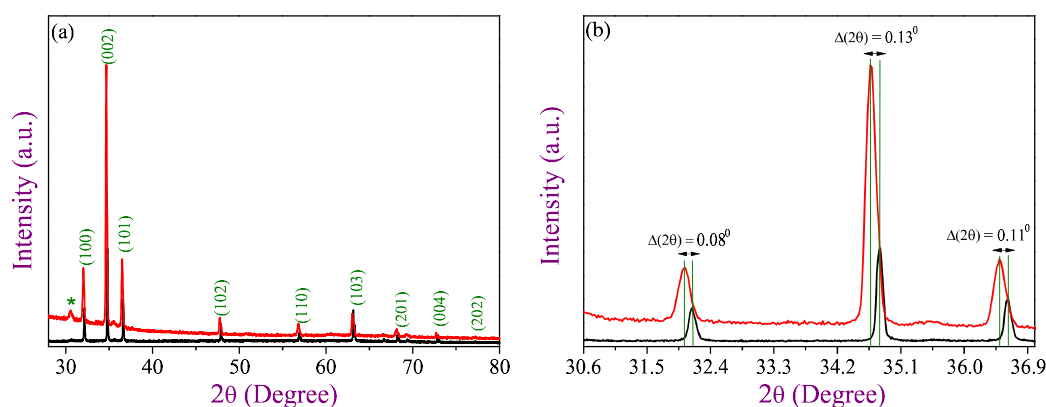


Figure 6.3: (a) Glancing angle XRD patterns of undoped and 2.5% Mn-doped ZnO nanorods. (b) The magnified view of (100), (002) and (101) Bragg diffracted peaks. The Green vertical lines are guide for eyes and show the difference between two Bragg peaks [5].

The perseverance of wurtzite structure indicates possible Mn-doping throughout the nanorods as also seen in the EDX mapping [5]. We notice that except for the (002) peaks, some other Bragg peaks of ZnO indexed as (100), (101), (102), (110), (103), (201), (004) and (202) are also present. However, none other phases related to other oxides or Mn ions are observed. The lattice mismatch between ITO and ZnO can be a possible cause for the presence of such additional phases of ZnO. The panel (b) of figure 6.3 represents the enlarged view of (100), (002) and (101) Bragg diffracted peaks. Interestingly post Mn-doping, these Bragg peaks show a remarkable shift towards lower theta value like the earlier reports [10]. The shift in Bragg peaks is consistent with the fact that such shift in XRD patterns originates from the replacement of Zn^{2+} ions by Mn^{2+} ions. The replacement of Zn^{2+} ions of lower ionic radius by Mn^{2+} ions of larger ionic radius results in the evolution of stress in the host matrix, which is responsible for such shift by the expansion of the unit cell [10]. In XRD patterns, the peak marked as * is

originating from ITO substrate.

6.3 Optical properties

This section is devoted to the study of the influence of Mn-doping on luminescent, absorption and nonlinear absorption characteristics of Mn-doped ZnO nanorods, using PL, UV-visible spectroscopy, and Z-Scan technique respectively.

6.3.1 Study of near band edge emission and absorption edge

Panel (a) of figure 6.4 shows the PL spectra of Mn-doped samples. For a comparative study of the influence of Mn-doping on luminescent characteristics of ZnO nanorods, the room temperature PL spectrum of un-doped nanorods is shown in the inset of figure 6.4 (a). The PL spectrum of each doped sample shows a dominating UV emission followed by an emission center in the visible range, whereas the PL spectrum of the undoped sample exhibits only the NBE excitonic transition. The presence of such additional emission is a distinct signature of the presence of defect states caused by Mn-doping and can be associated with either zinc vacancies (V_{Zn}) or oxygen vacancies (V_O). Except for additional emission center, an asymmetry is also seen in the PL spectra of Mn-doped samples, indicating either the strong electron-phonon interaction in the subsystem or the presence of some other transition centers. However, a detailed analysis of these PL spectra can provide better insight into the evolution of various defect states induced by Mn-doping, and is presented in the next section. The appearance of visible emissions and asymmetry in PL spectra of Mn-doped nanorods insist for the study of the absorption edge of the samples, because the presence of defect states may modify the absorption edge of ZnO nanorods [19]. For this purpose, the study of the absorption edge of Mn-doped ZnO nanorods was carried out using UV-visible spectroscopy and the absorption spectra of undoped and Mn-doped samples are presented in panel (b) of figure 6.4. An asymmetry in the absorption spectra of Mn-doped samples is observed. This can be attributed to the presence of various defect states like Zn_i , V_{Zn} or V_O , close to the band-edge, and may offer new absorption edge. In order to extract the absorption edge of undoped and doped samples, their respective absorption spectra were converted into Tauc plots [20] and are shown in figure 6.4 (c). At the $h\nu$ turning point, the linear part of each Tauc plot is fitted with a straight line (dotted line) followed by its extrapolation up to the intersection at the energy axis. Panel (d) plots the extracted values

of absorption edge (band gap) as a function of Mn concentration(%), where the zero value of Mn concentration represents the undoped sample. From the plot, it is observed that the band gap of Mn-doped samples shows a drop of around 0.7eV compared to un-doped sample. Such narrowing nature of absorption edge of nanorods is reported as due to V_{Zn} or V_O [21] and supports our argument to assign visible emission in PL spectra to V_{Zn} or V_O . The presence of these defect states may introduce two-photon absorption (TPA) in Mn-doped nanorods for a frequency-doubled near-infrared laser excitation source of wavelength 532 nm. For the detailed study of asymmetry in PL peaks and confirmation of the presence of defect states we deconvoluted each PL spectrum.

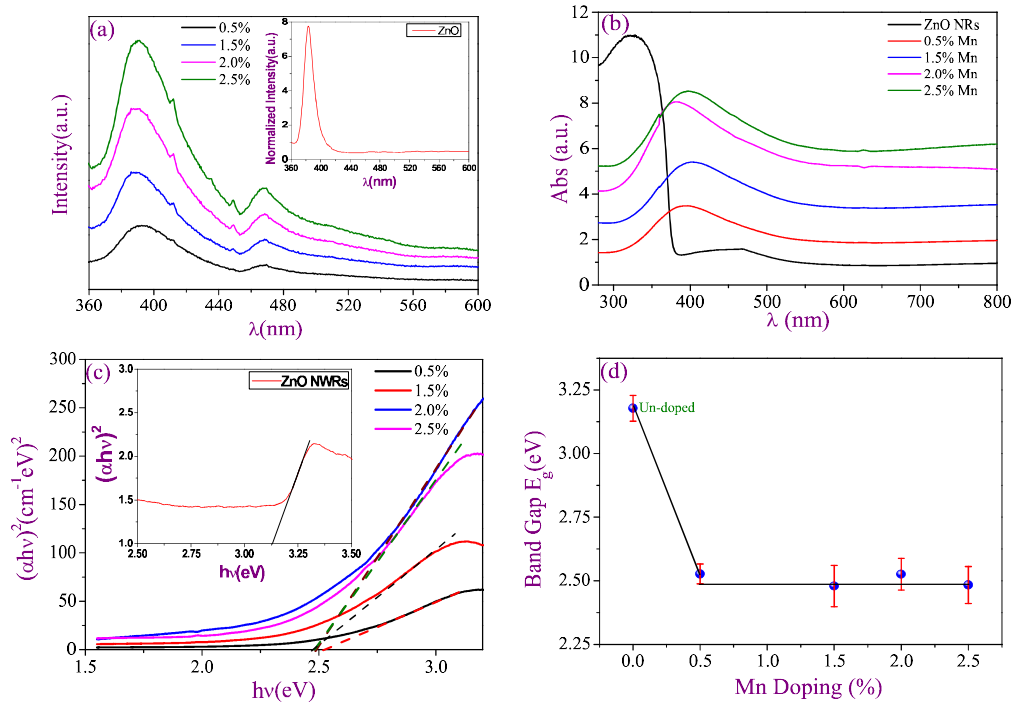


Figure 6.4: (a) Room temperature (RT) PL spectra of Mn-doped ZnO nanorods. The inset shows RT PL spectrum of undoped ZnO nanorods. (b) Absorption spectra of undoped and Mn-doped ZnO nanorods. (c) Tauc plots of Mn-doped nanorods, the dotted lines are eye guide for extracting band gap from these plots. The inset depicts extraction of the band gap from the Tauc plot of undoped nanorods by fitting a straight line (Black solid line). (d) A symbolic plot for extracted band gap of undoped and Mn-doped nanorods. The black solid lines are eye guides for variation in band gap [5]. The error bars were obtained from the fitting of straight line in the respective Tauc plots.

Figure 6.5 (a) and (b) show the sample images of deconvoluted PL spectra of un-doped

and 0.5% Mn-doped samples. Distinct differences are seen in these spectra. The PL spectrum of the un-doped sample is fitted with two peaks centered at 382.5 nm (3.24eV), and 391nm (3.17eV), and we attribute them as FX and FX-1LO peaks. Each PL spectrum of Mn-doped samples was fitted with six peaks including FX (382.5 nm) common to un-doped sample and five other peaks originating at 395nm (3.14eV), 418.5nm (2.96eV), 436.5nm (2.84eV), 477nm (2.59eV), and 498nm (2.49eV). In literature, the transition energy 3.14eV is attributed to the optical transitions from Zn_i to the valence band [22]. The optical transitions originating at 2.96eV, and 2.84eV are attributed to the transitions from conduction band (C.B.) to O_i [23], and Zn_i to Zn_O [22], respectively.

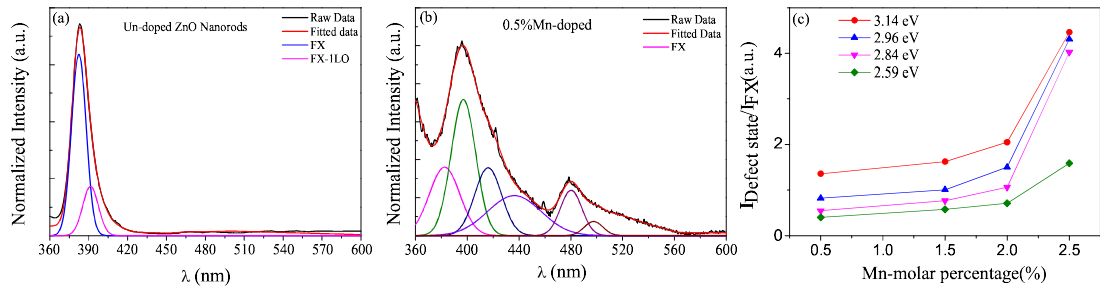


Figure 6.5: (a), (b) Sample deconvoluted spectra of un-doped and 0.5% Mn-doped ZnO nanorods, respectively. (c) Plots for the $I_{Defect-state}/I_{FX}$ versus Mn-doping percentage.

The peaks emerging at 2.59eV and 2.49eV are attributed to the C.B. to V_O and Zn_i to V_O [22]. In addition, the PL spectra of doped samples exhibit dominant nature of transitions associated with Zn_i over FX emissions, which indicates that after Mn-doping has replaced Zn ions at the interstitials as seen in XRD pattern as well (figure 6.3 (b)), and the optical transition probability of these states is higher than the FX emissions. For clarity, with Mn-doping percentage, we have plotted the ratios of the integrated intensities of each defect-related emission and the integrated intensity of FX emission ($I_{Defect-state}/I_{FX}$) and is shown in figure 6.5 (c). The variation in the plot shows that with increasing doping percentage, the concentration of defect-levels increases which further confirms Mn-doping in nanorods.

6.3.2 Nonlinear optical properties

The NLO spectra of undoped and 0.5% Mn-doped nanorods are presented in figure 6.6, and were recorded in the transmittance mode by translating the samples about their focal points. The transmitted light from the samples is measured in two geometries: (a) close aperture (CA)

and (b) open aperture (OA) modes. The power density of the incident light was ranging between 1-3 GWcm⁻², for both the geometries. The CA transmittance plots of undoped and 0.5% Mn-doped nanorods are shown in figure 6.6 (a) and (c), respectively, and panels (b) & (d) show the OA transmittance spectra of both the respective samples. Details of the NLO characteristics of Mn-doped samples as a function of doping % can be found in our paper Singh and Kumar et. al. [5]. The pre-focal maxima and post-focal minima in CA transmittance plots of both the undoped and 0.5% Mn-doped nanorods samples exhibit the feature of self-defocusing effect or negative value nonlinear refractive index (n_2). A similar characteristic was seen for other Mn-doping concentrations (not shown here). In both the figures 6.6 (b) and (d) a dip are seen at the focal point in the OA transmittance, suggesting a positive value of the TPA coefficient(β). Interestingly, for other Mn-doping concentrations, at focal point a peak is observed in the OA transmittance plots [5], which was not seen earlier. The peak in OA transmittance plots indicates saturable absorption characteristic for Mn-doping greater than 0.5%. In order to identify any contribution from the substrate, CA and OA transmittance measurements were performed under identical experimental conditions, indicating an almost negligible contribution from the substrate. For the analysis of NLO characteristics of both samples, the experimental plots were fitted with equation 6.1 and 6.2, which provide the theoretical essence of normalized transmittance in CA and OA geometries respectively [24, 25].

$$T(z, \Delta\phi_0) = 1 - \frac{4\Delta\phi_0 x}{(x^2 + 9)(x^2 + 1)} - \frac{2(x^2 + 3)\Delta\psi_0}{(x^2 + 9)(x^2 + 1)} \quad (6.1)$$

$$T(z, S = 1) = 1 - \frac{\beta I_0 L_{eff}}{2^{3/2}(x^2 + 1)} \quad (6.2)$$

Where $x = z/z_0$, $\Delta\phi_0 = kn_2 I_0 L_{eff}$ is phase change due to nonlinear refraction, and $\Delta\psi_0 = \beta I_0 L_{eff}/2$ is phase change due to nonlinear absorption. I_0 is the on-axis irradiance at focus ($z = 0$), L_{eff} is the effective sample thickness and $S = 1$ corresponds to the OA geometry.

The nonlinear optical parameters (n_2 and β) for undoped nanorods were found 2.1×10^{-10} cm² W⁻¹ and 3.5×10^{-5} cm W⁻¹, whereas for 0.5% Mn-doping were found -1.88×10^{-10} cm W⁻¹ and 1.32×10^{-5} cm W⁻¹ respectively [5]. From CA transmittance plots it can be seen that both the undoped and Mn-doped ZnO nanorods exhibit self-defocusing effects with an order of magnitude higher n_2 values compared to ZnO thin films [14, 16, 17, 26]. Even though, there is a significant degree of inconsistency in the sign of nonlinear absorption (β) of ZnO thin-films, and the β values for Mn-doped ZnO nanorods exhibit significantly higher values in

comparison to ZnO thin-films [14, 16, 17, 26]. One may notice the geometrical arrangement of nanorods from the figure 6.1, where even nanorods are randomly oriented but a small scale ordering exists in the geometrical arrangement of nanorods. Such small-scale ordering within the architecture provides a FabryPerot-like localized resonance resulting in the enhancement of the local field and resulting in the higher n_2 and β values in undoped nanorods as compared to thin films [27, 28]. For Mn-doping, along with the enhancement of the local field the presence of additional defect states enhances NLO interactions causing the higher n_2 and β values. We notice that both the undoped and 0.5% Mn-doped nanorods samples TPA absorption unlike the higher doping concentration of Mn (not shown here). For 0.5% Mn-doping, TPA is attributed to its absorption edge, whereas for undoped ZnO nanorods it takes place through some virtual states [17].

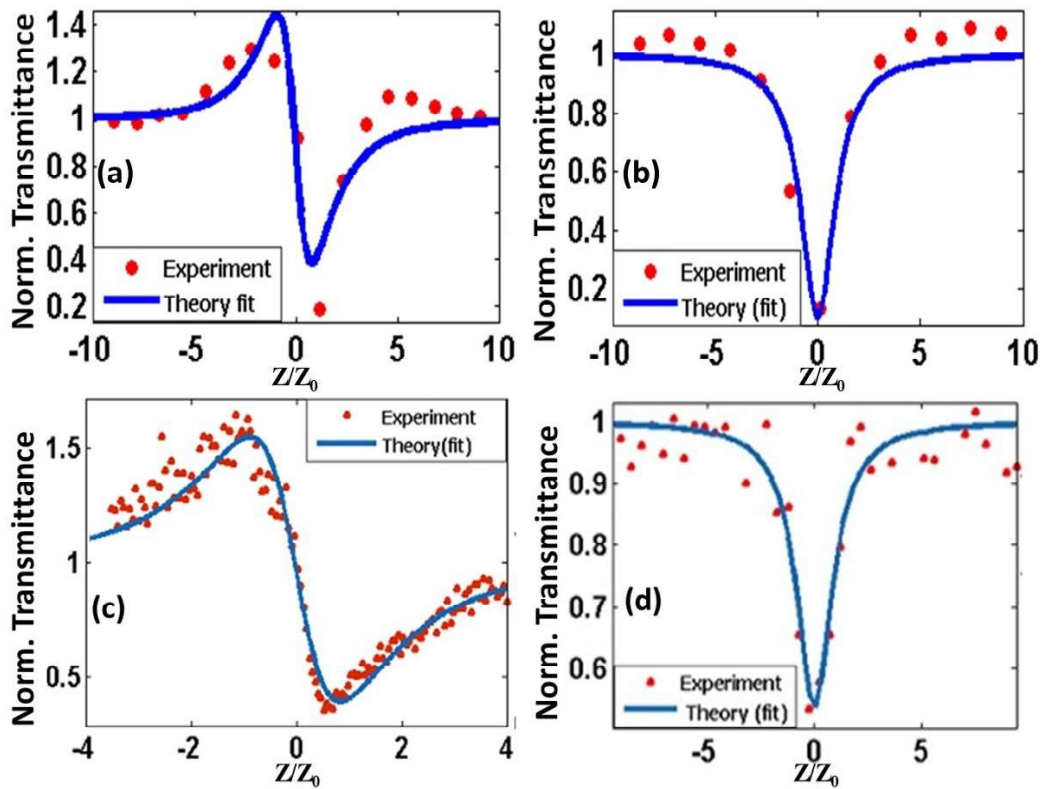


Figure 6.6: (a, c) Close aperture (CA) transmittance plots of undoped and 0.5% Mn-doped nanorods respectively. (b, d) open aperture (OA) transmittance plots undoped and 0.5% Mn-doped nanorods, respectively. In each plot, solid lines are the theoretical fits to the experimental data.

Assuming band-to-band transitions take place via the simultaneous absorption of two photons, the defect-state essentially mediates the transition from lower energy band to a higher

band. In addition, the relaxation lifetimes from defect-state to ground-state are smaller for lower Mn-doping concentrations. This reduces the possibility of saturation for the defect state and enhances the probability of absorption of photons at higher intensities.

6.4 Summary

In summary, Mn-doped ZnO nanorods were grown on ITO coated glass substrates using the relatively low-temperature wet chemical method. The FESEM investigations exhibit that the hexagonal morphology of nanorods remains preserved even after Mn-doping. The presence of Mn signal in both the EDX map and spectrum confirmed Mn-doping in ZnO matrix. The shift towards lower 2θ value in XRD pattern further confirmed the doping of Mn at Zn sites resulting in expansion of ZnO unit cell. The study of the influence of point defects introduced by Mn doping on optical properties of ZnO nanorods exhibit a significant impact on PL and absorption edge. The Tauc plots showed a drop of 0.7eV in the band gap of Mn-doped samples compared to un-doped sample, and we attribute this to V_{Zn} and/or V_O . A significant difference between PL spectra of undoped and doped samples is seen, where the doped samples exhibit asymmetric UV emission followed by deep level emission, whereas the undoped nanorods exhibit only NBE emission. Such deep level emissions are the distinct signature of defect states associated with either V_{Zn} or V_O . The deconvolution analysis of each PL spectrum showed that Mn-doping in ZnO nanorods introduces various defect centers including Zn_i , O_i , V_{Zn} , and V_O , where the Zn_i dominate over other centers. The presence of dominating Zn_i supports the shift in XRD pattern and confirms the Mn doping at Zn sites. The CA nonlinear optical measurements on undoped and 0.5% Mn-doped nanorods exhibit self-defocusing effect with significantly higher n_2 values as compared to ZnO thin films. Mn-doping introduced randomly distributed point defects in ZnO nanorods. The defects introduce virtual mid-gap states resulting in the modifications in the band structure of nanorods. This leads to the large third-order NLO behavior of ZnO nanorods with Mn-doping. In OA measurements the TPA characteristics for 0.5% Mn-doping is attributed to its absorption edge, which is modified by the point defects. The NLO characteristics investigations suggest that Mn-doping in ZnO nanorods facilitates improved NLO interactions and can be utilized for fabricating ultra-fast photonic switches, efficient optical phase-shifters, and optical limiters etc.

Bibliography

- [1] V. Sreeramulu, K. K. Haldar, A. Patra, and D. N. Rao, *J. Phys. Chem. C*, **2014**, 118, 30333.
- [2] W. Wang, Y. Wu, Q. Wu, J. Hua and J. Zhao, *Nature Scientific Reports*, **2016**, 6, 22072.
- [3] H. Morkoc and U. Ozgur, WILEY-VCH, Weinheim, **2009**.
- [4] A. B. Djurisic and Y. H. Leung, *Small*, **2006**, 2, 944.
- [5] A. Singh, S. Kumar, R. Das and P. K. Sahoo, *RSC Adv.*, **2015**, 5, 88767.
- [6] R. Prasanth, L. K. van Vugt, D. A. M. Vanmaekelbergh and H. C. Gerritsen, *Appl. Phys. Lett.*, **2006**, 88, 181501.
- [7] B. F. Levine, *Phys. Rev. Lett.*, **1970**, 25, 440.
- [8] Z. L. Wang, *J. Phys.: Condens. Matter*, **2004**, 16, R829.
- [9] D. C. Kundaliya et al., *Nat. Mater.*, **2004**, 3, 709.
- [10] B. Panigrahy, M. Aslam and D. Bahadur, *J. Phys. Chem. C*, **2010**, 114, 11758.
- [11] D.L. Hou, R.B. Zhao, Y. Y. Wei, C. M. Zhen, C. F. Pan, G. D. Tang, *Current Applied Physics*, **2010**, 10, 124.
- [12] S. J. Han, J. W. Song, C.H. Yang, S. H. Park, J.H. Park, Y. H. Jeong and K. W. Rhie. *Appl. Phys. Lett.*, **2002**, 81, 4212.
- [13] R. K. Sharma, S. Patel and K. C. Pargaien, *Adv. Nat. Sci.: Nanosci. Nanotechnol.*, **2012**, 3, 035005.
- [14] X. Zhang, H. Fang, S. Tang and W. Ji, *Appl. Phys. B: Lasers Opt.*, **1997**, 65, 549.
- [15] J. H. Lin, Y. J. Chen, H. Y. Lin and W. Hsieh, *J. Appl. Phys.*, **2005**, 97, 033526.

- [16] H. W. Lee, K. M. Lee, S. Lee, K. H. Koh, J. Y. Park, K. Kim and F. Rotermund, *Chem. Phys. Lett.*, **2007**, 447, 86.
- [17] S. K. Min, C.-H. Oh, G. J. Lee, Y. P. Lee, S. K. Min and S. H. Han, *J. Korean Phys. Soc.*, **2009**, 55, 1005.
- [18] www.imagej.net.
- [19] J. Wang, Z. Wang, B. Huang, Y. Ma, Y. Liu, X. Qin, X. Zhang, and Y. Dai, *Appl. Mater. Interfaces* **2012**, 4, 4024.
- [20] J. Tauc, R. Grigorovici, A. Vancu, *Physica status solidi (b)*., **1966**, 15, 627.
- [21] C. Johnson, K. Kittilstved, T. Kaspar, T. Droubay, S. Chambers, G. Salley and D. Gamelin, *Phys. Rev. B: Condens. Matter Mater. Phys.*, **2010**, 82, 115202.
- [22] C. H. Ahn, Y. Y. Kim, D. C. Kim, S. K. Mohanta, and H. K. Cho, *J. Appl. Phys.*, **2009**, 105, 013502.
- [23] K. H. Tam et al., *J. Phys. Chem. B*, **2006**, 110, 20865.
- [24] M. Sheik-Bahae, A. A. Said, T.-H. Wei, D. J. Hagan and E. W. Van Stryland, *IEEE J. Quantum Electron.*, **1990**, 26, 760.
- [25] M. Yin, H. Li, S. H. Tang and W. Ji, *Appl. Phys. B*, **2000**, 70, 587.
- [26] J. H. Lin, Y. J. Chen, H. Y. Lin and W. Hsieh, *J. Appl. Phys.*, **2005**, 97, 033526.
- [27] C. Torres-Torres, M. Trejo-Valdez, H. Sobral, P. Santiago-Jacinto and J. A. Reyes-Esqueda, *J. Phys. Chem. C*, **2009**, 113, 13515.
- [28] S. Arab, P. D. Anderson, M. Yao, C. Zhou, P. D. Dapkus, M. L. Povinelli and S. B. Cronin, *Nano Res.*, **2014**, 7, 1146.

Chapter 7

Summary and future perspectives

This thesis is devoted to study the influence of extended and point defects on optical and electrical properties of aqueous grown ZnO nanorods. For this purpose, the extended defects in ZnO nanorods were incorporated in two different methods.

(I) In the first method, the extended defects were incorporated into the twin nanorods by sandwiching an amorphous layer between two crystalline segments of ZnO nanorods.

(II) In the second method, extended defects were produced by coating thin layers of Au (1 - 5nm) on the surface of vertically aligned ZnO nanotapers.

The point defects were created in ZnO nanorods using O^+ ion implantation and chemical doping of Mn. The point defects created by implantation are distributed inside the nanorods up to certain depth depending on the projectile range of ions, whereas the point defects created by chemical doping are randomly distributed throughout the nanorods. This dissertation aimed at the engineering of extended and point defects in ZnO nanorods and their utilization in optoelectronic, photonic and electronic applications. This chapter is dedicated to the conclusions of this study and their future perspectives in device applications.

The motivation for the study of 1D-ZnO nanostructures with a brief review of the literature was introduced in chapter 1. The literature also included the potential research area related to the direct and wide band gap ZnO nanostructures, showing the current state of the art ideas on the topic. The experimental and characterization techniques used in this thesis work were briefly described in the chapter 2. The findings of this thesis and their future perspectives are as follows:

Twin nanorods

In order to create extended defects, a unique CAC architecture of ZnO having an amorphous layer sandwiched between two crystalline segments of ZnO were synthesized using single step

aqueous growth technique. We call these unique structures twin nanorods. A wurtzite CAC homojunction in a single nanorod is a major finding. The low-temperature evolution of twin nanorods can effectively reduce the cost for the ultimate realization of nanoscale device fabrication based on a single nanorod. The morphology of TNRs was explored using FESEM, and the detailed characterization of the amorphous layer was carried out using HRTEM technique. The presence of amorphous layer in between two crystalline segments of nanorods confirmed the creation of extended defects in ZnO nanorods. The HRTEM results showed that the thickness of the amorphous layer was found to be tunable with the ramping rate of the reaction media. The optical properties of TNRs were studied using UV-visible and PL spectroscopic techniques. The study of band gap measurements of TNRs showed the strong dependency on the growth-induced stress developed inside the host matrix. In PL spectrum, the deconvolution analysis of the phonon replicas of the free exciton emission peak exhibits that beyond a certain thickness the amorphous layers in twin nanorods acts as effective phonon barrier. However, such nanoscale junction barriers will be transparent to long wavelength acoustic phonon modes, and the optical phonon mode excited on one crystalline side of the CAC junction is likely to get damped significantly at the amorphous barrier if the phonon mode wavelength is comparable to the thickness of the barrier. The results showed that the engineering of the thickness of the amorphous layer makes it transparent (4nm and 1.5nm) for the phonon modes and the TNRJs can be used as phonon tunnel device. This is a major finding of this work and has never been reported earlier. Measuring the transmitted intensity of phonons on one crystalline side of the barrier by exciting phonon modes on the other crystalline side, using micro-Raman and atomic force microscopy based techniques, would provide a direct measure of the phonon tunneling coefficient. Such junctions can be utilized in fabricating phonon tunnel devices for advancing ZnO nanorods based optoelectronic and electronic devices.

The analysis of temperature dependent PL spectra of TNRs exhibit that both the electron-phonon interaction and lattice dilation contribute to the redshift of FX emissions. The appearance of localized defect peaks at low temperatures confirms the presence of extended defects in twin nanorods and causes a loss in the near band edge emission intensity, which commensurate with the appearance of the defect peaks. The loss in emission intensity was caused by a non-radiative transfer of carriers from the conduction band to the defect bands.

Defects in TNRs probed with the lower excitation energy showed dominating DLE over NBE emission. These deep level emission unveiled strong temperature sensitivity in the cryogenic

temperature range, which show the applicability of the TNRs in non-contact nanothermometry applications.

Au-decorated nanotapers

The tip geometry of nanotapers are suitable for field emission. The topography of Au decorated nanotapers was characterized by FESEM, where the FESEM images showed corrugated decoration of Au on ZnO nanotapers. XRD technique was used for the study of the crystal structure of nanotapers. EXAFS technique was employed to study the local crystal structure of as-grown and Au-decorated nanotapers around the Zn-K edge. The work function of nanotapers was mapped using KPFM, which showed a strong dependence on the thickness of Au film. The FE properties of Au coated nanotapers were compared with as-grown nanotapers, where Au decorated samples showed efficient field emission characteristics over as-grown. The TUNA results also showed a very uniform and efficient tunneling current profile for Au-decorated nanotapers compared to as-grown nanotapers. We believe that metal induced mid-gap states formed at the Au-ZnO interface are responsible for the observed improved FE characteristics, as a consequence of the drop in the effective work function of Au decorated ZnO nanotapers. Since the low-cost hydrothermal method and corrugated metal evaporation techniques are easily scalable, the spatial uniformity and efficient field emission characteristics can be very useful for the fabrication of large scale field emission based devices and also significantly reduce their cost.

O⁺ ion implantation

This section includes the aqueous growth of vertically aligned ZnO nanorods and influence of O⁺ ions on their optical and electronic properties. The O⁺ ions were implanted in nanorods with three different energies 50, 100 and 350 keV. O⁺ ions of energies 50 and 350keV (at $\Phi = 5 \times 10^{16}$ ions/cm²) were implanted successively in nanorods to form tandem O-rich/as-grown/O-rich/as-grown structures in a single nanorod. O⁺ ions having energy of 100keV were implanted in nanorods at three different ion fluence $\Phi = 5 \times 10^{14}$ ions/cm², $\Phi = 5 \times 10^{15}$ ions/cm², $\Phi = 5 \times 10^{16}$ ions/cm². The morphological and structural characterization were carried out using FESEM and XRD techniques. The FESEM and XRD measurements reveal the c-axis oriented hexagonal structure of ZnO nanorods, and which remain preserved even after implantation. The XPS was employed to analyze the pre-implantation and post-implantation surface chemistry of the nanorods. The XPS results showed that at $\Phi = 5 \times 10^{16}$ ions/cm² the concentration of V_O decreases due to saturation in vacancy formation at high ion fluence and excess of O⁺

ions which form O_i . The influence of point defects induced by O^+ ion implantation on the RT optical properties of nanorods were studied by UV-visible, PL and Raman spectroscopy. Post-implantation, the optical absorption edge of samples showed a drop of 0.1eV compared to as-grown sample. This is consistent with the fact of formation of vacancies by ion implantation. The PL studies exhibit formation of nonradiative transition centres leading to complete suppression of NBE emission of ZnO nanorods. The annealing treatment of the samples in vacuum for 3 hours recovered the near band edge emission in the PL spectrum of each sample, followed by deep level emissions. In these PL spectra, the DLE dominated over the NBE emission. The deconvolution analysis of these PL spectra showed that these emissions are associated with O_i and V_O , where O_i dominate over V_O . We attribute this to the annihilation of V_O by the presence of the excess of O^+ and formation of more O_i at high-temperature annealing. The post-annealing PL results suggest that successive O^+ ion implantation in ZnO nanorods may create the O-rich/as-grown/O-rich/as-grown tandem like environment inside them, where O_i may act as shallow donor levels. C-AFM technique was employed to investigate the influence of O^+ ion implantation on their local electrical transport characteristics. The first derivative 2D current map of as-grown nanorods exhibits current burst from the side facets of nanorods, whereas it localizes for implanted samples. We attribute this to the trapping of charge carriers into the defects created by implantation. The local electrical transport characteristics of samples improved after annealing treatment.

Mn-doped nanorods

This part covers the aqueous growth of Mn doped ZnO nanorods on the ITO coated glass substrates and study the influence of point defects created by Mn doping on their nonlinear optical properties. In this context the morphology of nanorods and confirmation of Mn-doping was carried out using FESEM and EDX technique, respectively. The FESEM results showed that the nanorods were randomly oriented unlike the nanorods grown on seed Si substrates. The shift towards lower 2θ value of (002) peak in XRD pattern further confirmed the doping of Mn at Zn sites resulting in expansion of ZnO unit cell. The influence of point defects on optical properties of doped nanorods were studied using UV-visible, PL spectroscopy, and Z-scan technique. The Tauc plots showed a drop of 0.7eV in the band gap of Mn-doped samples compared to un-doped sample, and we attribute this to V_{Zn} and/or V_O . A significant difference between PL spectra of undoped and doped samples is seen. The deconvolution analysis of PL spectra showed that Mn-doping in ZnO nanorods introduces various defect centers including

Zn_i , O_i , V_{Zn} , and V_O , where the Zn_i dominate over other centers. The presence of dominating Zn_i supports the shift in XRD pattern and confirms the Mn doping at Zn sites. Plots for the $I_{Defect-state}/I_{FX}$ versus Mn-doping percentage showed that with increasing doping percentage of Mn the defect densities in nanorods increases and was found maximum for 2.5% Mn-doping concentration. The CA nonlinear optical measurements on undoped and 0.5% Mn-doped NRs exhibit self-defocusing effect with significantly higher n_2 values as compared to ZnO thin films. The remarkably large third-order NLO behavior could be appreciated by observing the modifications in the geometrical arrangement and band structure of ZnO NRs with Mn-doping. In OA measurements the TPA characteristics for 0.5% Mn-doping is attributed to its absorption edge. The investigations on NLO characteristics suggest that point defects in ZnO nanorods created by Mn-doping facilitate improved NLO interactions. The NLO results suggest that Mn-doped ZnO nanorods can be utilized for fabricating ultra-fast photonic switches, efficient optical phase-shifters, and optical limiters etc.

7.1 Future prospectives

1. The phonon tunneling phenomena in CAC structures is worth investigating to improve the functionality of nanoscale devices, because efficient phonon transport is essential from the perspective of waste heat management in the nanostructures for large-scale integration. From the theoretical point of view, the understanding of the role of defects in electron-phonon interaction in such CAC structures can be further explored. The CAC structures can be utilized for phonon tunnel devices, and nano-thermometry applications etc.
2. The simple hydrothermal method and corrugated metal evaporation techniques are easily scalable, the spatial uniformity and low turn on voltages observed in our measurements can be very useful for large scale field emission based devices.
3. The depth selective approach to create defects in ZnO nanorods can be utilized for the fabrication of single nanorod based electronic devices like p-n junction /p-n-p-n tandem junctions.
4. Different dopant concentration-dependent nonlinear optical properties of ZnO nanorods can be further explored for nonlinear optical device purpose. The two photon absorption and saturable absorption characteristics of Mn-doped ZnO nanorods can be utilized in fabricating photonic devices like optical limiters, phase-shifters, lasers, ultra-fast photonic switches.

Journal Publications, and Conference Proceedings

Journal Publications

1. Avanendra Singh, Kartik Senapati, Biswarup Satpati, Mohit Kumar, Pratap K. Sahoo, **Nanoscale interface engineering in ZnO twin nanorods for proposed phonon tunnel devices**, Phys. Chem. Chem. Phys., 2015, 17, 4277.
2. Avanendra Singh, Samir Kumar*, Ritwick Das and Pratap K. Sahoo, **Defect-assisted saturable absorption characteristics in Mn-doped ZnO nanorods**, RSC Adv., 2015, 5, 88767. (* equal contribution).
3. Avanendra Singh, Kartik Senapati, Mohit Kumar, Tapobrata Som, Anil K. Sinha, and Pratap K. Sahoo, **Role of work function in field emission enhancement of Au island decorated vertically aligned ZnO nanotapers**, Appl. Surf. Sci. 2017, 411, 117.
4. Avanendra Singh, K. Senapati, D. P. Datta, R. Singh, T. Som, S. Bhunia, D. Kanjilal, Pratap K. Sahoo, **Synthesis of p-n junctions in ZnO nanorods by O⁺ ion implantation**, Nucl. Instrum. Methods Phys. Res. B, 2017, 409, 143.
5. Avanendra Singh, Kartik Senapati, Biswarup Satpati, Pratap K. Sahoo, **Suppression of near band edge emission in specially engineered ZnO twin nanorods**, Phys. Chem. Chem. Phys., 2017, 19, 14012.
6. Vantari Siva, Debi Prasad Datta, Avanendra Singh, T. Som, P. K. Sahoo, **Nanocomposite Synthesis and photoluminescence properties of MeV Au-ion beam modified Ni thin films**, Appl. Surf. Sci., 2016, 360, 276. (not included in thesis)
7. Ranveer Singh, Mohit Kumar, Mahesh Saini, Avanendra Singh, Biswarup Satpati, Tapobrata Som, **Growth of TiO₂ thin films on chemically textured Si for solar cell applications as a hole-blocking and antireflection layer**, Appl. Surf. Sci., 2017, 418, 225. (not included in thesis)
8. D. P. Datta, V. Siva, Avanendra Singh, S. R. Joshi, D. Kanjilal, P. K. Sahoo, **Ion-beam-induced nanodots formation from Au/Si thin films on quartz surface**, Nucl. Instrum. Methods Phys. Res. B, 2016, 379, 48. (not included in thesis)
9. R. Panda, S. Bhattacharya, R. Samal, Avanendra Singh, P. K. Sahoo, P. K. Datta, S. K. Das, **Second harmonic generation of femtosecond pulses using ZnO nanorods grown by chemical bath deposition with drop casted seed layer**, Journal of Nonlinear Optical Physics and Materials 2016, 25, 1650029. (not included in thesis)

10. D.P. Datta, V. Siva, Avanendra Singh, D. Kanjilal and Pratap K. Sahoo, **Photoluminescent Au-Ge composite nanodots formation on the SiO₂ surface by ion induced dewetting**, Nucl. Instrum. Methods Phys. Res. B, 2017, 407, 141. (not included in thesis)
11. L. Khatua, R. Panda, Avanendra Singh, A. K. Nayak, P. Satapathy, D. Pradhan, Pratap Kumar Sahoo, S K S Parashar, S. K. Das, **Growth of significantly low dimensional Zinc Orthotitanate (Zn₂TiO₄) nanoparticles by solid state reaction method**, Science of Sintering (Accepted). (not included in thesis)

Conference Proceedings

1. Avanendra Singh, Kartik Senapati, K. K. Nanda, Pratap K. Sahoo, **Strong Red luminescent twin ZnO nanorods for noncontact Nano-thermometry applications**, MRS Advances, 2016, 1, 869.

Conference Presentations

1. Avanendra Singh, Mohit Kumar, K. Senapati, T. Som, and Pratap K. Sahoo, **Enhanced field emission from gold-corrugated ZnO nanorods**, Indo-French Symposium on Functional Metal-Organics: Applications in Materials and Catalysis, 2015, NISER, Bhubaneswar, India.
2. Avanendra Singh and Pratap K. Sahoo, **Room temperature ferromagnetism and optical properties of Mn doped ZnO Nanorods**, Indo-Japan workshop on Magnetism at Nanoscale (IJWMN), 2015, NISER, Bhubaneswar, India.
3. Avanendra Singh, Samir Kumar, Ritwick Das and Pratap Kumar Sahoo, **Nonlinear optical switching in Mn-doped ZnO nanorods**, Current trends in condensed matter Physics (CTCMP), 2015, NISER, Bhubaneswar, India.
4. Avanendra Singh, Debi Prasad Datta, Kartik Senapati and Pratap K. Sahoo, **Band Gap Tailoring and Optical properties of Aqueous Grown ZnO Nanowires by Oxygen Ion Implantation**, Radiation effects in Insulators, 2015, MNIT, Jaipur, India.
5. Avanendra Singh, Kartik Senapati, Karuna Kar Nanda and Pratap K. Sahoo, **Red luminescent twin ZnO nanorods for proposed phonon tunnel device and nano-thermometry application**, APS March meeting, 2016, Baltimore, USA.

Workshop/training

1. National Workshop on Fluorescence and Raman Techniques, 2014, IISER, Pune, India.